Microscopic study of the behavior of water in a single pore under vibration to intensify drying

Wangshu Chen

NNT : 2019SACLC054

Thèse de doctorat

Microscopic study of the behavior of water in a single pore under vibration to intensify drying

Thèse de doctorat de l'Université Paris-Saclay
préparée à CentraleSupélec

École doctorale n°579 Sciences mécaniques et énergétiques, matériaux et géosciences (SMEMAG)
Spécialité de doctorat : Génie des procédés

Thèse présentée et soutenue à Gif-sur-Yvette, le 2 juillet 2019, par

Wangshu CHEN

Composition du Jury :

M. Benoît GOYEAU Professeur, EM2C, CentraleSupélec	Président
M. Fethi ALOUI Professeur, Université Polytechnique Hauts-de-France	Rapporteur
M. Romain RÉMOND Maître de conférences, Université de Lorraine	Rapporteur
M. Mohamed El Amine BEN AMARA Maître de conférences, LESTE, Université de Monastir	Examinateur
M. Patrick PERRÉ Professeur, LGPM, CentraleSupélec	Directeur de thèse
M. Julien COLIN Maître de conférences, LGPM, CentraleSupélec	Encadrant

Acknowledgements

First, I would like to express my sincere thanks to my supervisors Prof. Patrick Perré, Prof. Moncef Stambouli, and Dr. Julien Colin for giving me such a precious opportunity to complete my research work. And I also need to show my gratitude to them for their continuous support, kind help and patience. Otherwise, I could not finish my thesis.

Meanwhile, I wish to give my respect and gratitude to my thesis committee: Prof. Benoit Goyeau, Prof. Fethi Aloui, Dr. Romain Remond, and Dr. Mohamed El Amine Ben Amara for their insightful and unique comments to help me improve my dissertation.

Moreover, I need to thank M. Joel Casalinho for the instruction and powerful support on the aspect of experimental devices. I also give my thankfulness to Mme. Corinne Roussel, Mme. Jamila El Bekri, Mme. Magali Dupuy, Mme. Sandra Julien-Anchier, Mme. Elisabeth Lobo, M. Cyril Breton, M. Vincent Butin, M. Pin Lu as well as all the staffs in LGPM for their kind help for my work and life in CentraleSupélec.

Then I would like to owe my sincere gratitude to my fellows and my friends, who helped and supported me during the past four years, I cherish this period of time in France with you: Xiaoxin Lu, Yu Liu, Huan Du, Li Gong, Jing Zhang, Na Cui, Angela La, Yuanyuan He, Manasa Periyapattana, Yong Tian, Jérôme Grenier, Moudhaffar Nouri, Moustapha Diallo, John Pachon, Clare Roussey, Wenbiao Jiang, Wei Ai, etc.

Additionally, I wish to express my gratitude to the financial support from China Scholarship Council.

Last but not the least, I would like to show my deepest gratitude and love to my parents for their understanding and consistent support through my life.

Table of contents

Notations

- **Symbols**

a	Acceleration	$m^2 \cdot s^{-1}$
A	Cross section	m^2
A	Amplitude	m
D	Diameter	m
D_v	Diffusion coefficient	$m^2 \cdot s^{-1}$
F	Force	N
f	Frequency	s^{-1}
f_r	Resonance frequency	s^{-1}
F_c	Capillary force	N
F_i（*chapter 4*）	Inertia	N
F_i（*chapter 5*）	Force acting on layer *i*	N
g	Acceleration of gravity	$m \cdot s^{-2}$
h_H	External heat transfer coefficient	$W \cdot m^{-2} \cdot K^{-1}$
h_M	External mass transfer coefficient	$kg \cdot m^{-2} \cdot s^{-1}$
j_v	Diffusion flux of the vapor	$kg \cdot m^{-2} \cdot s^{-1}$
k	Permeability	m^2
L	Length	m
L_e	Length of actual flow path	m
L_s	Length of straight path	m

l_w	Length of water	m
m	Mass	kg
N	Amplification coefficient	
n	Mole number	mol
N_c	Capillary effect	
N_v	Viscous effect	
Q	Volumetric flow rate	$m^3 \cdot s^{-1}$
R	Ideal gas constant	$J \cdot mol^{-1} \cdot K^{-1}$
r	Radius	m
r_c	Curvature radius	m
t	Time	s
T	Characteristic time of the signal	s
V	Volume	m^3
v	Velocity	$m \cdot s^{-1}$
ω_v	Mass fraction of vapor	
X	Dry-basis moisture content	
x	Displacement	m
Δp	Total pressure drop	Pa

- **Greek letters**

Γ	Vibration number	
δ	Thickness of Stokes boundary layer	m

ε	Noise level	
θ	Contact angle	°
κ	Curvature	m^{-1}
μ	Dynamic viscosity	Pa·s
ρ	Density	$kg \cdot m^{-3}$
σ	Surface tension	$J \cdot m^{-2}$
τ *(chapter 1)*	Tortuosity	
τ *(chapter 4)*	Characteristic viscous diffusion time	s
φ	Phase change	°
Φ	Porosity	
ω	Angular frequency	s^{-1}

- **Subscripts**

0	Initial value
a	Advancing
AB	Angular bisector
air	Air
c	Center of mass
cap1	On the left side of meniscus
cap2	On the right side of meniscus
DR	From point D to the right edge of image
ext	External wall of the capillary tube

gap	Discontinuous part of the curve
h	Horizontal
i	Sequence
max	Maximum
min	Minimum
notch	Mass center of the notch on the capillary external wall
p	Perpendicular line
Patm	Atmospheric pressure
P1	Air pressure of the blocked air
platform	Top external wall without the notch
pld	Point-line distance
r	Receding
s	static
spring	Spring
tube	Capillary tube
t-w	From tube to water index
v	Vertical
water	Water index
-x	Horizontal direction

- **Superscripts**

f	Friction
Poiseuille	Laminar Poiseuille flow

- **Constants**

R	8.31451	$J \cdot mol^{-1} \cdot K^{-1}$
g	9.8	$m \cdot s^{-2}$
P_{air}	101325	Pa
ρ_{water}	1000	$kg \cdot m^{-3}$

- **Abbreviations**

CV	Control volume
FID	Fine inner diameter
FPS	Frame per second
GS	Gray scale
$\lvert\Delta GS\rvert_{max}$	Maximum absolute grayscale change
$\overline{GS_1}$	Averaged grayscale of vertical scanning in top direction
$\overline{GS_2}$	Averaged grayscale of vertical scanning in bottom direction
$\overline{GS}$	Averaged grayscale of horizontal scanning
ΔGS	Grayscale change
P-HL	First point with grayscale change equaling to zero on the left of point P-H
P-HR	First point with grayscale change equaling to zero on the right of point P-H
P-V_B	Reference point of grayscale change vertical scanning in bottom direction
P-V_B*L*	First point with grayscale change equaling to zero on the left of point P-V_B
P-V_B*R*	First point with grayscale change equaling to zero on the right of point P-V_B
P-V_T	Reference point of grayscale change of vertical scanning in top direction

P-V_TL	First point with grayscale change equaling to zero on the left of point P-V_T
P-V_TR	First point with grayscale change equaling to zero on the right of point P-V_T
rc_max	Maximum curvature radius
rc_min	Minimum curvature radius
RD	Relative displacement between water and tube
RV	Relative velocity between water and tube
S1	Series 1
S2	Series 2
TID	Thick inner diameter

General introduction

Porous media are materials comprising matrix and pores. They widely exist on our daily life, such as the grains, papers, woods, and clothes, etc.[1]. A moist porous material is easy to corrupt or to deform. For the sake of preservation or utilization of these porous media, the drying seems particularly important.

In the modern industry, drying technology is applied extensively in different fields, such as the food industry[2–4] and pharmacy industry[5,6]. It is also one of the most energy-consumption units in the productive process. Since the energy crisis in 1970s, the topics of saving energy and improving production efficiency have obtained more and more attention. Several new technologies were introduced to assist the drying process, such as the infrared (IR)[7,8], the vacuum technology[9–12], the microwaves/high-frequency waves[13–16], and the vibrations[17–20]. Investigations conducted to understand the intensification mechanisms allowed to optimize the parameters (such as temperature, relative humidity, and air velocity) of the drying units.

Vibration technology is verified as an efficient assisted approach. The external heat and mass transfer coefficients at the surface of wet materials can be enhanced by the air turbulence caused by the sample vibration. The moisture migration inside the wet materials can be improved by activating the absorbed water, the cavitation effect, etc.[21–24]. The vibration can act on the solid, liquid, and gaseous phases and intensify the drying process at low temperature without inducing significant sample heating. This intensification approach makes sense for the drying of heat-sensitive materials, such as some pharmacies.

Although intensification of porous media drying assisted by vibration has been characterized, a better understanding of the involved mechanisms is still needed. Challenges for understanding the water behavior in two simplified pore models (symmetrical and asymmetrical geometries), which are investigated in this thesis, are summarized as below:

1. To develop efficient experimental and numerical tools to observe and characterize the water behavior in a single pore under vibration,

2. To investigate the effect of parameters of sinusoid vibrations (frequency and amplitude) on the water behavior.

In chapter 1, a brief introduction about drying of porous media will be given, from the fundamental concepts of drying to some intensification approaches applicable to the process, and the corresponding mechanisms.

In chapter 2, the experimental device to study the water behavior under sinusoid vibration is presented. It consists a capillary tube (simulating a pore) partially filled with water, a vibration chain, an optical bench, and a temperature/relative humidity sensor.

In chapter 3, we present an image processing procedure to automatically identify the water/air interface and analyze the liquid behavior in the capillary tube during vibration.

In chapter 4, we use experimental methods to study the effects of parameters of sinusoid vibration on water behavior in tubes with symmetrical geometry. Two new dimensionless numbers are introduced to identify the relevant conditions to apply for studying the coupled effects of amplitude and frequency.

In chapter 5, we focus on the water behavior in tubes with asymmetrical geometry under sinusoid vibration. Preliminary, a simplest model allows us to predict the resonance frequency for the system in order to find the relevant frequency range for tests. The effects of frequency on water behavior (water amplitude and phase change) are discussed. With advanced numerical tools, the effects of tube amplitude, dynamic viscosity of liquid, and contact angle on water behavior are also investigated.

Chapter 1: Intensification of drying through vibration: a state of art

1.1 Introduction

The moisture inside the porous media will cause a lot of inconvenience, such as the growth of bacteria in food during storage[25]. As another example, moisture content decreasing from wood leads to shrinkage of furniture and wood buildings[26]. To overcome these problems, drying is applied.

Drying intensification is a development tendency in process engineering, and it aims at the optimization of traditional technologies. It improves production efficiency, the process safety and the products quality with a low energy consumption[27]. The vacuum[10,11,28], the infrared red[29,30], the microwaves[31,32], and their hybrid technologies[33] were verified as efficient intensification methods. The vibration was also found to intensify the transfer mechanisms. The technology of vibrating drying has attracted more and more attention and been used in industry to improve the process, such as packed bed drying[34–36]: the vibration of particles can cause the mixing of the bed[37]. This results in an improving in the final quality of the dried products[38].

To optimize the drying process through intensification approaches, mechanisms have to be well understood. Previous works used both experimental and numerical methods, at macro- and micro-scales, and achieved fruitful results.

The purpose of this chapter is to introduce all the necessary elements for understanding the mechanisms involved in the drying intensification of porous media through vibration. The following content will give a detailed description of the porous media, the liquid water inside, and the drying of porous media.

1.2 Porous media at macroscale

1.2.1 Definition of the porous media

A porous media is defined as a material containing pores. It is composed of a solid phase (metal, mineral, organic materials, *etc*.) and a fluid phase (gas, liquid or their mix).

1.2.2 Examples of porous media

Figure 1-1. A picture of manufactured sand [39].

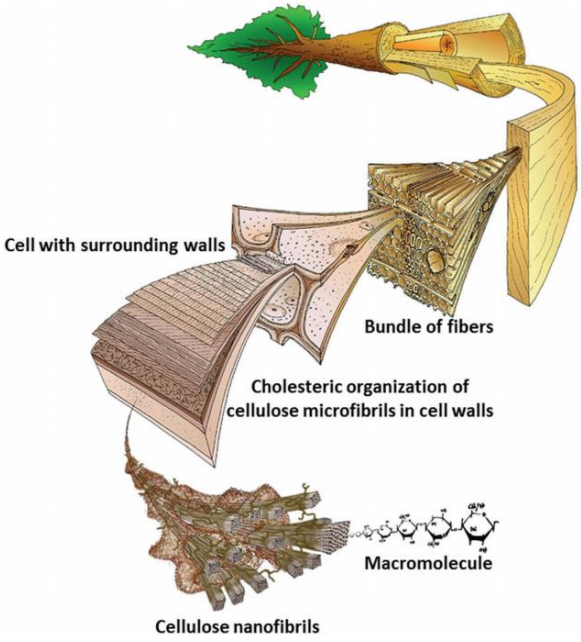

Figure 1-2 The hierarchical structure of the porous structure of wood [40].

Porous materials widely exist around us and play a significant role in many fields of our daily lives; such as food industry[20,41], wood industry[26,42], paper industry[43,44], and architecture. Natural porous media can be found universally, such as sand[45] (Figure 1-1), wood (Figure 1-2) and bones[46], plant leaves, wood, coral, pumice, and lava.

1.2.3 Macroscale properties

1.2.3.1 Porosity

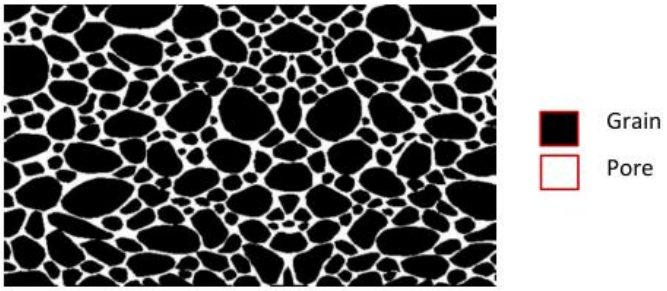

Figure 1-3 Cross-section image of a porous media[47]

The porosity of a porous media describes the volume fraction of void space in the material. Quantitatively, the porosity (∅) is the ratio of the pore volume over the total volume (Figure 1-3,). It is determined by

$$\emptyset = \frac{pore\ volume}{total\ volume} = 1 - \frac{grain\ volume}{total\ volume} \qquad \text{Equation 1-1}$$

In the two-phase flow (gas/liquid), the void fraction is defined as the fraction of gaseous phase in the flow-channels[48].

1.2.3.2 Permeability

Permeability (k) is defined by the Darcy's law. It is a measurement of the porous media's capacity

to transmit fluids due to a total pressure gradient. The Darcy's law is an equation describing the fluid flow passing through a porous media, with neglecting the gravitational forces[49]. It is given by

$$Q = \frac{kA\Delta p}{\mu L} \qquad \text{Equation 1-2}$$

where Q is the total flow, k is the permeability, A is the cross-section of the porous media, Δp is the total pressure drop, μ is dynamic viscosity, and L is the length over which the pressure drop is taking place.

Diffusion is another type of transfer whose driving force is a gradient of concentration.

1.2.3.3 Moisture content

Moisture content is the quantity of moisture inside the materials. The dry-basis moisture content (X) is given by[50]

$$X = \frac{m - m_0}{m_0} \qquad \text{Equation 1-3}$$

where m is the mass of the wet sample and m_0 is it oven-dried mass.

1.3 Porous media in microscale

The Macroscopic properties (transfer properties and the mechanical properties) of porous media depend on their internal morphology and on the properties of each phase of the porous media.

1.3.1 Pore structure

During the studying of porous media, many efforts have been taken into exploring the pore

structure to interpret the phenomena in it. The pore structure, represented by the internal morphology, is determined by the continuity of the phases, the pores geometry and the pore size distribution.

1.3.1.1 Continuity of phases and geometry of pores

The parameters of the macroscopic pore structure stand for the average behavior of a sample containing many pores[51]. The parameters of pore structure are those properties, which are entirely determined by the pore structure of the material and independent on other properties, such as the geometry and the pore size.

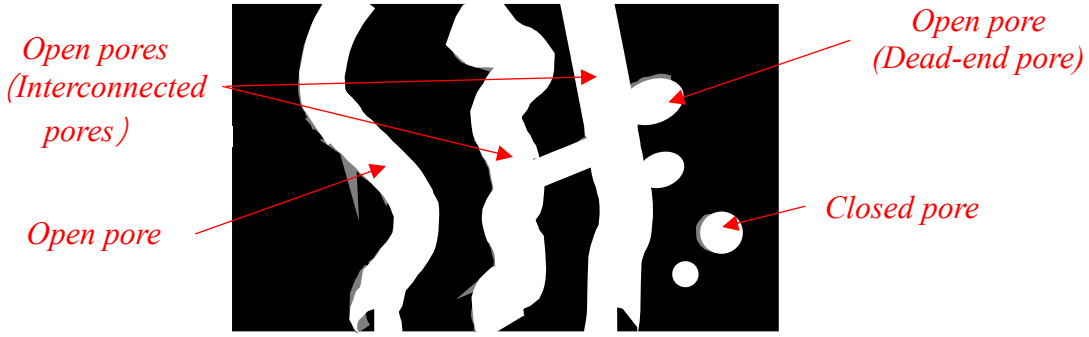

Figure 1-4 Schematic representation of the different type of pores

Inside the porous media, there are mainly two kinds of pores: the non-interconnected pores and the interconnected pores (Figure 1-4). The non-interconnected pores are also called isolated pores. They cannot make contribution to the fluid transfer inside the porosity, only the interconnected pores achieve. The dead-end pores are part of interconnected pore, but their contributions are limited in mass transport[51].

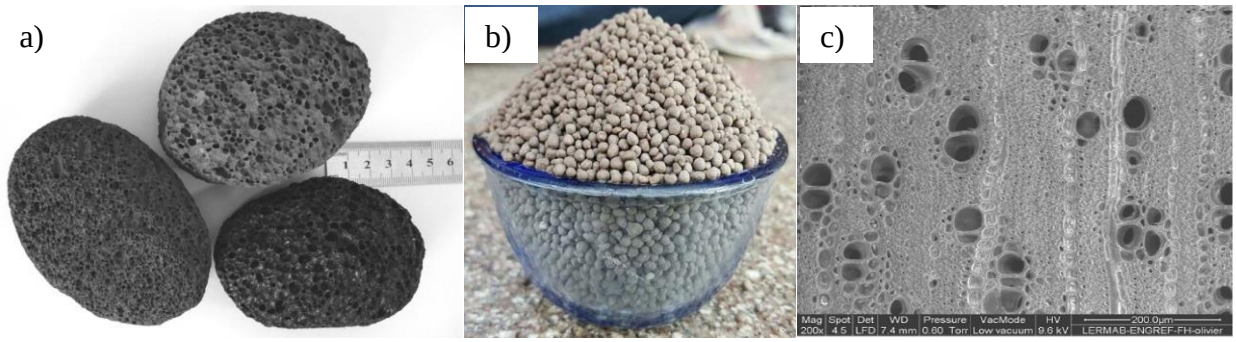

Figure 1-5 Pictures of (a)pumice[46], (b) brown sand pile [52],.and (c) Electronic microscopy of olive wood[53].

Different pore distributions inside the porous media form various continuities, of the solid matrix and of the voids. The foam-like structure (Figure 1-5a), the granular structure (Figure 1-5b), and the fibrous-like structure (Figure 1-5c) illustrate this diversity.

Thus, porous media can be classified according to the continuity of their solid and fluid phases. Table 1-1 displays some examples of porous media with the combination of different solid/liquid phases continuities.

Table 1-1 Porous media classification according to the continuity of the solid phase, liquid phase and examples

	Continuous solid phase	**Non-continuous solid phase**
Continuous fluid phase	Stem of plant, such as wood hemp, etc.	sand, grains and coffee beans
Non-continuous fluid phase	Expanded polystyrene	

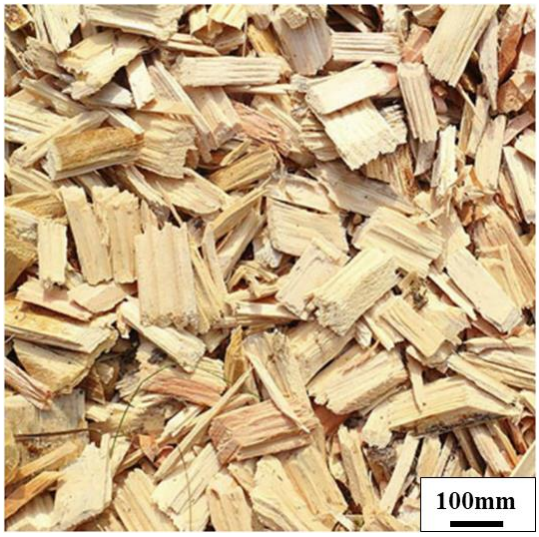

Figure 1-6. Picture of pine wood chips[54]

In some situation, a more complex combination of the solid/liquid phases also exists, such as the packed bed of wood chips (Figure 1-6). The packed bed is a granular media and each of its grains (chips) is also a porous media. There are two different scales of pores.

The pores geometry is often complex inside the porous media. If the fluid phase is continuous, the geometric tortuosity (τ) is one of the commonly used parameters for describing this pore geometry[55]. It is defined as the ratio of the actual length of the flow path (L_e) over the straight length (L_s) between two ends of the flow path[56]. Its expression is shown as Equation 1-4,

$$\tau = L_e/L_s \qquad \text{Equation 1-4}$$

Thanks to the improvement in imaging technologies, the 3-D pore geometry can be obtained, for example using the synchrotron micro-tomography (Figure 1-7). With these methods, information about the pore geometry can be acquired through image processing, if the pore is bigger than the voxel size.

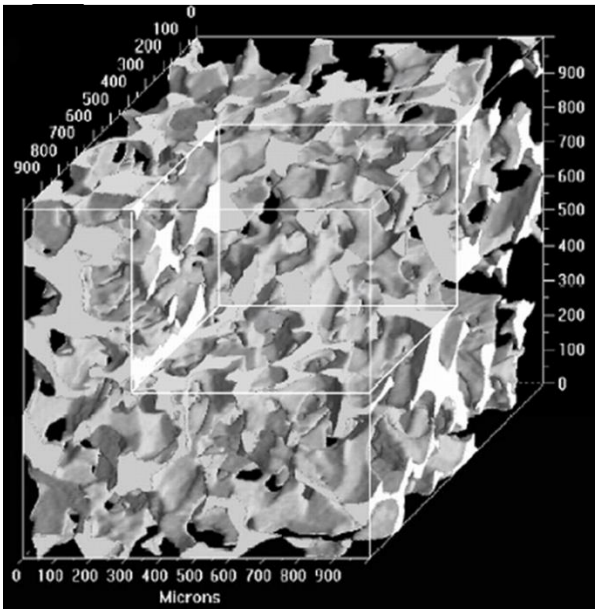

Figure 1-7 A 3-D image of sandstone by synchrotron tomography (pores are presented by grey part)[57]

1.3.1.2 Pore size

Everett D.[58] proposed a criterion for the classification of the pore size, as shown in Table 1-2.

Table 1-2 Classification of pores[58]

Classification of pores	**Size**
Micro-pore	< 2 nm
Meso-pore	2 – 50 nm
Macro-pore	> 50 nm

The pore size distribution is an important concept related to pore size. It is commonly used during the investigations of porous media. The pore size distribution can be defined by an image analysis method, which uses the largest sphere for fitting a pore, and obtains the statistical distribution of

the radius of these spheres inside the porous media[59]. It can be determined experimentally through several methods, such as mercury intrusion porosimetry, nitrogen adsorption measurements, and differential scanning calorimetry[60–65].

1.3.2 Water in porous media

1.3.2.1 Types of water

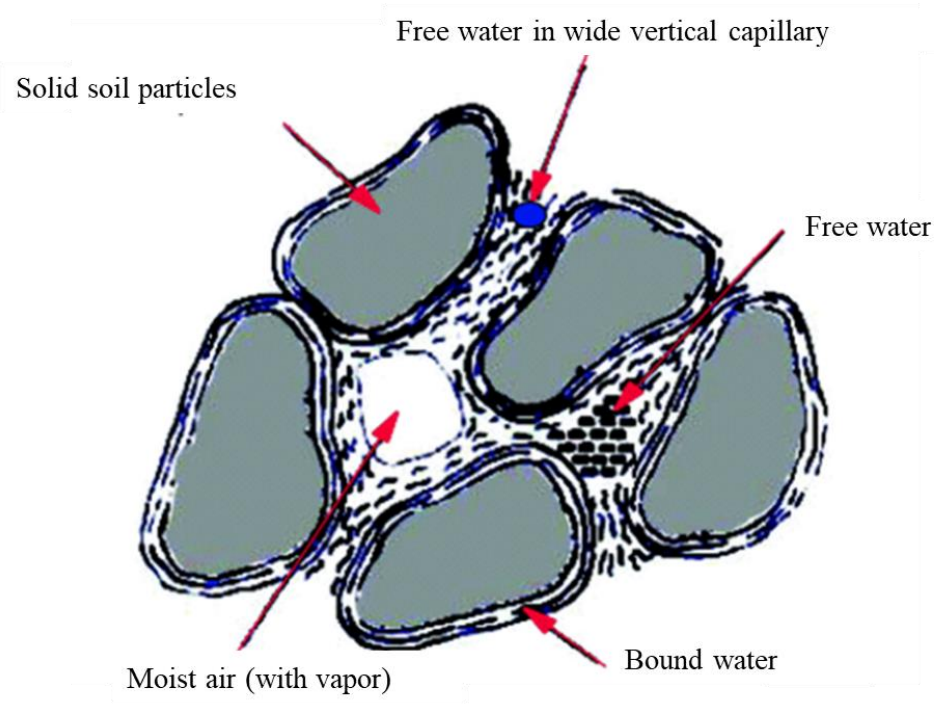

Figure 1-8 Schematic diagram of the water in the porous media[66]

Figure 1-8 presents all types of water in porous media, which are bound water, free liquid water and vapor.

The bound water is the water which is tightly linked to the solid phase of the material: it is adsorbed. Its enthalpy of vaporization is higher than the liquid water due to an additive differential energy of vaporization.

Free water is located in voids. Its properties are similar to the ones of liquid water.

If the voids are not filled with free water, they contain air including vapor.

The proportion of these three types of water depends on:

- Porosity (for free water),
- Hygroscopicity (for bound water),
- State of porous medium (saturated with liquid or not).

The water behavior inside the pores, such as the evaporation-condensation, and the migration, depends on its properties.

1.3.2.2 Liquid phase properties

1.3.2.2.1 Surface tension

Figure 1-9 Illustration of surface tension at the surface of a water droplet[67]

Surface tension is described as a tension acting perpendicularly on a unit length boundary of any two adjacent phases. Inside a pure liquid, each molecule is pulled equally in every direction by adjacent liquid molecules. Thus, the resultant force on these molecules is equal to zero. But the exposed molecules at the surface do not have neighboring molecules in all directions. On the contrary, they are pulled inward by the neighboring molecules (Figure 1-9), producing an internal pressure. In result, the liquid spontaneously contracts its surface area to keep the lowest surface

free energy. It makes the liquid acquire the least surface area possible[68].

1.3.2.2.2 Wettability

Wettability is the ability of a liquid to maintain contact with a solid surface, and it is controlled by the balance between the intermolecular interactions of adhesive type (liquid to the surface) and cohesive type (liquid to liquid)[69].

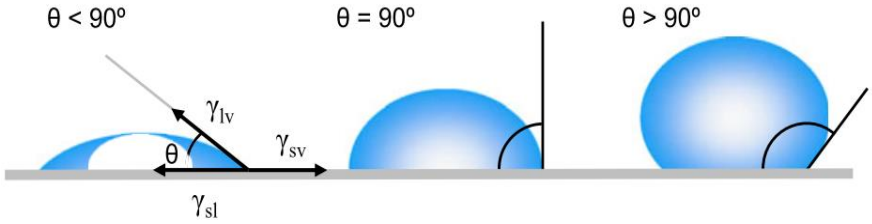

Figure 1-10. Illustration of contact angles of sessile liquid drops on a smooth solid surface[67]

For the characterization of the wettability of a solid, the contact angle is a significant parameter. It is the angle (Figure 1-10) measured where a liquid-gas interface encounters a solid surface. A unique equilibrium contact angle exists in a given solid/liquid/gas system at a certain pressure and temperature. Small contact angles (<< 90°) correspond to high wettability, while large contact angles (>> 90°) correspond to low wettability[67].

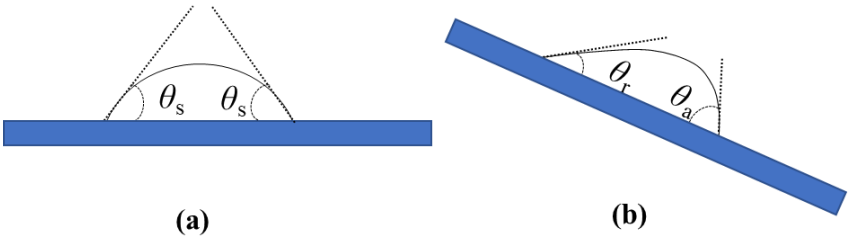

Figure 1-11 (a) A droplet on the horizontal plate with static(θ_s) contact angle, and (b) a droplet on the inclined plate with receding(θ_r) and advancing(θ_a) contact angle

When the liquid droplet is motionless, the contact angle is called static contact angle (θ_s). When it

moves, as Figure 1-11, the contact angle at the advancing edge of the liquid droplet is called advancing contact angle (θ_a), and that at the receding edge is called receding contact angle (θ_r), which are the upper and lower limit of the dynamic contact angle of the liquid droplet respectively[70].

1.3.2.2.3 Capillarity

Capillarity is one of the mains driving force for liquid migration in porous media. It occurs because of intermolecular forces between the liquid and surrounding solid surfaces. In a tube, the capillary force ($\overrightarrow{F_c}$) is given by

$$\overrightarrow{F_c} = 2\pi r\sigma cos\theta\overrightarrow{u_z} \qquad \text{Equation 1-5}$$

where σ is the surface tension, and θ is the contact angle. Therefore, the smaller the pore diameter is, the bigger, the capillary pressure is.

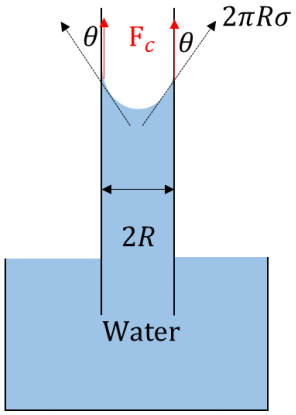

Figure 1-12 Schematic diagram of the capillary force effect in a capillary tube

For a tube in a container, the combination of the surface tension and wettability acts to raise up the liquid level[71] (Figure 1-12).

1.3.2.3 Viscosity

Dynamic viscosity (μ) of a fluid is the ratio of the shear stress (F/A) over the velocity gradient (dv_x/dz) (Figure 1-13) [50]. It is given by Equation 1-6:

$$\mu = \frac{F/A}{dv_x/dz} \qquad \text{Equation 1-6}$$

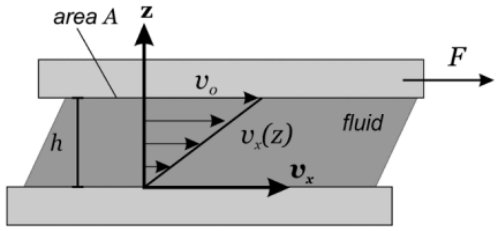

Figure 1-13 A description of the flow between two parallel plates [72]

The dynamic viscosity is due to the friction between the fluid molecules. Its unit is $Pa \cdot s$.

In the drying process, the liquid migration will be hindered in pores with small size due to the viscous resistance.

1.3.2.4 Saturation vapor pressure of air

The saturation vapor pressure of a system is the partial vapor pressure when there is an equilibrium between liquid phase and gaseous phase. It is a property of the liquid which is function of temperature[73]. It is related to the maximum quantity for vapor that can be included in moist air for a given temperature.

The gap between the vapor pressure and the saturated vapor pressure gives the potential of air to remove water from the porous media to dry.

1.4 Drying porous media and process intensification

1.4.1 Drying of porous media

Drying is the process of removing moisture. Its application to porous media can range from soil evaporation to the drying of food and building materials[74–78]. The convective drying is the most common approach.

As the statement in the literature[79–81], during the convection drying of porous media, the external influence factors are defined as the temperature, relative humidity, velocity and the direction of the air. Not only the external influence factors[82–86], but also the properties of the porous media can impact the drying kinetic, such as the permeability of porous media[87–89], and the size[90–92] and geometry[93] of samples.

Thus, in order to study of the porous media drying, a multiscale approach is needed, at both macroscale and microscale.

1.4.1.1 Macroscale study of porous media drying

The challenge of industrial drying is to balance product quality and economic performance, especially from energy and investments points of view. To meet a growing demand, more details about the products got attention, no longer just about the moisture content. Especially in the food industry, the effects of drying conditions on the nutrition content, color, and structure of the products[84,85,94–98] were studied. The drying optimization can be achieve through two complementary strategies: by using empirical approaches[29,99,100] or be developing 2D[101] to 3D[102,103] practical models with a good performance to make a prediction of the drying process or the properties of the products.

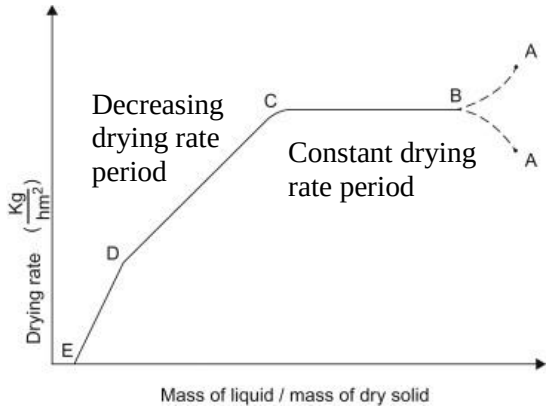

Figure 1-14 The variation of drying rate with respect to moisture content[104]

At the macroscale, the drying kinetic can be divided into a constant drying-rate period and a decreasing drying-rate period[81] (Figure 1-14). During the first period, the external surface of the porous media is supplied with free liquid water from the interior of the materials. The direction of liquid migration is from the region with high moisture concentration to that with lower moisture concentration. During the second period, the evaporation front migrates into the material.

1.4.1.2 Microscale study of porous media drying

For a deeper study of the moisture migration during the drying of porous media, phenomena and influence factors at microscale were also discussed.

During convective drying, the moisture transfer is due to three different mechanisms at microscale: liquid migration caused by capillary forces, bound water and vapor diffusion led by concentration gradients. Their relative importance varies during the process, depending on the considered drying period. First, the energy transfers from the surrounding to evaporate the moisture on the surface and internal moisture transfers to the surface of the solid due to capillarity and the subsequent evaporation occurs. Then, under a critical moisture content, the free water quantity is too low to ensure the continuity of the liquid phase in the pores from the core to the surface; the free water

will not migrate to the surface anymore. So, the evaporation front migrates inside the product. The diffusions (bound water and vapor) dominate[81].

Because of the efficiency of the first drying period, the capillary (related to the pore structure) transfer has to be well described. Moreover, any enhancement in liquid transfer to the surface would make this first period longer and thus improve the average drying rate of the process. For facilitating the study of liquid internal transfer at microscale, two kinds of methods were adopted to simplify the porous media structure.

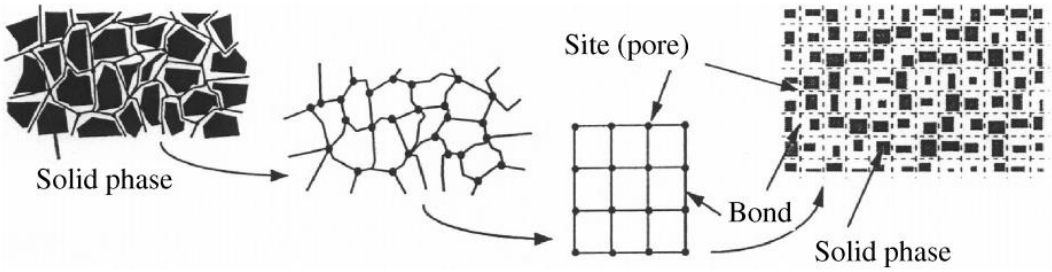

Figure 1-15 A description of porous media by pore network model[105]

One is pore networks approach[106–114] based on the network representation of the pore structure inside the porous media (Figure 1-15). With this method, an irregular shaped porous media can be simplified into a model with regular network structure[115–124]. It can be described as an offset of pore bodies – following size (diameter and length) and orientation distributions – and nodes[120]. This method is proper to study the effect of different parameters on the drying kinetics, such as the liquid viscosity[125], the pore shape[123], and the pore size distribution[126].

A simpler approach consists in the use of a single capillary tube approach. It simplifies the porous media to a bundle of parallel capillary tubes[127,128] or uses a single capillary tube to simulate a pore inside the porous media[129–135].

Inside the capillary tube, several phenomena related to the drying process have been investigated, such as the evaporation[136–139] and the migration of the liquid driven by capillary force[140].

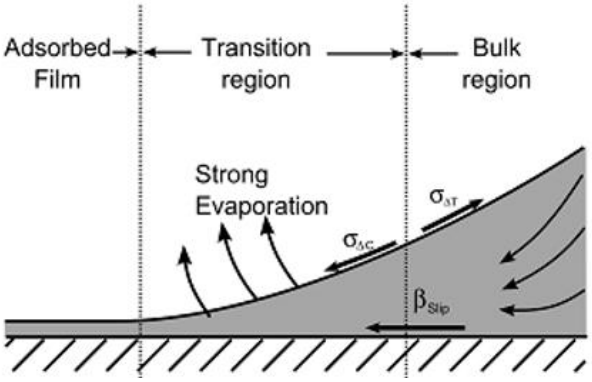

Figure 1-16 Discretization of an evaporating meniscus into three region based on the local dominant mass transfer mechanism[141]

The meniscus evaporation was widely investigated[141–146]. In these studies, the meniscus was divided into three regions[141,146], which are adsorbed film, transition region, and bulk region (Figure 1-16). In the adsorbed film, the conduction resistance is small, but the interfacial resistance is large, the attraction force between solid and liquid phase dominates. Thus, the evaporation is very small. In the bulk region, the meniscus curvature almost keeps constant. The interfacial resistance is small but the conduction resistance is large, which results in a lower evaporation intensity in this region. The transition region, between the adsorbed film and bulk region, is the one in which both resistances are small. The evaporation of the whole meniscus is mainly controlled by this region[147,148].

Afterwards, experimental and numerical studies focused on heat and mass transfer at the transition region, such as the determination of heat transfer coefficient[149] and Marangoni convection resulted by the temperature gradient across the region[150]. Different from the studies in a circular capillary tube, Prat et al.[130] studied the evaporation inside a square tube during the three periods of drying.

They found that the evaporation in a channel with corners is faster than that in a circular channel. Moreover, the effect of other pore shapes, contact angle, boundary layer thickness and capillary number on the drying were also studied[129,151]. In these studies, the capillary-viscous regime was divided into two sub-regimes depending on the position of the film tip: the first sub-regime with the film tip at the entrance of the tube, and the second sub-regime with receding film tip. It was found that the boundary layer thickness only has obvious effect in the first sub-regime; pore geometry and contact angle only have significant impact on drying in the second sub-regime; and the capillary number increasing makes the drying time approach the one measured for a circular capillary tube.

The liquid migration inside a vertical capillary tube driven by the capillary force was studied by Stange et al.[140]. They divided the rising flow into three continuous stages depending on which kind of force dominated against the capillary force. The dominating counter force in the first stage of flow is the inertia force. In this period, the velocity of meniscus increases. The significant counter force in the second stage is the total convective loss. The meniscus velocity keeps constant. The final stage of the flow is dominated by the friction force inside the capillary tube, and the meniscus velocity decreases in this stage.

1.4.2 Applied methods for drying intensification

Simultaneously to the exploring of drying mechanisms at both macroscale and microscale, many intensification approaches to assist drying are also developed. The process intensification in drying is aiming at enhance the removal rate of water by considering both internal and external heat and mass transfer.

All of them have their particularities and scope of application. In this section, several drying intensification technologies will be introduced, such as the vacuum, infrared, microwaves/high-frequency, and vibrations.

1.4.2.1 Infrared assisted drying of porous media

During the drying assisted by infrared, the material is exposed to the infrared radiation, the thermal energy can be absorbed by materials effectively. The radiant heat flux can be adjusted over a wide range of wavelengths to achieve a high drying rate for surface-wet materials[7,30,152–157]. The infrared (IR) radiation can be classified into 3 kinds according to the wavelength (near IR: 0.75 - 3 μm ; medium IR: 3 - 25 μm ; far IR: 25 - 100 μm). The application of infrared radiation on drying are common in the dehydration of coated films and in paper drying[158]. It presents significant advantages in comparison to conventional drying, such as reducing heating time, uniform surface heating and significant energy savings. But it is only a surface drying approach, its capital cost is about 1.67 times higher than for convection drying[158] and the process scaling up is not simple[159].

1.4.2.2 Vacuum assisted drying of porous media

Vacuum assisted drying is an efficient approach to dry the heat sensitive materials, those might discolor or decompose at high temperature. The reduction in pressure can result in the expansion and escape of gas inside pores, thus improving the moisture transfer, and forcing the moisture inside to the surface of the porous media[10–12,160–163].

It will improve all mass transfer types for which driving force is a gradient of pressure or partial pressure: vapor diffusion and capillarity. By decreasing the relative humidity, it will also improve the evaporating potential of air (difference between the vapor pressure and the saturated vapor

pressure). However, the external transfer is less efficient (especially heat transfer) due to the reducing of the volumetric heat capacity of air and of the external transfer coefficients. Moreover, it is not applicable for continuous operations because of the sealing requirements and the capital cost of vacuum drying is high because of the need of pump and thus a large amount of electricity consumption[164].

1.4.2.3 Microwaves/High frequency assisted drying of porous media

The applications of microwaves can also enhance the drying of porous media through volumetric heating[163]. It uses electromagnetic waves that can penetrate the material and makes the molecules vibrate. The applied frequency can vary from 300 MHz to 300 GHz but the most common used is 2.45 GHz, i.e. the resonance frequency of liquid water[165]. Microwave energy has been verified to have a proper low energy consumption to assist drying[166]. And the processing time reduction makes it an attractive method for intensifying the drying process. But some limitations have to be noticed, such as the high initial investment of industrial scale equipment and the specific sample size and shape required to achieve an effective drying[167].

1.4.2.4 Vibration assisted drying of porous media

Equipment is develop to make vibrabte material – with or without contact – during drying. Vibrations can enhance both external and internal mass transfer during the porous media drying, for example by decreasing the boundary layer thickness at the surface of the porous media and through internal heating up due to viscous dissipation. It can loosen the water in pores or between grains, and reduce the viscos effect of liquid diffusion[168]. In the meantime, it can also causes the cavitation to form bubbles. The expanding of bubbles inside pores can migrate the liquid phase,

and the implosion of these bubbles can result in the atomization at the liquid-gas interface[169]. But some other literatures[170,171] reported that the atomization at the liquid-gas interface may be caused by the rupture of the interface wave.

The industrial application of vibrations on porous media drying is realized by the vibration-fluidized bed dryer, escepially for drying granular materials[172], and a promising application is to be realized for drying clothes[173] or vegetables[3] by direct-contact ultrasonic technology.

Vibrations can intensify the drying process without increasing significantly the sample temperature and they preserve the integrity of products[168,174].

1.4.2.5 Contrast of different intensification methods

Table 1-3 Contrast of four intensification methods for drying

Methods	Mechanisms	Advantages	Disadvantages
Infrared	Convert the radiation to sensible heat	No direct contact	Surficial heating; high investment
Vacuum	Decrease the total air and partial vapor pressures	Low temperature	Not applicable for continuous operations; time consuming; energy consuming
Microwaves/ high frequency waves	Rotation of water molecules due to electromagnetic radiation	No direct contact; volumetric heating;	High initial investment; appropriate sample size and shape required
Vibration	Vibration of solid, liquid and gas phases	Low temperature; preserving product integrity	Experimental stage; noise

In Table 1-3, we make a summary of different approaches to assist the drying process with the corresponding mechanisms, advantages and disadvantages. Although the vibration assisted drying is still in experimental stage, it deserves our attention.

1.5 Focus on vibration assisted drying

Nowadays, the application of vibration is used in the coal industry, wood industry, and food industry[175,176]. The processing time for vibration assisted drying is shorter than common convective drying. It may result in a reduction of energy consumption[177]. Because its effects are mainly mechanical, it will not induce any significant sample heating, and the product quality could be preserved or enhanced[174]. It can also reduce viscosity, minimize diffusion boundary layer thickness and remove moisture from solid-liquid interfaces[19,21]. For elastic materials, a sponge effect can be caused by the ultrasound, this effect enhance the migration of liquid from the internal of the material to the solid surface[21].

With the support of vibration (ultrasound or acoustic), both internal and external resistances to mass transfer can be reduced[178]. According to the literature[179,180], the acoustic drying of foods acts on cavitation compression and expansion inside the biological tissues. The study of ultrasound assisted convective drying of fruits and vegetables[20] showed that the external mass transfer coefficient and effective moisture diffusivity were increased and the drying time was shortened.

During the investigations the effect of vibration on fluidized-bed drying, a significant dimensionless vibration number (Γ) was proposed[149–152]. It is the ratio of the maximum acceleration of vibration over the gravity acceleration, given by Equation 1-7

$$\Gamma = \frac{A(2\pi f)^2}{g} \qquad \text{Equation 1-7}$$

It is now a widely used indicator to characterize the vibration energy of vibration assisted fluidized-bed drying for granular particles. However, in the study of Meili et. Al.[184], it was found that different results were obtained under the same value of Γ, by varying amplitude and frequency simultaneously. Vibrations with low amplitude but high frequency could give a better drying result.

The impact of vibration on convection heat transfer was studied by Dawood et al.[175,185,186]. They found that the external heat transfer coefficient increased linearly with the rise of vibration frequency if the ratio of amplitude over tube diameter is higher than 0.5. Afterwards, they found that the heat transfer rate has a positive relationship with the intensity of vibration above a critical value of the amplitude and frequency product. And the correction approach for the external heat and mass transfer coefficients under the vibration were presented in the work of Strumillo and Kudra[175]. These corrections are proposed in Equation 1-8 and Equation 1-9:

$$h_{H,} = h_H(Af/u_A)^{0.65} \qquad \text{Equation 1-8}$$

$$h_{M,} = h_M(Af/u_A)^{0.65} \qquad \text{Equation 1-9}$$

where h_H is the external heat transfer coefficient (in W/m^2/K); A is the vibration amplitude (in m); f is the vibration frequency (in Hz), h_M is the external mass transfer coefficient (in kg/m^2/s) and u_A is the air velocity (m/s).

Inside a vertical capillary tube with one end sealed and the other end connecting to a reservoir, the effects of vibration on the motion of meniscus (liquid-gas interface) and thin film (extended part

of meniscus) were studied by Rao et al.[187]. It was found that there is a phase change between the meniscus and the thin film.

Although vibration has begun to attract more attention, a better understanding of mechanisms is required to optimize this technology. Especially, the characterization of evaporation at pore-scale will be useful for a multiscale modeling of the process.

1.6 The aim of this work

In this chapter, we described the drying of porous media at both macroscale and microscale, introduced some intensification approaches for the drying process and presented their corresponding mechanisms (advantages and disadvantages). Among them, we highlight the interest of vibration on the drying of porous media.

This study will focus on the porous media in microscopic scale (pore-scale) and investigate the water behavior under vibration inside a single pore.

To that end, we followed different steps:

- The first step of this work is to design and build up an experimental device in which a single pore – simulated by a capillary tube – is submitted to acoustic vibrations. An optical system is sued for data recording.
- We need to develop an effective image processing method to capture the water behavior inside the capillary tube.
- Thanks to these experimental and numerical tools, we will investigate the effects of the parameters of sinusoid vibrations (amplitude and frequency) on water behavior with

symmetrical and asymmetrical geometries. A set of properties (for example water amplitude and phase change) will be selected to assess the impact of applied vibration parameters (amplitude and frequency) on water behavior.

- Because of the numerous situations that could be studied by varying the amplitude and frequency, new dimensionless numbers (capillary effect and viscous effect) have to be defined in order to identify the relevant conditions to study.
- Finally, we will propose two models with the expectation to reproduce the water behavior and distinguish each phenomenon resulted by vibration.

.

Chapter 2: Materials and methods

This chapter will describe the details of the material, the experiment set-up, and all the preparation steps performed before experiments in order to study the liquid behavior at the pore scale. In this study, a capillary will be used to simulate a single pore of a porous medium.

2.1 Pore partially filled with water

2.1.1 Capillary tube

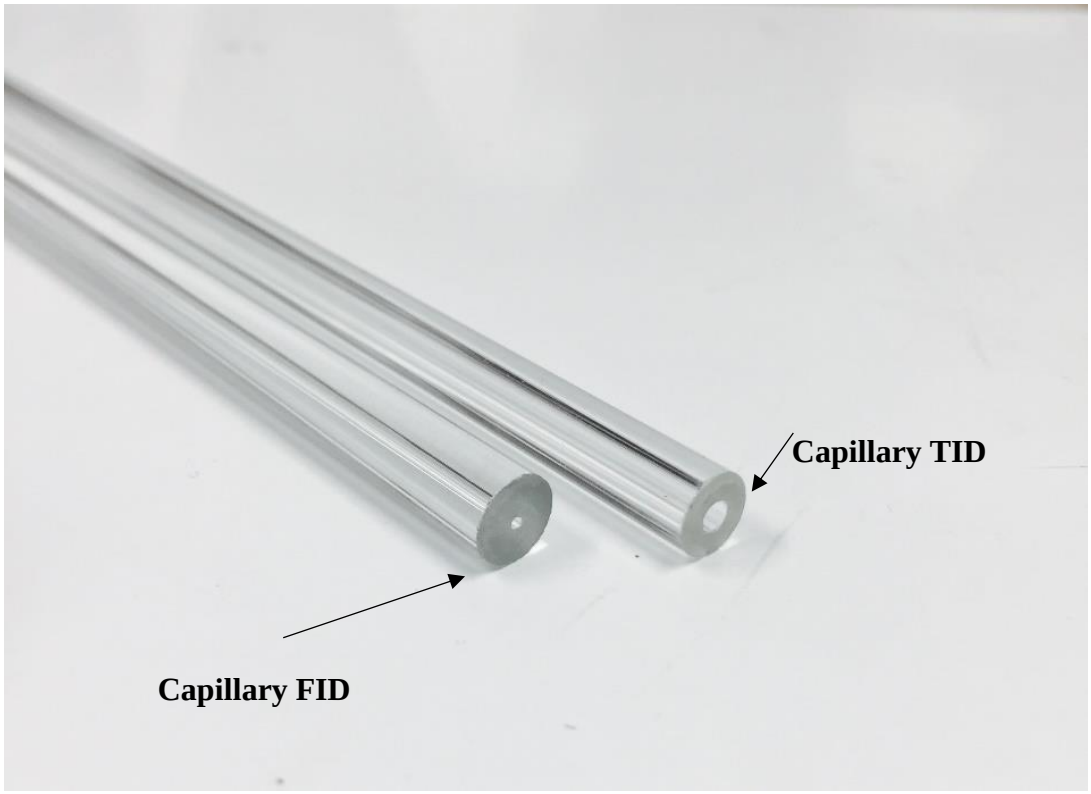

Figure 2-1. Photo of two capillary tubes
(Inner diameter: the left one-with fine inner diameter (FID)-0.6 mm, the right one-with thick inner diameter (TID)-2.2 mm)

The capillary tubes selected for the experiments are made of glass. Two sizes of tube were used, as shown in Figure 2-1. The external diameter was measured by a digital caliper and averaged over five measurements in different parts of a capillary. The precision of the caliper is 0.01 mm. The

external diameter of the capillary tube with fine inner diameter, marked as FID, is 6.39 mm, and the external diameter of capillary tube with thick inner diameter, marked as TID, is 6.27 mm. After the measurement of the external diameter, we took a photo perpendicular to the cross-section of the capillary tube. Then we imported the image to the software (ImageJ). According to the measured external diameter, we could know the length per pixel in the picture. In the software, we used a square to cover the centered circle in the cross-section. Then, we measured the side length and treated it as the inner diameter (ID) of the capillary tube. With this method, we obtained ID = 0.6 mm for capillary FID, and ID = 2.2 mm for capillary TID. A capillary tube with the total length of 1 m was cut to the desired length using a saw and a diamond blade produce by Struers.

2.2.2 Water

Figure 2-2 Photo of Elix® Water Purification System-20

Research has shown that the ions will impact the viscosity[188], the surface tension[189], and contact angle[190] of water. To maintain the consistency of water and the repeatability of the tests, we used Elix® Water Purification System-20 (Figure 2-2) to process the tap water and obtained the

deionized water, which was used in all the experiments of this thesis. Table 2-1 displays the specifications of the processed water from the water purification system.

Table 2-1 Product water specifications processed by the Elix® Water Purification System[191]

Ion rejection (RiOs Essential)	> 95 %
Particle rejection (RiOs Essential)	> 95 %
Resistivity	> 5 MΩ.cm @ 25 °C
Conductivity	< 0.2 μS/cm @ 25 °C
Total Organic Carbon	< 30 ppb
Micro organisms	< 100 cfu/mL
Dissolved silica	< 5 ppb

2.2.3 Cleaning of the capillary tube

There may be impurities spreading over the inside and outside of a capillary tube, such as dust and small oil drop. The existence of these impurities will influence the experimental results seriously. To avoid the negative effect of the impurities, the capillary tube needs to be cleaned before the injection of the water drop. This section presents the cleaning process of the capillary tube. All the materials used for the cleaning are displayed in Table 2-2.

The impurities, especially oil, inside of the capillary tube are not easy to completely clean only by water. So, we choose a kind of effective liquid detergent widely used for cleaning[192], which is

called Mucasol. This detergent is a high-performance alkaline concentrate, which is efficient for labware and instruments made of glass, porcelain, plastics, rubber and metal instruments. Items can be cleaned without mechanical help. Mucasol replaces chromosulfuric acid, is free from chlorine and caustic alkalis, and is non-toxic, non-aggressive and biodegradable.

Table 2-2 A list of materials used for pretreatment

Title	Specification	Quantity	Remarks
Dry gas	650 mL	-	JELT®
Detergent	5 L	-	Mucasol™
Microsyringe	5 μL	1	Hamilton
Pipette	100 μL	1	Eppendorf
Graduated cylinder	10 mL, 200 mL	2	
Wash-bottle	500 mL	2	
Capped tube	>10 cm	4	

For the cleaning process by Mucasol, a solution with a volumetric concentration of 3 % is recommended[193]. To obtain the desired diluted solution of Mucasol, we measure 9 mL of concentrated Mucasol liquid with a graduated cylinder, and put it into an empty wash-bottle, then measure 291 mL of deionized water and pour it into the same bottle.

We rinsed the inside of a capped tube and both the inside and outside of the capillary tube with the

deionized water and then with the diluted Mucasol solution. After that, we fill the capped tube with the diluted solution and put the capillary tube to clean inside this capped tube. For entirely cleaning, we need to wait for at least 24 hours.

The capillary tube to be used must be rinsed inside and outside with deionized water; then we dry the outer part of the capillary tube with tissues except for the area near two orifices to avoid the fiber of tissue getting into the tube. To dry the near-orifice area and the inside of the capillary tube, we select the bottled compressed dry air mentioned in Table 2-2. Indeed, we cannot use the compressed air from the network, as it contains oil traces that would contaminate the tube surface.

2.3.4 Water injection into the capillary tube

In the test, we use a drop of deionized water as a liquid index. After the cleaning process of the capillary tube, we need to inject deionized water into the capillary tube. The volume of liquid (V) to be injected into the capillary tube is calculated as a cylinder volume:

$$V_w = \frac{\pi D^2}{4} l_w \qquad \text{Equation 2-1}$$

where D is the capillary inner diameter and l_w is the length of the desired liquid index. Then we can easily set the volume of water needed by an injector.

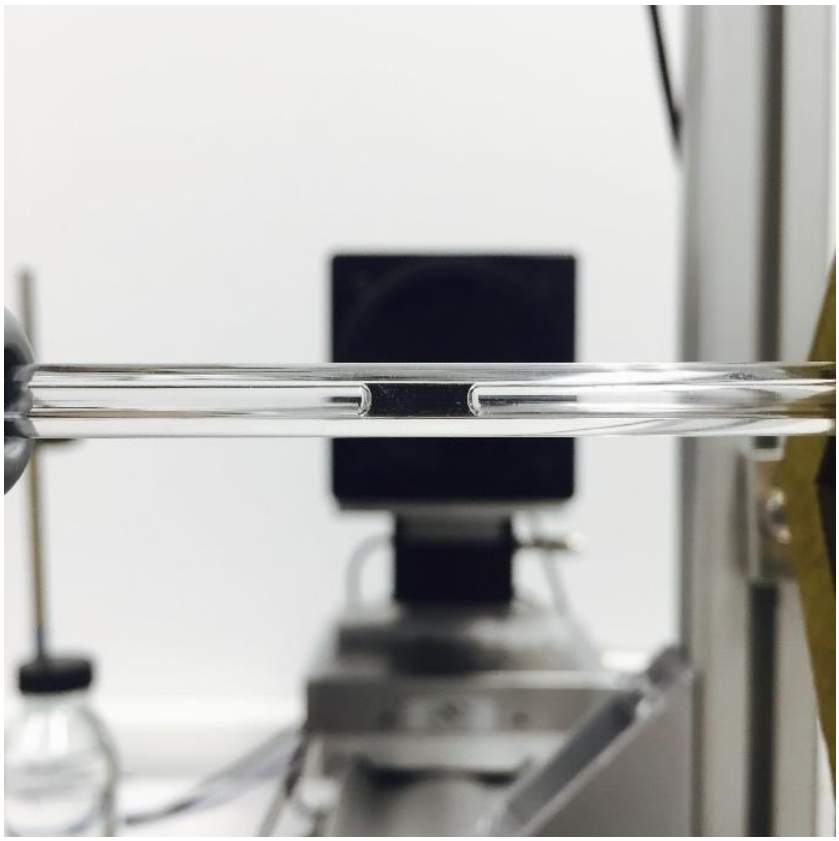

Figure 2-3 Picture of a capillary tube (inner diameter = 2.2 mm) with deionized water inside

For the formation of water index, we have a system consisting of a micrometer syringe (max 5 mL) or a pipette (max 100 mL) depending on the volume and a capillary tube. We take the necessary volume and then inject the deionized water into the capillary tube, as shown in Figure 2-3.

2.3 Experimental set-up

The capillary tube is subject to horizontal vibration through an experimental setup depicted in Figure 2-4. It consists of a vibration chain, an optical bench, and a PC.

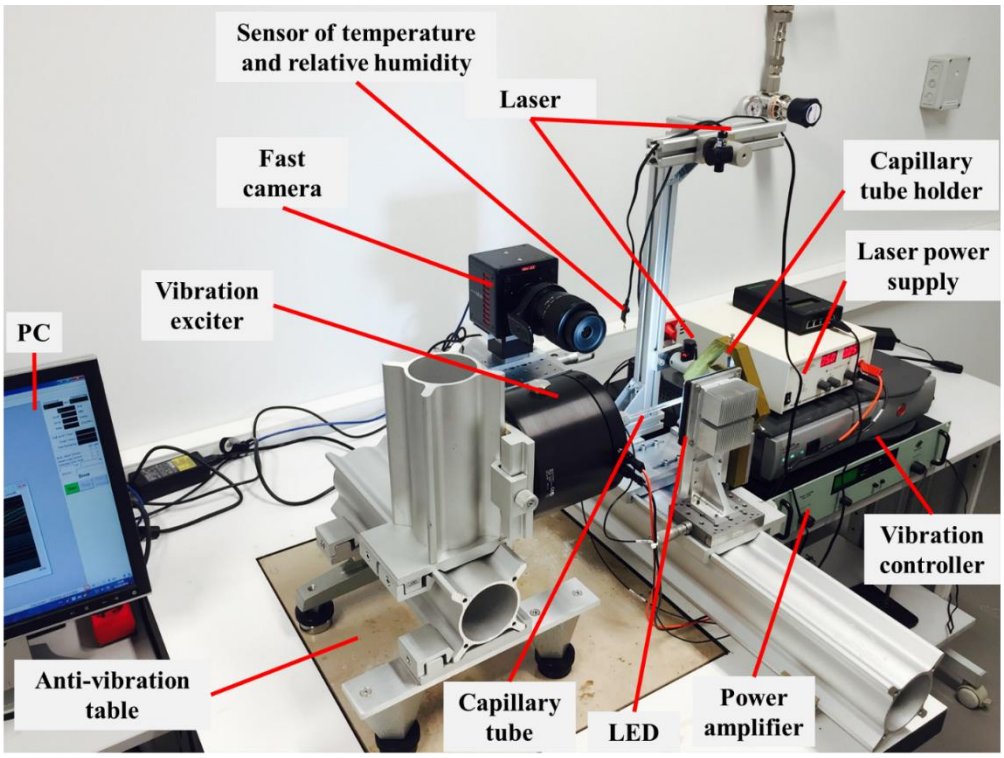

Figure 2-4. A general view of the experimental set-up

2.3.1 Vibration chain

All the tests were performed with sinusoidal vibrations:

$$x_{tube}=A\sin(\omega t)=A\cdot\sin(2\pi ft) \qquad \text{Equation 2-2}$$

where x_{tube} is the displacement of the capillary tube, A is the amplitude, ω is the angular frequency, f is the frequency and t is the time.

A vibration chain (Figure 2-4) is set to vibrate the capillary tube. Figure 2-5 displays the schematic diagram of the vibration chain. A power supply amplifies the signal from the control system to the vibration exciter. An impedance head, fastened between the exciter and the tube, and connected to the signal generator, allows a feedback control. At the other end of the tube, a 3D-printed holder

reduces the vertical oscillations due to the gravity.

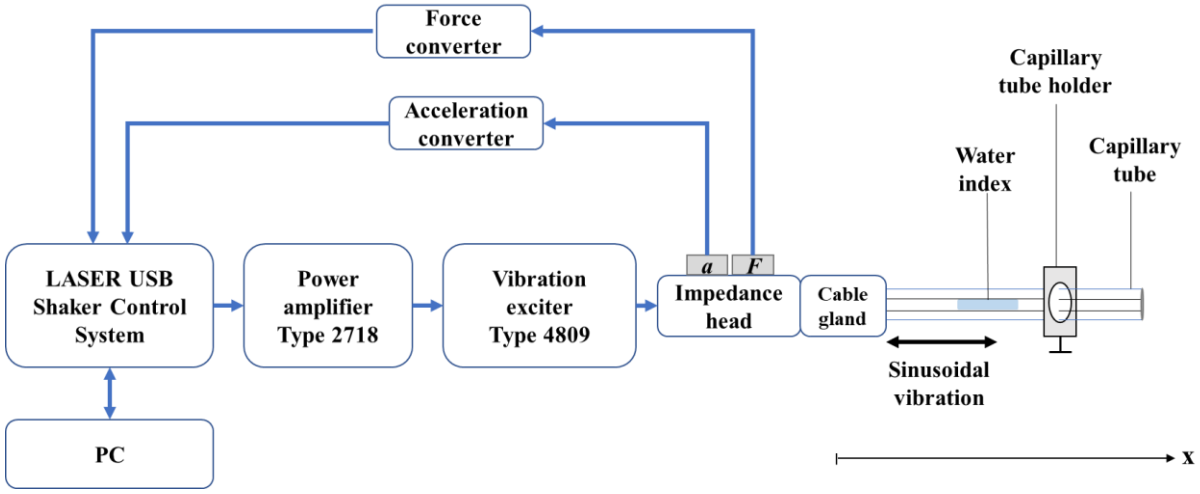

Figure 2-5 Schematic diagram of the vibration chain

The following section will detail the specification of each segment of the vibration chain.

2.3.1.1 Vibration exciter

The capillary tube is linked to a Brüel&Kjær (B&K) type 4809 linear vibration exciter. The exciter offers versatility and dependability for a range of applications, including mechanical impedance and mobility measurements and accelerometer calibration[194].

It features a wide frequency range (10 Hz - 20 kHz) and a displacement of 8 mm peak-to-peak. It can impart 45 N of sine force. It can also impart 60 N with assisted cooling, but this situation will not be used in this study.

The vibration exciter is horizontally fixed on an adjustable carrier, and the carrier can move on an aluminum frame in the vertical direction (Figure 2-6). This design allows the capillary tube to be adjusted to a suitable height for the optical bench. A 3-feet configuration on the bottom of the

aluminum frame ensures the structural stability. The 4th foot is not in contact with the table: it serves only for security.

To obtain relaible observation, it is mandatory to secure the optical bench from any vibration. To isolate the transfer of the vibrational effect caused by the exciter, the support of the vibration exciter is placed on the marble slab of the anti-vibration table (Figure 2-4).

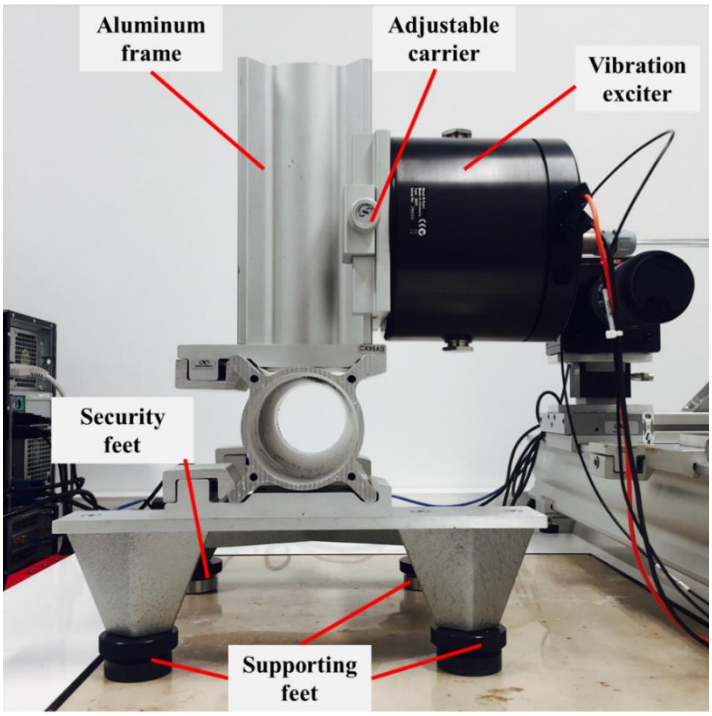

Figure 2-6 Picture of the aluminum frame for vibration exciter

2.3.1.2 Impedance head

A feedback loop for the vibration chain is created thanks to a B&K type 8001 impedance head. This type of impedance head offers a simple way to measure the mechanical mobilities of point and the impedances, and the operating frequency ranges up to 10 kHz[195]. In the impedance head, a piezoelectric accelerometer and a force gauge are installed, and they are linked to the control

system with two converters. With the support of the impedance head, the system can follow the real displacement by integrating the acceleration and adjust the signal amplification in order to obtain the wanted displacement amplitude.

2.3.1.3 Vibration controller

The movement of the B&K type 4809 vibration exciter depends on the applied signal. This signal originates from LDS $LASER_{USB}$ vibration control system (Figure 2-7). The control system is flexible, reliable, and easy to install and operate including a controller module and Windows®-based application software named PFV[196]. It can be configured with different signal shapes (such as sine wave, sawtooth wave and impulse wave) and analysis applications[197]. Here, we focus on sine excitations. The controller module exerts real-time control-loop operations with support of accelerometers of the impedance head (which can measure the acceleration and force) independently of the host PC, hence allowing users to concurrently analyze data and prepare test reports.

Figure 2-7 Picture of the vibration control system and the power amplifier

2.3.1.4 Power amplifier

The signal from the generator needs to be amplified. A B&K type 2718 power amplifier (Figure 2-7) has a maximum voltage gain of 40 dB and flat frequency response from 10 Hz to 20 kHz (±0.5 dB) [198]. The output impedance is lower than 0.04 Ω as the frequency range is from 10 Hz to 5 kHz, and that is lower than 0.08 Ω as the frequency range is from 5 kHz to 20 kHz. It also combines with the power rating, provides low distortion and enables operation in acoustical measurement devices.

2.3.1.5 Connector of capillary tube and vibration exciter

The connector between the capillary tube and the vibration exciter is a cable gland (Figure 2-8). The capillary tube is inserted into the cable gland, which is then tightened. A rubber ring will compress the external wall of the capillary tube and hold it during vibration without breaking it. An air hole is also drilled through the cable gland to maintain the air pressure of the capillary tube at the atmospheric pressure.

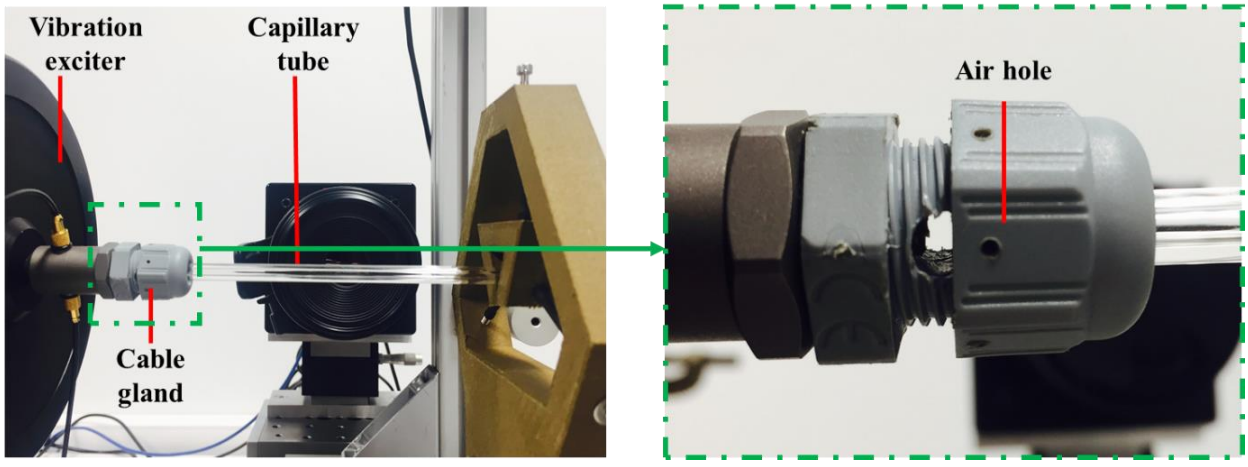

Figure 2-8 Picture of the cable gland

2.3.1.6 Capillary tube holder

The capillary tube connected to the vibration exciter forms a cantilever structure. Moreover, the tube is held with a rubber ring. Consequently, during the horizontal vibration of the capillary tube, vertical displacement may occur on the unfixed end of the capillary tube. This would lead to complex water behavior impossible to analyze.

To avoid the uncontrollable factor caused by the vertical vibration, a capillary tube holder (Figure 2-9) has been designed. The capillary holder is produced by 3D-printing technology, with the function of balancing the effect of gravity on the capillary tube.

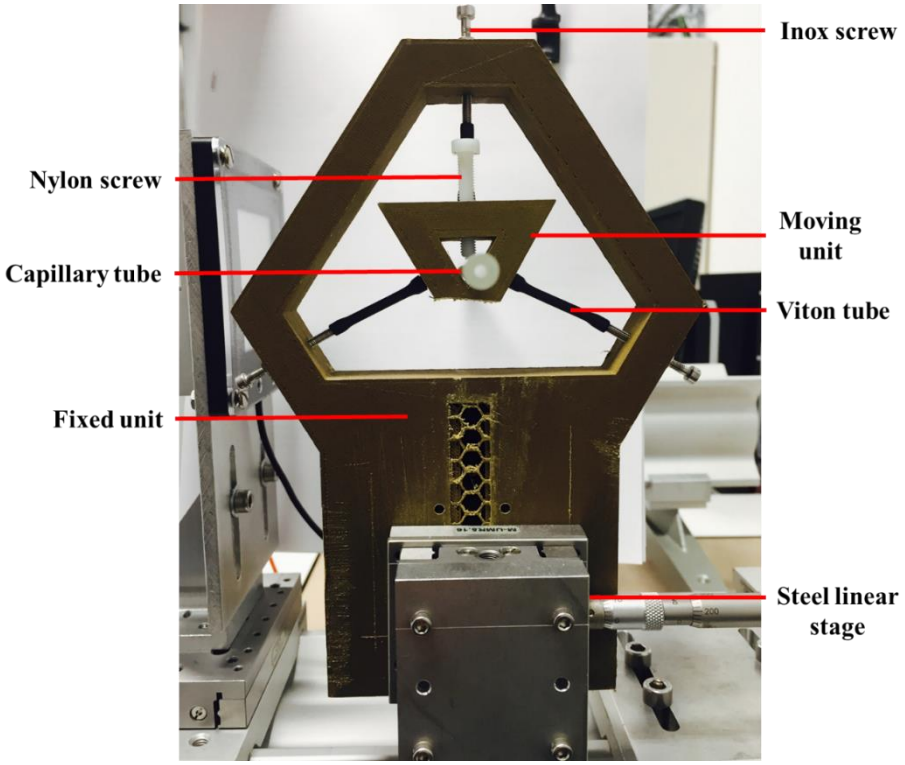

Figure 2-9. A photo of the 3D-printing capillary holder

The capillary tube holder consists of two parts, a fixed unit, and a moving unit, with a mechanical link by 3 Viton rubber tubes. The fixed unit is fastened on a ULTRAlign™ integrated crossed-

roller bearing steel linear stage produced by Newport Company. With this linear stage, the holder can be adjusted precisely to ensure the horizontal and vertical alignment of the tube with the vibrator. The tension of Viton tube is adjusted with steel screws so that the movement of the moving part is linear. The moving unit is comprised of a hollow trapezium and a nylon screw. When the capillary tube is placed through the hollow, the nylon screw will tighten the capillary tube on the trapezium, without breaking the tube during vibration.

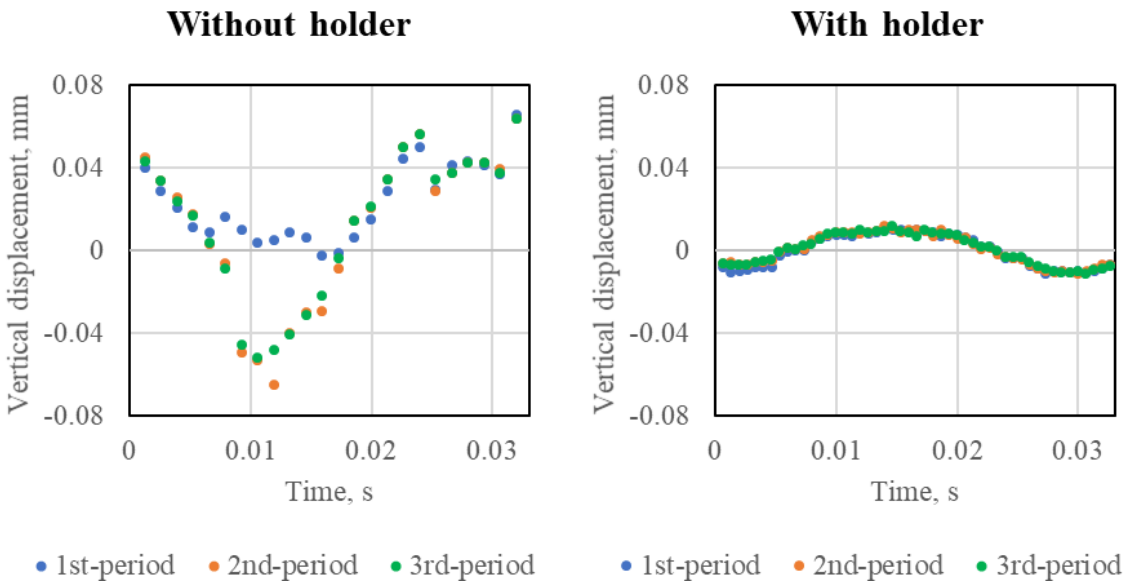

Figure 2-10 Comparison of the stability (vertical displacement) of the right end of the capillary tube (far from the vibrator) without and with the capillary tube holder during vibration (ID = 2.2 mm, A = 2 mm, f = 30 Hz)

Figure 2-10 depicts a stability comparison of the unfixed end of the capillary tube (*ID* = 2.2 mm) without and with the capillary tube holder during vibration (*A* = 2 mm, *f* = 30 Hz). In the figure, points in three colors represent the vertical displacement of the right end of the capillary tube (far from the vibrator) for three successive periods. The vertical amplitude of the tube without the holder reaches 0.065 mm (3.25 % of the horizontal amplitude), while the one with holder decreases to 0.012 mm (0.6 % of the horizontal amplitude). Meanwhile, the motion of the tube with holder

is repeatable over successive periods, with is a great advantage for data analysis.

2.3.1.7 Laser

The position of the tube before each experiment is checked using two lasers. Table 2-3 lists the specification of the laser device. The LaserLyte-Flex is an entry-level laser alignment system, which is a product of Global Laser Company. It uses interchangeable optics and a semiconductor laser diode to project a highly visible dot, line, cross, or a combined line and central dot. We use the line style in the calibration. Two lasers are set on a right-angle beam. Figure 2-11 shows the results of the two lasers.

Table 2-3. Specification of LaserLyte-Flex[199]

Lens material	Acrylic
Lens type	Moulded multi-rod
Exit aperture	5 mm
A/R coated	No
Typical input beam size	5 by 1.5 mm
Typical fan angle	60^{o}
Typical transmission loss (650 nm)	$\leq$ 25 %
Power	10 mW

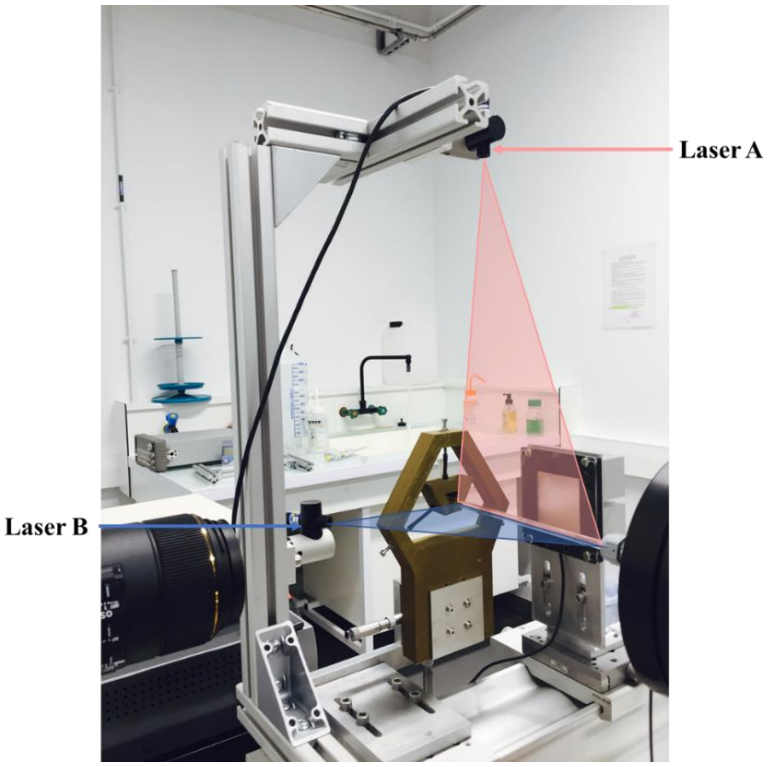

Figure 2-11 The schematic diagram of the laser beam

2.3.2 Optical bench for data recording

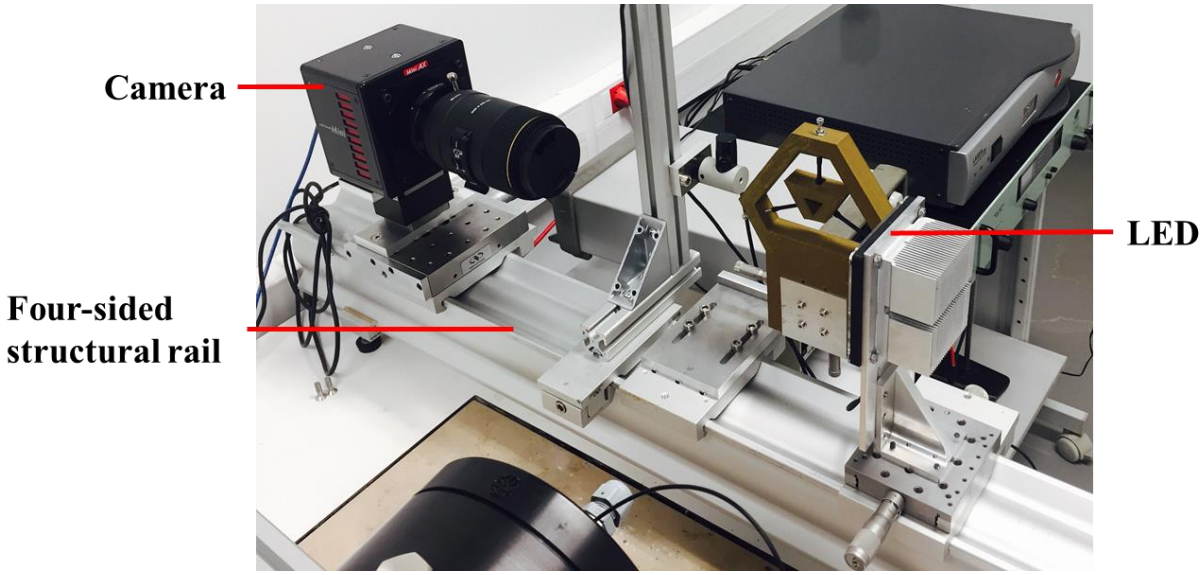

Figure 2-12 Picture of the optical bench

The tube and liquid movement are monitored thanks to an optical bench (Figure 2-12), comprising a high-speed camera (FASTCAM Mini AX100, by Photron) controlled by a PC and a backside illumination (LED). The LED is used to assist the imaging in the camera in a dark room and create repeatable light conditions.

2.3.2.1 High-speed camera

The Photron FASTCAM Mini high-speed camera provides high frame rates, high light sensitivity and high image quality in a compact, with lightweight and rugged camera design. This camera allows a full-field up to 4000 frames per second (FPS). Higher rates need a trade-off between speed and field: from 4000 for 1024^2 pixels to 540000 FPS for 128×16 pixels. It is also available with memory options up to 16 GB for extended recording times and triggering flexibility.

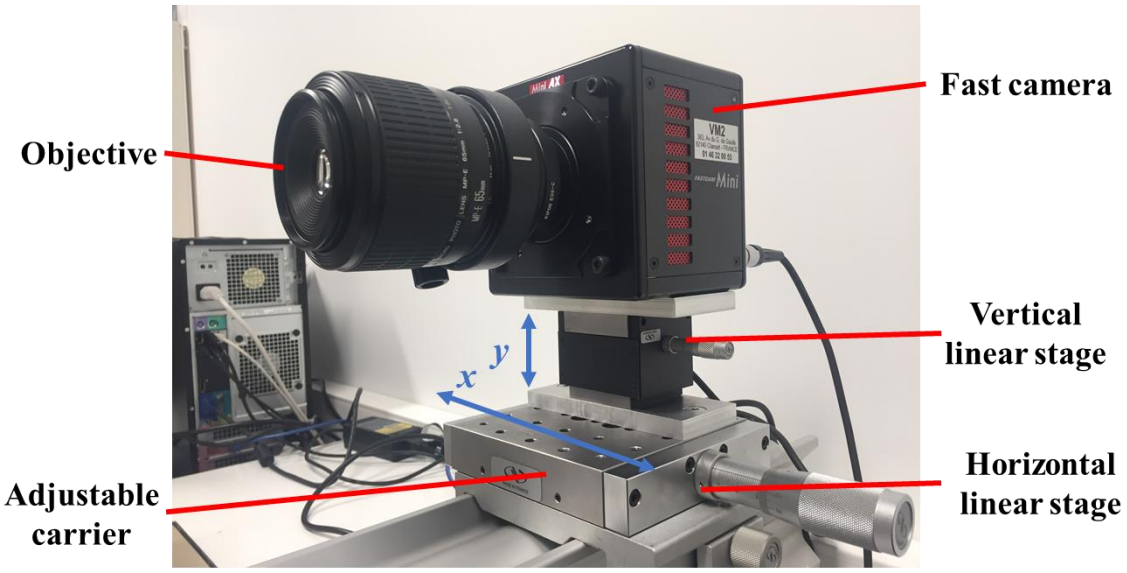

Figure 2-13 Picture of the camera system

Figure 2-13 shows the picture of the fast camera with a Canon-MP-E 65 mm-f/2.8-1-5x macro objective. It is a manual focus objective for use on the electro-optical system. It can magnify

subjects up to 5 times. The objective is equipped with ultra-low dispersion glass to eliminate chromatic aberrations which frequently occur with high magnification[200]. Another objective is also used in the experiments: a SIGMA-105 mm-f2.8-EX-DG macro objective. The feature comparison of these two objectives is shown in Table 2-4. The selection of the objective depends on the desired region of interest. When we need to focus on the meniscus behavior during vibration, the Canon objective is chosen because it allows a maximum magnification of the tube in vertical direction compatible with the picture dimension. Otherwise, the SIGMA objective is used to observe the whole water index (both meniscus).

Table 2-4 Features of two objectives used in the experiments

Model	Canon-MP-E 65 mm-f/2.8-1-5x	SIGMA-105 mm-f2.8-EX-DG
Focus mode	Manual	Manual
Amplification	1-5x	1x
F-number	2.8	2.8
Focal length	65 mm	105 mm

The camera is fixed on a vertical linear stage, which permits the height of the camera to be adjusted precisely. Then the vertical linear stage is settled on a horizontal linear stage to ensure the horizontal movement (precise movement for optical focus). The horizontal linear stage is bolted on a steel carrier, which can make the camera adjustable on the structural rail (coarse movement to choose the object magnification).

2.3.2.2 LED

The experiment was performed in a dark room to avoid the effect of uncontrolled light on the imaging of the capillary tube and water index. Then, we choose a $50\ mm \times 50\ mm$ LED light which can produce strong and homogeneous light. The power of the light is 10.56 W. The minimum luminance of LED is 70 000 cd/m^2 in a continuous mode with a source type of white color LED. The max operating temperature of this device is 50 ^oC under the power supply of 110V or 220 V.

When the LED light works, vast heat is produced, and the temperature of the light will rise sharply. For security, a set of steel fins are combined on the back of the light to assist the heat dissipation. The LED is settled on a steel linear stage which can be adjusted horizontally. The stage connects to a carrier which can be moved and fix on the structural rail. The light direction of the LED is set to face the camera lens. Meanwhile, the direction of the strong light is also parallel to the line of sight of the operator during the experiment, to avoid the vision damage.

2.3.2.3 Monitoring of the capillary tube position

For monitoring the movement of the capillary tube, a mark is necessary. Initially, we tried to mark the capillary tube with a paint drop (Figure 2-14). The problem is that the depth of field of the camera is not large enough to focus on the paint drop and the meniscus at the same time. In this condition, the objective cannot focus on both at the same time. Another deficiency is that we cannot maintain the mark all the time. Each time when we need to clean the capillary tube, the paint drop will bring some troubles. Thus, to avoid these problems, we changed to a second option. We machined several notches on the external wall of the tube using a diamond wire sawn (Figure 2-15a). This method has two advantages. One is that the shape of the mark is stable for all the

experiments, and another one is that the notches will not bring extra contamination for the cleaning. Figure 2-15(b) shows a captured image of a period of the capillary tube with a notch on the external wall. Obviously, we can track the position of the notch to record its movement.

Figure 2-14 Picture of capillary tube marked by a paint drop

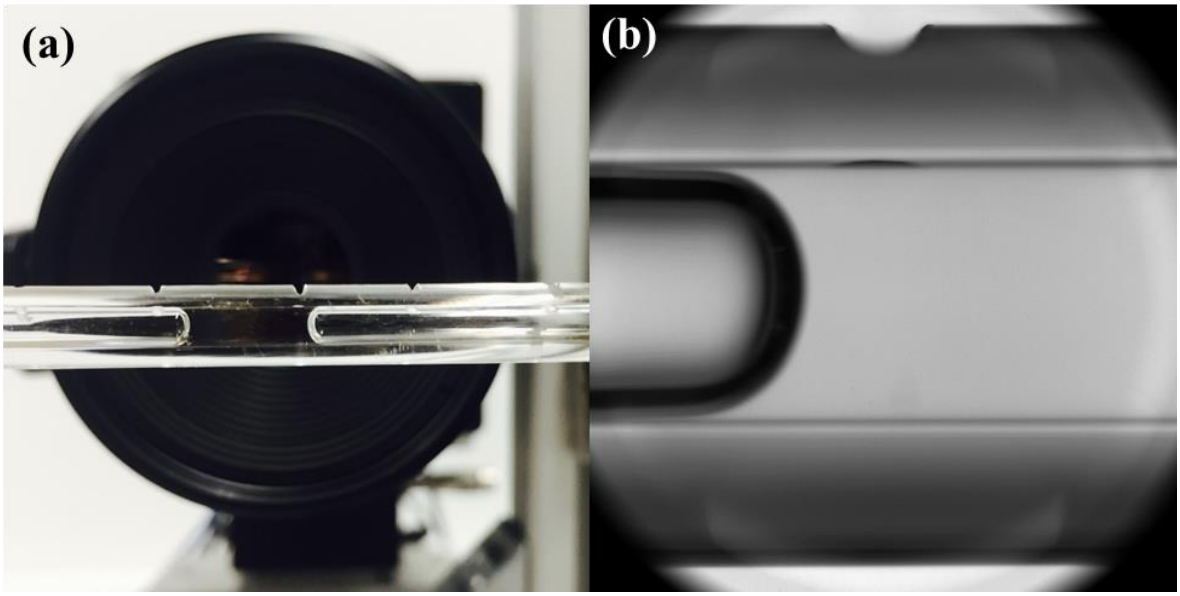

Figure 2-15 (a) Picture of a capillary tube (ID = 2.2 mm) with several notches on its external wall and (b) the corresponding image grasped by the camera

2.3.2.4 Adjusting process

The aim of the adjusting process is to make the water index observable for the camera. Before starting the experiment, we must ensure the parallelism between the base of the vibration exciter and the four-sided structural rail by using an H-shape beam (Figure 2-16(a)). Figure 2-16(b) gives the mode for the usage of the H-shape beam. While to avoid the vibration transmission from the exciter to the optical bench, we need to withdraw the H-shape beam before the activation of the vibration chain. Then we need to insert the capillary tube containing the deionized water into the cable gland connecting to the impedance. We tighten the gland to fix the capillary tube. Thus, one end of the capillary tube is connected to the vibration exciter, and the other end is fixed on a tube holder. After the fixation of the capillary tube, the alignment of the devices should start by adjusting the integrated crossed-roller bearing steel linear stage. This ensures the horizontality of the capillary tube and makes its main axis perpendicular to the direction of the objective. When the capillary tube position is well set, the position adjustment of the water index inside the tube can be proceeded by a rubber bubble. With the rubber bubble, we can cover it over the tube orifice near the holder change the water position in the tube.

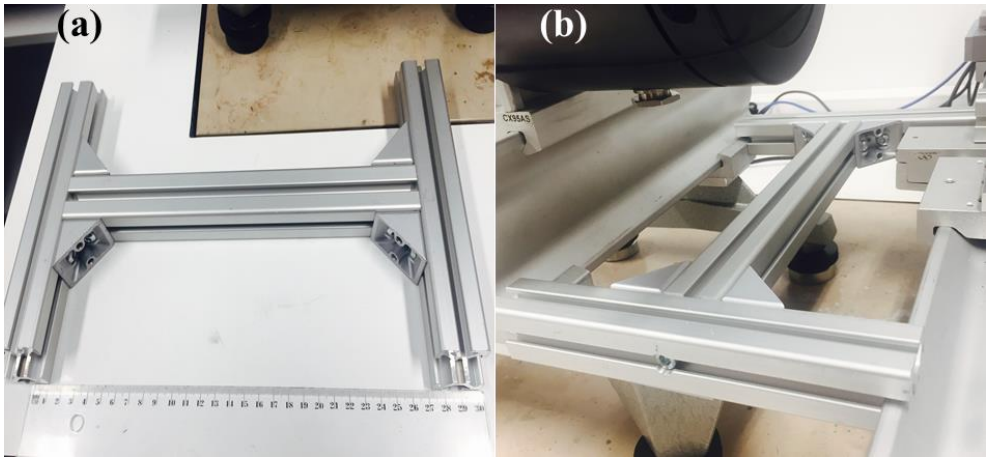

Figure 2-16 Picture of (a) the H-shape beam and (b) the mode of usage

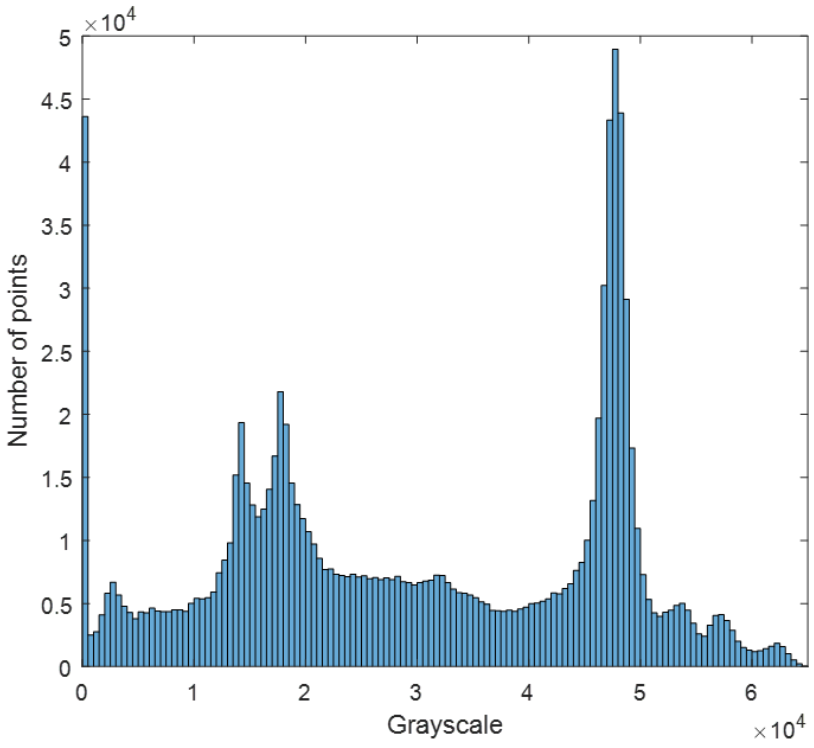

Figure 2-17 Desired histogram of the grayscale image

Afterwards, we push on the camera and the LED light, and run the PFV software for the camera. After the focusing, the water index is visible from the PFV software. Meanwhile, we must ensure that both upper and lower sides of the capillary tube are visible from the camera. Indeed, the external tube diameter is used to scale the image in millimeter per pixel. The pixel size (in millimeter) is a very important parameter in analyzing the movement of tube and water. For the observation of the water index, we first focus on the whole water index to measure its length.

In this step, we aim to obtain an unsaturated grayscale image with a double peak histogram (as depicted in Figure 2-17). We need to set the appropriate shutter speed and frame rate. To achieve this goal, we tested the effect of different shutter speed on the histogram of the image and finally we choose one for the present situation. The applied optical parameters for the experiment are

displayed in Table 2-5. The very short exposure time, allowed thanks to the camera sensibility and LED power, guarantees the sharpness of the image in spite of the movement, whatever the magnification.

Table 2-5 The optical parameters for all the tests

Magnification	×3
The distance between tube and LED	10 mm
The distance between tube and camera	246 mm
Frame rate	50× vibration frequency fps
Shutter	1/60 000 s

2.3.3 Temperature and relative humidity sensor

The ambient of the experiments is recorded by a temperature-relative humidity sensor (SHT75) [201] produced by SENSIRION company connecting to a data converter. For our experiments, the temperature ranges from 26 to 29 ℃ and the relative humidity from 36 to 40 %.

2.4 Conclusions

The experimental set-up comprises a series of precise devices from Brüel&Kjær, precision steel stages, carriers, and structural rails from Newport, a fast camera from Proton, a macro objective from Canon, a laser calibration system, and a 3D-printing holder. The configuration is efficient and easy to set. The camera and the objective provide a high image quality. A set of strict protocol was

made to ensure the cleanness of the capillary tube and the repeatability of the experiments. The parameters selected make sure the obtained images are relevant and easy to process.

After all the manipulations introduced in this chapter, we can activate the vibration chain. In turn, press the power button on the amplifier and the vibration control system, and set the vibration parameters to test (amplitude, frequency). Then, we launch the vibration to a stable state and begin to record images for the desired period.

Chapter 3: Image processing and analyzing

3.1 Introduction

For each experiment performed by the set-up described in chapter 2, hundreds of 16-bit grayscale images were captured for each set of parameters. From each image of a single experiment, we aim at obtaining the information of (a) the meniscus curvature (the radius of the blue circle in Figure 3-1), (b) the displacement of the most prominent point on the meniscus (point *A* in Figure 3-1), (c) the displacement of the tube (point *N* in Figure 3-1). The variation of the curvature radius is used to assess the shape-shifting of the meniscus. The displacement of point A is used to indicate the displacement of the water index. Point N is the mass center of the capillary tube notch, and its displacement is representative of the tube motion.

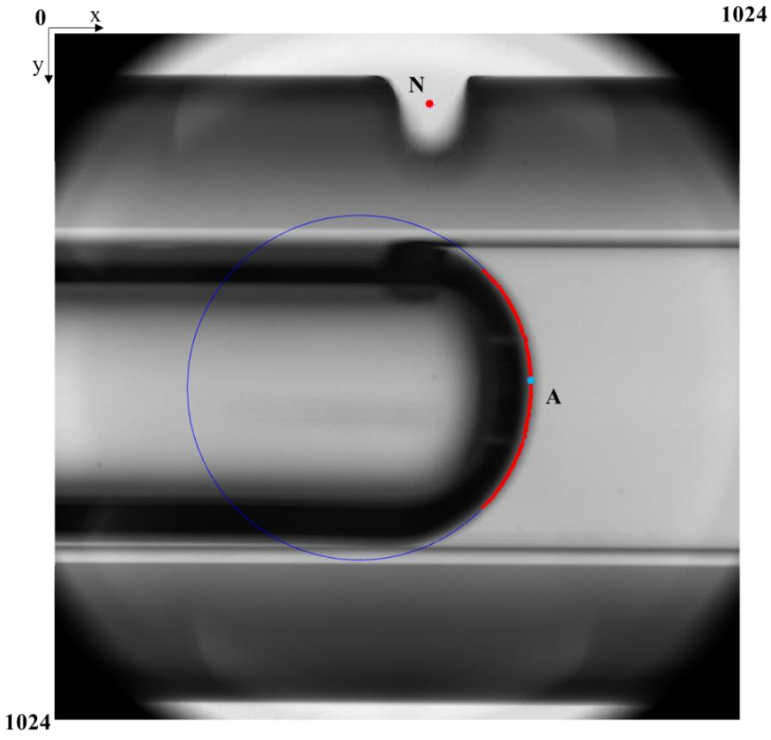

Figure 3-1 An image of the interface of water and air (meniscus) and a notch on the external wall of a capillary tube.

Due to a large quantity of images to analyze, an automatic way to process the captured images is mandatory. Thus, a code was written using the platform MATLAB to process each series of images, extract the useful information and plot their time-evolution.

The essential problem to solve in processing the gray-scale image is to find the target boundary. During the past decades, the image binarization was considered as an effective way[202–213]. The image thresholding is a technique that uses a threshold to separate the image into two classes. One class contains the gray values above the threshold value, and another one contains the remaining pixels[203]. Examples of thresholding applications such as document image analysis[207], map processing[212]. According to the survey of the Sezgin Mehmet and Sankur Bülent[205], 40 automatic thresholding methods were categorized into the six classes: histogram shape-based methods, clustering-based methods, entropy-based methods, object attribute-based methods, the spatial methods and local methods based on the local characteristics of each pixel. For each thresholding method mentioned above, the information loss cannot be avoided. Another deficiency is that the determined position of the boundary depends on the value of the threshold. In reference to some method used in the thresholding, a grayscale method is applied to recognize the target boundary in the present work, which can minimize information loss.

It is worth mentioning that we started with classical image analysis functions, but all our attempts in this way failed due to the complexity of situations encountered in our images: problems of contrast variations, problems of meniscus shape near the inner tube walls, problems of non-monotonic variation of the gray level through the interfaces, etc. The final treatment is therefore quite complex and will be described in detail in this chapter.

3.2 The algorithm of image processing and analyzing

For automatically processing hundreds of images, we need to create a loop of reading and processing image above all. Thanks to the PFV software provided by Photron, the grabbed images are named by numbers successively. All images are saved in the "TIFF" format. The code detects automatically the number of TIFF files in the given folder. This quantity defines the ceiling (*k_max* in Figure 3-2) for the loop. The software starts from the first image and then processes all images in sequence until the ceiling. Once done, it saves the extracted results.

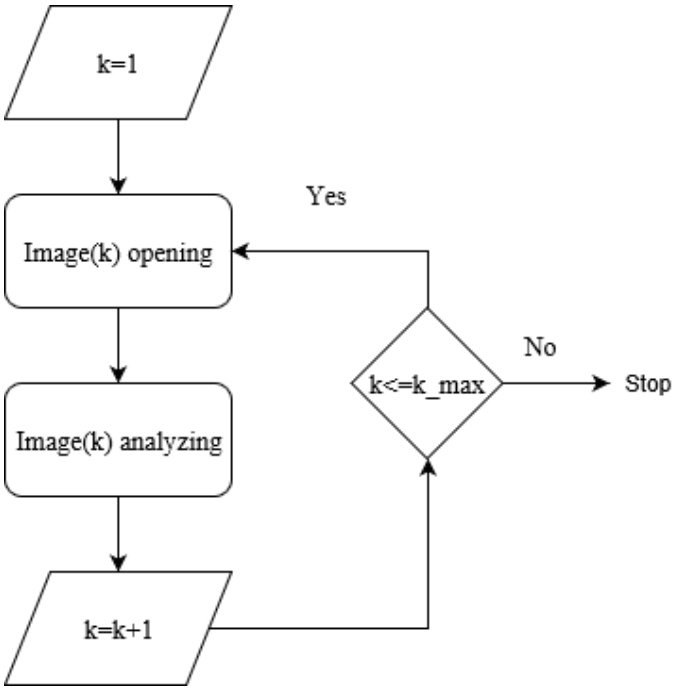

Figure 3-2 The algorithm of the overall loop of reading and analyzing images

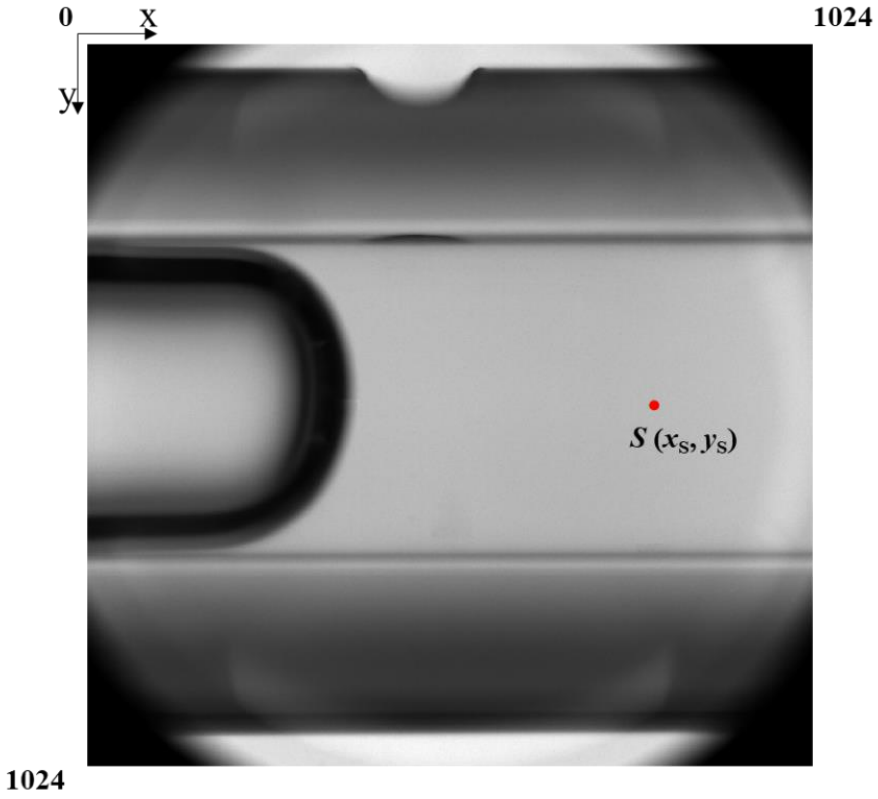

Figure 3-3. A captured image with a mark of a point selected manually (red dot)

Figure 3-4 summarizes the image analyzing code which consists of one step with manual manipulation and four automatic steps. After running the code, the program asks the user to select a point in the water index between two inner walls. The position of *S* must be chosen so that (1) this point is close to the middle height of the tube and (2) the meniscus never overlaps during vibration, as the red point *S* in Figure 3-3. Then the program executes the step of determining the approximate position of the meniscus.

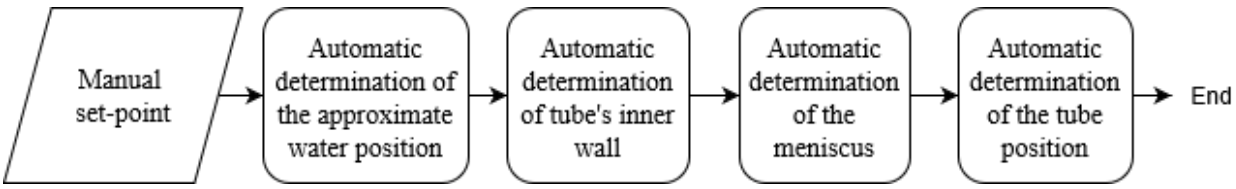

Figure 3-4 The detailed process of the image analyzing

3.2.1 Determination of the approximate position of the water

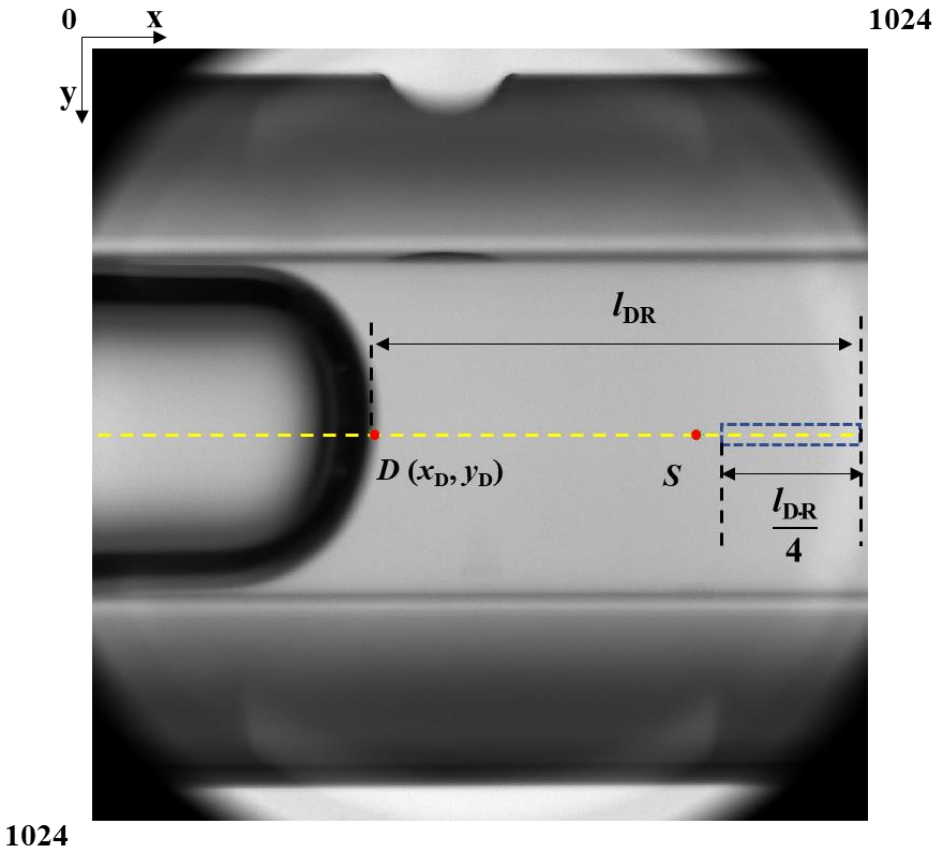

Figure 3-5 A captured image with point S and D

After the selection of the starting point *S*, the approximate position of the water (point D in Figure 3-5) is to be determined. The code records the grayscale values of all the points on the horizontal line $y = y_S$. Figure 3-6 is a double coordinate diagram. It shows the grayscale, GS, versus the abscissa, x, (blue curve) and the corresponding grayscale change, ΔGS, versus the abscissa, x, (red curve). The grayscale change is calculated by Equation 3-1:

$$\Delta GS(x) = \frac{GS(x+1) - GS(x-1)}{2} \qquad \text{Equation 3-1}$$

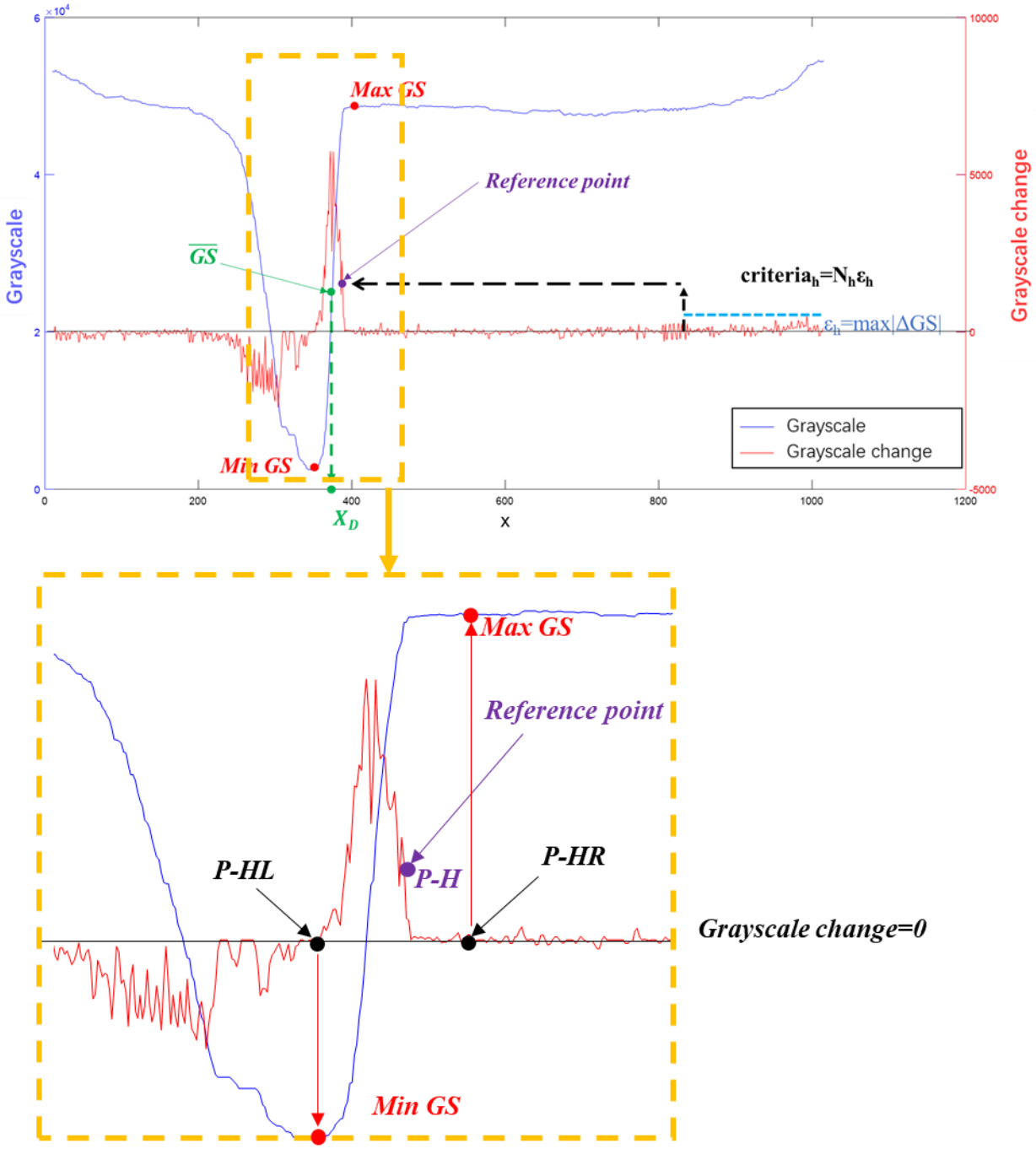

Figure 3-6. The variation of grayscale & its numerical derivative plotted versus the abscissa

In Figure 3-6, the obvious single peak in the ΔGS curve indicates a sudden change on the grayscale curve. Figure 3-5 tells us that this peak corresponds to the sudden gray scale change between the

air and the water index. To find the target peak, we need to define a proper criterion. To do so, we analyze the grayscale in a regionfar from the meniscus on the right part of the image, inside the water index (the blue rectangular in Figure 3-5). Taking a zone far away from the meniscus ensures that no overlap exists between the meniscus and the area for the selection of criterion during vibration. The distance between point *D* and the right edge defines a horizontal reference distance (l_{DR}). The region used to determine the criterion locates on the right side of the image, whose width is equal to 10% of image width.

The maximum absolute grayscale change ($|\Delta \mathrm{GS}|_{max}$) in this zone is computed by the code. The obtained value (ε_h) is set as an evaluation of the noise level. This value is multiplied by an amplification coefficient (N_h), to obtain the final horizontal criterion ($N_h \varepsilon_h$), that allows us to avoid any artefact that could be due solely to a noise effect. In the current imaging condition, the amplification coefficient (N_h) is set as 3. The code can scan along the ΔGS curve from the right edge to the left with$N_h \varepsilon_h$. When the grayscale change is equal or greater than $N_h \varepsilon_h$, the code stops scanning and record the coordinate of this point (*P-H*). Base on *P-H*, search the first point with a negative ΔGS or zero on the left (*P-HL*) and right (*P-HR*) of *P-H*. The grayscale of *P-HL* is treated as the minimum grayscale (Min *GS*) and that of *P-HR* is treated as the maximum grayscale (Max *GS*). Then the averaged grayscale ($\overline{GS}$) can be calculated as Equation 3-2:

$$\overline{GS} = \frac{Max\ GS + Min\ GS}{2} \qquad \text{Equation 3-2}$$

Because the slope of the grayscale curve between the Min *GS* and the Max GS is very high, an error on the Min *GS* or Max *GS* will only impact the result slightly. With this robust method, the code finds the target position (Point *D* in Figure 3-5) with a gray level equal to $\overline{GS}$ the average

between Min *GS and* Max *GS*.

3.2.2 Determination of inner wall of the capillary tube

After the determination of the approximate position of the meniscus, we can also apply the same method in the vertical direction($x = x_S$). The algorithm expresses as in Figure 3-7.

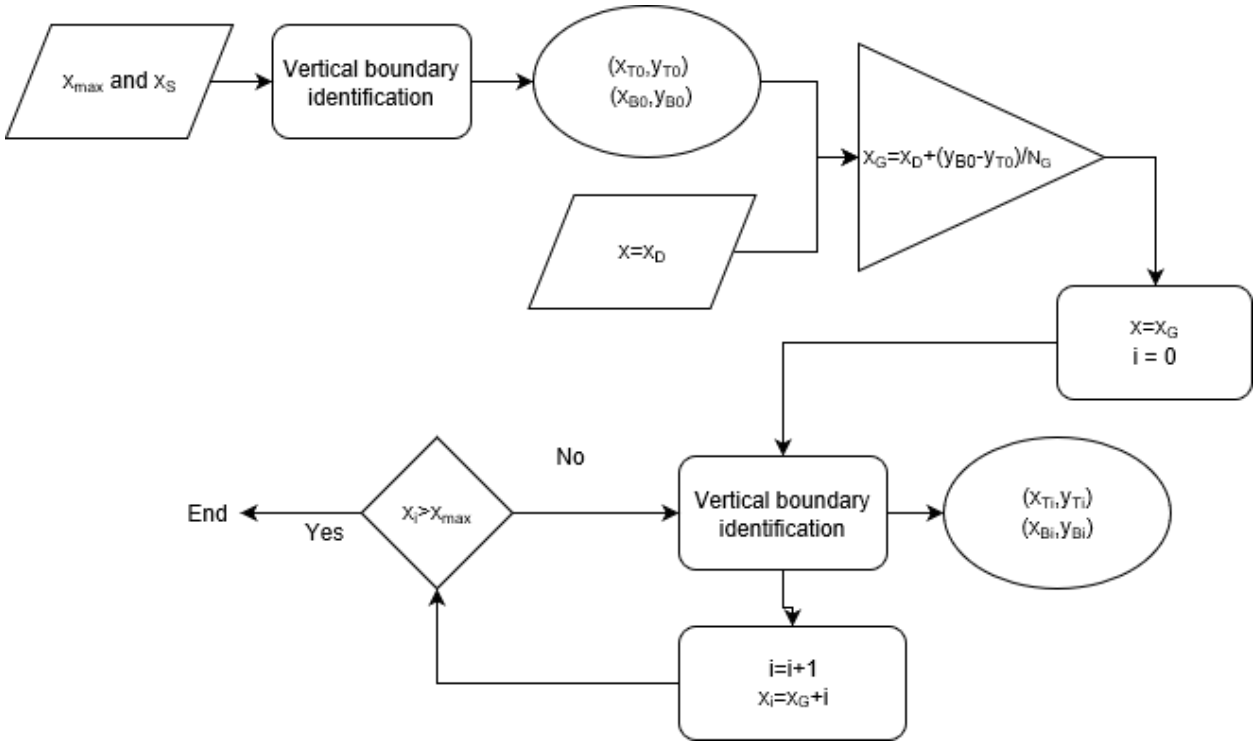

Figure 3-7 The algorithm of the inner wall determination

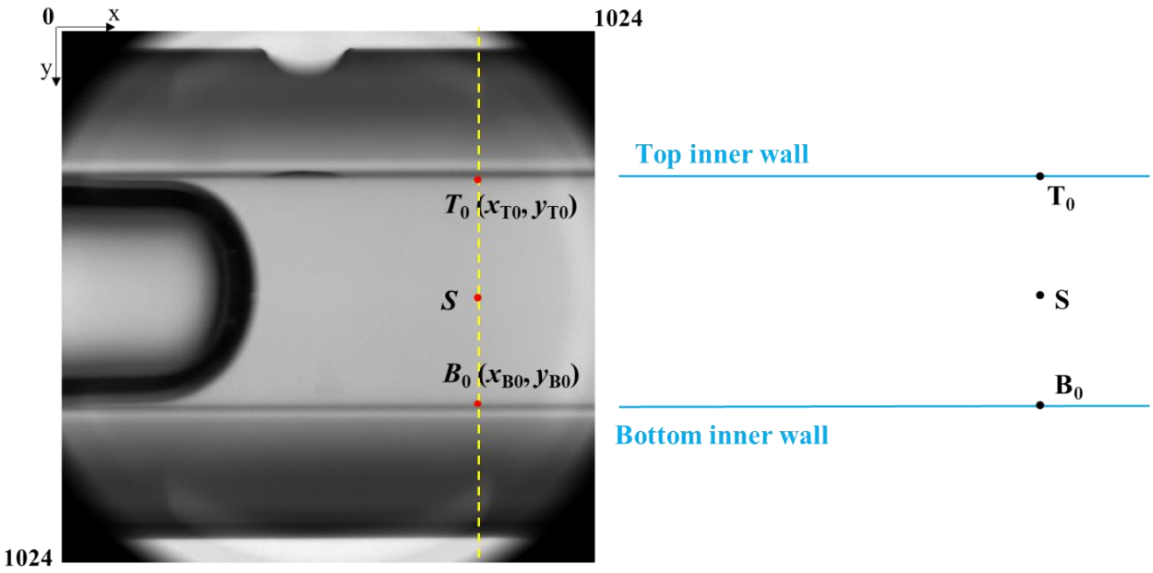

Figure 3-8 A projection of the inner wall of the capillary tube

In Figure 3-8, we respectively call the top and bottom projections of the inner wall on the picture as *top inner wall* and *bottom inner wall*, for convenience. Figure 3-9 shows the variation of the grayscale and the grayscale change along the vertical line $x = x_S$ (the yellow line in Figure 3-8).

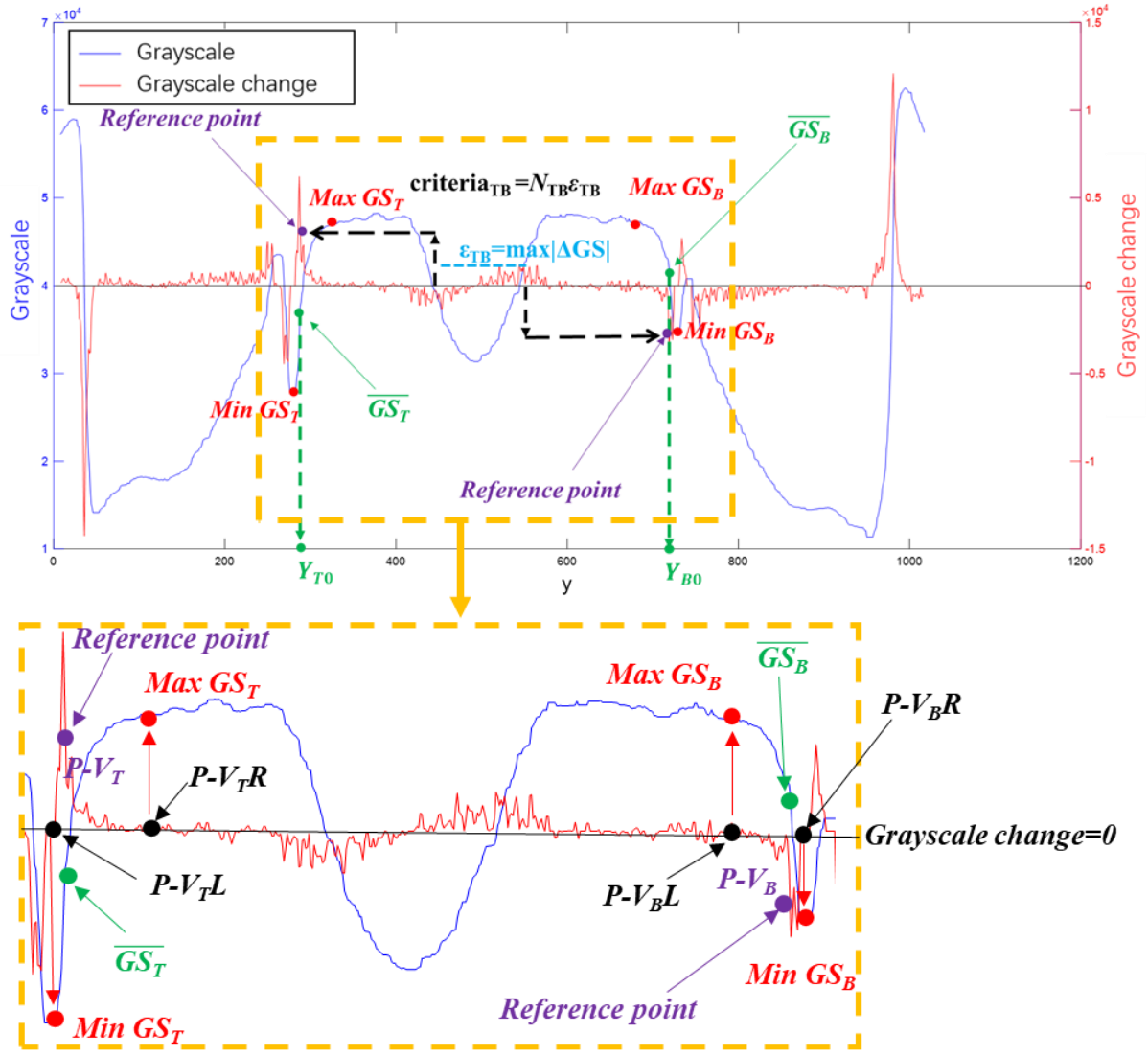

Figure 3-9 The variation of grayscale & grayscale change along a vertical line.

In Figure 3-9, the $|\Delta GS|_{max}$ in the range close to the tube axis can be recognized by the code. This range is centered by the axis of the tube ($y_{axis} = \frac{y_{T0}+y_{B0}}{2}$). Its width is set as 25 % of the distance between T_0 and B_0. The obtained value is set as a basic vertical evaluation of the noise level (ε_v). As before, the basic vertical criterion is multiplied by an amplification coefficient (N_v), to obtain the final vertical criterion ($N_v\varepsilon_v$), likely to eliminate any noise artifact. The amplification coefficient (N_v) is set as 3. The code performs the value comparison along the ΔGS curve from the

center to both sides with $N_v\varepsilon_v$ respectively. When the ΔGS is equal or greater than $|N_v\varepsilon_v|$, it stops the value comparison and records the coordinate respectively. For the two stop points, the one with minor ordinate is named *P*-V_T and the one with greater ordinate is called *P*-V_B. Based on *P*-V_T and *P*-V_B, we apply the method described in 3.2.1 to determine the points with minimum grayscale (Min GS_T *and* Min GS_B) and maximum grayscale (Max GS_T *and* Max GS_B) around *P*-V_T (*P*-V_T*L* and *P*-V_T*R*) and *P*-V_B (*P*-V_B*L* and *P*-V_B*R*). The averaged grayscale $\overline{GS_T}$ and $\overline{GS_B}$ for top and bottom parts can be calculated respectively by averaging the corresponding extreme grayscales. By the nearest method, we can find the target points (Point T_0 and B_0 in Figure 3-8) on the top inner wall and bottom inner wall. This process will be called the vertical identification in the following paragraphs.

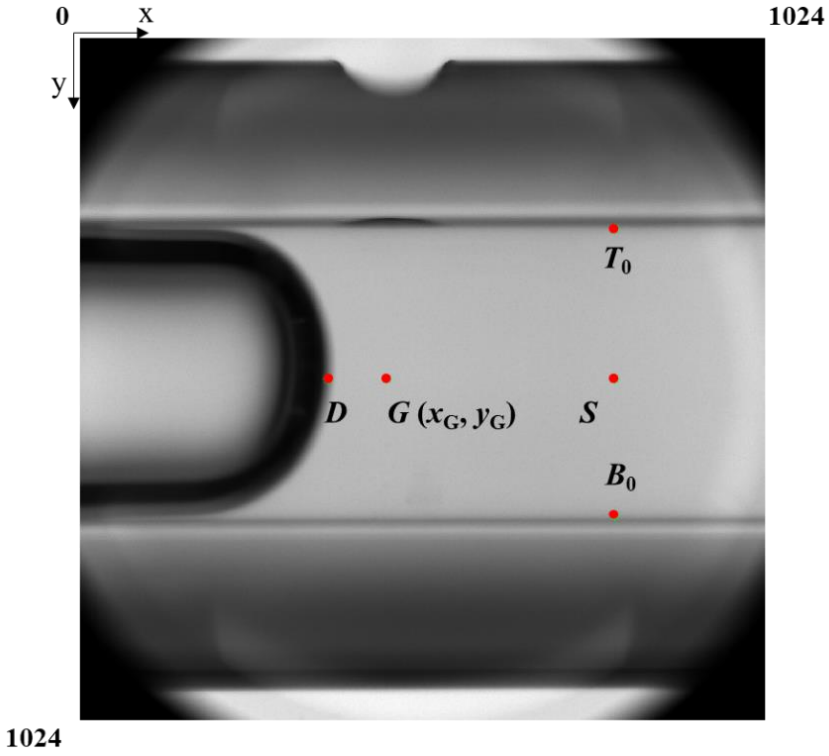

Figure 3-10 A captured image with point S, D, T_0, B_0 and G.

The determination of the inner wall of the capillary tube is a significant step for identifying the meniscus. To avoid the interference of the meniscus on vertical processing, we make the code start the vertical identification from a point G on the right of point D. G is chosen to be away from the meniscus by a fraction of the tube diameter. The abscissa of point G (as Figure 3-10) is determined by Equation 3-3:

$$x_G = x_D + \frac{y_{B0} - y_{T0}}{N_G} \qquad \text{Equation 3-3}$$

Here, we choose $y_G = y_D$ and N_G =8. In the captured image, the code repeats the vertical identification from the abscissa $x = x_G$ to x =1024.

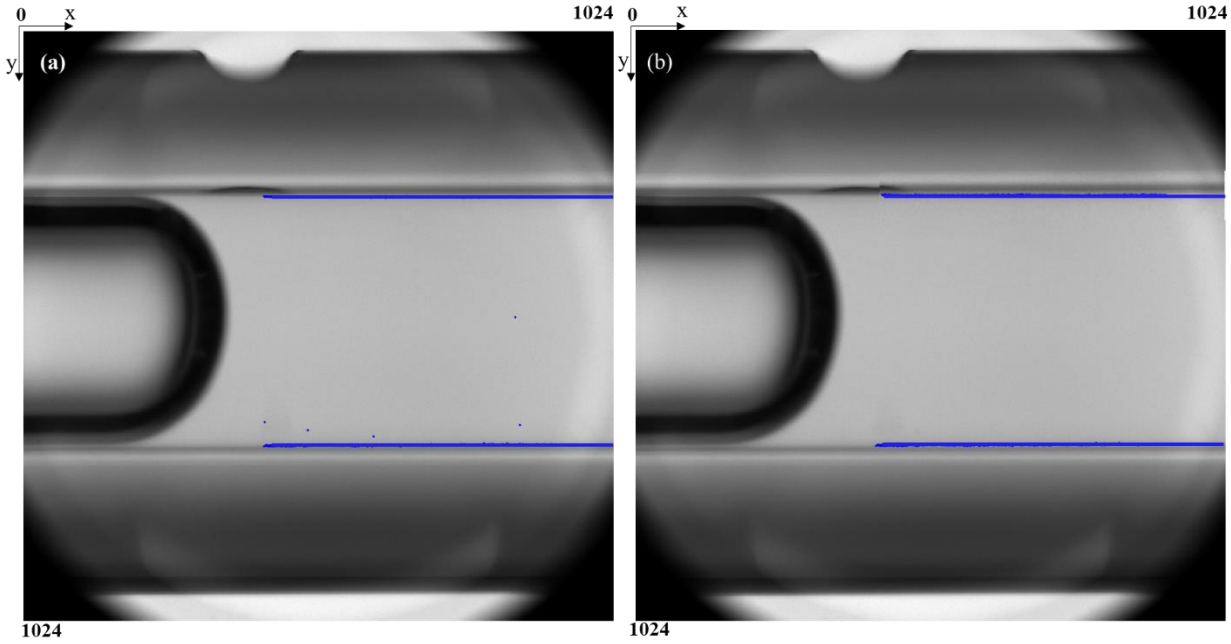

Figure 3-11 A captured image with (a). the original results of inner wall determination and (b). the results after outlier elimination

As we can notice in Figure 3-11(a) that several defaults appear in this identification procedure. To eliminate the outliers, a 1-D median filter is applied to the results. The median filter[214215], a non-

linear filter, is a simple rank selection . It was introduced by Tukey in 1971. He attempted to remove impulse noise by changing the luminance value of the center pixel of the filtering window with the median of the luminance values of the pixels contained within the window. In this code, we set a window size to 9. The results after outlier elimination are shown in Figure 3-11(b).

3.2.3 Determination of the meniscus

3.2.3.1 Determination of the full description of the meniscus

In order to obtain the reliable data, some actual situations must be taken into consideration. For example, if the capillary tube is placed non-perpendicular to the direction of the camera lens, the inner wall projections of the tube will not be parallel. It will bring some trouble in the determination of the meniscus, if we supply assume horizontal lines for the detection (Figure 3-12).

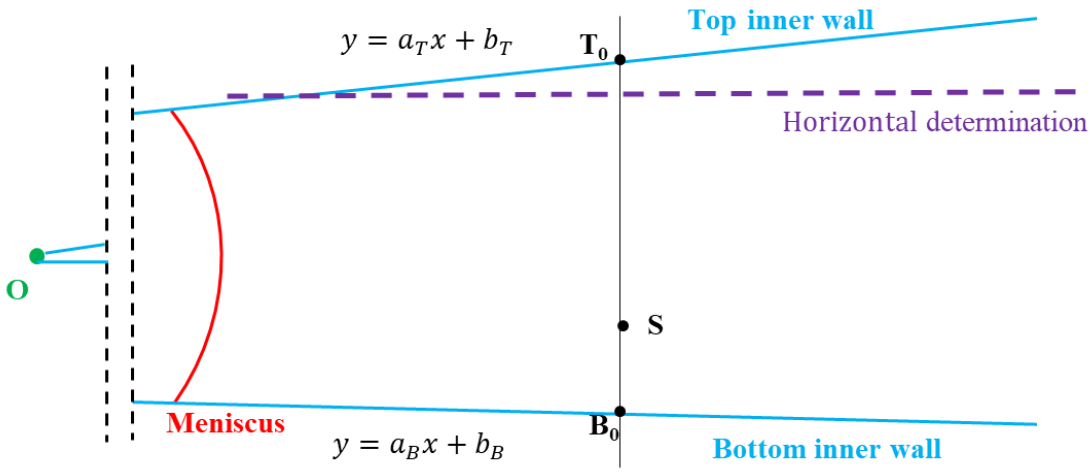

Figure 3-12 A scheme of the tube inner walls in a non-ideal case

To avoid this kind of problem, we propose a quasi-radar-scanning method to achieve this goal. First, we make a linear fitting for top and bottom inner wall in Figure 3-11(b), respectively. Then

we obtain two expressions: $y = a_T x + b_T$ for top inner wall and $y = a_B x + b_B$ for bottom inner wall.

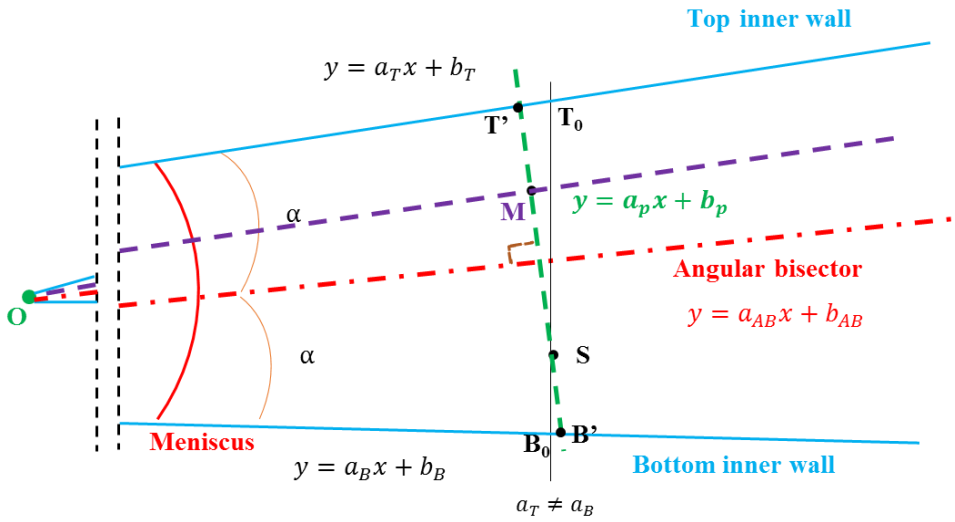

Figure 3-13 A sketch map of the quasi-radar-scanning method

If the top inner wall and the bottom inner wall are not parallel, they must have an intersection, as the point O (x_O, y_O) in Figure 3-13. The coordinate of point O is calculated depending on the expressions of the top and bottom inner wall, as Equation 3-4 and Equation 3-5:

$$x_O = \frac{b_B - b_T}{a_T - a_B} \qquad \text{Equation 3-4}$$

$$y_O = \frac{a_T b_B - a_B b_T}{a_T - a_B} \qquad \text{Equation 3-5}$$

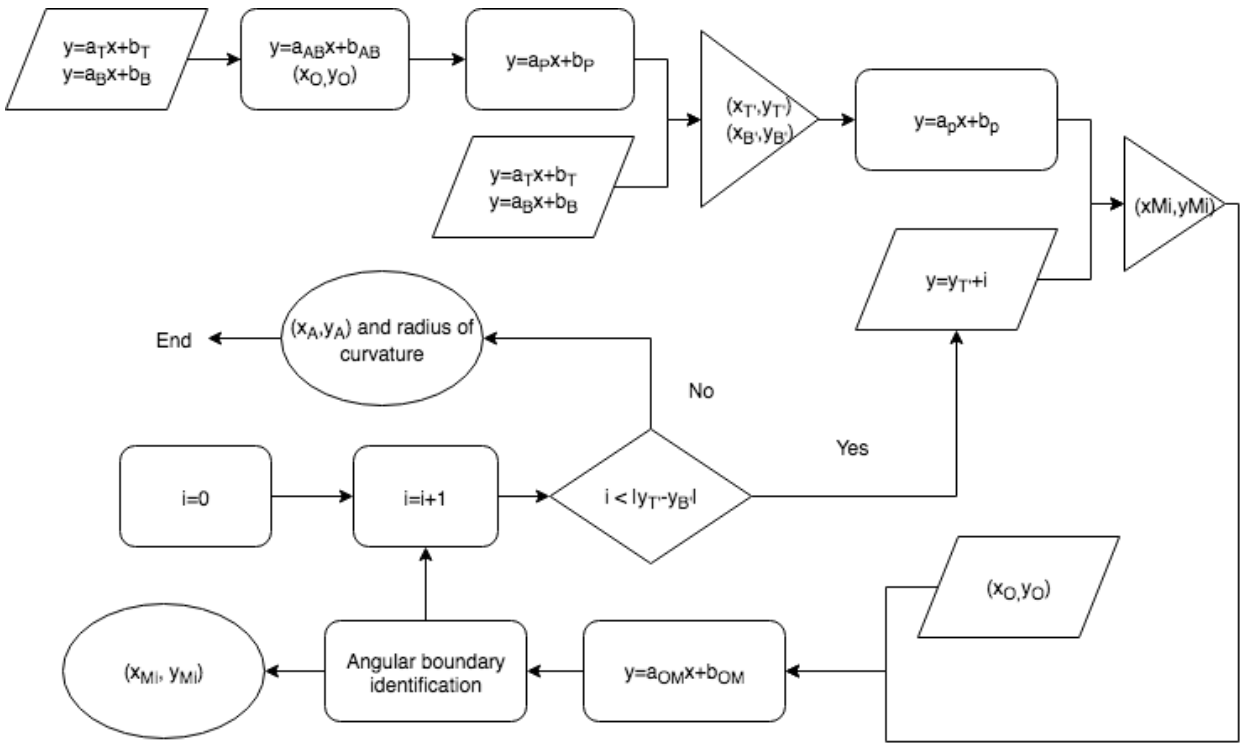

Figure 3-14 The algorithm of meniscus identification.

Figure 3-14 depicts the operation flow-sheet of the quasi-radar-scanning method in the situation $a_T \neq a_B$. The expression of angular bisector (AB, as Equation 3-6) of top and bottom inner walls is calculated based on the expressions of top and bottom inner walls:

$$y = a_{AB}x + b_{AB} \qquad \text{Equation 3-6}$$

$$a_{AB} = tan(\frac{arctan(a_T)+arctan(a_B)}{2}) \qquad \text{Equation 3-7}$$

$$b_{AB} = y_O - a_{\mathrm{AB}}x_O \qquad \text{Equation 3-8}$$

Thus, the expression of the perpendicular line including point S, (the green line in Figure 3-13) of the angular bisector is easy to get, as expressed in Equation 3-9.

$$y = a_P x + b_P \quad \text{Equation 3-9}$$

$$a_p = \frac{1}{a_{AB}} \quad \text{Equation 3-10}$$

$$b_P = y_s - \frac{x_S}{a_{AB}} \quad \text{Equation 3-11}$$

In Figure 3-13, T' and B' are the intersections of the perpendicular line of angular bisector and top and bottom inner walls, respectively. O is the intersection of top and bottom tube inner walls. M is a point on the line segment T'B'. The line OM (the path for meniscus recognition) can be expressed as:

$$y = a_{OM} x + b_{OM} \quad \text{Equation 3-12}$$

The expressions of a_M and b_M are shown in Equation 3-13 and Equation 3-14,

$$a_{OM} = \frac{d_{T'M} a_B + d_{MB'} a_T}{d_{B'T'}} \quad \text{Equation 3-13}$$

where $d_{T'M}$ is the distance between the point T' and the point M, $d_{MB'}$ is the distance between the point M and the point B', and $d_{B'T'}$ is the distance between the point T' and the point B'.

$$b_{OM} = y_O - a_{OM} x_O \quad \text{Equation 3-14}$$

Where (x_O,y_O) are the coordinates of point *O*.

In order to obtain the meniscus shape, we applied the principle meniscus detection previously described in detail for the line *OM*. This process is repeated for all points *M*, located on the segment

[T'B']. A series of points on the water-air interface is then obtained, as depicted in Figure 3-15(a), are obtained. Obviously, outliers exist in the obtained results, such as the two isolated points in Figure 3-15(a). The median filter is also efficient to eliminate these erroneous points. The final results of meniscus identification, after this least median filter, are shown in Figure 3-15(b).

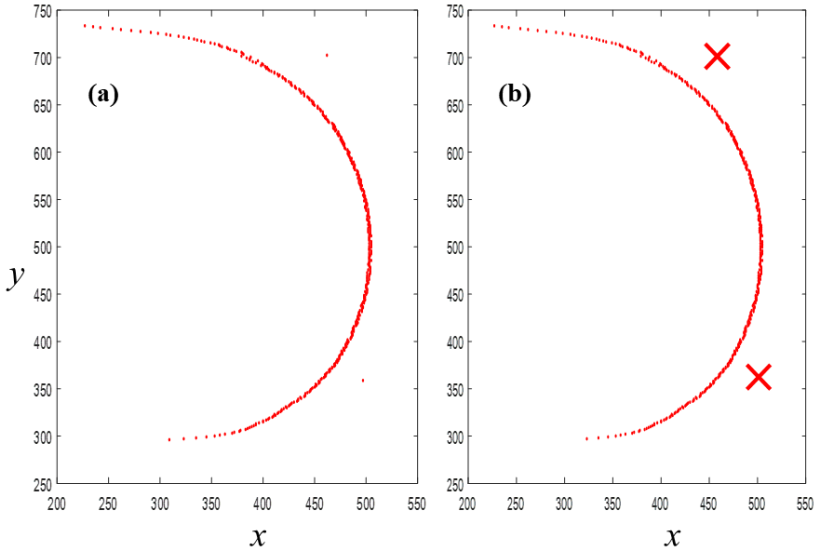

Figure 3-15. (a). The results of meniscus identification and (b). the results after outlier elimination

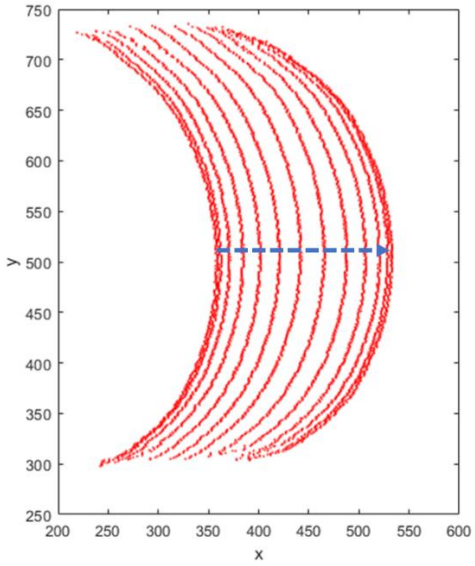

Figure 3-16 Meniscus variation in half-period for the experiment ID=2.2 mm, A=2 mm, f=10 Hz

Figure 3-16 shows the variation of the meniscus for half a period. From the figure, we may find that it is not easy to describe such a result with only one parameter. So, we will divide the description into two parts: the position of the water/air interface and the shape of the interface.

3.2.3.2. The determination of the position of the water/air interface

The target of this section is to find a point on the meniscus with a consistent standard to present the position of the water/air interface, as Figure 3-17. To complete the target, we propose to select the point with the max abscissa on the outlier-eliminated meniscus as a reference to show the position of the interface. We call the selected point as the most advanced point and mark it with A. Due to the gravity, the meniscus is not symmetrical, thus the position of point A is not in the middle of the meniscus. Figure 3-18 displays the variation of the point A abscissa over three periods.

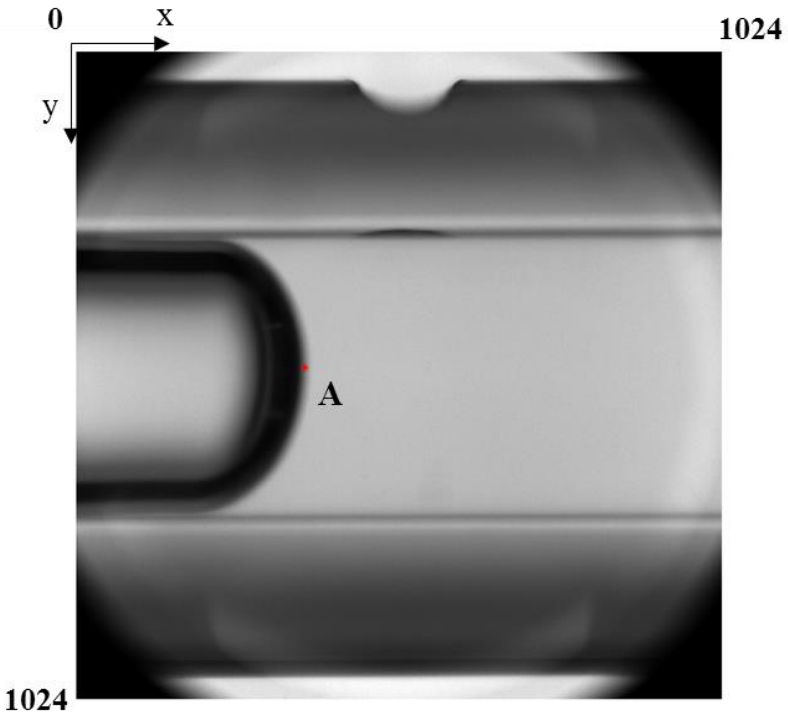

Figure 3-17 A captured image with a desired point on the water/air interface

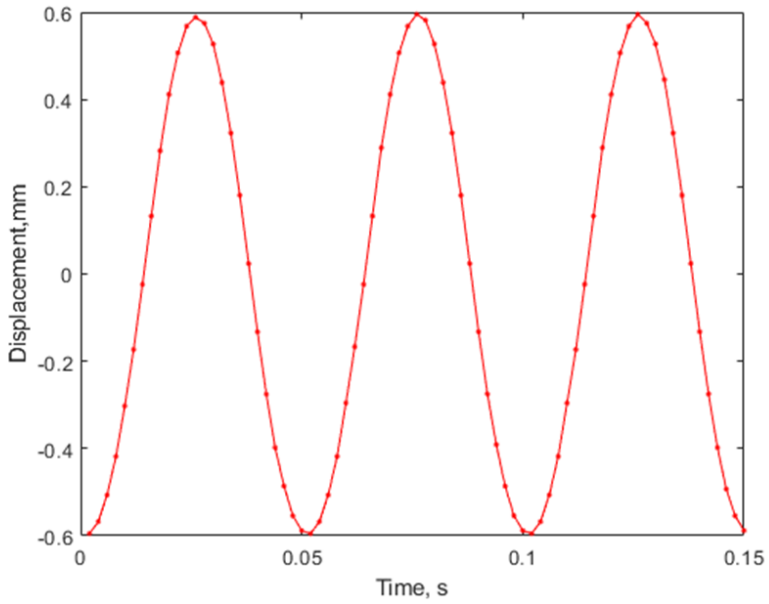

Figure 3-18 The displacement of water for the experiment ID=2.2 mm, A=2 mm, f=20 Hz

3.2.3.3 Determination of the shape of the meniscus

To describe the shape of the water/air interface, we decided to use the curvature radius of the meniscus. In this study, we cannot consider the full meniscus because of the non-circular shape of the meniscus. The aim of this step is to find a proper proportion of meniscus to fit a circle. There are two criteria:

1. The proportional selection of the meniscus should be centered on point *A*. As previously written, its position is a little lower than tube axis, due to the effect of the gravity. Then, the meniscus is divided into two parts: a short arc (lower than point *A*) and a long arc (higher than point *A*). Thus, half the selected quantity of the points cannot exceed the points quantity of the short arc.

2. The coefficient of determination (R^2) of the fitted results must exceed 0.99 for all the experiments with the selected proportion in this study.

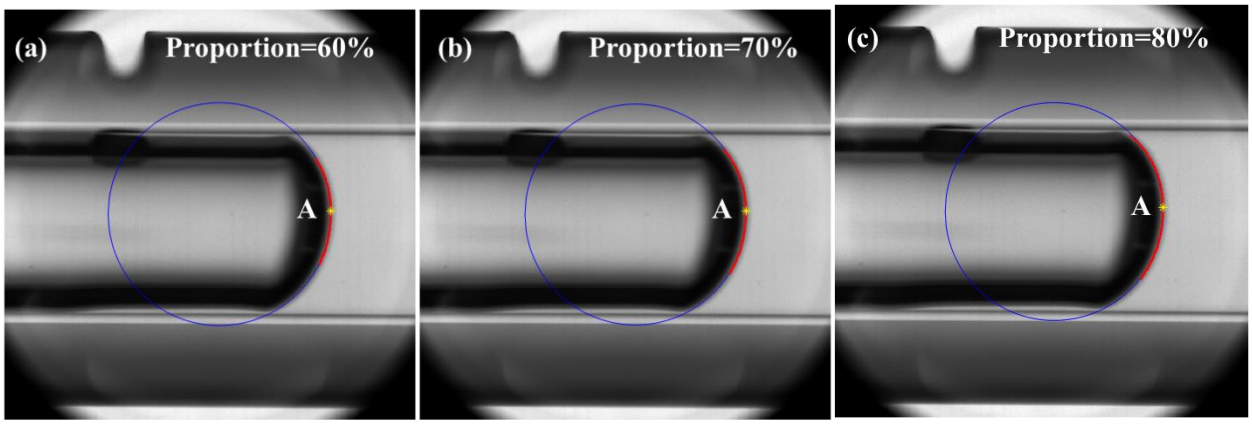

Figure 3-19 The fitting results for different proportions (60-80 %) of the full meniscus (the image is from the experiment ID = 2.2 mm, A = 2 mm, f = 30 Hz)

In order to tune these criteria, we took an experiment with the following parameters as an example: *ID = 2.2 mm, f = 30 Hz, A = 2 mm*. Indeed, thanks to preliminary tests, we know that the meniscus shape of the most deformed among the studied parameter ranges (see paragraph 4.3.1). To calculate the radius of the curvature for the selected meniscus, we apply a non-linear fitting method based on the total least squares provided by MATLAB. Figure 3-19 depicts the fitted results with different proportions of meniscus from 60 % to 80 %.

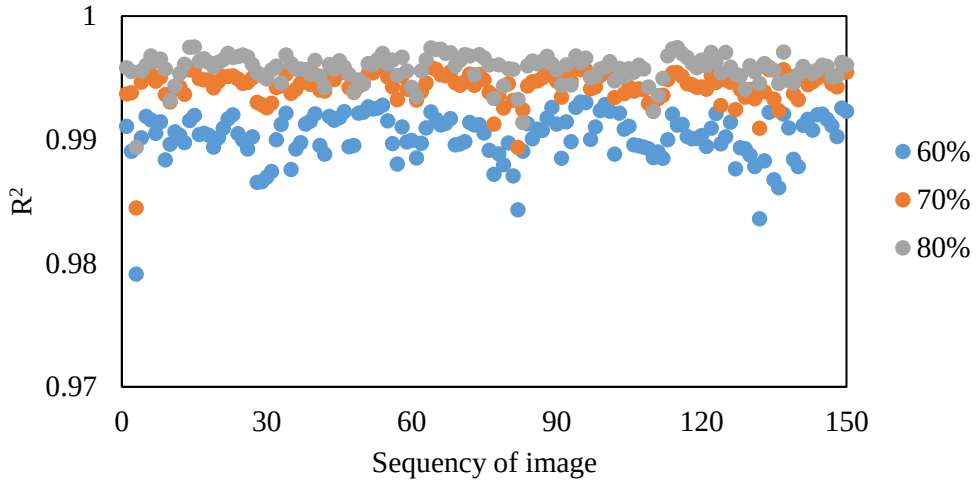

Figure 3-20 The contrast of the coefficient of determination (R^2) for the results fitted by four different proportions of meniscus (60 % - 80 %) for 3 periods

Figure 3-20 depicts the coefficient of determination for the results fitted with three different proportions (60 % to 80 %) of meniscus over three periods. It is obvious that almost all the data are near the unit value. This means that, for the majority of situations, the three proportions are suitable. Moreover, we also applied the proportion equal to 90 % on the circle fitting for meniscus, but it cannot be achieved under some situations, especially when there is a big transformation of the meniscus. Half numbers of the selective points exceed the quantity of points on the short arc. Consequently, we fixed the proportion at 80% to get the meniscus radius for all result analysis. Figure 3-21 gives one example of curvature evolution fitted using 80 % of the smaller half-arc of meniscus around point A during three vibrational periods.

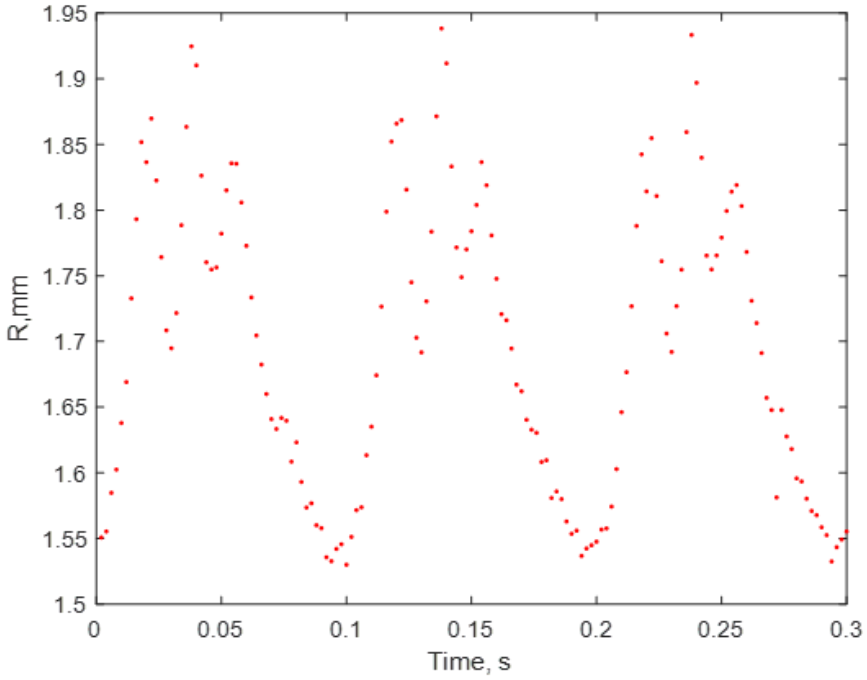

Figure 3-21 The variation of radius curvature during 3 vibrational periods (ID = 2.2 mm, f = 30 Hz, A = 2 mm)

3.2.4 Determination of the tube position

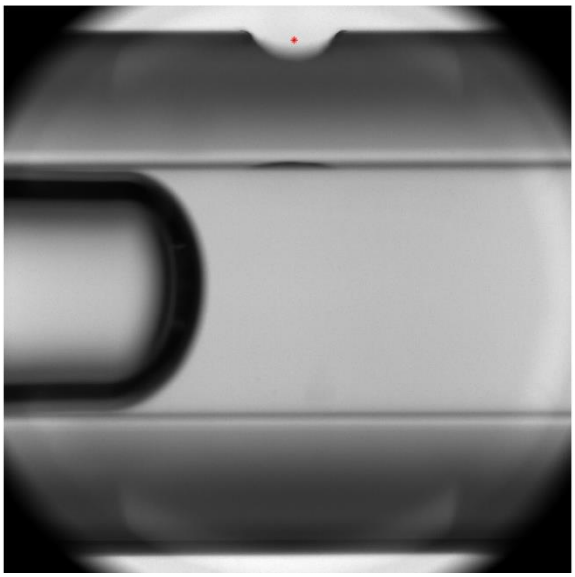

Figure 3-22 A captured image with a mark of the mass center of the notch

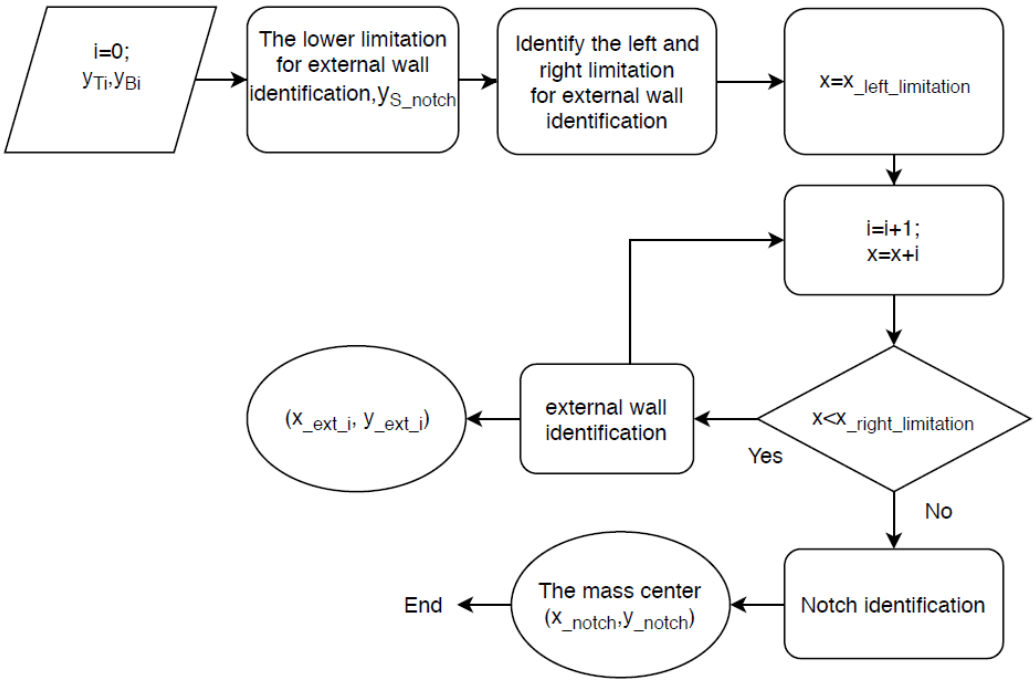

Figure 3-23 The algorithm to identify the mass center of the notch

The aim of this section is to find the mass center of the notch on the external wall of the capillary tube (see Figure 3-22) as accurate indicator of the tube position. Figure 3-23 displays the algorithm

for the total process to obtain the desired result in Figure 3-22.

3.2.4.1 Defining the external wall of the tube

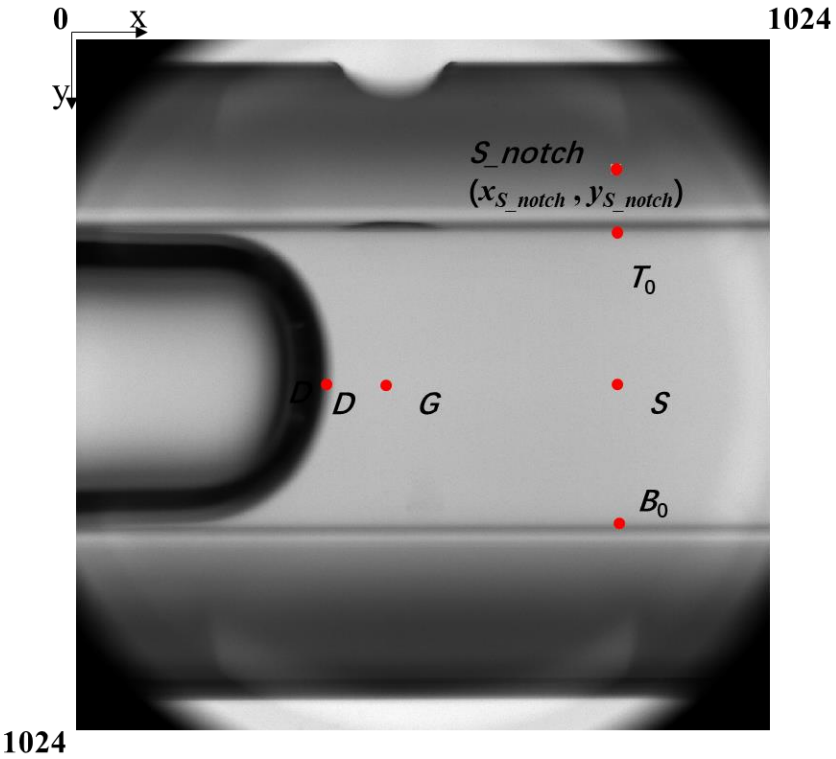

Figure 3-24. A captured image with point S, D, T, B, G, and S_notch

The identification of the notch starts from the definition of a relevant ROI. The upper limit is the top of the captured image, and the lower limit is determined by the position of point *S_notch*, a point within the tube wall, as calculated by Equation 3-15:

$$y_{S\_notch} = y_{T_0} - \frac{y_{B0} - y_{T0}}{N_{S\_notch}} \qquad \text{Equation 3-15}$$

where $N_{S\_notch}=5$.

Figure 3-24 shows the location of point *S_notch*. The line $y = y_{S\_notch}$ is the floor for the external

wall determination. The left and right limits are determined by a more complicated way, which depends on the features of the grayscale change in vertical direction. Figure 3-25 displays 5 classes of grayscale variation and the corresponding position, which contains all the features of grayscale variation.

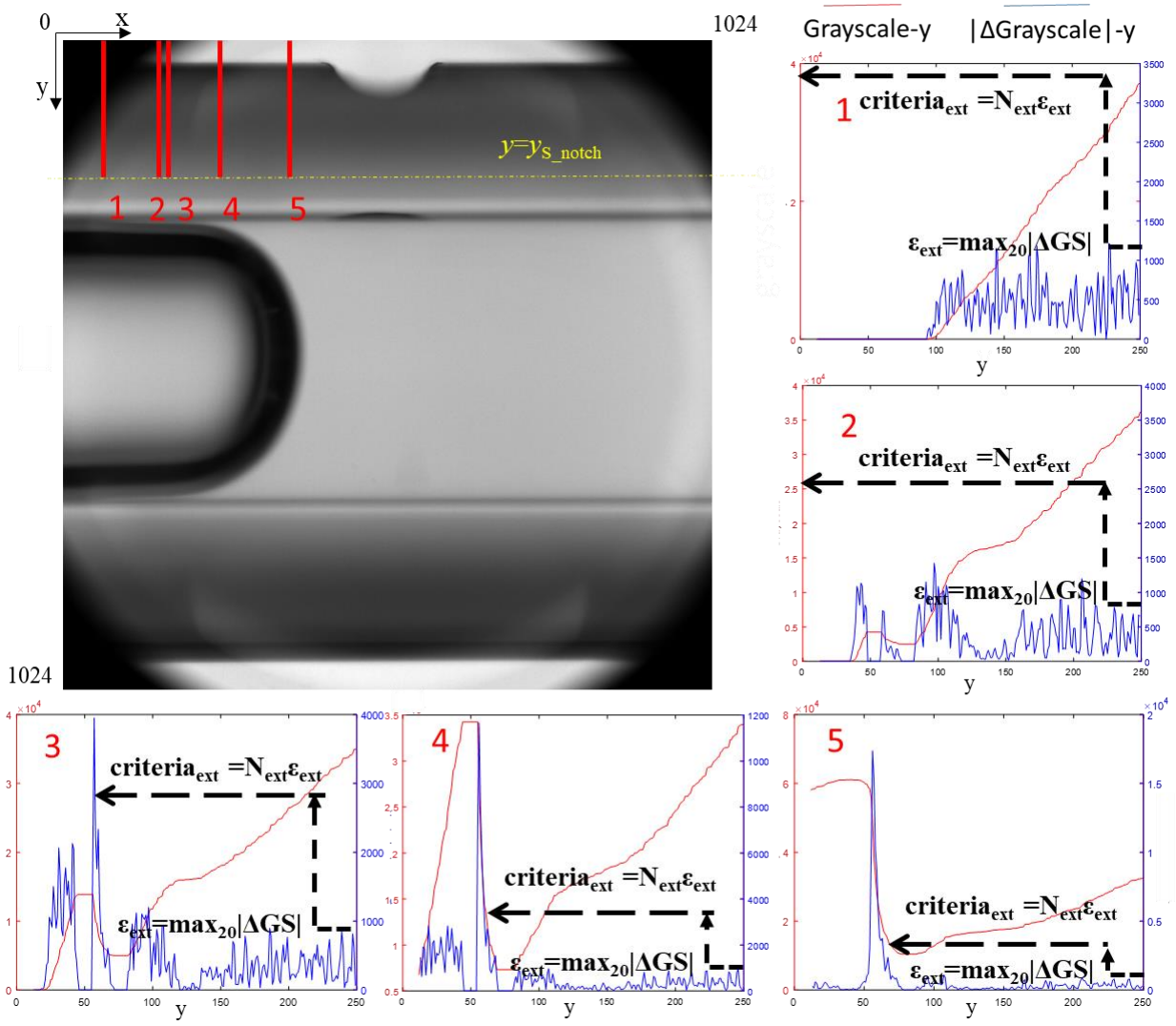

Figure 3-25. A scheme of the determination of left and right limits

The $|\Delta GS|_{max}$ over the nearest 20 points to the floor is set as the basic external wall criterion ε_{ext}. The basic external wall criterion is multiplied by an amplification coefficient (N_{ext}), then we obtain

the final external wall criterion ($N_{ext}\varepsilon_{ext}$). If the $|\Delta GS|_{max}$ is lower than $N_{ext}\varepsilon_{ext}$, such as the situation 1 and 2 in Figure 3-25, the corresponding abscissae will be excluded in the target scope of the external wall. Thus, the left and right limit for external wall identification can be confirmed.

Depending on the features of the image, the region of interest about the external wall focuses on the first decreasing slope of the GS-y curve. The desired point can be acquired by the method applied in bottom inner wall identification. After the initial identification, a median filter is applied to remove the outliers, and the final result is shown in Figure 3-26.

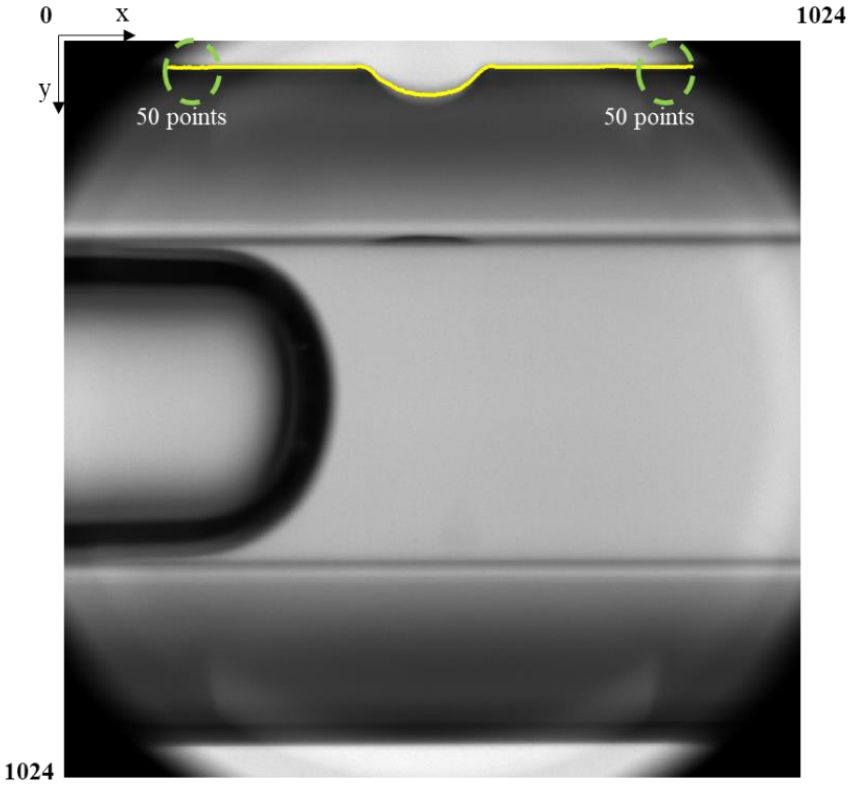

Figure 3-26. The result of external wall identification

The following step of external wall identification is to find out the coordinate set of the notch. In order to avoid the overlap with the notch during vibration, 50 points on left and right edges are

selected respectively. The code performs a linear fitting of the selected coordinates to get the slope $a_{platform}$ and the intercept $b_{platform}$. Then, we use Equation 3-16 to represent the external wall line without the notch:

$$y = a_{platform}x + b_{platform} \quad \text{Equation 3-16}$$

3.2.4.2 The identification of the notch

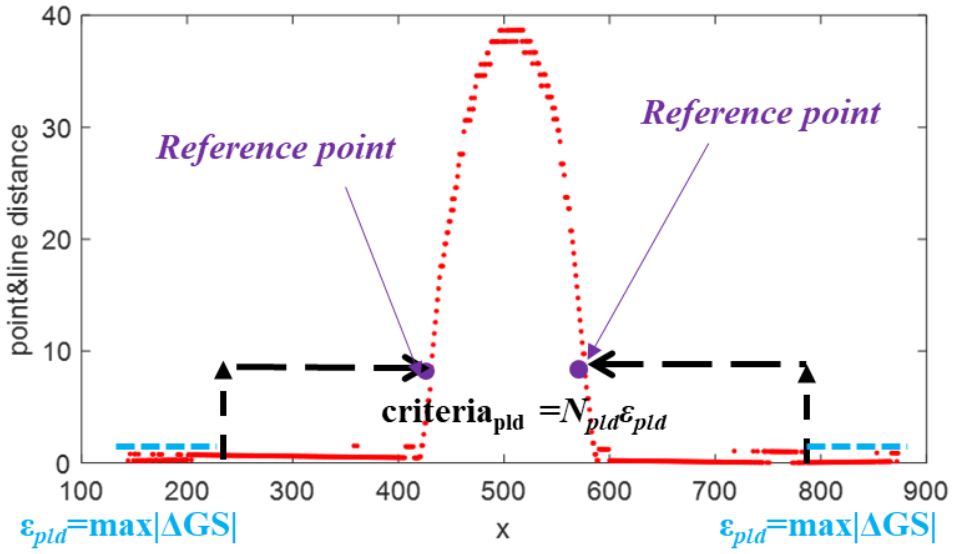

Figure 3-27. A figure of point-line distance versus abscissae

After the identification of the external wall, the code calculates the distance between each identified point to the platform. Figure 3-27 shows a curve of point-line distance versus abscissae. The maximum distance among the 100 points near both ends is set as the basic point-line distance criterion ε_{pld}. The basic point-line distance criterion is multiplied by an amplification coefficient (N_{pld}), then we obtain the final point-line distance criterion($N_{pld}\varepsilon_{pld}$). Then all the points with distance higher than $N_{pld}\varepsilon_{pld}$ in Figure 3-27 will be imported in the initial matrix of notch identification.

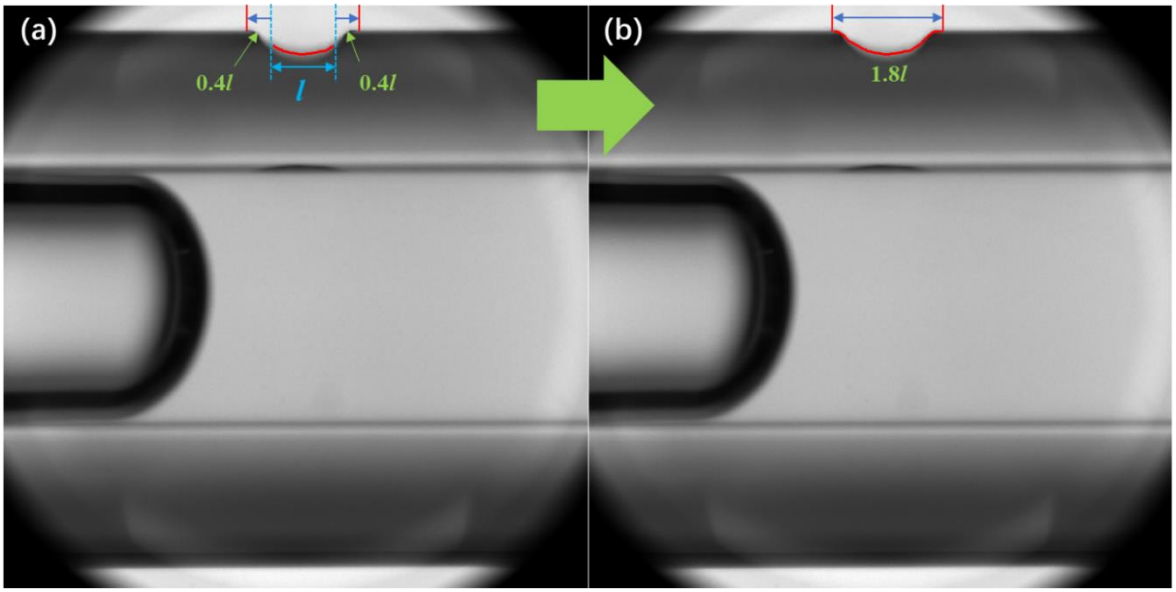

Figure 3-28. The results of the second-step of notch identification

Obviously, some notch area will not be included in the initial matrix due to the criterion. Then we set an expansion for the results. Based on this matrix, we expand an extra 40% of the width of the initial notch on both sides to contain all the notch area. Figure 3-28(b) shows the expansion results.

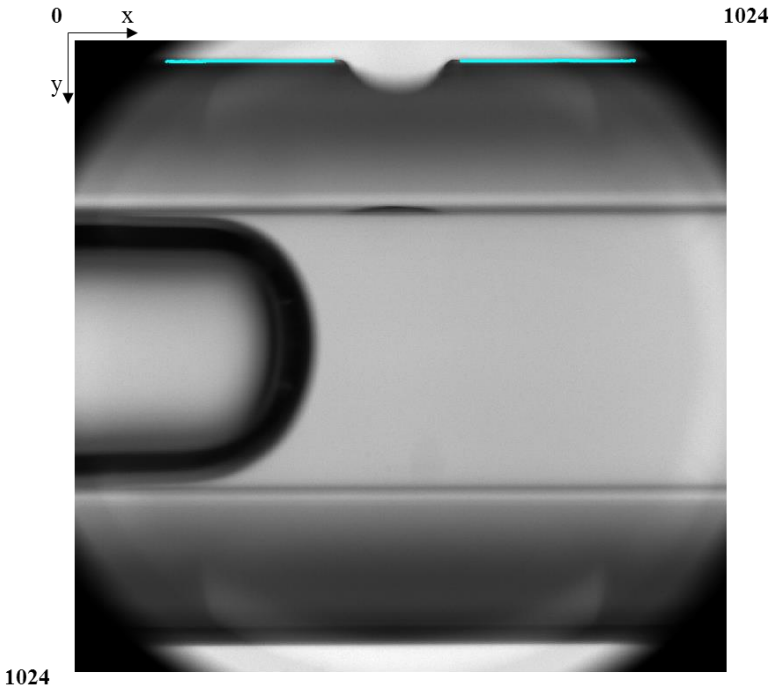

Figure 3-29 The platform after the second-step of notch identification

Except for points present in Figure 3-28(b), the remaining part of the points on the external wall (Figure 3-29) are linear fitted to determine a new platform. The new platform is more accurate to present the external wall as it does not consider the notch. It will replace the role of the previous robust one which was fitted by 50 points on each edge. It can be expressed as Equation 3-17:

$$y = a_{platform2}x + b_{platform2} \qquad \text{Equation 3-17}$$

For the selected notch points, the new platform is applied to close the curve, shown as Figure 3-30. This step aims to precise the scope of the notch in order to calculate the coordinate of the mass center. The code will find two intersections of notch and the new platform near the center and set them as the left and the right limit for the desired notch. The area must be perfectly closed for the mathematical determination of the center of mass. However, some points might be missing during the vertical determination of the external wall due to the image quality.

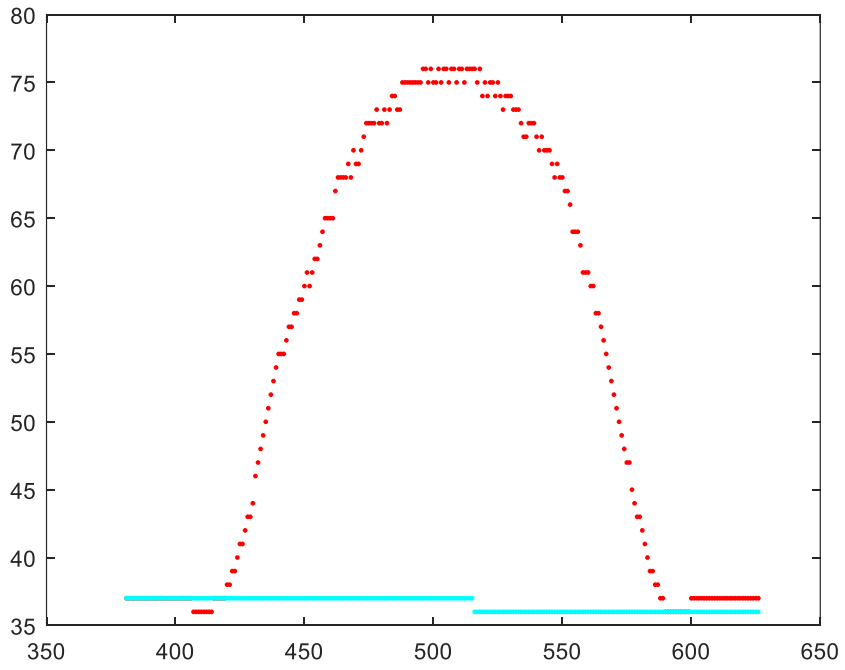

Figure 3-30. The expanded notch and the new platform in notch range

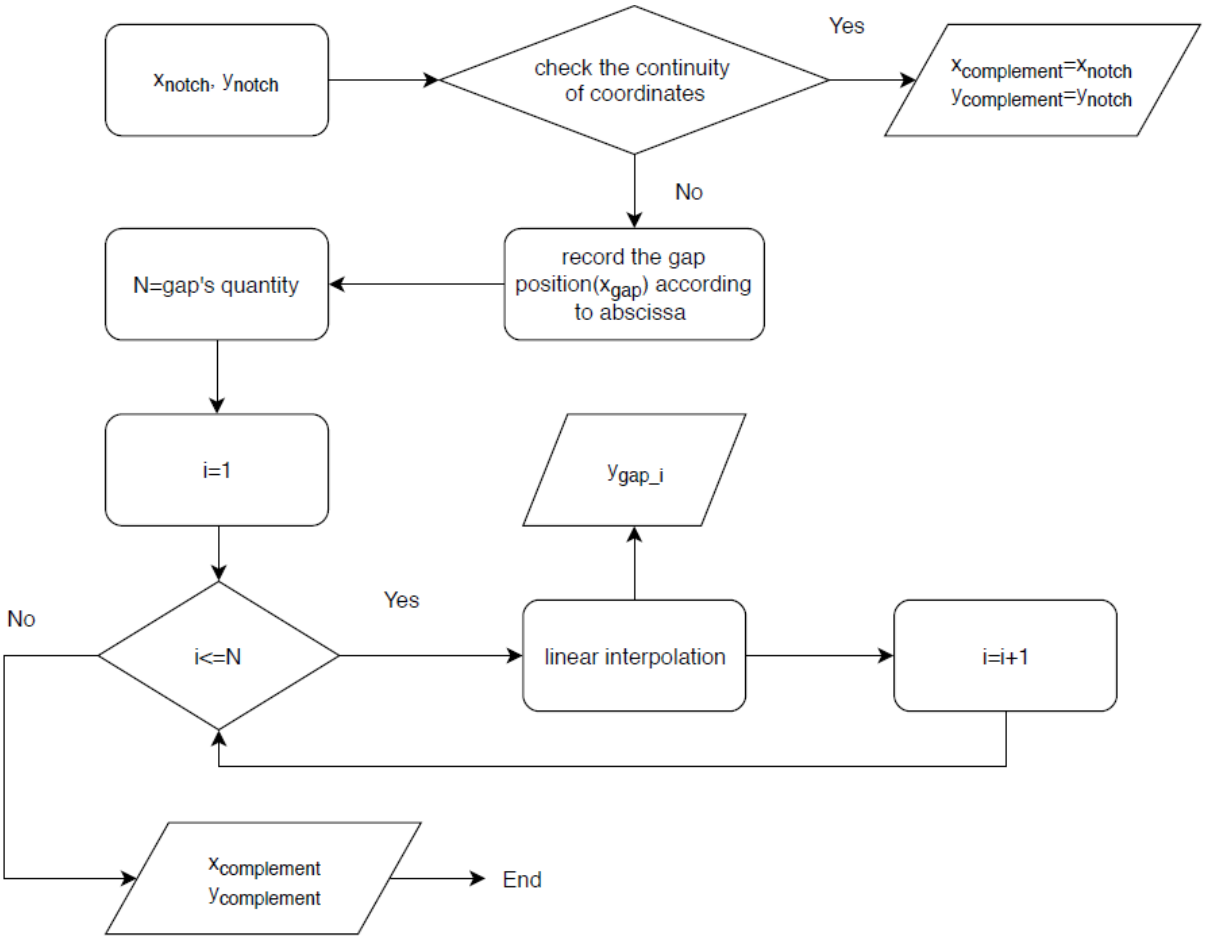

Figure 3-31. The algorithm of linear interpolation

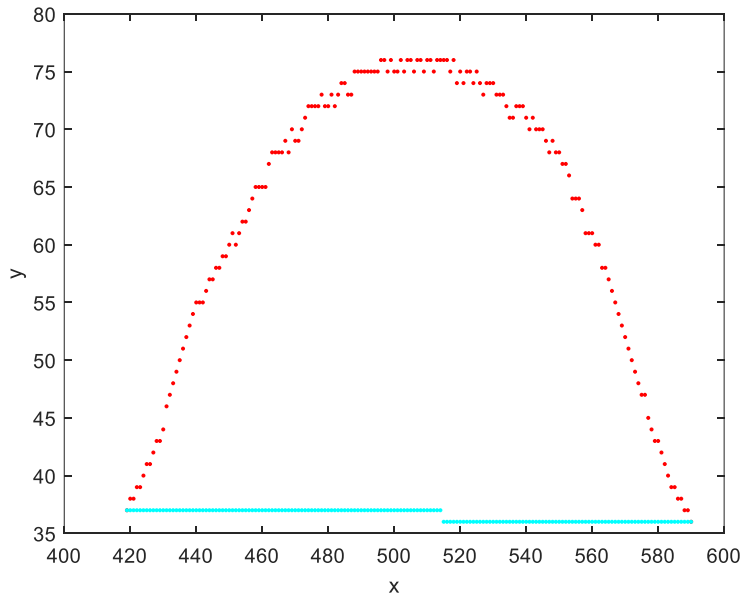

Figure 3-32. The closed area of the notch

To complete the notch border, a linear interpolation method is applied (Figure 3-31). After the complementary step, we can obtain a perfect closure area of the notch as shown in Figure 3-32.

The mass center of the closed area is calculated by Equation 3-18:

$$x_c = \frac{\sum P_i x_i}{\sum P_i} \qquad \text{Equation 3-18}$$

where $P_i = \left| y_i - \left(a_{platform2} x_i + b_{platform2} \right) \right|$

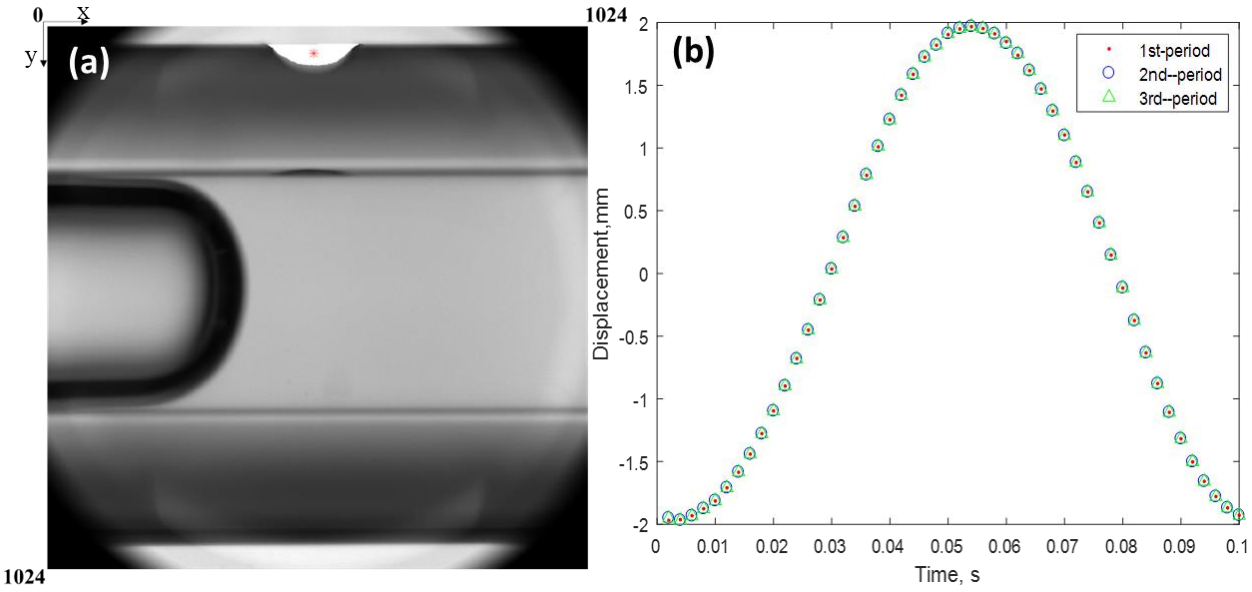

Figure 3-33 (a) A captured image with the identified notch area and the mark of mass center and (b) the merged displacement of the tube for the experiment ID=2.2 mm, A=2 mm, f=10 Hz in 3 periods

Figure 3-33(a) shows the identified results of the notch area and the mass center, and Figure 3-33(b) depicts the displacement of the mass center for three vibrational periods. The analyzed result confirms the vibrational parameters and proves that the method of capillary tube tracking is efficient.

3.3 Conclusions

In this chapter, we proposed a detailed description of the image processing and analyzing method. The code aims at identifying the variation of the air/water interface and the motion of the capillary tube.

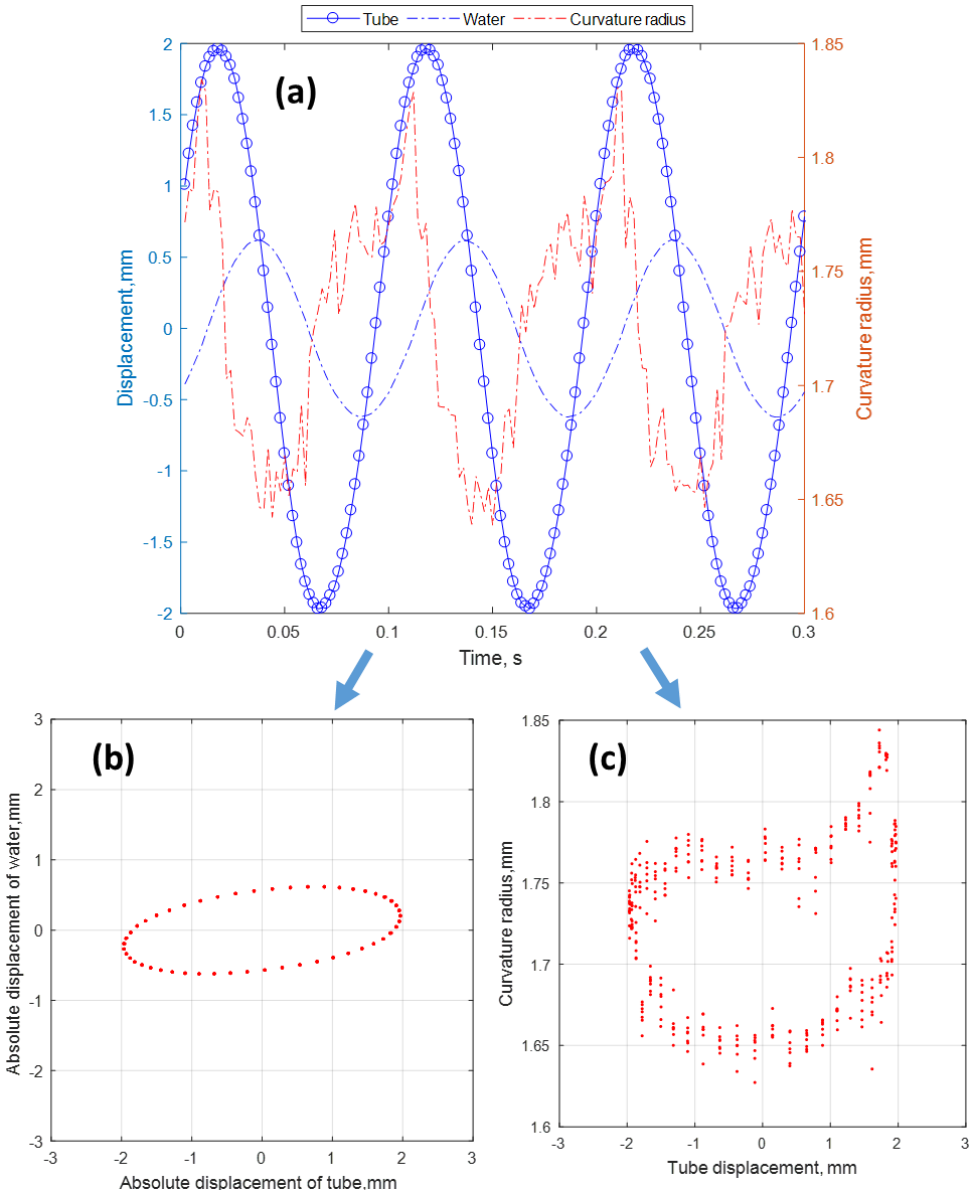

Figure 3-34 (a) The variation of tube position, water position, and curvature radius of meniscus according to time, (b) absolute displacement of the water versus that of tube (c) curvature radius of meniscus variation versus absolute displacement of the tube

To achieve this goal, local analysis of the grayscale was systematically applied. In particular, we treated the grayscale information along various lines to define specific intersection in an accurate and robust manner. This method is applied for all the boundaries, such as the gas-liquid interface, the inner tube wall and the notch on the external wall of the tube.

Meanwhile, we also considered the tube deviation from the horizontality and from perpendicularity to the optical axis. In these cases, the top and bottom projections of the inner wall may not be horizontal or parallel. For all the identification, we use a 1-D median filter to eliminate the outliers and get a smooth result.

Thus, we can obtain three types of result: position of the tube, position of the air/water interface and curvature of the meniscus. Figure 3-34 depicts the variation of tube position, water position, and meniscus curvature as a function of time. From these values, one can plot the Lissajous curve, absolute displacement of water versus that of tube, or the variation of curvature versus the absolute displacement of tube.

Lissajous curve is also known as Bowditch curve[216,217]. It is a graph of parametric equations as Equation 3-19. It is often used to describe harmonic motion. Practically, this method is also used for real-time analysis of the phase relationship between two periodic signals:

$$\begin{cases} x = A_x sin(\omega t) \\ y = A_y sin(\omega t + \varphi) \end{cases} \qquad \text{Equation 3-19}$$

In this study, $\omega_x = \omega_y = \omega$ and φ is the phase difference. Lissajous curve is a practical way to observe the phase difference between the motion of tube and water, and the effect of tube displacement on the variation range of curvature radius of the meniscus.

Finally, the reliability of the code was verified step by step. With this code, we can obtain reliable data for further analysis of the water behavior in the capillary tube as a function of the applied signal.

Chapter 4 Investigation of water behavior in a vibrating capillary tube with a symmetrical configuration

4.1 Introduction

In this chapter, we experimentally investigated the effect of symmetrical vibration on the evaporation in a capillary tube and analyzed the underlying mechanisms. In the first part, we compare the evaporation rate of the water index with and without vibration. So that, we can determine the intensification efficiency of the vibration.

Then, we compare the intensification ratios of the evaporation and the position of water index in the tube. To investigate the mechanisms involved in the intensification, we will focus on the variation of the water meniscus (displacement and geometry). This provides a direct description of the water index behavior.

4.2 The effect of symmetrical vibration on the evaporation in a capillary tube

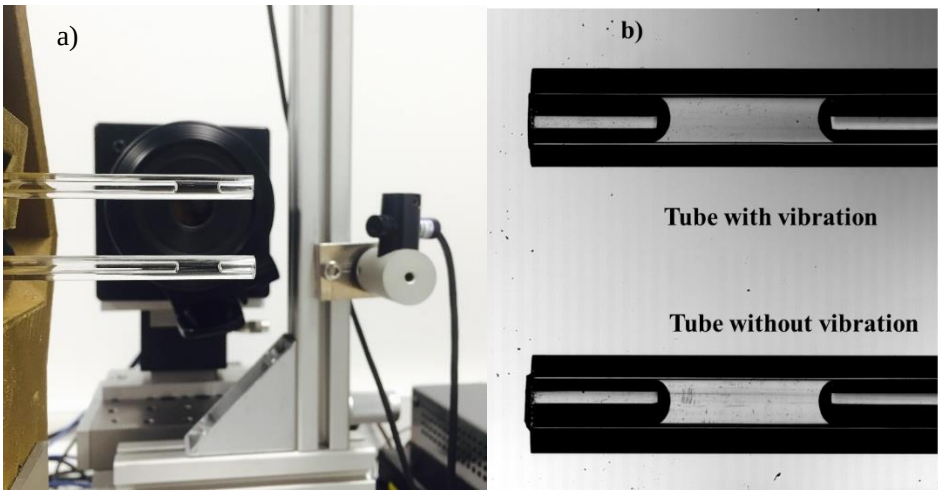

Figure 4-1 A photo of the contrast experiment of evaporation intensification by vibration

Two capillary tubes with the same length (*L_tube* = 210 mm) and inner diameter (ID = 2.2 mm) were selected. Figure 4-1a is an overview of the experimental setup and Figure 4-1b is an image directly grabbed by the camera. The upper tube is subject to vibration while the lower one,

submitted to the same conditions (temperature and relative humidity), remains static. Approximately 38 μL of deionized water (about 12 mm in length) was injected into each of these capillary tubes. Both water indexes were adjusted to the same position using a rubber suction bulb: the external meniscus where placed about 7 mm away from tube orifice (as Figure 4-1 a). The vibration was performed at the frequency of 30 Hz and with an amplitude of 2 mm. This experiment lasts 7 hours. The room temperature remained in the range 25 to 27 ℃ and the relative humidity between 40.5 % and 44.5 %.

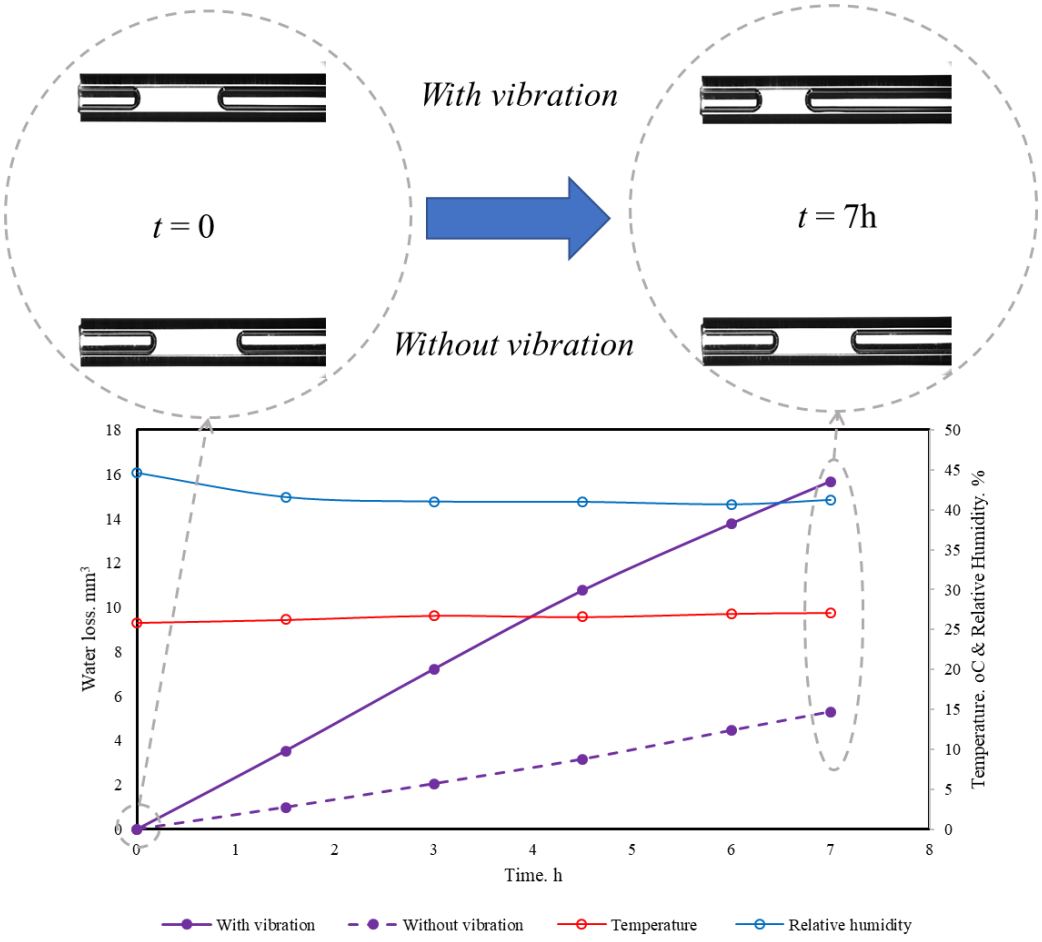

Figure 4-2 Water loss versus time with and without vibration

Figure 4-2 depicts the water loss in the tube obtained under the conditions mentioned previously.

The volume of water is calculated by the Equation 2-1.

The figure exhibits an obvious intensification of the water evaporation. In the blank experiment, the natural evaporation rate is 0.75 mm^3/h, while the one intensified by vibration reaches 2.38 mm^3/h, which is almost triple of the blank test. The vibration is therefore an efficient way to intensify the process of mass transport in a capillary tube. We can define the intensification ratio as follows:

$$intensification\ ratio = \frac{evaporation\ rate\ with\ vibration}{evaporation\ rate\ without\ vibration} \quad \text{Equation 4-1}$$

In a static capillary tube, we can neglect convection and focus on the diffusion due to the tiny radius of the tube. For the evaporation in a static tube, the diffusion of vapor is governed by Fick's law:

$$j_v = -\rho_g D_v \frac{d\omega_v}{dx} \quad \text{Equation 4-2}$$

where j_v is the diffusion flux of the vapor, D_v the diffusion coefficient of vapor in air, ω_v the mass fraction of vapor and x is the position.

Equation 4-2 can be used to evaluate the drying rate in the static tube; Assuming that the evaporation rate is small enough and the heat exchanges large enough to consider, the configuration can be considered as isothermal. Due to the huge contrast of density between liquid and vapor, the interface position can be considered as almost fixed compared to the vapor flux. A stay-state diffusion can therefore be assumed in the gaseous part of the tube.

As the tube has two opening to the air, the two distances of the meniscus to the openings should be considered (Figure 4-3). The total evaporation rate $Q_v$of the static tube reads as:

$$Q_v = S\rho_g D_v(\omega_{vs} - \omega_{v\infty})\left(\frac{1}{L\_left} + \frac{1}{L\_right}\right)$$ Equation 4-3

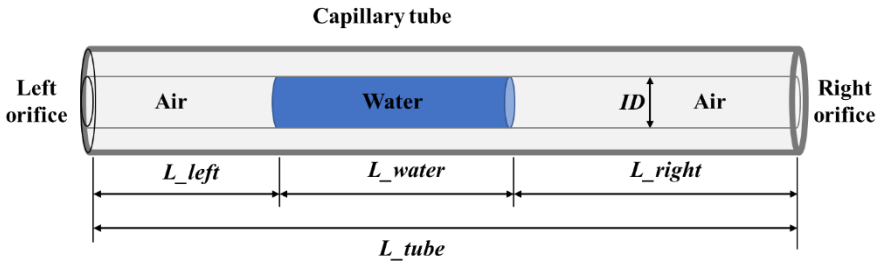

Figure 4-3 A scheme of the tube with water inside

To test the effect of the water position in the tube, one series of experiments were designed. Five different positions in the tube were selected as shown in Table 4-1. It displays the distances between two interfaces of water index to the corresponding tube orifices as Figure 4-3. The theoretical flux computed from Equation 4-3 is compared to the experimental flux of the static tube. Classical expressions were used to compute the saturated vapor pressure and the binary diffusivity of water in air at 26 °C (respectively 3333 Pa and $2.66.10^{-5}$ m^2 s^{-1}).

Table 4-1 Drying tests performed with various values of the two distances from the tube ends. Experimental drying rate measured with the static tube and theoretical value computed using Equation 4-3.

L_left **mm**	***L_right*** **mm**	***Drying rate with vibration*** ***mm^3/h***	***Drying rate without vibration*** ***mm^3/h***	***Theoretical rate*** ***mm^3/h***
7	191	2.3	0.75	0.77
14	184	1.23	0.52	0.40
21	177	0.84	0.40	0.28
29	169	0.55	0.34	0.21
40	158	0.28	0.18	0.16

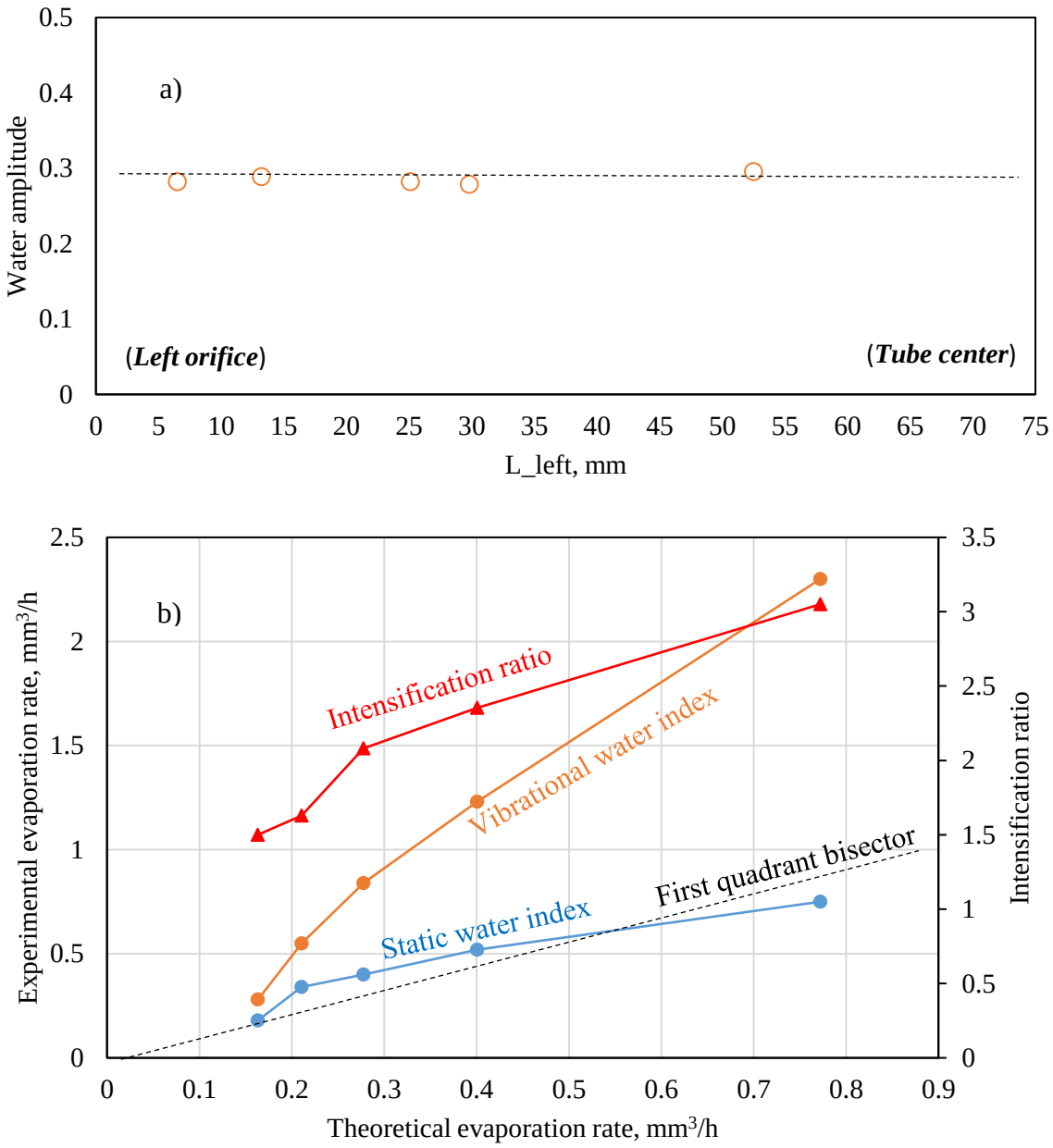

Figure 4-4.(a) The water amplitude and (b)the variation of the intensification ratio of the water evaporation with the index of water-tube orifice distance

Figure 4-4 depicts the whole set of data obtained for this series of experiments. It is worth noting that the water amplitude was almost the same for all tests (ca. 0.30 mm) in Figure 4-4a. This proves that the driving force of water motion at different positions on the air in the tube are the same. This

figure confirms that the static tube behavior is quite well defined by the simple diffusion model. This is simply explained by the small tube diameter which ensures a gas at rest inside the tube. In expression 4.3, the boundary layer was neglected in comparison to the diffusion distance: the experimental results prove that this assumption was relevant. Figure 4.4b depicts a significantly decreasing trend of the intensification ratio when the nearest tube orifice increases. For the fluid in the capillary tube, the intensification of the mass transfer by the vibration may due to four reasons: 1) viscous dissipation; 2) the increase of external transfer coefficient; 3) the decrease of average concentration of vapor in the tube; 4) the increase of internal transfer. Besides, the internal transfer can be neglected, because the fluid in this experiment is pure water. Viscous dissipation is likely to heats up the index and increase the partial pressure of water. However, the constant frequency and the amplitude of the water are constant. So, the intensification is not due to the first two phenomena. This confirms the low resistance to vapor diffusion in the boundary layer, already stated in the case of static tube. This interesting observation therefore tells us that the intensification is more related to a faster diffusion inside the tube, due to meniscus vibration. Thus, we need to explore the possible decrease of average vapor concentration in the tube.

This may due to a pumping effect from the water motion. During the vibration, the motion of water expels the air with higher relative humidity outside of the capillary tube and inhales the air with lower relative humidity from the environment into the tube. Then the vapor concentration decreases. This effect is more remarkable when the water is closer to the orifice because of a higher proportion of the refreshed air, regarding the air volume between the tube orifice and the water.

The intensification rate depends on the position of the water index. It also depends on the motion of the water, which may vary with the frequency and the amplitude of the tube vibration. The effect

of both parameters has to be investigated.

4.3 The effect of symmetrical vibration on the water behavior

To test the impact of vibration on the water system, an exploration of water behavior in a capillary tube with two open ends with symmetrical vibrations (f = 10 - 30 Hz, A = 0.5, 1 and 2 mm) was carried out. The images are treated using the method described in chapter 3. Two dimensionless numbers are introduced to help the analysis of the water index behavior during vibration.

4.3.1 Experimental protocol

To study a wide range of contrasted situations, the values of three parameters were systematically tested, as shown in Table 4-2. Thus, we obtained a dataset of 18 experiments. For each test, we registered 50 pictures per period, over 7 periods. Figure 4-5 presents the images grabbed during one cycle for ID = 2.2 mm, f = 30 Hz and A = 2 mm. The dashed line presents the previous position, and the full line represents the current position. The red color is the mark of the capillary tube, and the blue color stands for water. For this test, we notice that the menisci are not perfectly symmetrical to the horizontal plane: gravity is not negligible anymore for a 2.2 mm-inner diameter tube.

Table 4-2. Parameter values tested for sinusoidal vibration of water inside a capillary tube.

Inner diameter	**Frequency**	**Amplitude**
0.6 and 2.2 mm	10, 20 and 30 Hz	0.5, 1 and 2 mm

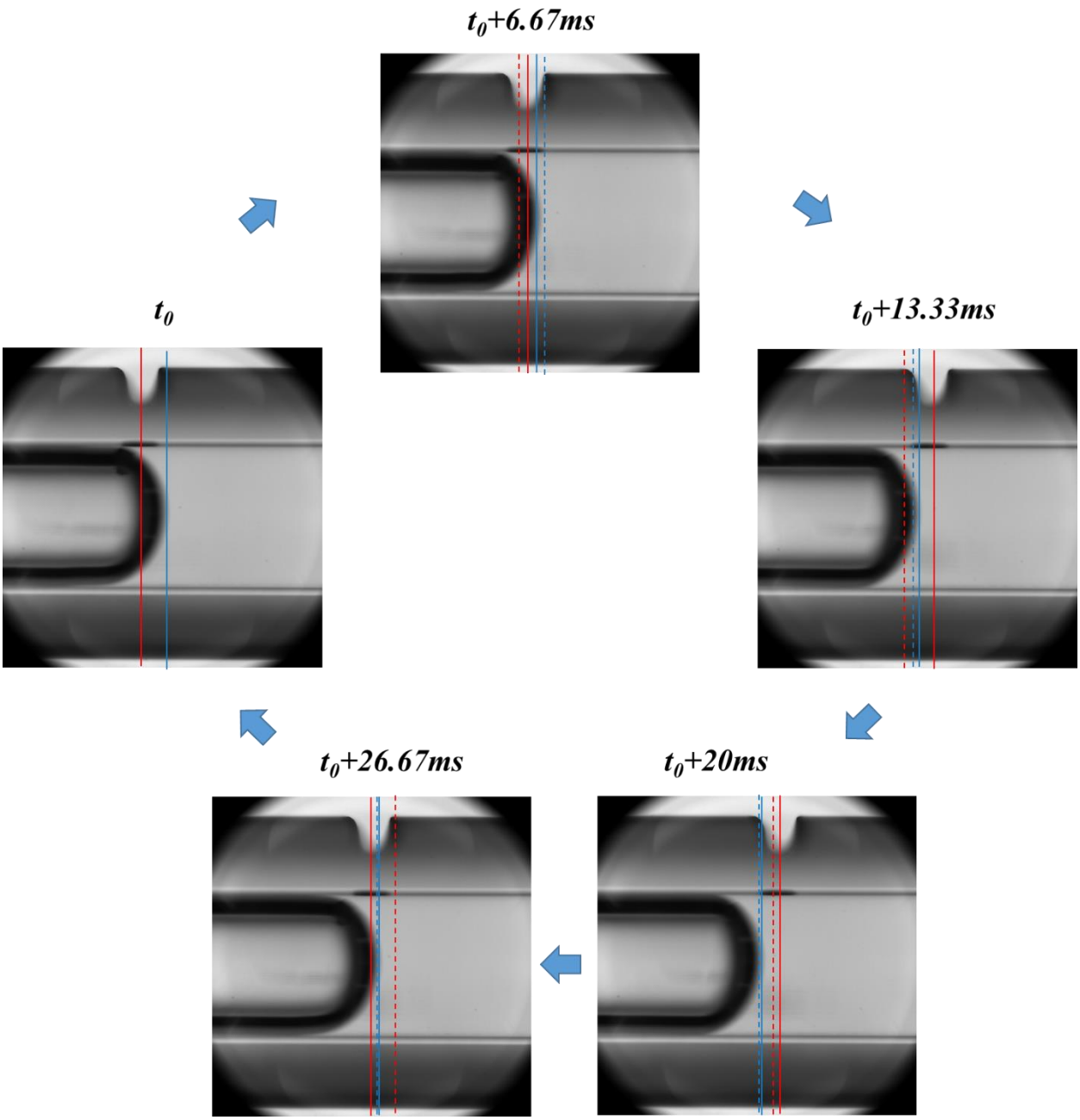

Figure 4-5. Water displacement during one period (ID = 2.2 mm, f = 30 Hz, A = 0.5 mm)

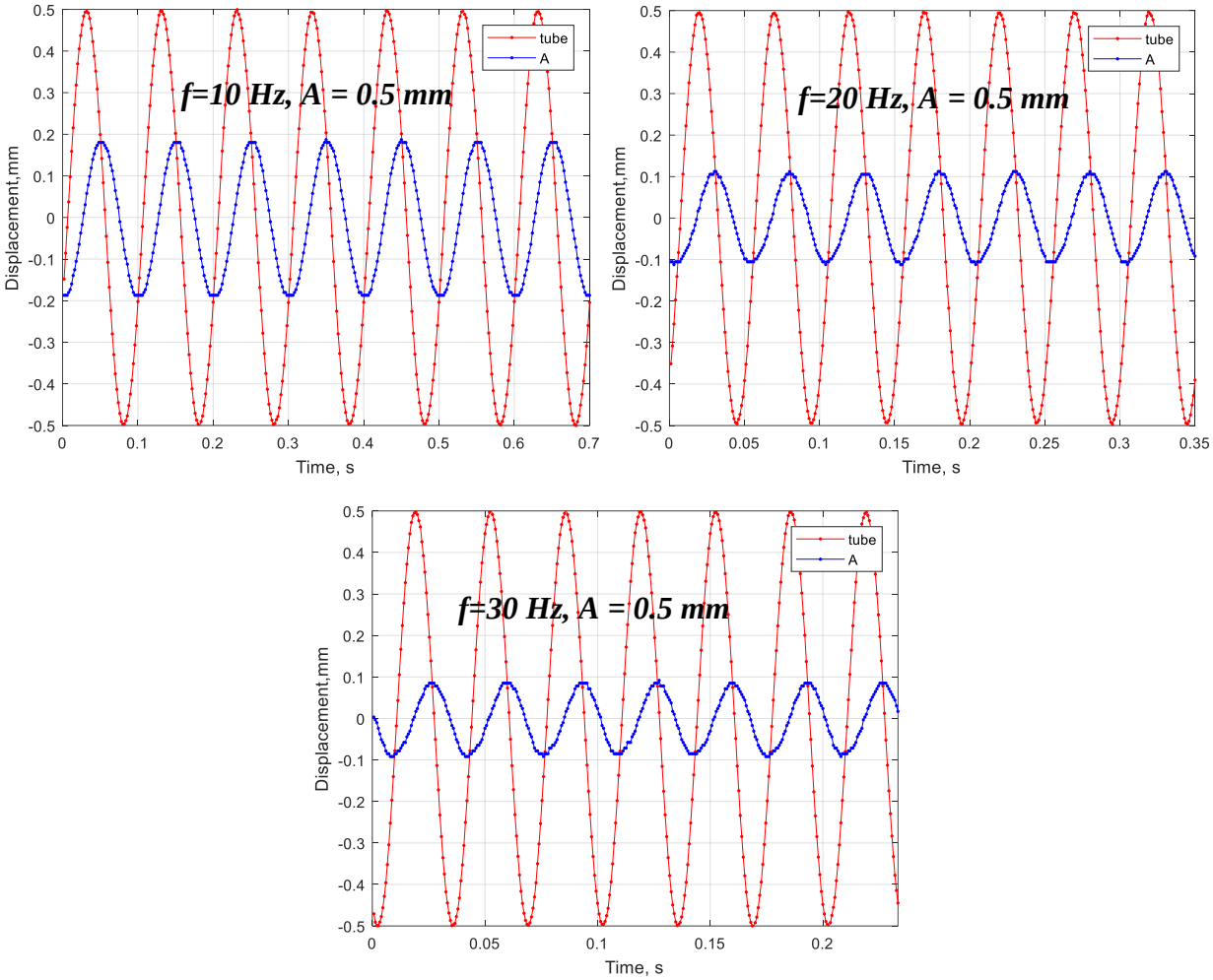

Figure 4-6. Absolute displacements of water and tube vs. time (ID = 2.2 mm, f = 10, 20, 30 Hz, A = 0.5 mm)

Figure 4-6 depicts the absolute displacement of the most advanced point in the meniscus (point A), as a reference of water index, and of the capillary tube, under three set of vibration parameters. We can notice that the absolute displacement amplitude of the water index is lower than the one of the capillary tubes. Moreover, we can also find that the water amplitude declines with the rise of frequency.

At the high frequency (f = 30 Hz), inertia dominates the viscous and capillary forces acting on the system i.e. the water index. In this case, as the absolute movement of water (Figure 4-6) is much

smaller than the tube movement, the relative movement of water inside the tube has almost the same amplitude of the imposed movement. For these parameters, the phase changes of water movement are close to $\pi/2$ gradually with the increase of the frequency.

4.3.2 Characterization of dimensionless numbers

For the characterization of fluid dynamics, scientists began to use dimensionless numbers as an effective tool since 1883[218]. Such as the Reynolds number, which is the ratio of inertia and viscous force; the Weber number, which quantifies the relative importance of the fluid's inertia compared to its surface tension; the Ohnesorge number, that relates viscous forces to inertial and surface tension forces; the Sherwood number, which represents the ratio of the convective mass transfer to the rate of diffusive mass transport; the Schmidt number, defined as the ratio of momentum diffusivity and mass diffusivity[219–221], etc.

The images analysis for all tests depicts a high diversity of water index behavior, especially for menisci shape and displacement amplitude. To explain this variability, it is mandatory to quantify the relative importance of three parameters: surface tension, viscosity, and inertia. For this purpose, we introduce two dimensionless numbers.

4.3.3 The capillary effect

The capillary effect (N_c) is defined as the ratio of capillary forces (F_c) over inertia F_i

$$N_c = \frac{F_c}{F_i} \qquad \text{Equation 4-4}$$

The capillary force is originated from the capillarity, which is linked to:

the surface tension (σ) at the interface between the liquid phase and gas phase

the wettability of fluids at the solid surface; the value of the capillary force is connected with the contact angle (θ). It is given by: [140]

$$F_c = 2\pi r\sigma cos\theta \quad \text{Equation 4-5}$$

In the case of perfect wetting, the contact angle equals to 0, and $cos\theta$ equals to 1. Thus, we obtain the maximum value for the capillary force:

$$F_c = 2\pi r\sigma \quad \text{Equation 4-6}$$

where r is the inner radius of the capillary tube and σ the surface tension.

The inertia of the system is the product of its mass multiplied by its acceleration,

$$F_i = ma = \pi r^2 l\rho A\omega^2 \quad \text{Equation 4-7}$$

where l the length of the water index, and ρ is the density.

Hence:

$$N_c = \frac{2\sigma}{rl\rho A\omega^2} \quad \text{Equation 4-8}$$

4.3.4 The viscous effect

N_v is the ratio of the characteristic time of the signal (T, half-period) over the characteristic diffusion time (τ):

$$T = \frac{1}{2f} \quad \text{Equation 4-9}$$

The characteristic diffusion time (τ) reflects the delay to transmit the mechanical information from the inner wall to the center of the tube:

$$\tau = \frac{\rho r^2}{\mu} \qquad \text{Equation 4-10}$$

where μ is the dynamic viscosity of water.

Hence,

$$N_v = \frac{T}{\tau} = \frac{\mu}{2f\rho r^2} = \frac{\delta^2}{r^2} \qquad \text{Equation 4-11}$$

where δ is the thickness of the Stokes boundary layer.

4.3.5 Dimensionless number map

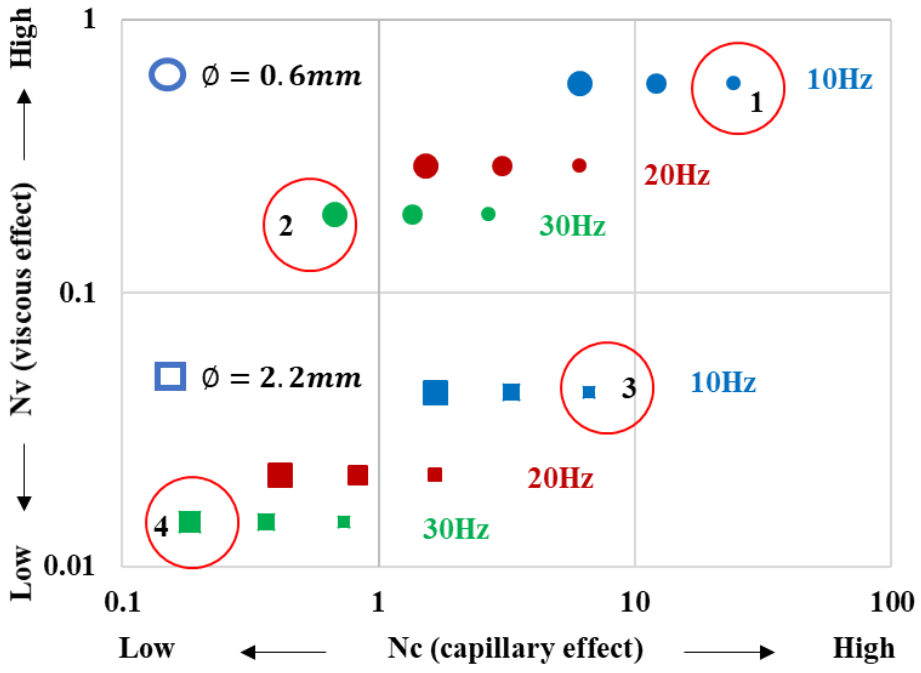

Figure 4-7. Representation of all tests performed in the present study according to their respective effects of capillary forces and viscosity;

All tests performed in this study can, therefore, be represented by one marker in the plane defined by the values of N_c and N_v. In Figure 4-7, one color represents one frequency value (blue = 10 Hz, red = 20 Hz, green = 30 Hz), each marker shape represents one tube diameter (square = 2.2 mm, circle = 0.6 mm), and one marker size represents the signal amplitude, (small = 0.5 mm, medium = 1 mm and large = 2 mm). From all these tests, four contrasted situations are selected for an in-depth study (Table 4-3).

Table 4-3. Our selection of contrasted situations.

Inner diameter (ID)	No. on Figure 4-7	Frequency(f)	Amplitude(A)
0.6 mm	1	10 Hz	0.5 mm
	2	30 Hz	2 mm
2.2 mm	3	10 Hz	0.5 mm
	4	30 Hz	2 mm

4.4 Results and discussion

4.4.1 Experimental results

To provide an in-depth analysis of the relative effects of the physical phenomena (viscosity, surface tension and inertia), Lissajous curves were plotted for the selected tests in Figure 4-7. These curves consist in plotting the absolute displacement of the water index as a function of the tube displacement. On these closed curves, we can easily observe the ratio between the tube and water amplitude (respectively width and height of the ellipse) and the phase change linked both to the slope and opening of the ellipse, as depicted in Figure 4-8.

1) *ID* = 0.6 mm, *f* = 10 Hz, *A* = 0.5 mm

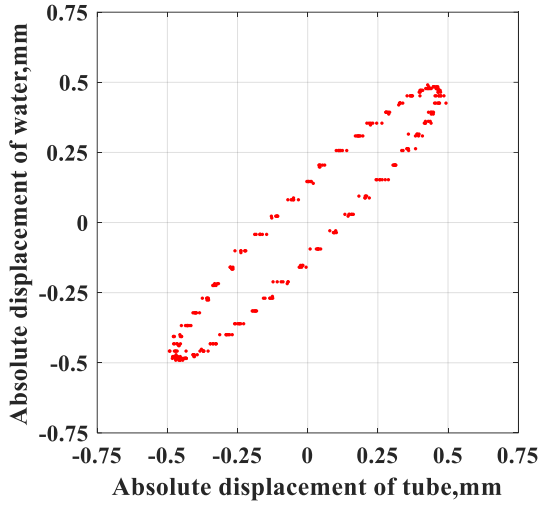

2) ID = 0.6 mm, *f* = 30 Hz, A = 2 mm

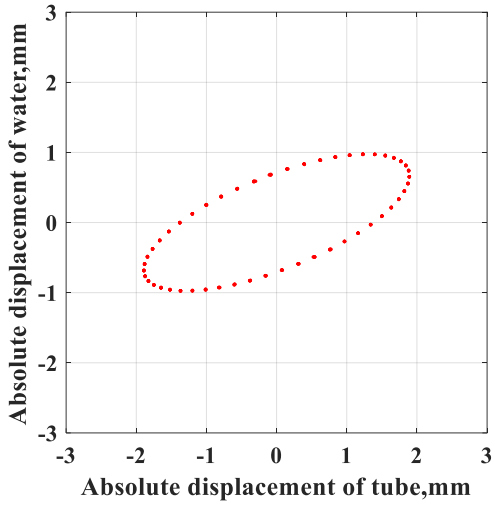

3) ID = 2.2 mm, *f* = 10 Hz, A = 0.5 mm

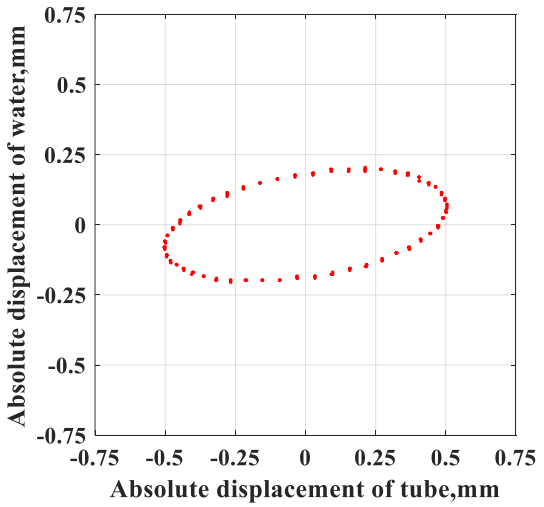

4) ID = 2.2 mm, *f* = 30 Hz, A = 2 mm

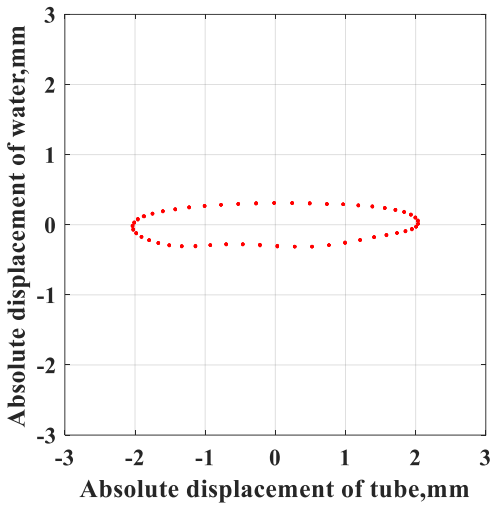

Figure 4-8. Lissajous curves for the four configurations selected for the in-depth analysis (Table 2 and Figure 3)

For test 1 (ID = 0.6 mm, *f* = 10 Hz, A = 0.5 mm), the capillary effect dominates inertia, but the viscous effect is not negligible (point 1 in Figure 4-7). As a result, the water index follows the tube movement with a slight hysteresis. This explains why the Lissajous curve is along the direction 45°: almost same amplitudes with a slight phase change. For the same tube diameter (0.6 mm) but a larger frequency and a larger amplitude (test 2), N_c is smaller than the unit. Consequently, the

water index is not able anymore to follow the tube movement: the water index amplitude is ca. half the signal amplitude and the signals depict a large phase change.

For test 3, as seen in Figure 4-7, the capillary effects are quite important, but the viscous effects are now negligible, due to the larger tube diameter. Finally, test 4 lies at the very bottom-left of Figure 4-7, which means very weak viscous and capillary forces. Accordingly, the water index is almost at rest in spite of the tube movement.

4.4.2 Water amplitude

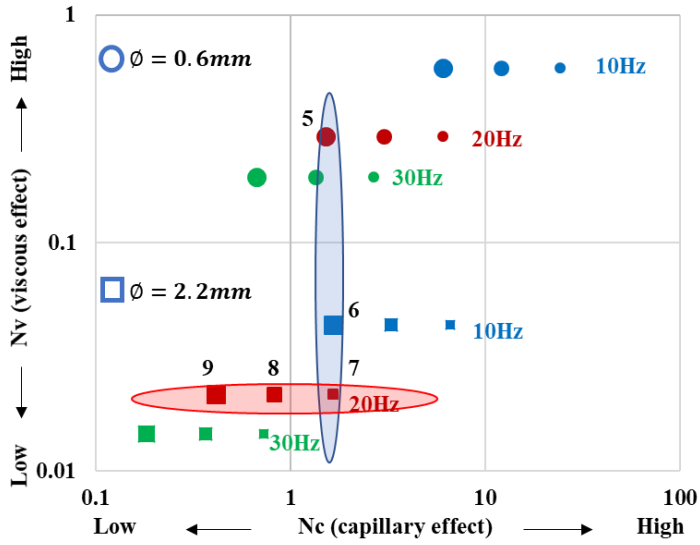

No.	ID (mm)	F (Hz)	A (mm)	N_c	N_v	Amplitude ratio
5	0.6	20	2	1.52	0.29	0.66
6	2.2	10	2	1.66	0.04	0.31
7	2.2	20	0.5	1.66	0.02	0.23
8	2.2	20	1	0.83	0.02	0.21
9	2.2	20	2	0.41	0.02	0.19

Figure 4-9 The selective contrast conditions for discussing the effect of N_c and N_v on water amplitude ratio

Figure 4-9 displays the contrast conditions selected to discuss separately the capillary effect (N_c) and the viscous effect (N_v) on water amplitude.

In a first series (S1, the blue ellipse), the N_c values of the points are similar. With the increase of the viscous effect, the water amplitude increases, and the amplitude ratio (water amplitude over the

tube amplitude) increases. This is coherent with the definition of N_v: the thickness of the Stokes boundary layer increases compared to the radius of the tube. So, the diffusion time of the momentum transfer from the boundary layer to the center of the water index decreases in comparison to the signal period.

We selected a second set of contrasted conditions (S2, red ellipse) to explore the impact of capillary effect. We choose a set crossing the boundary N_c = 1 with a balanced distribution (from No.7 to No. 9). The boundary N_c = 1 means that the impacts of the capillary force and the inertia are similar. The values of the viscous effect on the points belonging to S2 are identical. It is obvious that a higher capillary effect will result in a decrease of water amplitude. When the liquid-gas phase encounters a solid phase, the contact angle is generated. If the water index is motionless, the contact angle of the water meniscus is called the static contact angle which is the same at left and right ends of the index. When the water moves, the contact angles at its opposite ends of the index reach two different values:

- advancing contact angle (θ_a),
- the receding contact angle (θ_r).

The sum of both capillary forces is given by:

$$\sum F_c = -sign(\dot{x}_{water} - \dot{x}_{tube}) \times 2\pi R\sigma \times \left(cos(\theta_r) - cos(\theta_a)\right) \quad \text{Equation 4-12}$$

For a given inner diameter, this sum value remains constant. It is the case for S2.

Indeed in this case N_c decreases due to the increase of F_i, which depends on the tube amplitude. Therefore, we have to observe the evolution of the amplitude ratio (water amplitude over tube

amplitude): consistently, this ratio decreases with N_c.

N_c may not be relevant to explain the evolution of water amplitude as a function of the signal parameters (frequency and tube amplitude). It would be interesting to introduce a new dimensionless number: the ratio of the friction force over the inertia. Unfortunately, it is difficult to estimate the value of the friction force. Two approaches will be discussed in chapter 5.

The discussion above is only based on the 1-D analysis. For a comprehensive evaluation of the impact of N_c and N_v, we will introduce a 2-D figure including all the tests of Figure 4-10,

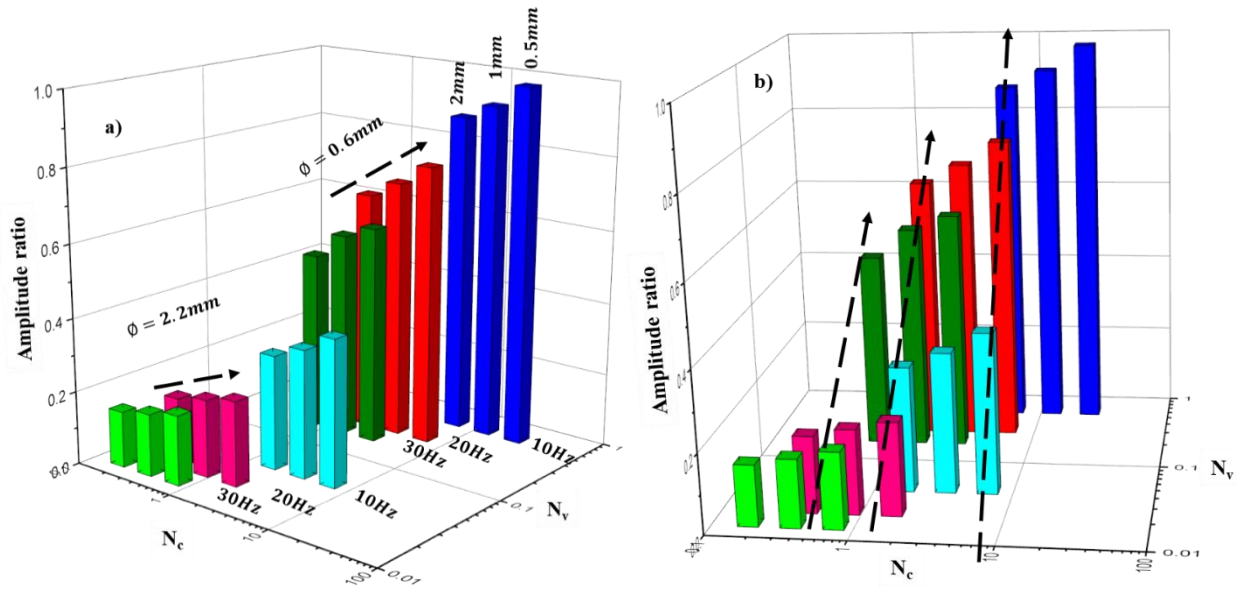

Figure 4-10 The water amplitude ratio (water amplitude over tube amplitude) as a function of N_c and N_v

Colors blue, red and olive represent the tests conducted under 10, 20 and 30 Hz in the capillary tube ID = 0.6 mm; colors cyan, pink and green represent the test performed under 10, 20, 30 Hz in the capillary tube ID = 2.2 mm; the bars from left to right represent the tests done with an vibrational amplitude of 2 mm, 1 mm, and 0.5 mm respectively.

According to Figure 4-10a, it is obvious that the amplitude ratio (water amplitude over tube amplitude) increases with the increase of the capillary effect under any constant viscous effect. This result is completely consistent with the previous conclusion in 1-D scale. It proves that the variation of the amplitude ratio related to the capillary effect. Thus, as what has been written previously, N_c may not be relevant to explain the evolution of amplitude ratio.

Figure 4-10b is obtained by rotating the Figure 4-10a. In Figure 4-10b, we can easily find that under a similar viscous effect, the water amplitude rises with the increase of the viscous effect. It is in accordance with the analysis in 1-D analysis.

4.4.3 Phase change

The phase change (φ) is defined as the difference between the phase position of the tube motion and that of the water motion. To estimate the phase change, we fit the Lissajous curves with mathematical functions to ease the analysis. In the following section, all the tests were used to discuss the impact of the viscous effect and the capillary effect separately.

Lissajous curve is the graph of a system of parametric equations, as Equation 4-13:

$$\begin{cases} x=A_1 sin\left(2\pi f_1 t\right) \\ y=A_2 sin\left(2\pi f_2 t+\varphi\right) \end{cases} \quad \text{Equation 4-13}$$

which can provide a description of the complex harmonic motion. Based on the obtained Lissajous curves, as Figure 4-8, obviously the water amplitude is different from the one of the tube ($A_1 \neq A_2$), but the frequency remains the same ($f_1 = f_2$) . In this situation, we suppose that the shape of the Lissajous curve in this study is an ellipse, which the general expression is:

$$ax^2+bxy+cy^2+dx+ey+f=0 \quad \text{Equation 4-14}$$

Moreover, the center of the ellipse is supposed to locate on the zero point, then the expression of the ellipse can be simplified as Equation 4-15:

$$a'x^2+b'xy+c'y^2+1=0 \quad \text{Equation 4-15}$$

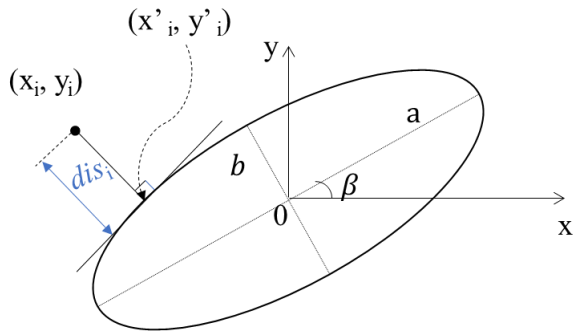

Figure 4-11. An ellipse centered at 0 with axis lengths a, b and angle β. The nearest point (X_i', Y_i') on the ellipse from a given point (X_i, Y_i) satisfies the orthogonal contacting conditions, and lies in the same quadrant of standard position as the given point.[222]

In order to identify the values of the function parameters (a', b' and c'), we applied in the Matlab the least-square orthogonal distances (total least-square) method introduced in the literature[222] on the obtained experimental data. The method defines the ellipse paramters by minimizing the sum of the square of the geometric distance (the length of dis_i in Figure 4-11) from the point to the fitting ellipse as,

$$Residual = \sum_{i=1}^{n} dis_i^2 = \sum_{i=1}^{n} H^2(J(x_i, y_i), K(x'_i, y'_i)) \quad \text{Equation 4-16}$$

where dis_i is the orthogonal distance between a point and an ellipse, n is the quantity of the given points, H is a function to calculate the orthogonal distance between a point and a curve, $J(x_i, y_i)$ is the coordinate of the given points and $K(x'_i, y'_i)$ is the function of an ellipse.

The obtained curves fit all the Lissajous curves. The fitting results are shown in Figure 4-12. They prove that the assumption of Equation 4-15 is relevant.

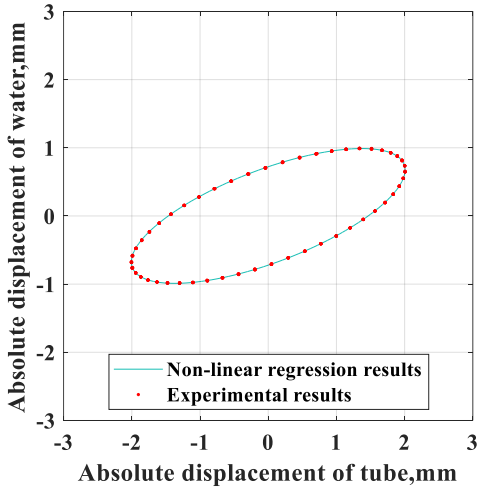

Figure 4-12. Lissajous curve and the non-linear regression fitting results (*ID = 0.6 mm, f = 30 Hz, A = 2 mm*)

Appendix I lists the fitting coefficients of Equation 4-15 by non-linear regression for all the experiments.

To determine the precise phase change (φ), we can apply the method described in the literature[223], as Equation 4-17:

$$\varphi = arcsin(\frac{h}{Y_{max}}) \qquad \text{Equation 4-17}$$

where h is the positive ordinate of the intersection between Lissajous curve and the y-axis, and Y_{max} is the maximum ordinate on the Lissajous curve.

At any time t, we have

$$ax^2(t) + bx(t)y(t) + cy^2(t) + 1 = 0 \qquad \text{Equation 4-18}$$

When the displacement of tube equals to 0, $t = t_0$, we have:

$$cy^2(t_0) + 1 = 0 \qquad \text{Equation 4-19}$$

$$y(t_0) = \pm\sqrt{-\frac{1}{c}} \qquad \text{Equation 4-20}$$

That is $h=\sqrt{-\frac{1}{c}}$.

When we derivative the equation with respect to time t, we can obtain:

$$2ax(t)\frac{dx}{dt}(t) + by(t)\frac{dx}{dt}(t) + bx(t)\frac{dy}{dt}(t) + 2cy(t)\frac{dy}{dt}(t) = 0 \qquad \text{Equation 4-21}$$

$$-\frac{2ax(t)+by(t)}{bx(t)+2cy(t)} = \frac{dy/dt(t)}{dx/dt(t)} \qquad \text{Equation 4-22}$$

When the displacement of water reaches the maximum (in positive direction), $t = t_{Aw}$, $\frac{dy}{dt} = 0$, we have:

$$\frac{2ax(t_{Aw})+by(t_{Aw})}{bx(t_{Aw})+2cy(t_{Aw})} = 0 \qquad \text{Equation 4-23}$$

Thus:

$$2ax(t_{Aw}) + by(t_{Aw}) = 0 \qquad \text{Equation 4-24}$$

$$x(t_{Aw}) = -\frac{by(t_{Aw})}{2a} \qquad \text{Equation 4-25}$$

$$ax(t_{Aw})^2 + bx(t_{Aw})y(t_{Aw}) + cy^2(t_{Aw}) + 1 = 0 \qquad \text{Equation 4-26}$$

$$a(-\frac{by(t_{Aw})}{2a})^2 + b(-\frac{by(t_{Aw})}{2a})y(t_{Aw}) + cy^2(t_{Aw}) + 1 = 0 \qquad \text{Equation 4-27}$$

$$y(t_{Aw}) = \pm\sqrt{\frac{4a}{b^2-4ac}} \qquad \text{Equation 4-28}$$

That is $Y_{max}=\sqrt{\frac{4a}{b^2-4ac}}$, then we can obtain the phase change between the motion of tube and water as Equation 4-17

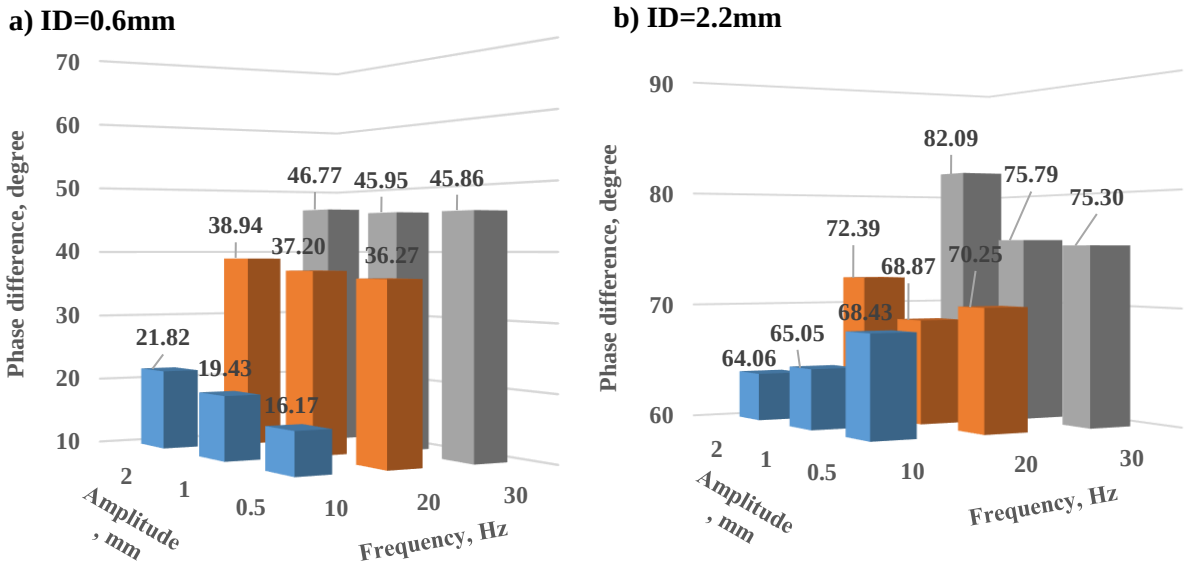

Figure 4-13. The phase change of all the tests performed in this research

Figure 4-13 plots the phase change of all the tests performed in this research. In the Figure 4-13a, we can find easily that the phase change has a positive correlation with the frequency and amplitude in capillary tube with small inner diameter (ID = 0.6 mm). And in Figure 4-13b, the effect of frequency on phase change in capillary tube with larger inner diameter (ID = 2.2 mm) keeps consistent with what we obtained in Figure 4-13a. However, the correlation between tube amplitude and phase change of motion is not clear in capillary tube with larger inner diameter.

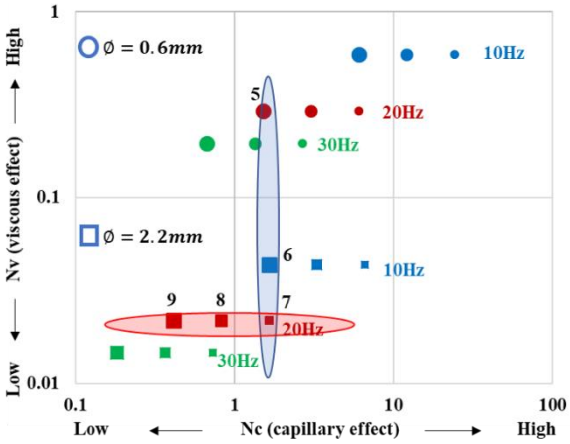

No.	ID (mm)	F (Hz)	A (mm)	N_c	N_v	Amplitude ratio	φ (degree)
5	0.6	20	2	1.52	0.29	0.66	38.94
6	2.2	10	2	1.66	0.04	0.31	64.15
7	2.2	20	0.5	1.66	0.02	0.23	70.54
8	2.2	20	1	0.83	0.02	0.21	68.70
9	2.2	20	2	0.41	0.02	0.19	72.32

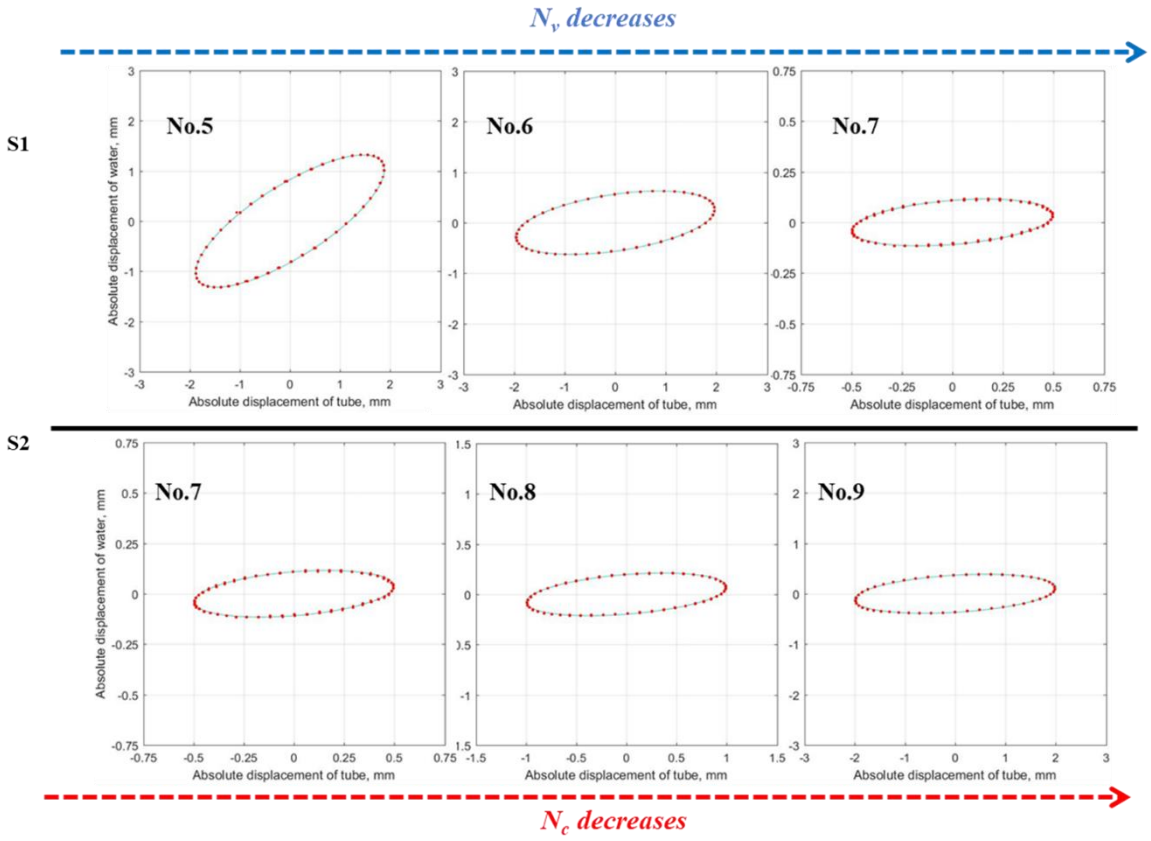

Figure 4-14 The selective contrast conditions for discussing the effect of N_c and N_v on phase change

In order to characterize the viscous effect and capillary effect on the phase change seperately, we can also focus on the selected conditions proposed in section 4.4.2. Figure 4-14 shows the Lissajous curves for these conditions. For the series S1, from No.5 to No. 7, the capillary effect of these three

tests are similar. The phase change decreases with the increase of the viscous effect. The increasing amplitude ratio could also explain the phase change evolution. When the characteristic time in half period is longer than the characteristic diffusion time, the water index in the center of the tube will gain more momentum from the inner wall. It couples the water index and tube motions. Thus, with the increase of N_v, the motion coupling is improved. Indeed, for this last configuration (No. 5), the amplitude ratio increases dramatically compared to the other tests, as a results of the much larger value of N_v. The actual inertia if therefore different from the simple calculation done in the dimensionless numbers, in which the index amplitude is assumed to be that of the tube.

For S2, despite the exponential increase of the capillary effect, the phase changes for the selected conditions is not monotonic, contrary to what was expected. It means that the evolution of the capillary effect could not give a good explanation for the phase change. As what have been proposed previously, the ratio of the friction force over the inertia may be helpful for understanding the phase change evolution in this region.

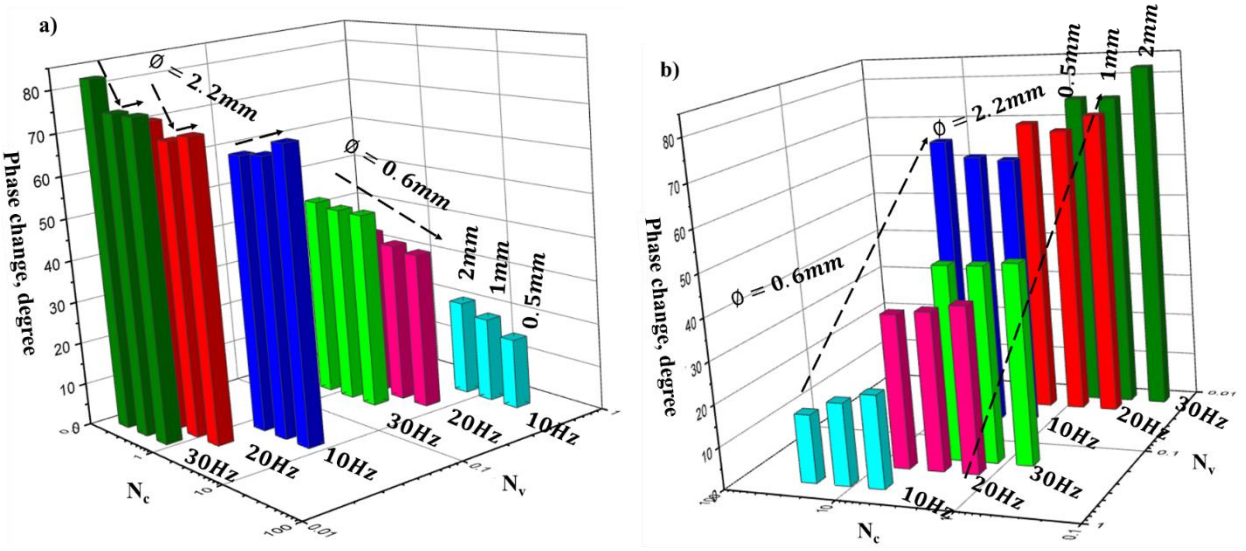

Figure 4-15 The phase change as a function of N_c-N_v

Colors blue, red and olive present the tests conducted at 10, 20 and 30 Hz for the capillary tube ID = 0.6 mm; colors cyan, pink and green present the test performed at 10, 20, 30 Hz for the capillary tube ID = 2.2 mm; the bars from left to right present the tests done with an vibrational amplitude of 2 mm, 1 mm, and 0.5 mm respectively in Figure 4-15a. Figure 4-15b is a rotation of Figure 4-15a. To see the tendency clearly, we convert the axis for N_c, which should be noticed.

Figure 4-15a plots the phase change as a function of the position in the N_c-N_v map. It gives a decreasing tendency of the phase change with the increase of the capillary effect under a certain viscous effect, i.e. when N_v is higher than 0.1. The tendency of the phase change regarding to the viscous effect is clear under a similar capillary effect as shown in Figure 4-15b. It increases with the increase of the N_v. Both conclusions from the whole tests verified the previous observations. As explained above, one must keep in mind that the capillary number N_c accounts for the potential inertia of that test (the tube amplitude) rather than the actual index amplitude. When the dimensionless number varies significantly, the amplitude ratio may change also significantly, which explains non monotonic behaviors.

The phase change is a significant index that reflects the intensity of the mutual effect between the capillary tube and the fluid inside. A strong interaction will result in a drastic viscous dissipation, which is an efficient way of converting the mechanical energy into internal energy, and then to enhance the evaporation of the liquid phase.

4.4.4 The radius of curvature

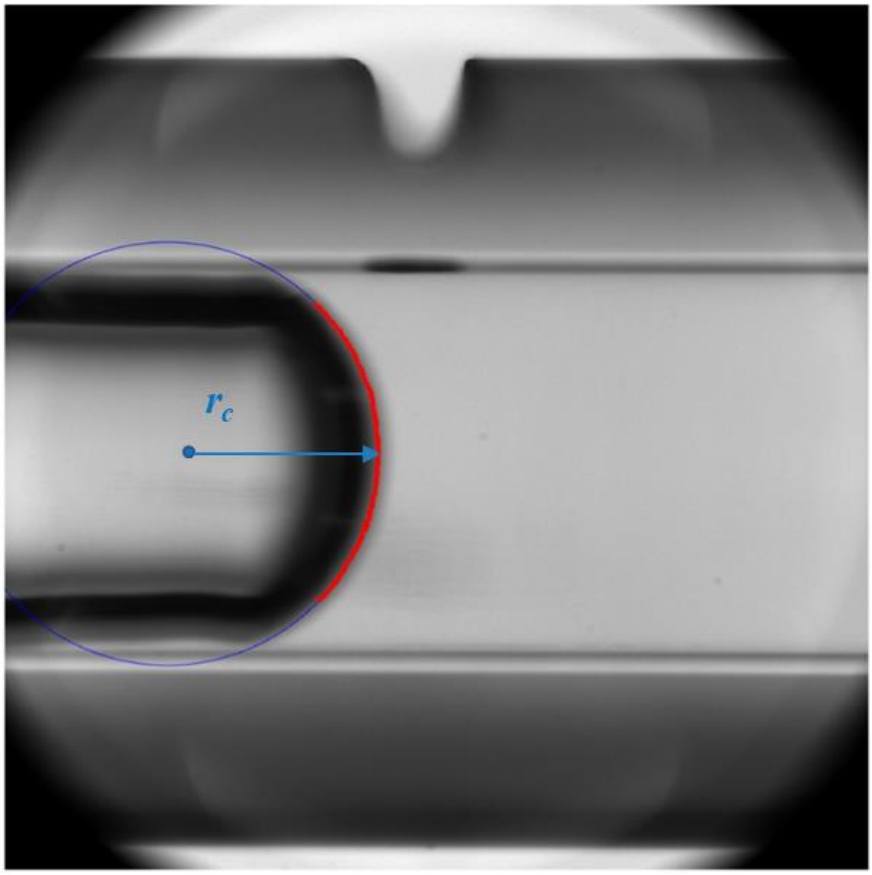

Figure 4-16. The selected meniscus and the corresponding fitting circular arc

In this study, the radius of curvature will be used for characterizing the geometry deformation of the meniscus. The radius of curvature is the reciprocal of the curvature, as:

$$r_c = \frac{1}{\kappa} \qquad \text{Equation 4-29}$$

where r_c is the radius of the curvature, and the κ is the curvature.

For the water meniscus in the capillary tube, in this study, the radius is obtained as the best fit of a circular arc over 80 % of the meniscus (Chapter 3.2.3.3). In Figure 4-16, the red line is the

meniscus shape and the blue circle is the best fit.

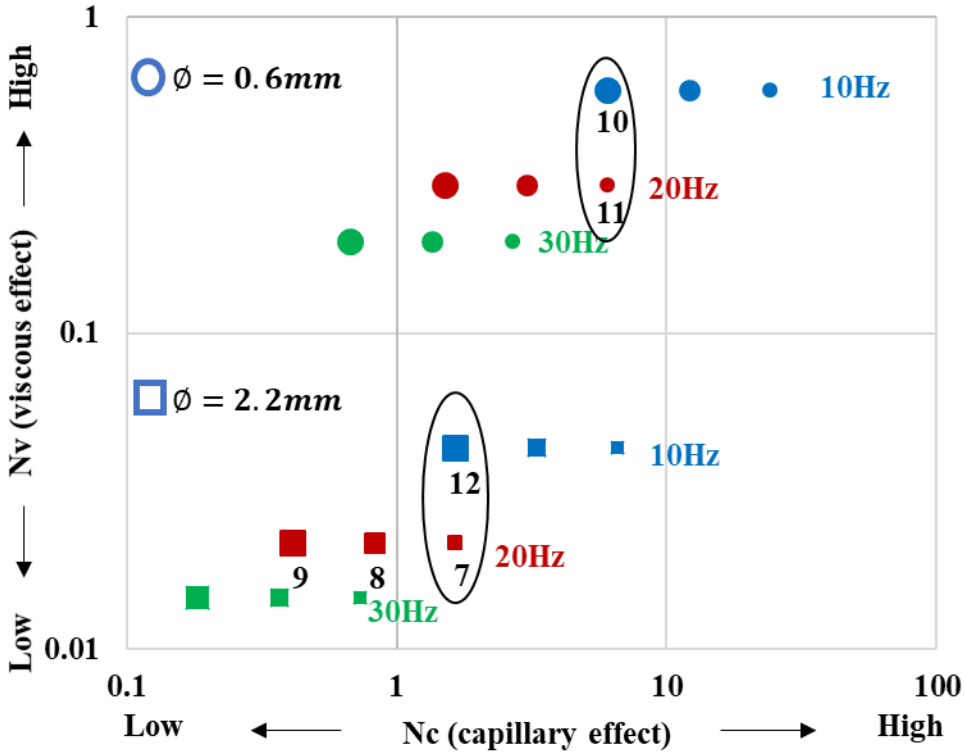

Figure 4-17. The contrasted conditions selected to discuss the impact of the viscous effect.

To discuss the viscous effect on the curvature radius, we selected one pair of contrasted conditions for each capillary tube (Figure 4-17): No. 10 and No. 11 for small tube (ID = 0.6 mm); No. 12 and No. 7 for large tube (ID = 2.2 mm).

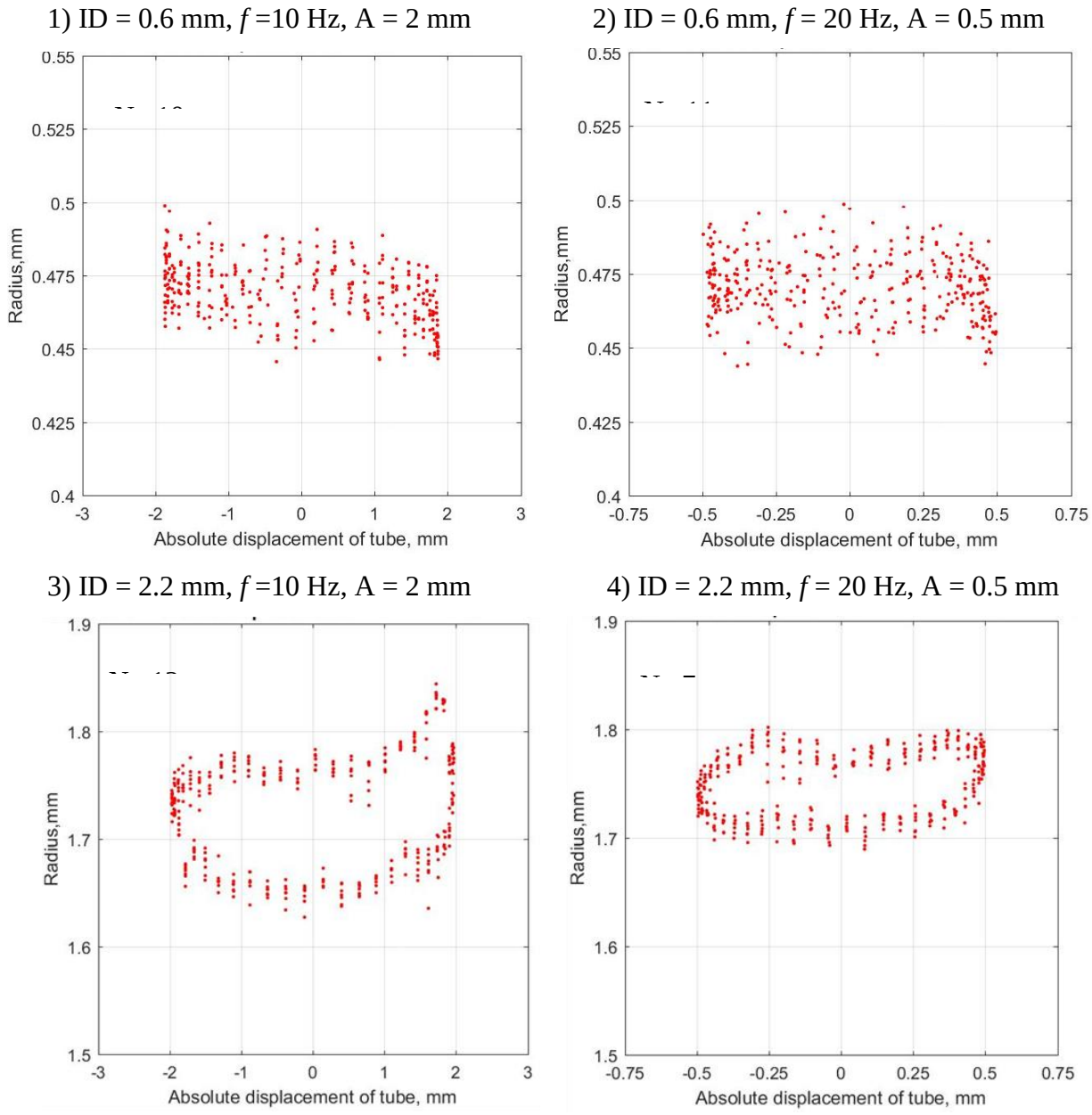

Figure 4-18 Curvature radius for two pairs of contrasted conditions presented using Lissajous curves (1 and 2 correspond to No. 10 and No. 11, 3 and 4 correspond to No.12 and No. 7 in Figure 4-17)

Figure 4-18 displays the curvature radius variation of the meniscus versus the absolute amplitude of the capillary tube for two pairs of contrasted situations. The results of No.12 and No. 7 present

a good repeatability of the data obtained in the capillary tube with larger inner diameter. But those obtained in the small tube (No.10 and No.11) have much noise because of the resolution of the camera. Depending on the distribution of the points on these figures, we can still know the rough amplitude of the curvature radius. When N_v gets closer to the unit, the viscosity effect increases and diffusion has enough time to propagates the movement throughout the radius. The curvature of meniscus should be kept almost constant. This is consistent with what is observed for the small tube (No. 10 and No. 11).

When this value decreases and becomes smaller than 0.1 (No.12 and No.7), the situation becomes more complex. Capillary forces and viscosity acts on the water index to make it try to follow the tube movement, but with partial success and without success at all, respectively. If this is dominated by the capillary forces, the curvature will change very little. If viscous forces participate in the trial to follow the tube, the meniscus shape will be affected. It is due to the viscous forces near the tube wall as N_v is small and the inertia acting all over the curvature radius. The difference in amplitude between No.12 and No.7 is therefore easily explained.

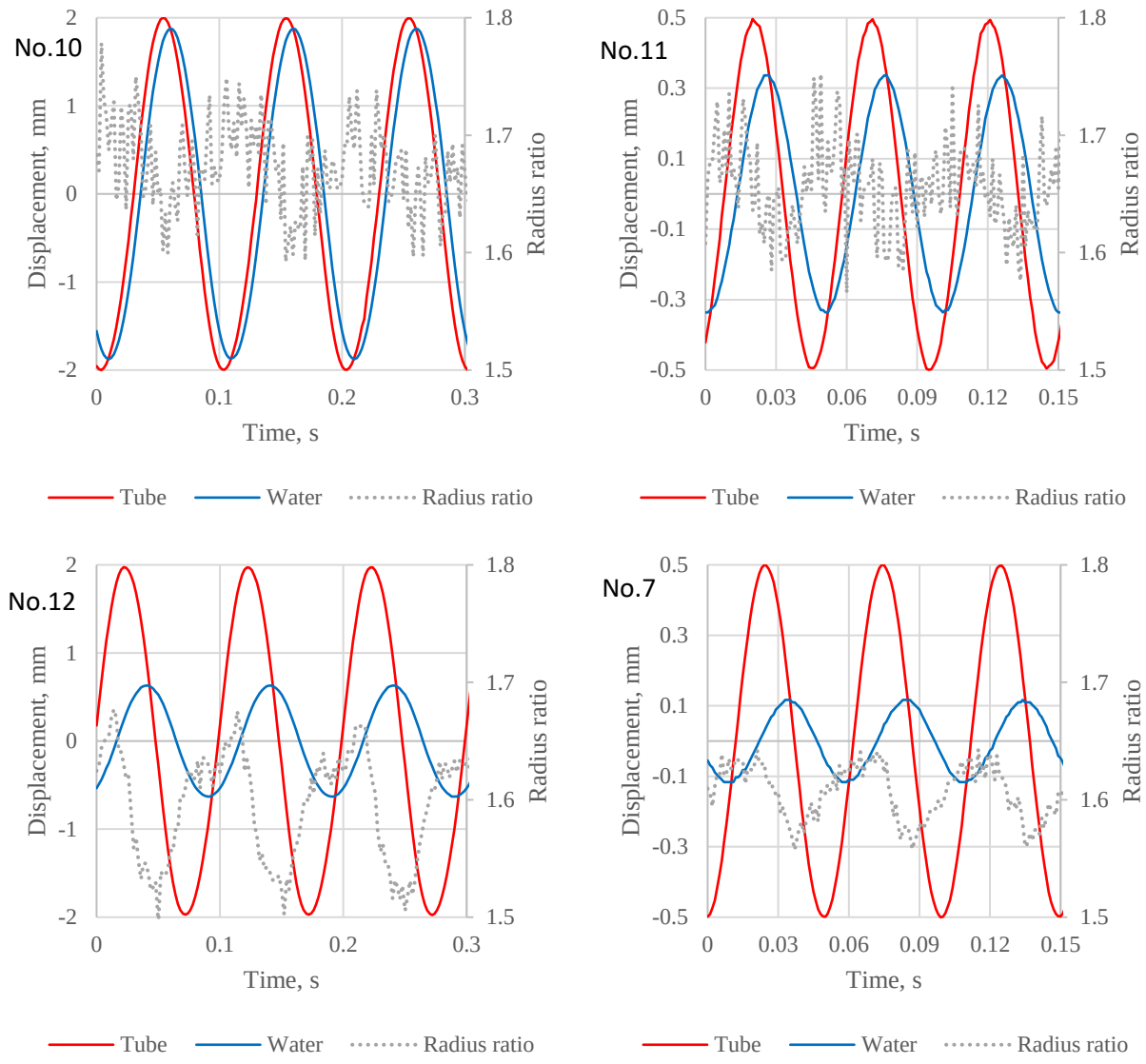

Figure 4-19 Tube displacement, water displacement and radius ratio with respect to time for tests No.10, No. 11, No.12 and No.7

To eliminate the effect of inner radius on the curvature radius amplitude, we make a normalization of the curvature radius by calculating the ratio of the curvature radius over the inner radius of the tube. The results are shown in Figure 4-19. They are consistent with those we obtained from Figure 4-18. The time evolution allows us to observe easily the phase shifts. For the large values of N_v (test numbers 10 and 11) the viscosity acts efficiently. The water displacement follows quite well

the tube movement, with a similar amplitude and a very small phase change. This is particularly for test 10 which has the largest N_v value. The meniscus radius is noisy due to the small tube diameter but is clearly in opposition of phase with the other signals. It depicts a relatively small amplitude. Its change might be explained by the difference between the receding and advancing contact angles.

When the viscous effect is reduced (test number 12 and 7), the water amplitude is much smaller than the tube amplitude and exhibits a significant phase shift (of the order of 90°). This visible phase shift permits us to observe that the curvature is in opposition of phase with the water displacement rather than with the tube displacement. The amplitude of curvature variations is larger for test No.12 than for test No.7. For test No.12 (10 Hz) the viscous effect is likely to affect the meniscus shape over a layer than is large enough to change the curvature as determined by our image processing algorithm. At higher frequency (test No.7, 20 Hz), the layer affected by viscosity might be too small to be captured by the image treatment.

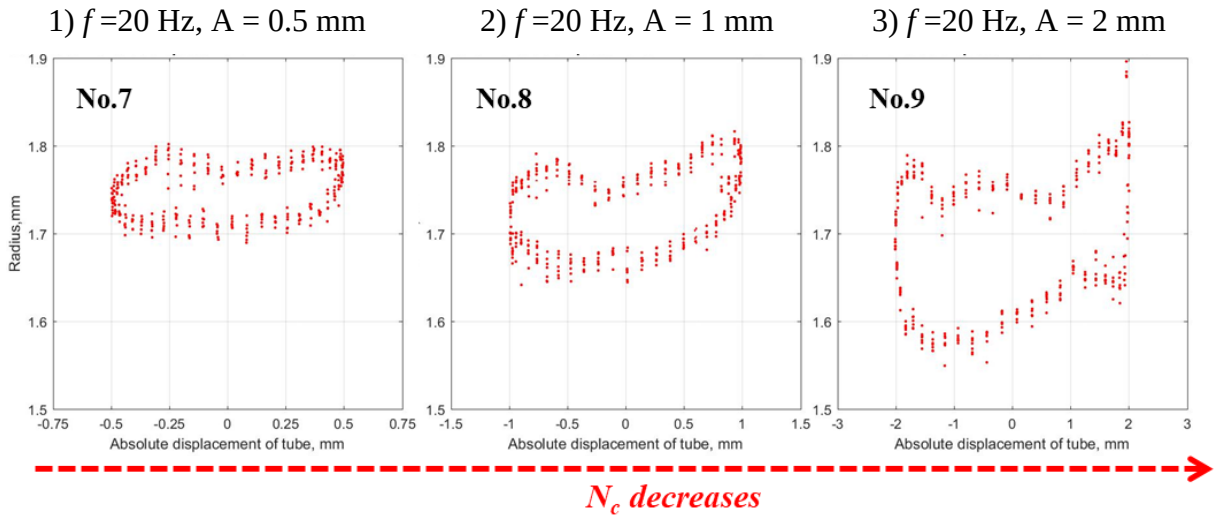

Figure 4-20. The variation of curvature radius with respect to the amplitude of the tube for three selective contrast conditions from No. 7 to No. 9 in Figure 4-14(ID = 2.2 mm)

Figure 4-20 depicts the variation of the curvature radius concerning the absolute displacement of

the tube. All the three figures were obtained under the frequency of 20 Hz in the capillary tube with inner diameter of 2.2 mm. N_v is constant, so this set enable to investigate the effect of N_c on the curvature radius. With the decreases of the capillary effect, the inertial forces increase in relative effect, hence the variation of curvature radius increases as well.

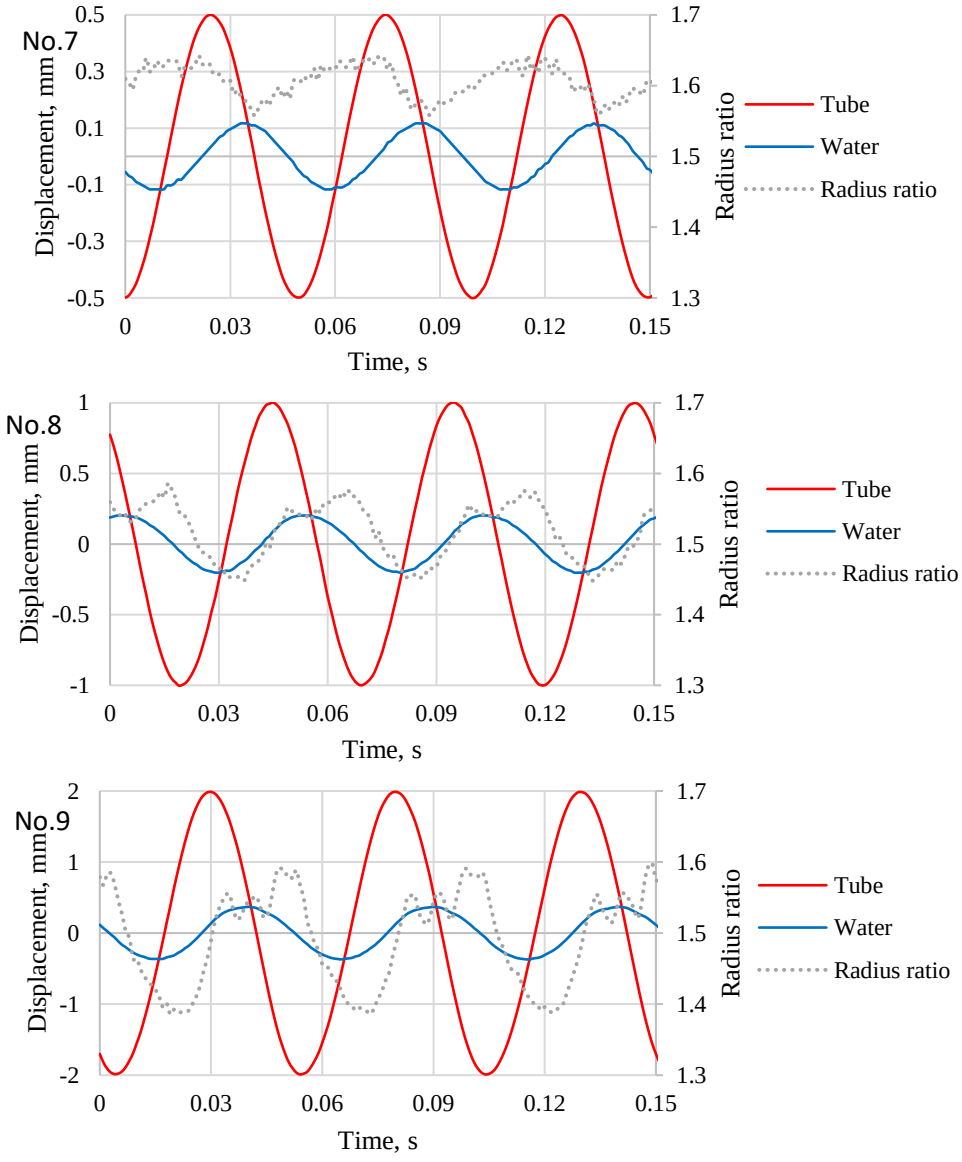

Figure 4-21 Tube displacement, water displacement, and radius ratio with respect to time for tests 7 to 9

Figure 4-21 depicts a clear variation by giving a normalized results of radius ratio (curvature radius over tube inner radius) for three contrasted tests (7, 8 and 9). The decrease of capillary effect causes a lower radius ratio, but a larger amplitude, which is consistent with the observation in Figure 4-20.

It is interesting to notice that the phase shift between water displacement and meniscus curvature is strongly affected by the tube amplitude. For the smaller amplitude (test n°7), as previously commented, water displacement and curvature are in perfect opposition of phase. Surprisingly, at higher tube amplitude (tests n° 8 and 9), these two signals are in phase. One can note that the ratio of water and tube amplitudes keeps almost the same ratio for these three tests. This indicates that the water amplitude increases by a factor two from test 7 to test 8 and from test 8 to test 9. N_c at constant tube diameter is in this case a rigorous indication of the effect of inertia (one should remember that N_c is evaluated with the tube amplitude). The change of phase shift therefore tells us that, for tests 8 and 9, inertia dominates and is likely to inverse the meniscus curvature compared to the sole effect of contact angle.

4.5 Conclusions

In this chapter, a set of evaporation experiments with a symmetrical configuration were introduced. The symmetrical configuration includes the symmetrical geometry of the capillary tube and the symmetrical shape of the vibration signal. The evaporation experiments were conducted on similar tubes set in the same environment, with one static tube and one vibrating tube. The results demonstrated that the symmetrical vibration intensifies the evaporation process in the capillary tube, and the closer to the tube orifice the water is, the stronger the intensification factor.

To study the water behavior under the symmetrical vibration, eighteen experiments were performed.

The capillary effect and viscous effect were quantified by two dimensionless numbers. The capillary effect is given by the ratio of the capillary force over the inertia. The viscous effect is that of the characteristic time in half period over the characteristic diffusion time. Then, these eighteen experiments were plotted in the plane generated by these two dimensionless numbers. This dimensionless mapping allows the behavior of the water index in a symmetrically configuration to be clearly analyzed.

By selecting relevant experiments, the impact of two effects on water amplitude were explored separately. As expected, the water amplitude (more precisely the ratio of index amplitude over tube amplitude) rises with the increase of the viscous effect. When we focus on the impact of the capillary effect, we can find that a higher capillary effect results in a decrease of the water amplitude (but increase of the amplitude ratio).

For a better understanding, we propose to introduce a new dimensionless number: the ratio of the friction force over inertia. This needs further study for a better characterization of this friction force.

Then, the impact of two effects on phase change were also explored separately. To do that, the Lissajous curves were fitted to the ellipse equation by the non-linear regression with a total least squares method in MATLAB. This allowed the phase changes of all the tests to be obtained. The results express that the phase change between the motion of the capillary tube and that of the water index is positively correlated to both amplitude and frequency in the small tube. But in large tube, it is only positively correlated to the frequency. After the analysis of the dimensionless number map and the figure of phase changes, it is found that the variation of the phase change was negatively impacted by the capillary effect increase due to the inertia decreasing when N_v is higher

than 0.1. When the viscous effect is too weak (N_v < 0.1), the variation of phase change is not relevant to the change of capillary effect. Another factor may be introduced for the explanation, such as a ratio of friction force over the inertia. Moreover, a negative correlation was observed concerning the influence of the viscous effect on the phase change.

The changing of the curvature radius of the water meniscus was discussed, it was found that the increase of capillary effect would carry out a shrink of the range of the meniscus curvature radius due to the inertia. The viscous effect on it needs to be further explored.

Table 4-4 displays a summary of the impact of capillary effect and viscous effect on the main parameters of the water behavior.

Table 4-4 The summary of the impact of capillary effect and viscous effect on the main parameters of the water behavior

	Amplitude ratio	Phase change	Curvature radius of meniscus
N_c↗	+	No clear trend	The span of the evolution shrinks, and the deformation of the meniscus is less complex.
N_v↗	+	-	The enhance of the deformation of the meniscus is only obvious when the viscous effect is weak.

With this study, we can assess how the signal amplitude and frequency may intensify the drying process of the porous media: by the pumping effect – through the amplitude of the water relative displacement –, the increasing external transfer coefficients close to the meniscus – due to the periodic deformations of the water index –, and the viscous dissipation – also due to the deformations of the water index – arisen from the symmetrical vibration. These results complement

the one related to the drying intensification as a function of the water index location inside the tube.

Chapter 5 Investigation of the index behavior in a capillary tube with asymmetrical configuration

5.1 Introduction

In the porous media, besides pores open on the two opposite faces, pores with dead end exist. Without vibration, the evaporation rate in the pores with dead end is lower than that in the continuous pores during the drying process, due to the unique path for vapor migration. In this chapter, we will discuss whether the vibration is an efficient way to intensify the evaporation in the pores with dead end.

To test the effect of vibrations on the evaporation in a pore with dead end, we used a capillary tube with one end closed to simulate the asymmetrical geometry and applied symmetrical vibrations. Experiments were conducted first, and a simple modelling approach was also derived to help the analysis. Through the modelling, we can study the effect of the amplitude, frequency, viscosity and contact angles on the water behavior. It also helps in finding the optimized parameters for the drying process.

5.2 Experimental study

5.2.1 Materials and methods

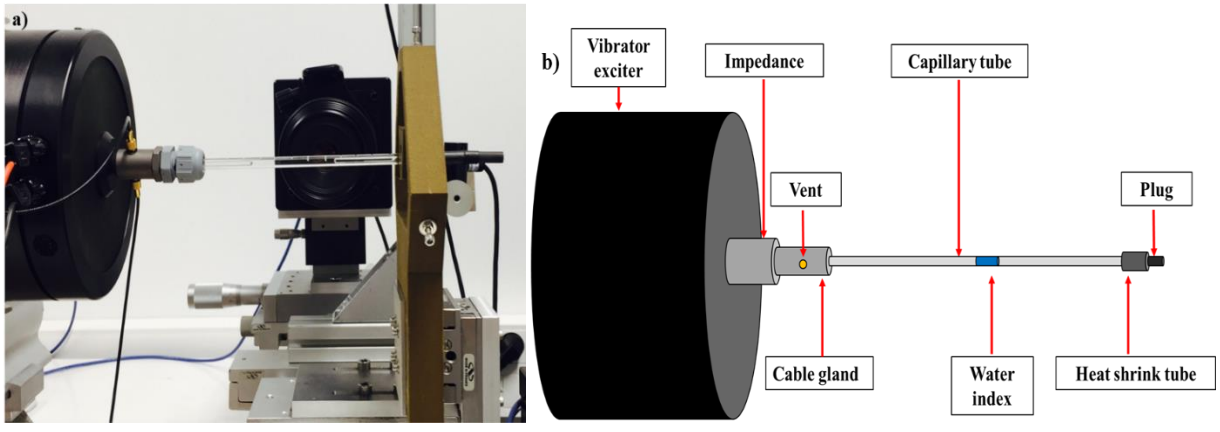

Figure 5-1 A photo of the asymmetric configuration and the corresponding schematic diagram

The asymmetric configuration consists in an asymmetrical geometry with symmetrical vibrations. As before, two sizes of capillary tubes (ID = 0.6 mm and ID = 2.2 mm) with a length of 210 mm were used in the experiments.

Water is injected into the capillary tube with a micro syringe (for ID 0.6 mm tube) or with a micro pipette (for ID 2.2 mm tube). Then, one end of the capillary tube is blocked off with a PVC rod. To achieve the sealing, the PVC rod and the capillary tube are fastened by a heat-shrink-tube (HST) with the length of 3 cm. The HST is made by high polymer materials with a linear structure. The structure will convert to a reticular structure after a certain chemical reaction or radiation[224–227]. When we heat the HST, it shrinks rapidly in both axial and radial direction, hence squeezing the rod and the tube together to realize the sealing. The open end of the capillary tube is connected to the vibration exciter by the cable gland. The photo and the schematic diagram of the asymmetrical configuration are shown in Figure 5-1.

Table 5-1 Experimental parameters of the two capillary tubes

ID	A	l_{air}	l_{water}	P_{atm}	ρ_{water}
0.6 mm	*0.5 mm*	*76 mm*	*52 mm*	*101 kPa*	*1000 kg/m^3*
2.2 mm	*0.5 mm*	*76 mm*	*51 mm*	*101 kPa*	*1000 kg/m^3*

The parameters for both ID 0.6 mm tube and ID 2.2 mm tube are shown in Table 5-1. **ID** is the inner diameter of the tube, A is the tube amplitude, l_{air} is the length of the blocked air, l_{water} is the length of the water index, P_{atm} is the atmospheric pressure, and ρ_{water} is the water density.

All the images were captured with the parameters shown in Table 5-2. The distance between the camera and the tube depends on the magnification of the objective. Here, it is fixed to 246 mm for

a magnification equals to 3 times. The only parameter to determine is the frame rate of the camera. It depends on the selected frequency. The criteria for the determination of frame rate is to ensure that at least 20 images will be captured during one vibrational period.

Table 5-2 Parameters for image capture

Resolution	Exposure time	Distance between light and tube
1024 × 1024	*1 / 60 000 s*	*10 mm*

The waveform of the signal applied by the exciter is a sine wave.

5.2.2 Experimental protocol

To explore a suitable range of frequencies, we propose a preliminary numerical study using a simple 0-D model.

5.2.2.1 Preliminary numerical study

5.2.2.1.1 Description of the model

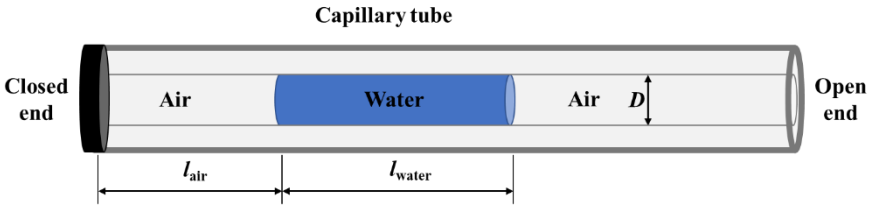

Figure 5-2 A schematic of a blocked capillary tube with a water index.

Figure 5-2 displays the mechanical system which comprises a capillary tube with one end closed and a water index inside the tube. The length of the blocked air between the closed end and the water index is l_{air}, the length of the water index is l_{water}, and the inner diameter of the capillary tube is D. During the sinusoidal vibration, the water moves inside the tube. So, it acts on the blocked

air, whose volume changes. According to the ideal gas law, Equation 5-1, the pressure of the blocked air change is a function of its volume.

$$P=\frac{nRT}{V} \qquad \text{Equation 5-1}$$

where *P* is the pressure of the gas, *V* is the volume of the gas, *T* is the absolute temperature of the gas; *n* is the number of moles of gas, and *R* is the ideal gas constant, equals to 8.314 *J/*(*mol K*).

n and *T* are assumed to be constant over some periods. Therefore, we obtain:

$$P(t)V(t) = P(t=0)V(t=0) = P_{atm}V(t=0) \qquad \text{Equation 5-2}$$

Then, we can deduce the pressure of the blocked air at time *t* as

$$P(t)=P_{atm}\frac{V(t=0)}{V(t)} \qquad \text{Equation 5-3}$$

Based on the volumetric equation in a column, $V = \frac{\pi D^2}{4} l$, Equation 5-3 can be expressed as

$$P(t)=P_{atm}\frac{l_{air}(t=0)}{l_{air}(t)} \qquad \text{Equation 5-4}$$

where $l_{air}(t=0)$ is the initial length of the blocked air, $l_{air}(t)$ is the length of the blocked air at time *t.*

Based on the description above, we can make assumptions to build a simplified model: 1) the friction force between the water index and the capillary tube (due to viscosity) is neglected; 2) the contact angles of the meniscus on both sides are equal and constant during the vibration, so the capillary forces vanish.

5.2.2.1.2 Problem formulation

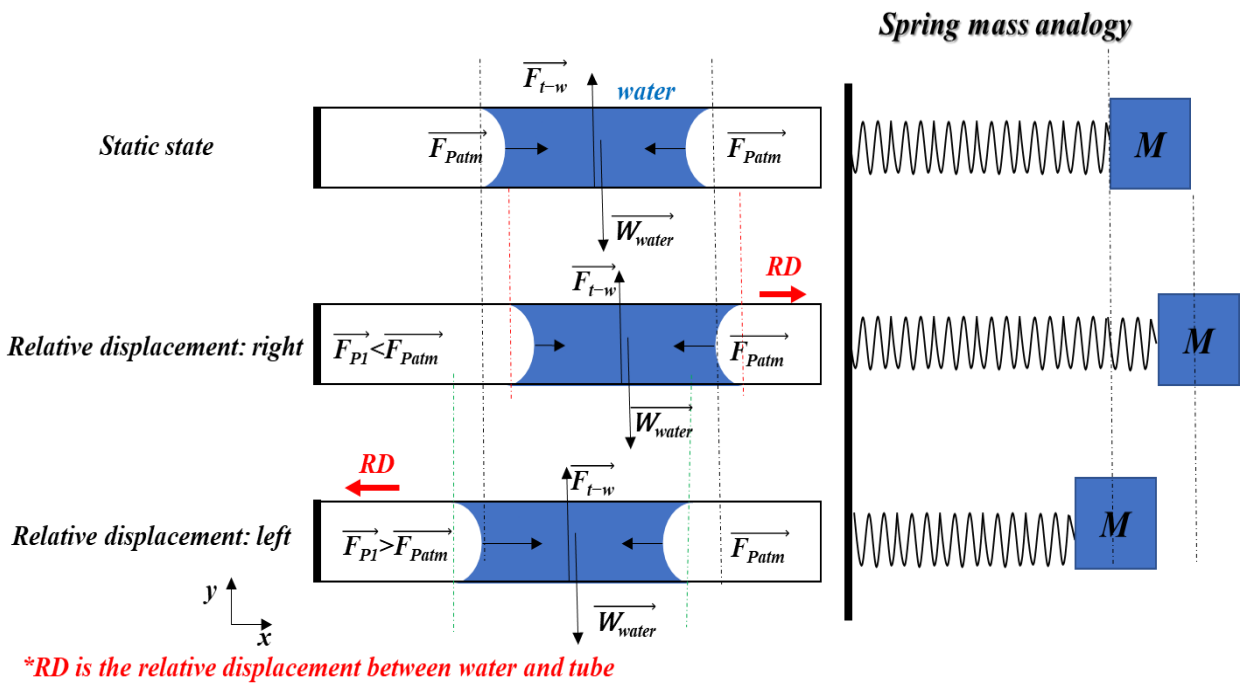

Figure 5-3. Spring mass model of the asymmetrical configuration

Figure 5-3 shows the system at different states (different relative positions). At the static equilibrium state, the pressure at both sides of the water index are equivalent. When the relative displacement of the water index is to the right of the tube, the blocked air is under partial depression and the force acting on the water is lower than the one due to the atmospheric pressure acting on the opposite side of the water index. When the relative displacement of the water index is to the left, the blocked air is compressed, and the force acting on the water increases. The figure also gives the analogy with the spring mass system under different states.

Choosing the water index as mechanical system and according to the Newton's second law of motion, for a mass *m*, the acceleration of the system ($\vec{a}$) is proportional to the sum of the external forces applied to the system $\sum \overrightarrow{F_{ext}}$ and expressed as:

$$\sum \overrightarrow{F_{ext}} = m\vec{a} \qquad \text{Equation 5-5}$$

Following our assumptions, the external forces on the water index are linked to the pressure of the blocked air, the atmospheric pressure on the opposite side, the weight of water, and the force from tube to water, which writes as

$$\sum \overrightarrow{F_{ext}} = \overrightarrow{F_{P1}} + \overrightarrow{F_{Patm}} + \overrightarrow{W_{water}} + \overrightarrow{F_{t-w}} \qquad \text{Equation 5-6}$$

where $\overrightarrow{F_{P1}}$ is the force of the blocked air on the water index and $\overrightarrow{F_{Patm}}$ is the atmospheric pressure (P_{atm}) on the water index, $\overrightarrow{W_{water}}$ is the gravity of water and $\overrightarrow{F_{t-w}}$ is the reaction force against the water.

According to the assumption, the friction is neglected, thus, we have $\overrightarrow{W_{water}} + \overrightarrow{F_{t-w}} = \vec{0}$.

To calculate $\overrightarrow{F_{P1}}$, we need to apply Equation 5-4. Then we can obtain the expression of $\overrightarrow{F_{P1}}$ as:

$$\overrightarrow{F_{P1}} = P_{atm} \frac{l_{air}(t=0)}{l_{air}(t)} S \cdot \overrightarrow{u_x} \qquad \text{Equation 5-7}$$

where *S* is the surface of the cross-section of the tube inner wall.

Because the resultant force in vertical direction equals zero, the external force become

$$\sum \overrightarrow{F_{ext}} = \sum \overrightarrow{F_{ext-x}} = \overrightarrow{F_{P1}} + \overrightarrow{F_{Patm}} = \left(\frac{P_{\mathrm{atm}} \cdot S}{l_{air}(t)}\right) (l_{\mathrm{air}}(\mathrm{t}=0) - l_{\mathrm{air}}(t)) \cdot \overrightarrow{u_x} \qquad \text{Equation 5-8}$$

$$l_{air}(t) = l_{air}(t=0) - \Delta l_{air} \qquad \text{Equation 5-9}$$

where Δl_{air} is the change of the blocked air length at time *t*.

Assuming Δl_{air} to be far less than $l_{\mathrm{air}}(\mathrm{t}=0)$, $\frac{P_{\mathrm{atm}} \cdot S}{l_{air}(t)} \approx \frac{P_{\mathrm{atm}} \cdot S}{l_{air}(t=0)}$. Then Equation 5-8 can be simplified

as:

$$\sum \overrightarrow{F_{ext}} = \sum \overrightarrow{F_{ext-x}} = \overrightarrow{F_{P1}} + \overrightarrow{F_{Patm}} = \left(\frac{P_{\text{atm}}.\text{S}}{l_{air}(t=0)}\right)(l_{\text{air}}(\text{t}=0) - l_{\text{air}}(t))\,\overrightarrow{u_x} \quad \text{Equation 5-10}$$

Based on the analogy above, the blocked air behaves like a linear spring connected to the weight. As is well known, the spring-mass system, the elastic force of the spring is calculated as

$$F_{\text{spring}} = k(l_{\text{spring}}(t=0) - l_{\text{spring}}(t)) \quad \text{Equation 5-11}$$

where *k* is the spring stiffness; F_{spring} is the force of the spring; $l_{\text{spring}}(t=0)$ is the initial length of the spring and $l_{\text{spring}}(t)$ is the length of the spring at time *t*.

Thus, we can make an analogy of the parameters between the spring-mass system and the blocked air-liquid system, as Table 5-3.

Table 5-3 A contrast between the spring-mass system and the blocked air-liquid system

System	*Spring-mass system*	*Blocked air-liquid system*
Mass	m	$m_{water} = \frac{\pi D^2}{4} l_{water} \rho_{water}$
Force	$k(l_{\text{spring}}(t=0) - l_{\text{spring}}(t=0))$	$\left(\frac{P_{\text{atm}}.\text{S}}{l_{\text{air}}(t=0)}\right)(l_{\text{air}}(t=0) - l_{\text{air}}(t))$
Spring stiffness	k	$\frac{P_{\text{atm}}.\text{S}}{l_{\text{air}}(t=0)}$
Resonance frequency (f_r)	$\frac{1}{2.\pi}\sqrt{\frac{k}{m}}$	$\frac{1}{2.\pi}.\sqrt{\frac{P_{atm}}{\rho_{water}.l_{water}.l_{air}(t=0)}}$

5.2.2.1.3 Model-assisted definition of the experimental plan

The frequency range is chosen to explore the water behavior near the resonance frequency.

With the model, we can make a prediction of this resonance frequency for the experimental configuration (Table 5-1). We get a resonance frequency for tubes ID 0.6 mm and ID 2.2 mm equal to 25.7 Hz and 25.9 Hz, respectively. Following the rule for the determination of the frame rate, the camera is set to 1000 frames per second (FPS) for both capillary tubes.

For the experiments, the water amplitude was determined from 20 Hz to 30 Hz with a step of 1 Hz. For each frequency, we observed at least 33 images per periods, which fulfils our goal of 20 fps.

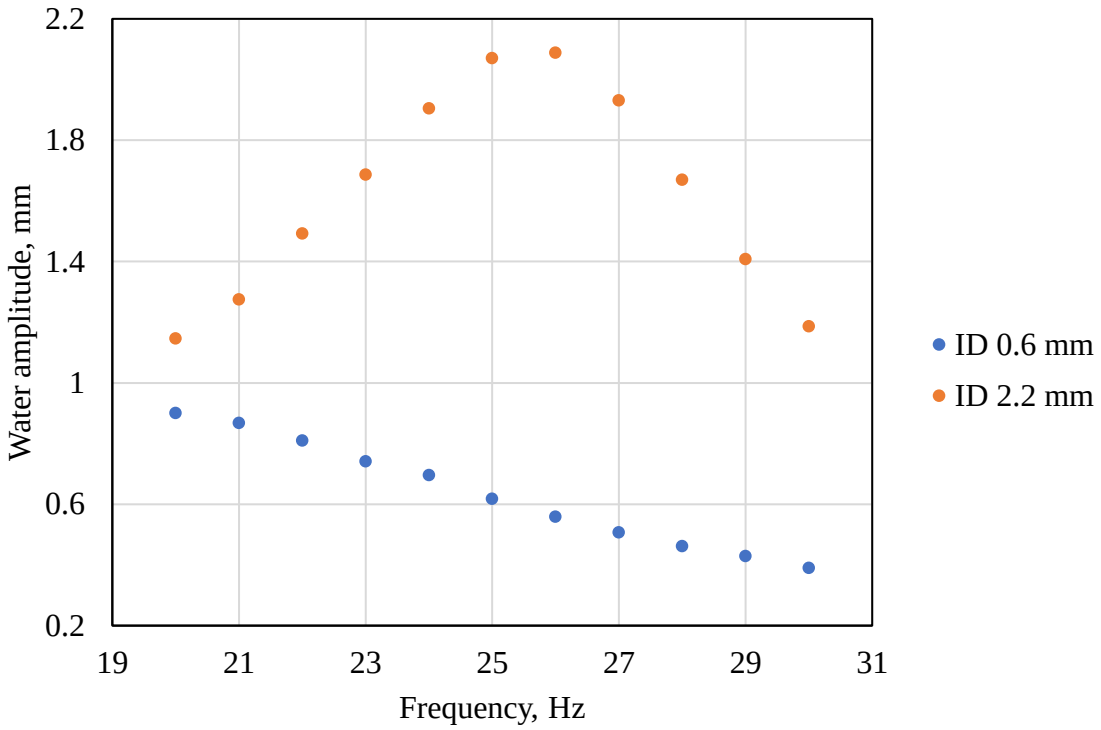

Figure 5-4 The evolution of the water amplitude with frequency for the two tubes.

Figure 5-4 depicts the evolution of water amplitude as a function of frequency. The difference between the two tubes is obvious.

The resonance frequency for the 2.2 mm tube is about 26 Hz, which is in good agreement with the simple model. Based on the curve shape, the region of interest ranging from 23 Hz to 27 Hz is to be further investigated to confirm the resonance frequency, with an internal of 0.2 Hz.

From the shapes of both curves, the resonance frequency for the 0.6 mm tube seems to be much lower. Therefore, another exploration of the frequency for ID 0.6 mm tube is needed. A set of new parameters for testing the resonance frequency of ID 0.6 mm tube are shown as Table 5-4.

Table 5-4 Parameters for testing the resonance frequency of ID 0.6 mm tube

ID	**A**	l_{air}	l_{water}	f	**Interval**
0.6 mm	*0.5 mm*	*76 mm*	*52 mm*	*15 Hz~25 Hz*	*1 Hz*

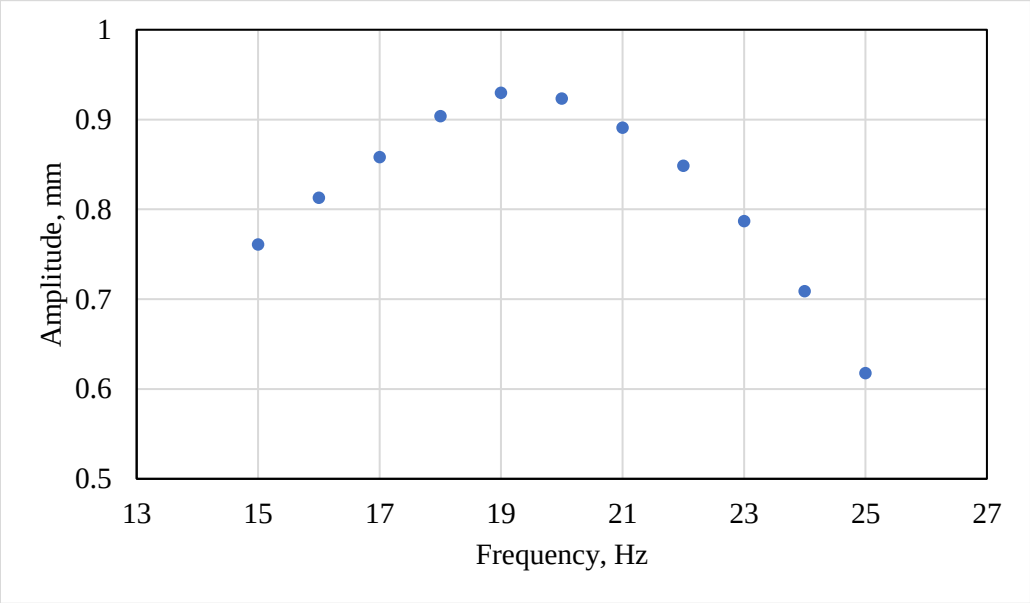

Figure 5-5 The water amplitude versus frequency for the 0.6 mm tube (f = 15 – 25 Hz)

The water amplitude evolution over this new frequency range is depicted in Figure 5-5. The resonance frequency for the ID 0.6 mm tube is about 19 Hz. Then, to find the precise resonance frequency, we will make a detailed study between 17 Hz and 21 Hz, with an interval of 0.2 Hz. Meanwhile, in order to save time for the image processing, the selected frame rate for all the tests in ID 0.6 mm tube will be adjusted to 500 FPS, according to the criteria for the determination of

frame rate. Then, we can obtain at least 20 images per period.

5.2.2.2 Experimental plan

Table 5-5 Parameters tested for sinusoidal vibration of water inside the capillary tube

Reference	Inner diameter	Frequency	Interval
E06-1	*0.6 mm*	*15 Hz~25 Hz*	*1 Hz*
E06-2	*0.6 mm*	*17 Hz~21 Hz*	*0.2 Hz*
E06-3	*0.6 mm*	*15 Hz~25 Hz*	*1 Hz*
E22-1	*2.2 mm*	*20 Hz~30 Hz*	*1 Hz*
E22-2	*2.2 mm*	*23 Hz~27 Hz*	*0.2 Hz*
E22-3	*2.2 mm*	*20 Hz~30 Hz*	*1 Hz*

For a systematic study of the water behavior under asymmetrical configuration around the resonance frequency, a group of experiments for each capillary tube were designed (Table 5-5). In each group (E06 and E22 in Table 5-5), there are three series. The group name E06 and E22 represent the experiments conducted in the ID0.6 tube and ID2.2 tube, respectively. The first series is what we have done previously to test the evolution of the water amplitude with respect to frequency with a 1 Hz step. It also helps to find the range of interest. The range of interest is the area around the resonance frequency. The second series is to make a detailed study of this range of interest with a 0.2 Hz step. The third series is to verify the repetition of the experiments: we repeat the same sequence as the first one.

Table 5-6 Parameters setting in the PFV software

ID	Resolution	Exposure time	Frame rate	Distance between light and tube
0.6 mm	*1024 × 1024*	*1 / 60 000 s*	*500 FPS*	*10 mm*
2.2 mm	*1024 × 1024*	*1 / 60 000 s*	*1000 FPS*	*10 mm*

The parameters in *PFV*, the software controlling the fast camera, were set as Table 5-6. These parameters will be suitable for all the tests in the following contents.

For all the captured images, we analyzed the meniscus with the method introduced in chapter 3.

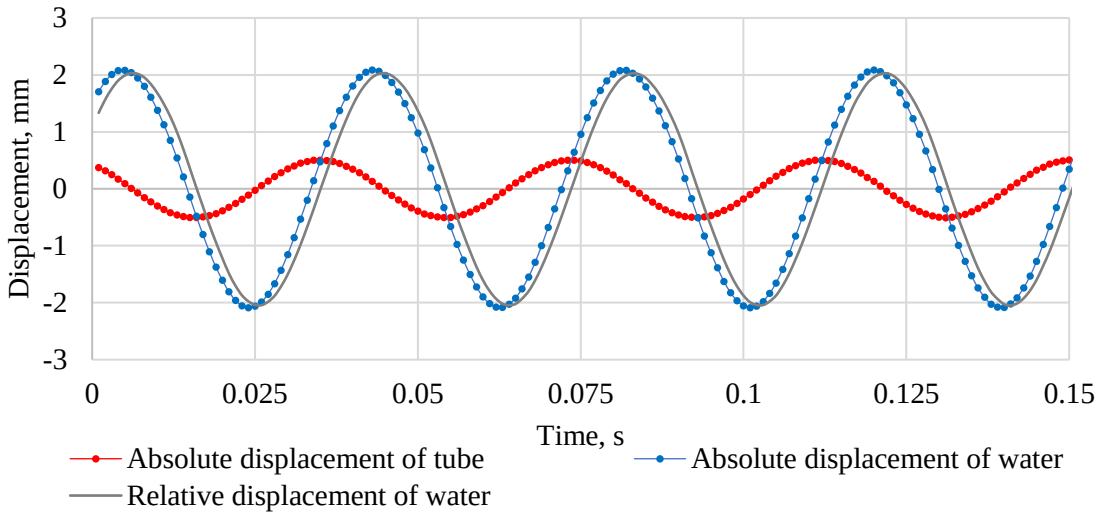

Figure 5-6 The evolution of the displacements with time (ID = 2.2 mm, f = 26 Hz, A = 0.5 mm; dotted lines are the absolute displacement; line is the relative displacement between tube and water)

Then, we can obtain the raw data of the displacement of the capillary tube and the water index (Figure 5-6). We can notice that the water amplitude is much higher than the tube amplitude. The gray line shows the corresponding relative displacement between the water index and the tube.

We can find that the amplitude of the relative displacement equals to 2 mm, 4 times higher than the tube displacement amplitude. For the given parameters, the phase change between the tube and the water index is close to $\pi/2$.

5.2.3 Results and discussions

5.2.3.1 Effect of vibration on drying rate in asymmetrical geometry

5.2.3.1.1 Evaporation rate

Table 5-7 Parameters for evaporation experiments in different geometry

Reference	ID	A	l_{air}	l_{water}	f	Remark
E22-S	*2.2 mm*	*0.5 mm*	---	*51 mm*	*25 Hz*	*Symmetrical geometry*
E22-AS	*2.2 mm*	*0.5 mm*	*76 mm*	*51 mm*	*25 Hz*	*Asymmetrical geometry*

In chapter 4, it has been verified that the vibration is effective to intensify the drying process in continuous pores. To make a contrast between symmetrical and asymmetrical configurations, a pairs of evaporation experiments were carried out (Table 5-7). The duration of both experiments was 36 h. Both experiments were conducted under the same conditions (water volume, index position, applied signal, *etc*.) except the configuration of the capillary tube. ***E22-S*** used the ID 2.2 mm tube with two open ends, and ***E22-AS*** used the same tube with one end plugged.

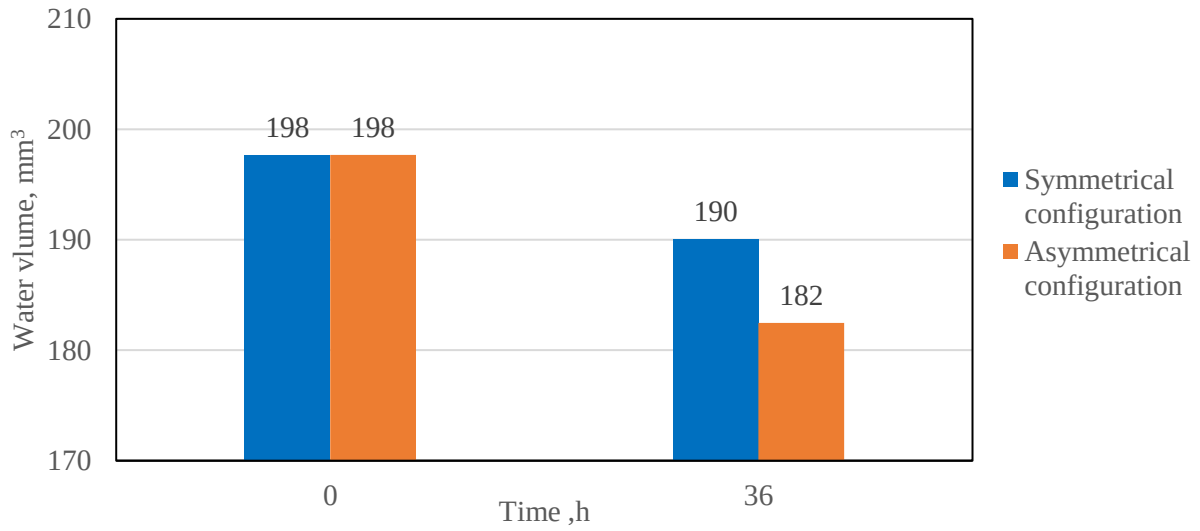

Figure 5-7 The evolution of water volume before and after 36 hours of drying (ID = 2.2 mm, A = 0.5 mm, f = 25 Hz)

To estimate the volume of the water index, we measured the water length in both capillary tubes by a ruler before and after the experiments.

Figure 5-7 shows the water volume before and after the evaporation for both configurations. We can notice that the water loss under the asymmetrical configuration is twice higher than that under the symmetrical configuration. Due to the two opening of the symmetrical configuration, the evaporation rate of the symmetrical configuration was expected to be higher than that of the asymmetrical one. Indeed, we obtained an opposite effect. Further analysis is then needed.

5.2.3.1.2 Amplitude of water index

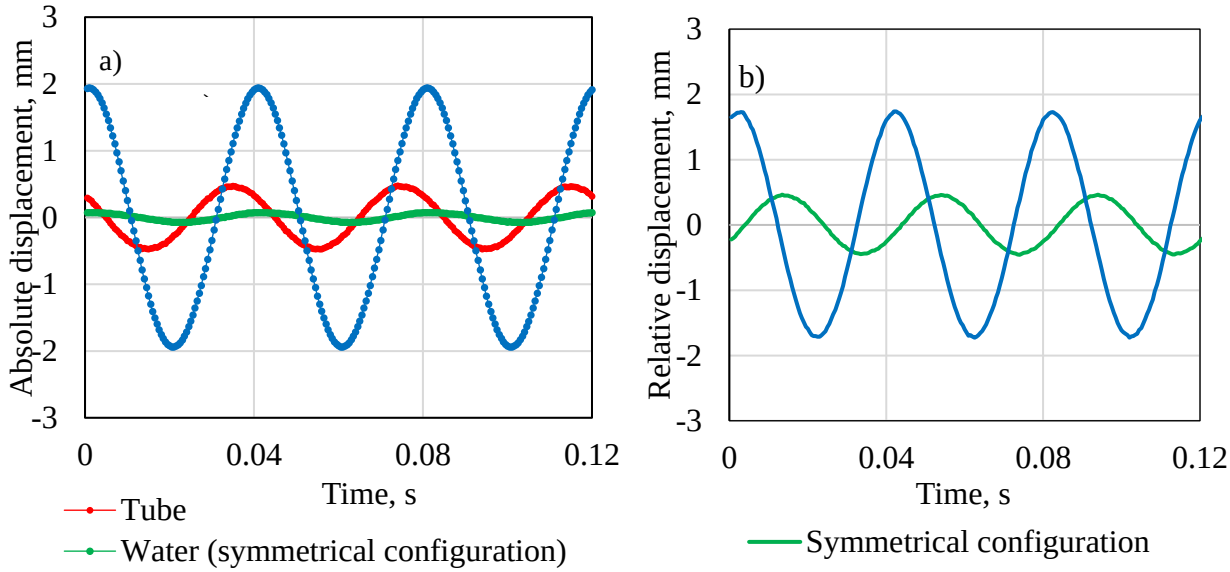

Figure 5-8 The displacement of the capillary tube and the water index (ID = 2.2 mm, A = 0.5 mm, f = 25 Hz; a. absolute displacement; b. relative displacement between water and tube)

Figure 5-8 displays the contrasted results of the water displacement obtained with symmetrical (***E22-S***) and asymmetrical (***E22-AS***) configurations. In this situation, the relative displacement amplitude of the asymmetrical configuration is 1.7 mm, against 0.5 mm for the symmetrical configuration is. The difference of relative displacement amplitude between both configurations is 3.4 times. It means the pumping effect under asymmetrical geometry is much higher than that of

symmetrical geometry. Meanwhile, the dissipation of mechanical energy resulted by the index friction on the tube surface is also higher under asymmetrical configuration than the symmetrical one. Indeed, a higher relative displacement amplitude means a higher relative velocity under the same amplitude and the index friction is proportional to the relative velocity between the water and the tube. That are two of the reasons likely to explain the higher intensification ratio.

5.2.3.1.3 Curvature radius of meniscus

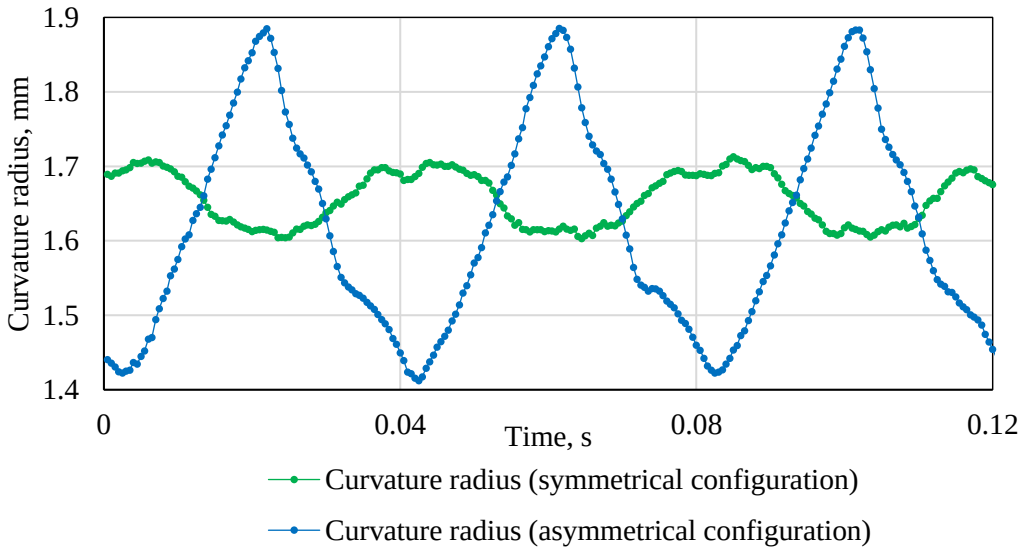

Figure 5-9 The evolution of meniscus curvature radius for the symmetrical and asymmetrical configurations (ID = 2.2 mm, A = 0.5 mm, f = 25 Hz)

Figure 5-9 depicts the evolution of the meniscus curvature radius for the symmetrical and asymmetrical configurations. From the figure, we can find that the evolution range of curvature radius under the asymmetrical configuration is much higher than that under the symmetrical configuration. It indicates that the external mass transfer around the water/air interface under the asymmetrical configuration is improved in comparison to that under the symmetrical one. Besides the effect on external mass transfer, the higher evolution range of curvature radius also means a higher thermal dissipation of the mechanical energy caused by a stronger index deformation which

reveals a higher internal recirculation of water. They are additive reasons to explain the increased drying rate.

5.2.3.2 Effect of frequency on water behavior

Based on the previous observations, it is worth to make an in-depth study for the asymmetrical configuration. From the obtained results, we have known that the water amplitude will be much higher than the imposed amplitude. Subject to the capability of the camera lens, we cannot capture the motion of water index with a high amplitude. Thus, we will focus on the effect of frequency in the experimental part. The effect of tube amplitude will be discussed in the numerical part.

5.2.3.2.1 Effect of frequency on the water amplitude

The preliminary analysis of experimental data for water amplitude under asymmetrical configuration allows us to determine the frequency range to investigate. Thanks to the decrease in frequency step, we can now propose an accurate study of the effect of frequency on water behavior, including the validation of experiments repeatability.

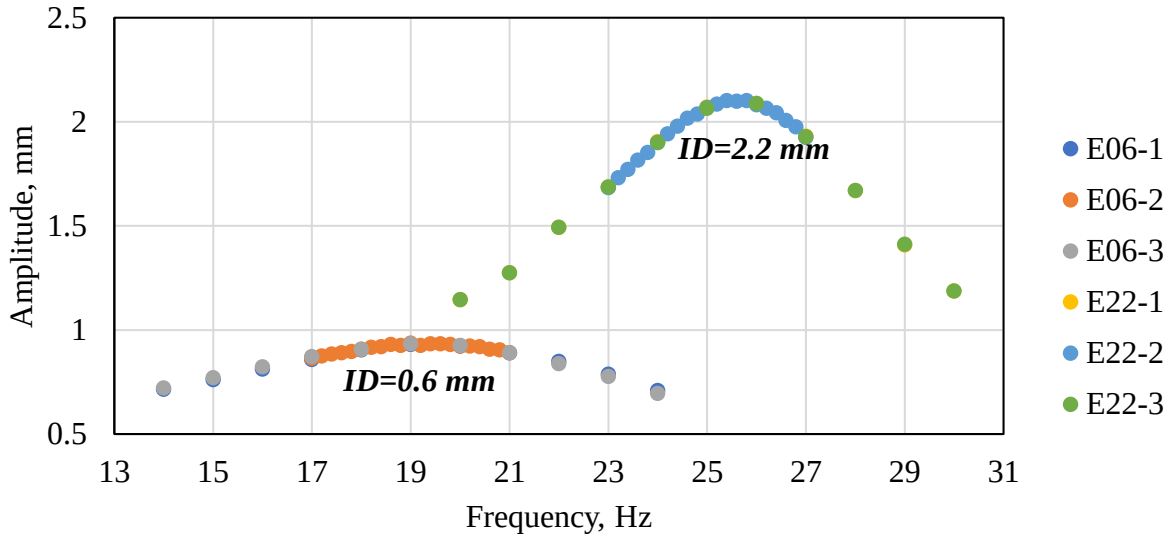

Figure 5-10 The water amplitudes of all the test in Table 5-5

Figure 5-10 depicts the evolution of the water amplitude with respect to the frequency for all the tests shown in Table 5-5. The high repeatability of the results assesses the reliability of the experiments. From the figure, we can find that all the excited water amplitudes are higher than the tube amplitude. This is due to the resonance of the mass-spring system. As expected[228–230], with the increase of the frequency, the amplitude of the water index in both capillary tubes increases primarily, and reaches the peak, then declines.

The resonance frequency in ID 0.6 mm tube is identified as 19 Hz, and that in ID 2.2 mm tube is equal to 25.8 Hz. Except the inner diameter, all other parameters are the same from one experiment to the other. The resonance frequency difference is obviously due to the viscous forces that can be supposed to be small for the large tube, but important for the small tube.

5.2.3.2.2 Effect of frequency on the phase change

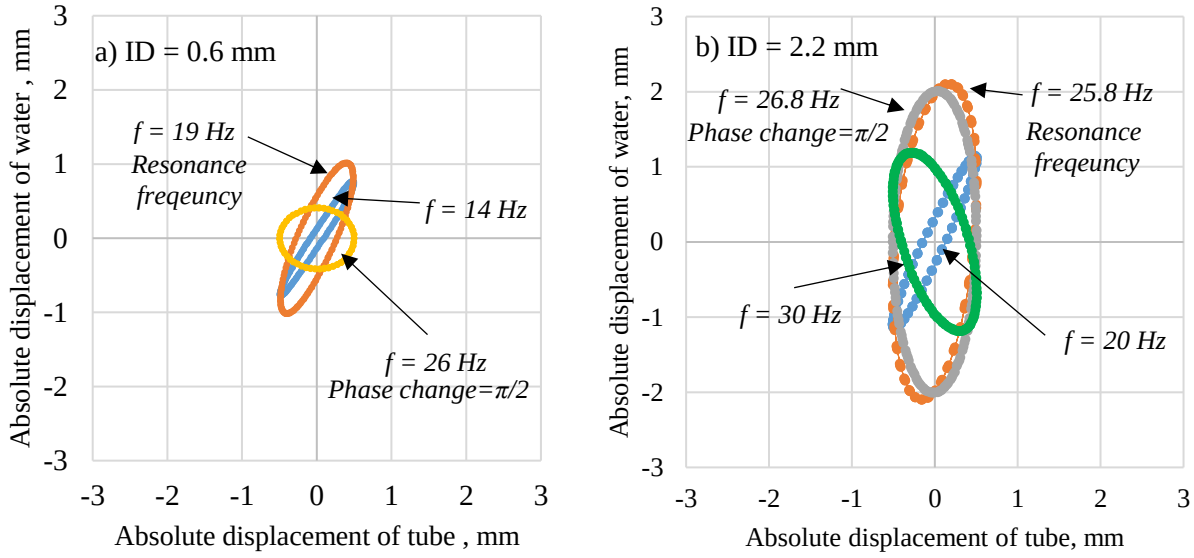

Figure 5-11 Lissajous curves of the experiments at selected frequencies (a. ID = 0.6 mm, f = 15, 19, 26 Hz; b. ID = 2.2 mm, f = 20, 25.8, 26.8, 30 Hz)

The phase change between the motion of the capillary tube and that of water index can be obtained

by analyzing the corresponding Lissajous curve. Figure 5-11 displays some examples of the Lissajous curves obtained respectively from the experiments in (a) ID 0.6 mm tube and (b) ID 2.2 mm tube. The increasing slope of the main axis indicates an increasing tendency of the phase change with the rise of frequency. For the 0.6 mm tube, the final frequency presents a phase change equal to π/2. For the 2.2 mm tube, the last frequency depicts an angle larger than π/2 (negative slope).

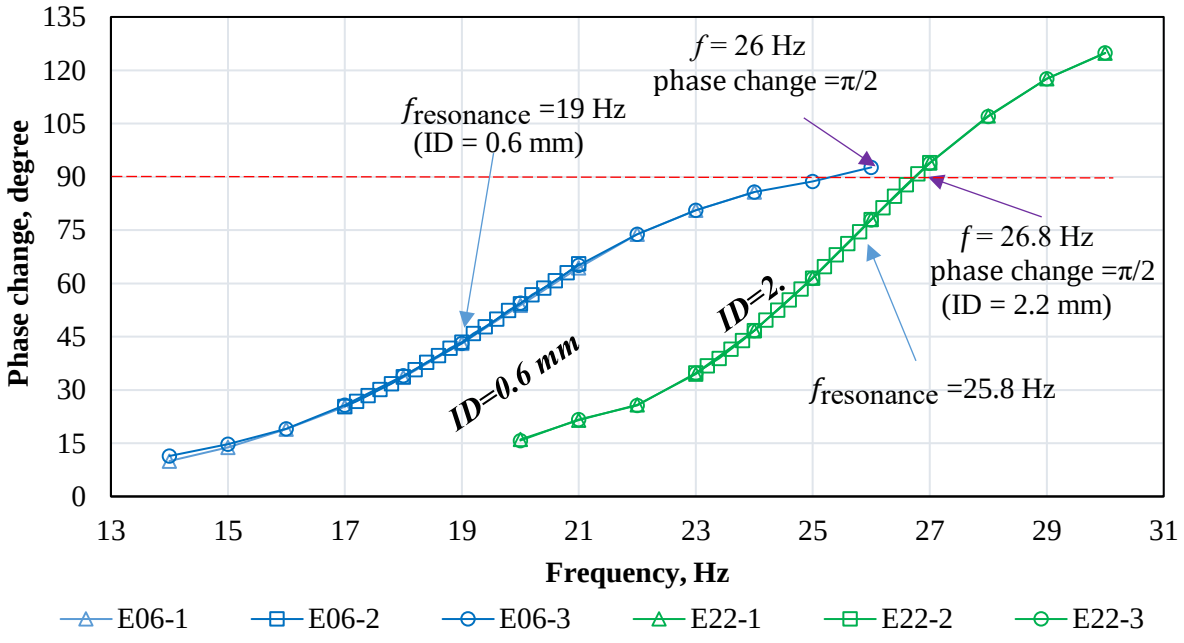

Figure 5-12 Phase change of all tests of Table 5-5

Because of the different water amplitudes, the phase change was determined following the approach developed in 4.4.3, In Figure 5-12, each color represents a series of experiments. It is obvious that the phase change increases with the rise of the frequency under the asymmetrical configuration for both capillary tubes. As shown in Equation 4-7, the inertia of the water index is proportional to the acceleration. For a given amplitude, the increase of frequency results in a rise of the acceleration, which increases the delay between the motion of water index and that of the

tube. As the system is not an ideal harmonic oscillator, the phase change at resonance is lower than π/2.

5.2.3.2.3 Effect of frequency on the curvature radius

The curvature is a criterion to quantify the extent of the meniscus transformation during the vibration. The evolution of curvature radius not only impacts the external mass transfer of the water index, but also affects the heat dissipation of mechanical energy caused by viscous dissipation.

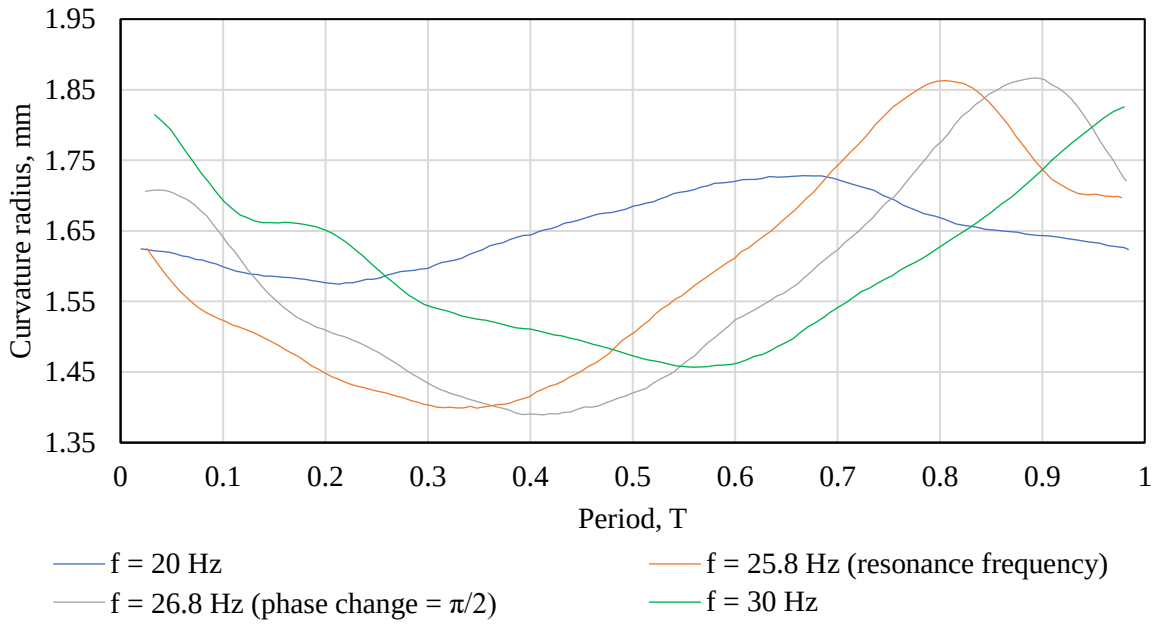

Figure 5-13 The curvature radius variation with time (ID = 2.2 mm; A = 0.5 mm; f = 20, 25.8, 26.8 and 30 Hz)

The results of curvature evolution over one period obtained at four different frequencies (initial test frequency, resonance frequency, frequency for a phase change equal to π/2 and final test frequency) are shown in Figure 5-13. We can see an obvious shift of the curves with the increase of the frequency due to index inertia. The amplitude of curvature radius far from resonance (20 and 30 Hz) are significantly lower than the others. The amplitude of curvature radius at resonance frequency is 0.23 mm, and that at 26.8 Hz (phase change = π/2) is a little higher, 0.24 mm.

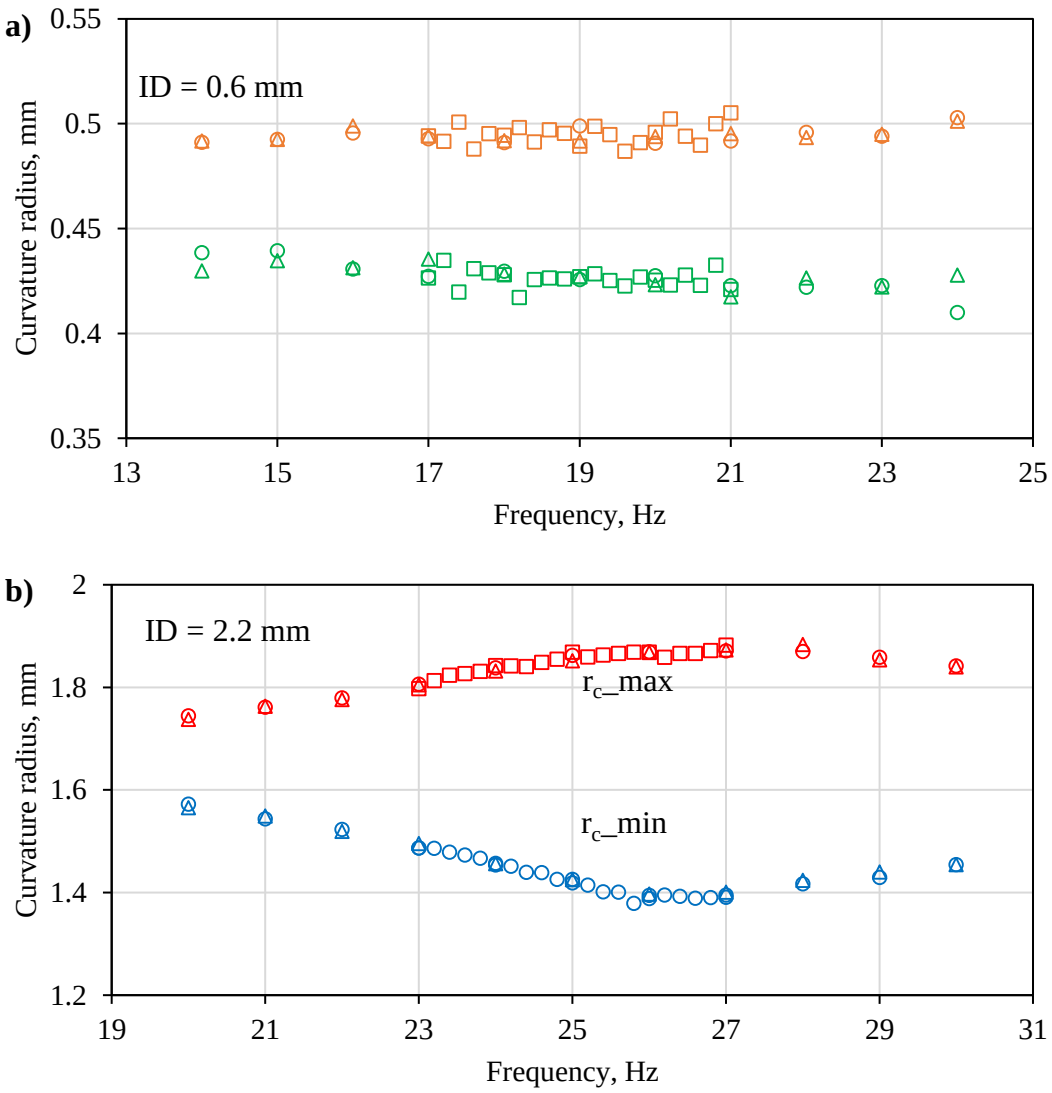

Figure 5-14 The maximum and minimum curvature radius (rc_max and rc_min) with respect to frequency (a for ID 0.6 mm tube; b for ID 2.2 mm tube)

To have a clear view of the span evolution for the curvature radius with frequency, we selected the maximum curvature radius (r_c_max) and the minimum curvature radius (r_c_min) of each test, as shown in Figure 5-14. For ID 2.2 mm tube, the max curvature radius increases with the frequency until the peak value at resonance frequency, then declines. The minimum curvature radius presents an opposite trend. For ID 0.6 mm tube, the evolutions of r_c_max and r_c_min with frequency are not obvious, even when the frequency is extended to 30 Hz for the ID 0.6 mm tube. Two reasons can explain the difference between results obtained for both ID. First, it is due the resolution of the

image. Second, with this small ID, the trend may also due to high capillary and viscous effects in comparison with inertia.

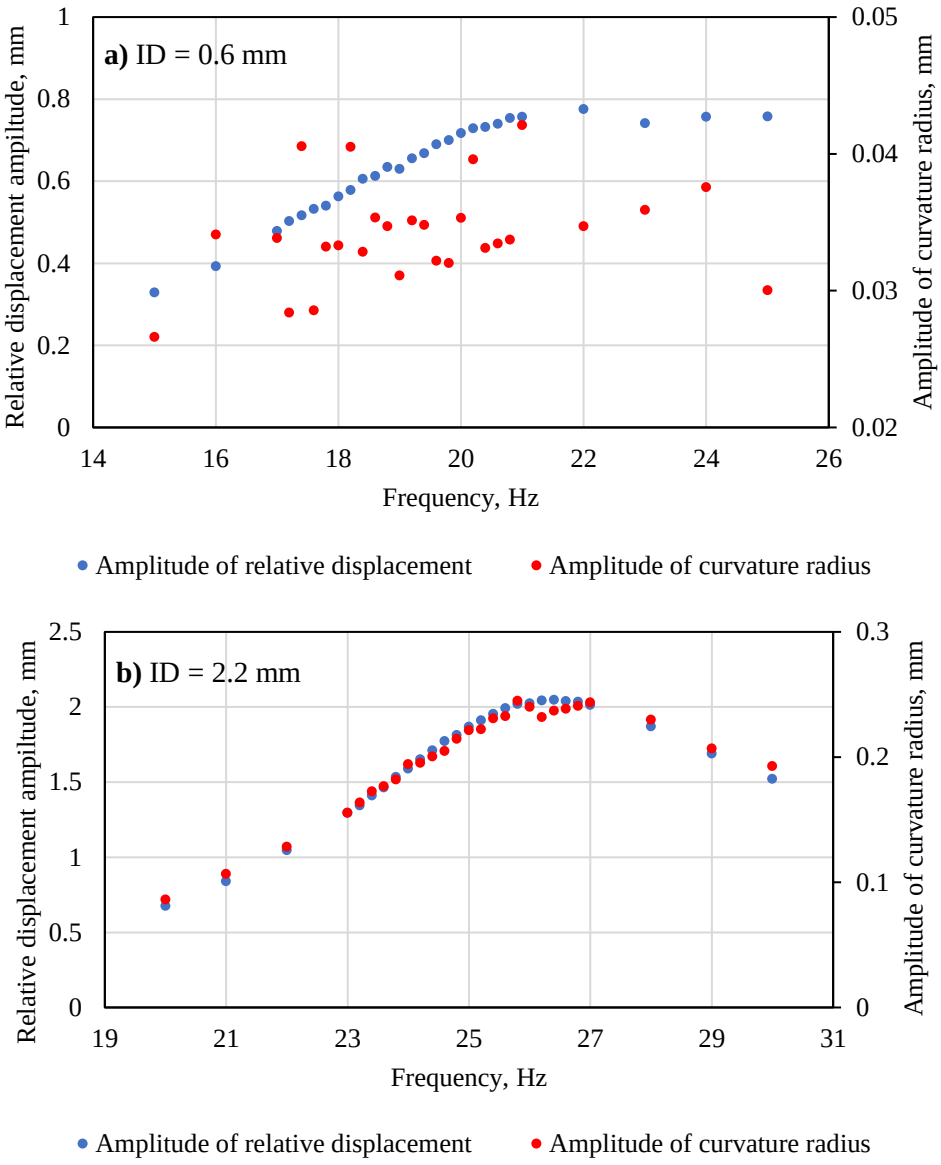

Figure 5-15 Evolution of relative displacement (water/tube) amplitude and evolution of curvature radius amplitude with frequency (a. ID = 0.6 mm tube; b. ID = 2.2 mm tube)

We also speculate that the amplitude of the curvature radius may be related to the amplitude of the relative displacement between the water and tube. To investigate this question, we display both values for each tube size in Figure 5-15. For the ID 0.6 mm tube, the noise of the curvature radius

provides us to confirm a concomitant increase of both values. On the contrary, the 2.2 mm tube, exhibits a clear correlation. Clearly, the combination of inertia and viscous effects at the inner wall of the tube gives rise to an important deformation of the meniscus near the resonance. This will be further investigated in a modelling approach.

5.3 Theoretical / numerical study

The simplistic spring mass model described above was proved to be very limited. In this part, two improved models are proposed: a 0-D model accounting for viscous effects and a 1-D spatio-temporal model. Both are written in the R language. All the relevant parameters and code are displayed in the appendix.

5.3.1 The 0-D model

5.3.1.1 Description of the model

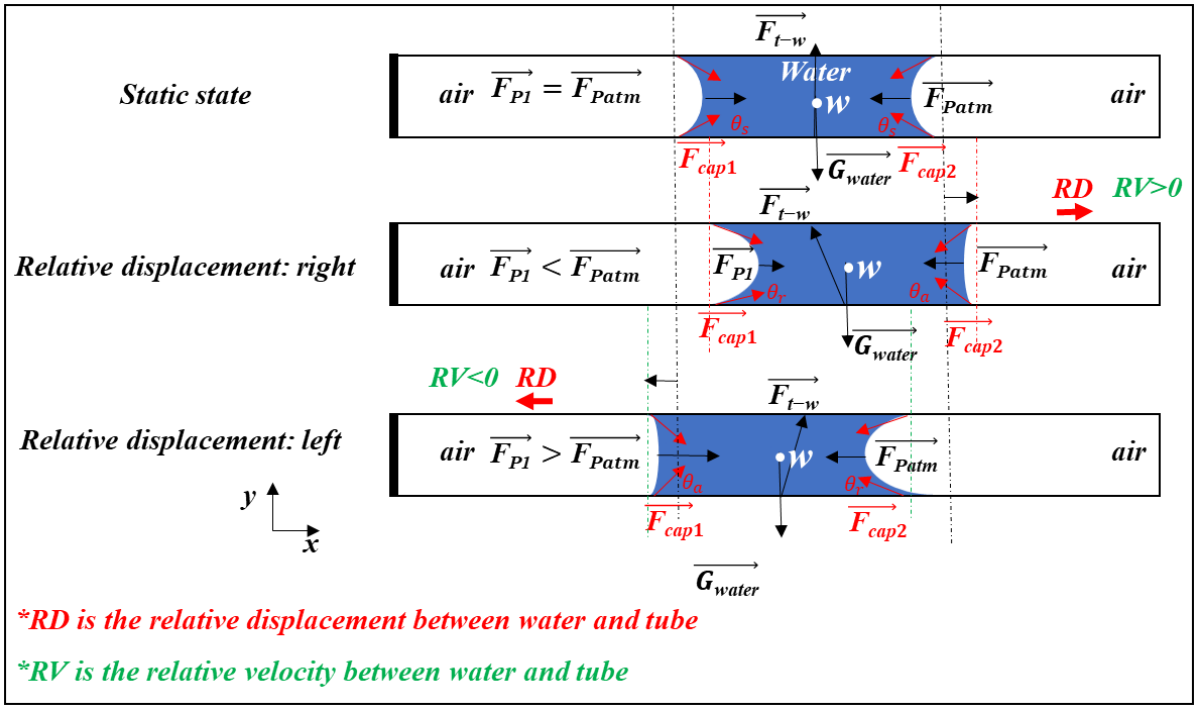

Figure 5-16 Temporal model of the asymmetrical configuration

The water index is defined as the system in all the numerical studies. In this section, we will study the evolution of the forces applied to the system temporally related.

The schematic of the 0-D model under different states are shown in Figure 5-16, w is the mass center of the water index, and the x-axis is positive towards the right.

As shown in Figure 5-16, several external forces act on the system (the water index): $\overrightarrow{F_{P1}}$ is the force from the blocked air acting on the left surface of the water index, $\overrightarrow{F_{Patm}}$ is the force from the atmosphere (101 kPa) acting on the right surface of the water index, $\overrightarrow{F_{cap1}}$ is the capillary force on the left meniscus, as:

$$\overrightarrow{F_{cap1}} = \pi D\sigma \cos(\theta_1)\,\overrightarrow{u_x} \qquad \text{Equation 5-12}$$

where θ_1 is the contact angle between the left meniscus and the tube;

$\overrightarrow{F_{cap2}}$ is the capillary force related to the right meniscus, as

$$\overrightarrow{F_{cap2}} = \pi D\sigma \cos(\theta_2)\,\overrightarrow{u_x} \qquad \text{Equation 5-13}$$

where θ_2 is the contact angle between the right meniscus and the tube.

$\overrightarrow{G_{water}}$ is the weight of the water index, expressed as:

$$\overrightarrow{G_{water}} = \frac{\pi D^2}{4} l_{water}\rho_{water}\vec{g} \qquad \text{Equation 5-14}$$

$\overrightarrow{F_{t-w}}$ is the force from the tube to the water.

At the static state, the forces from the gas on both sides of the water index are equivalent to the atmospheric pressure over the surface, the contact angles on both menisci are the same. The contact

angle at static state is defined as static contact angle[231], expressed by θ_s. We have:

$$\overrightarrow{F_{P1}} + \overrightarrow{F_{Patm}} = \vec{0} \quad \text{Equation 5-15}$$

$$\overrightarrow{F_{cap1}} + \overrightarrow{F_{cap2}} = \vec{0} \quad \text{Equation 5-16}$$

$$\overrightarrow{G_{water}} + \overrightarrow{F_{t-w}} = \vec{0} \quad \text{Equation 5-17}$$

In the dynamic state, the direction of the friction between water and tube (the component force of $\overrightarrow{F_{t-w}}$ in axial direction, due to water viscosity) is opposite to that of the relative velocity and the direction of the force from the blocked air on the water index depends on the relative displacement between the water and the tube, as for the simple mass-spring model.

According to the Newton's second law, the resultant force acting on the water index reads:

$$\sum \overrightarrow{F_{ext}} = m\overrightarrow{a_{water}} = \overrightarrow{F_{P1}} + \overrightarrow{F_{Patm}} + \overrightarrow{F_{cap1}} + \overrightarrow{F_{cap2}} + \overrightarrow{G_{water}} + \overrightarrow{F_{t-w}} \quad \text{Equation 5-18}$$

The calculation of $\overrightarrow{F_{P1}}$ and $\overrightarrow{F_{Patm}}$ have been mentioned in the spring mass model. The sum of $\overrightarrow{G_{water}}$ and the vertical component force of $\overrightarrow{F_{t-w}}$ equals to $\vec{0}$.

The capillary force depends on the contact angle. When the relative velocity between water and tube is positive, the left meniscus is the receding meniscus, and the right one is the advancing one. The contact angle on the receding meniscus (the left one, θ_1) is equal to the receding contact angle ($\theta_r < \theta_s$), The contact angle on the advancing meniscus (the right one, θ_2) is equal to the advancing contact angle ($\theta_a > \theta_s$). When the relative velocity between water and tube is negative, the situation is contrary. It exists a transition state for the contact angle varying between θ_r and θ_a,when the direction of the relative velocity is inverted.

To simplify the calculation, we neglect the transition state of the contact angle (from θ_a to θ_r and

the opposite). We assume that only receding and advancing contact angle existing on the meniscus when the relative velocity is not equal to zero:

$$F_{cap1} + F_{cap2} = \text{sign}(v_{tube} - v_{water}) \cdot \pi D\sigma(\cos(\theta_r) - \cos(\theta_a)) \quad \textit{Equation 5-19}$$

where $\text{sign}(v_{tube} - v_{water})$ is the sign of the difference between the absolute velocities of tube and water.

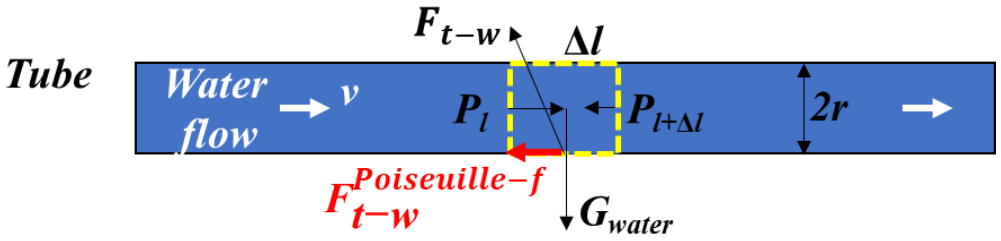

Figure 5-17 The schematic diagram of water flow (laminar) in a tube

To evaluate the viscous force in this 0-D model, we assume that the motion of the water index inside the tube during vibration is similar to a laminar Poiseuille flow (Figure 5-17). A volume of the water is selected at position *l* by the yellow square with a length of Δl. ΔP is the pressure drop between both sides of this volume of the water. The viscous force on the meniscus $F_{t\text{-}w}^{Poiseuille-f}$ simply reads:

$$F_{t-w}^{Poiseuille-f} = S\Delta P \qquad \text{Equation 5-20}$$

Where S is the section area of the tube. Using the classical solution of a steady laminar flow in a tube, we obtain:

$$\Delta P = \frac{8\mu LQ}{\pi r^4} = \frac{8\mu LS\bar{v}}{\pi r^4} \qquad \text{Equation 5-21}$$

$$F_{t-w}^{Poiseuille-f} = \text{S}\Delta P = S\frac{8\mu LS\bar{v}}{\pi r^4} = 8\mu\pi\Delta l \cdot \bar{v} \qquad \text{Equation 5-22}$$

where μ is the dynamic viscosity of the water. Q is the volumetric flow rate, equals to $S \cdot \overline{v}$, $\overline{v}$ is the averaged velocity of the flow and L is the length of the tube.

Thus, the friction force ($\overrightarrow{F_{t-w}^{f}}$) is given by:

$$\overrightarrow{F_{t-w}^{f}} = \overrightarrow{F_{t-w}^{Poiseuille-f}} = S\Delta P \cdot \overrightarrow{u_x} = 8\pi\mu l_{water}(\overrightarrow{v_{tube}} - \overrightarrow{v_{water}}) \quad \text{Equation 5-23}$$

Finally, according to the second Newton's law, we will obtain:

$$\overrightarrow{a_{water}} = \frac{\overrightarrow{F_{t-w}^{f}} + sign(v_{tube} - v_{water})(\overrightarrow{F_{cap1}} + \overrightarrow{F_{cap2}}) + \overrightarrow{F_{P1}} + \overrightarrow{F_{Patm}}}{m} \quad \text{Equation 5-24}$$

A projection over the x-axis gives a scalar expression:

$$a_{water} = \frac{8\mu l_{water}(v_{tube} - v_{water}) + sign(v_{tube} - v_{water}) \cdot D\sigma(cos\theta_r - cos\theta_a) + \frac{P_{atm}D^2}{4l_{air}(t=0)}(x_{tube} - x_{water})}{\rho_{water}\frac{D^2}{4}l_{water}}$$

Equation 5-25

In this study, the temporal discretization is achieved by the second-order explicit Newton's method[232]

$$x_{water}(t + \Delta t) = x_{water}(t) + \frac{v_{water}(t) + v_{water}(t+\Delta t)}{2}\Delta t \quad \text{Equation 5-26}$$

$$v_{water}(t + \Delta t) = v_{water}(t) + \frac{a_{water}(t) + a_{water}(t+\Delta t)}{2}\Delta t \quad \text{Equation 5-27}$$

$a_{water}(t)$ and $a_{water}(t + \Delta t)$ are the acceleration of the water at time t and $t + \Delta t$, respectively. $a_{water}(t)$is given by:

$$a_{water}(t) = \frac{8\mu\big(v_{tube}(t) - v_{water}(t)\big)}{\rho_{water}\frac{D^2}{4}} + \frac{sign\big(v_{tube}(t) - v_{water}(t)\big) \cdot \sigma(cos\theta_r - cos\theta_a)}{\rho_{water}\frac{D}{4}l_{water}}$$

$$+ \frac{P_{atm}\big(x_{tube}(t) - x_{water}(t)\big)}{l_{air}(t=0)\rho_{water}l_{water}} \quad \text{Equation 5-28}$$

The displacement and velocity of the capillary tube are obtained as imposed conditions:

$$x_{tube}(t) = A_{tube}\sin(\omega t) \qquad \text{Equation 5-29}$$

$$v_{tube}(t) = \omega A_{tube}\cos(\omega t) \qquad \text{Equation 5-30}$$

A similar expression applies for $a_{water}(t + \Delta t)$.

Besides, the primary estimation of the displacement and velocity of water index at $t + \Delta t$ will be achieved by the first-order Newton method, as:

$$x_{water}(t + \Delta t) = x_{water}(t) + v_{water}(t)\Delta t \qquad \text{Equation 5-31}$$

$$v_{water}(t + \Delta t) = v_{water}(t) + a_{water}(t)\Delta t \qquad \text{Equation 5-32}$$

with the initial value $v_{\text{water}} = 0$, $x_{\text{water}} = 0$, and for the convergence the value of Δt is recommended to set as low as possible. We checked that the solution does not depend of the chosen value of Δt.

5.3.1.2 Numerical results of the 0-D model

Table 5-8 Parameters for the temporal model

ID	***$l_{air}(t=0)$***	***l_{water}***	***Surface tension (σ)***	***Dynamic viscosity (μ)***	***Advancing contact angle (θ_a)***	***Receding contact angle (θ_r)***	***A***	***f***	***Time step***
2.2 mm	*76 mm*	*51 mm*	*72 mN/m*	*1.002 mPa/s*	*40^{o}233*	*4^{o}233*	*0.5 mm*	*20 ~ 30 Hz*	*1 ms*

The simulation of temporal model was conducted under the conditions of Table 5-8.

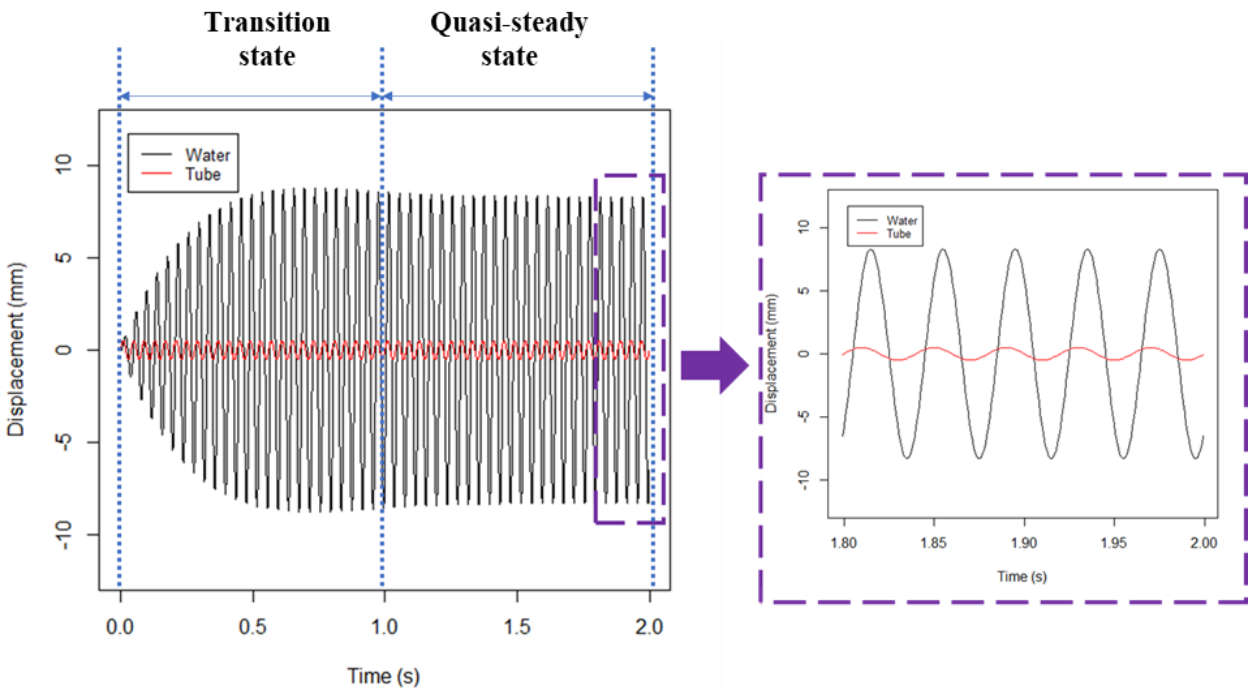

Figure 5-18 The displacement of water and tube simulated by Temporal model (ID = 2.2 mm, A = 0.5 mm, f = 25 Hz)

With this model, we can get the displacement evolution of the water index and that of the capillary tube versus time, as shown in Figure 5-18. In the transition area, the water is excited by the imposed vibration of the tube from the static state: the index movement amplitude increases up to a stationary regime. Consistently with the resonance regime, we notice that the amplitude of water is much higher than the amplitude of the capillary tube. From the simulation results, we can also plot Lissajous curves to determine the phase change as we did for the experimental data.

In the following, the 0-D model is compared to our experimental results.

Water amplitude evolution

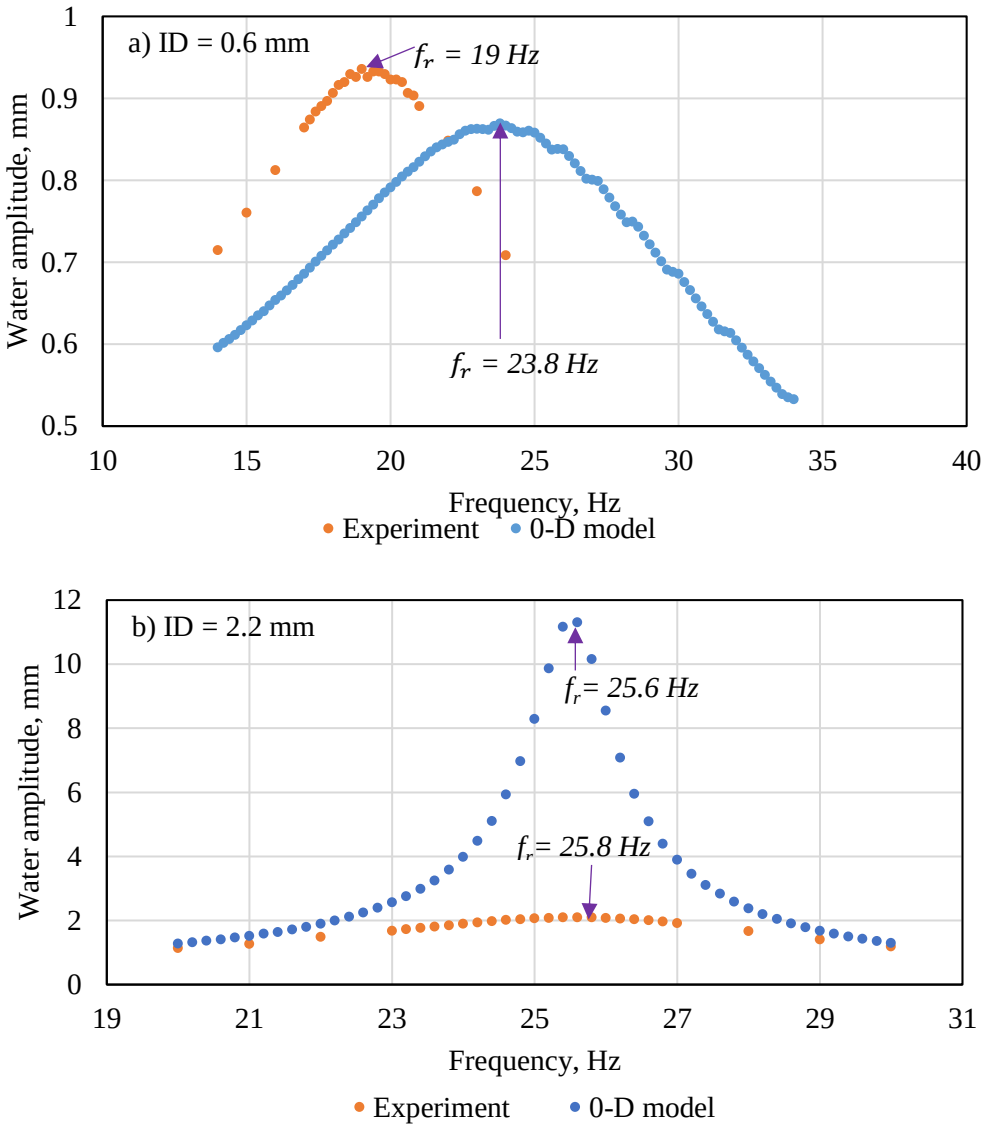

Figure 5-19 The water amplitude evolution: comparison between the 0-D model and the experiments (a for ID 0.6 mm tube; b for ID 2.2 mm tube)

Figure 5-19a plots both experimental and numerical results in ID 0.6 mm tube, and Figure 5-19b gives that in ID 2.2 mm tube. It is clear that the trends of experimental and numerical results are similar. With the increase of frequency, the water amplitude rises until the max at the resonance frequency and then decreases.

For the ID 0.6 mm tube, the resonance frequency obtained from the 0-D model (23.8 Hz) is higher than the experimental one (19 Hz), but the shapes of both curves are similar. For the ID 2.2 mm the resonance frequency simulated by temporal model (25.6 Hz) is close to the experimental one (25.8 Hz), but the shapes of both curves are different. An obvious resonance peak exists in the curve obtained with the 0-D model. For the large tube, the assumption of Poiseuille flow is certainly not valid.

Comparison of phase change evolution

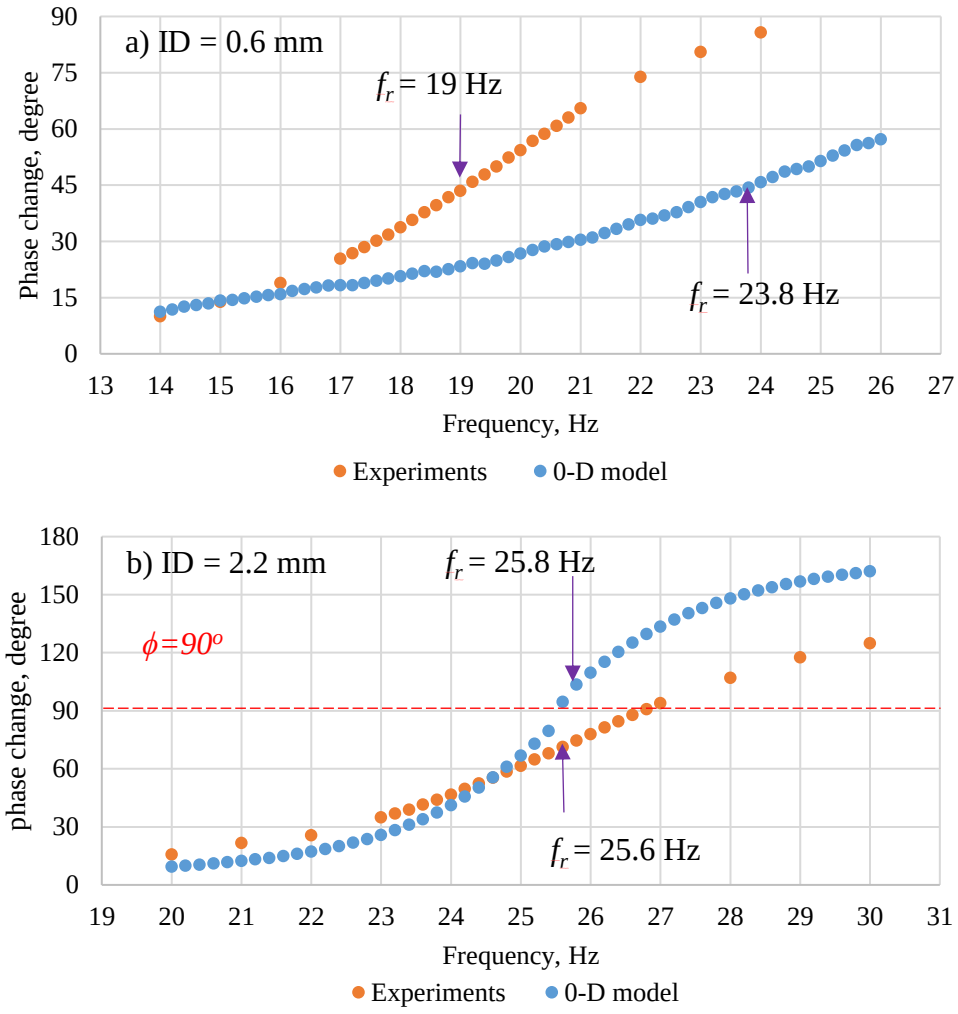

Figure 5-20 The contrast of phase change evolution between the 0-D model and experiments (a for ID 0.6 mm tube; b for ID 2.2 mm tube)

Figure 5-20 plots the evolution of phase change with the frequency for the 0-D model and the experiments. Whatever the tube diameter, the phase change increases with frequency, both for the experiment and for the model.

For the 0.6 mm tube, the numerical results start at the same level as the experimental points when the frequency is lower than 16 Hz. Then, the model depicts a smaller increase than the experimental ones. For both, the phase change remains lower than $\pi/2$. Note that the discrepancy between the model and the experiment is consistent with the gap already observed regarding the resonance frequency: the phase change is the same at the respective resonance frequencies.

For the 2.2 mm tube, the phase change increases slowly and linearly with the rise of the frequency for the experiments. The shape of the phase change is much steeper for the model. Its sigmoidal shape is consistent with the step resonance previously observed for the index amplitude. Even though the phase change amplitude is much larger for the model, the phase changes at the corresponding resonance frequency are both close to $\pi/2$. The shape difference of two curves is certainly due to the coarse assumption regarding viscous forces of the 0-D model.

To explore the effect of different parameters on the water behavior, we tested the effects of amplitude, viscosity, and difference between $\cos\theta_r$ and $\cos\theta_a$ for ID 2.2 mm tube in the 0-D model.

Effect of tube amplitude

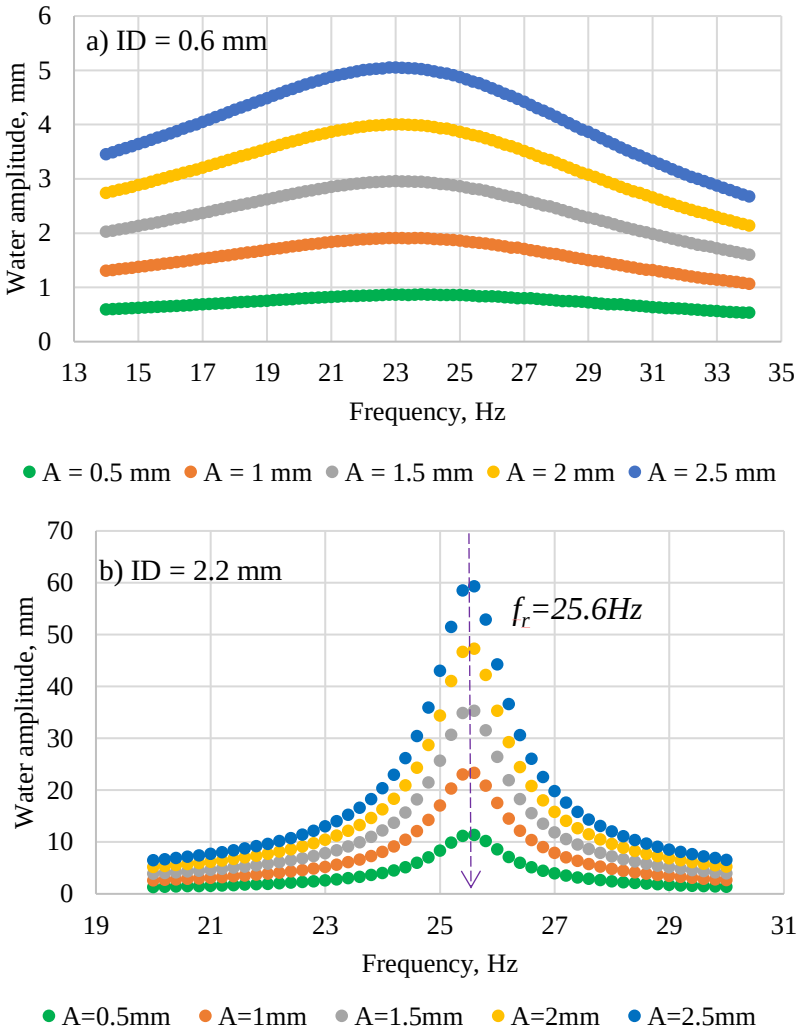

Figure 5-21 The variation of the water amplitude with frequencies under different tube amplitudes. (a. ID = 0.6 mm, A = 5~25 mm, f = 15-35 Hz with interval of 0.2 Hz ; b.ID = 2.2 mm, A = 5~25 mm, f = 20-30 Hz with interval of 0.2 Hz)

Figure 5-21 shows the water amplitude evolution with frequency under different tube amplitudes. The tube amplitude results in a slight resonance frequency shift for system in small tube, but does not influence the resonance frequency of the system in large tube. The water amplitude however increases with the tube amplitude due to the increasing volumetric change of the blocked air. Indeed, except for the capillary forces, all forces involved in the 0-D model are linear: consistently, the amplitude curves are almost proportional to the tube amplitude.

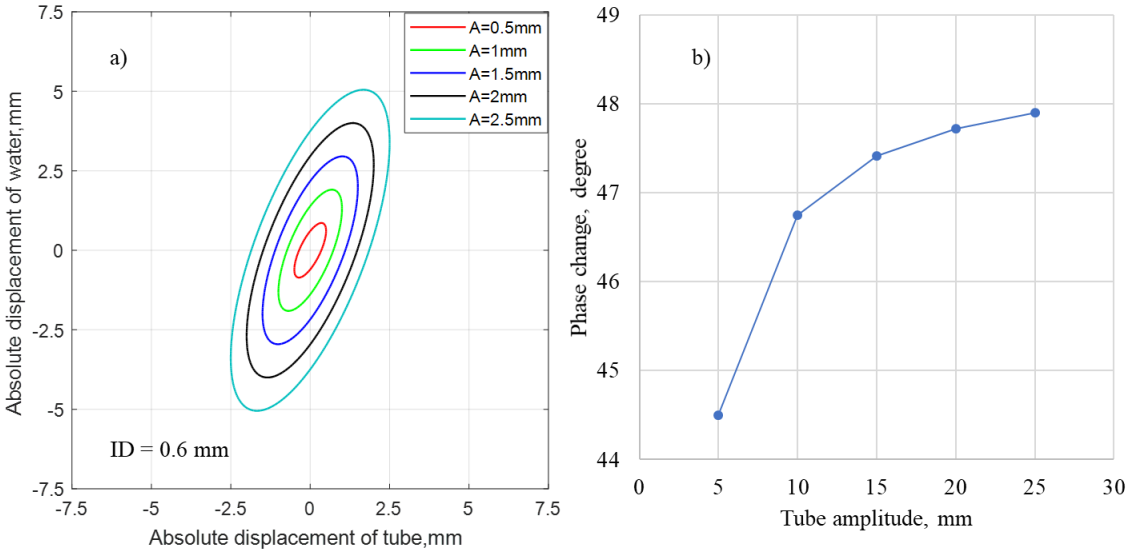

Figure 5-22 Lissajous curves and phase change between water motion and tube motion with respect to the tube amplitude (ID = 0.6 mm, f_r = 23.8 Hz; a. Lissajous curves; b. phase change)

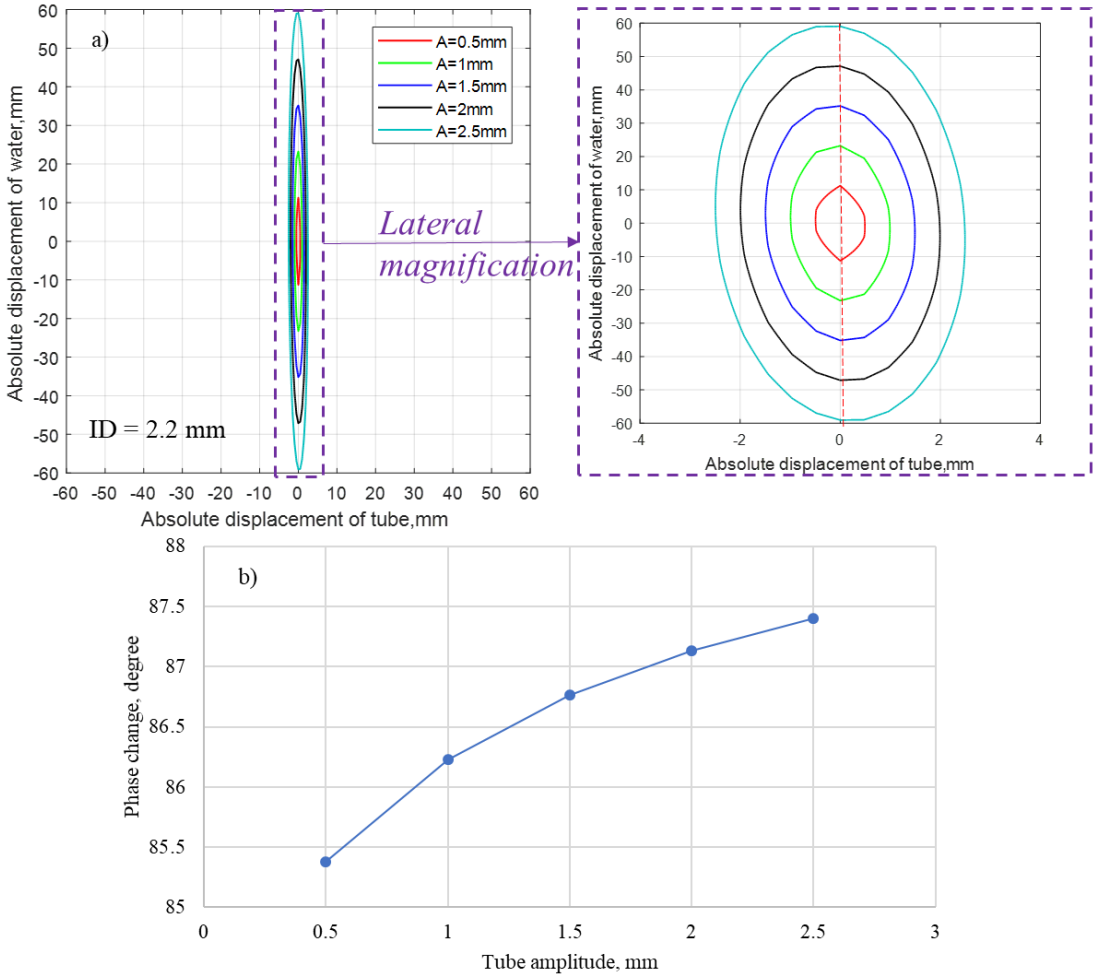

Figure 5-23 Lissajous curves and phase change between water motion and tube motion with respect to the tube amplitude (ID = 2.2 mm, f_r = 25.6 Hz; a. Lissajous curves; b. phase change)

Figure 5-22 and Figure 5-23 exhibit the Lissajous curves and phase change for different tube amplitudes in 0.6 mm tube and 2.2 mm tube, respectively. We can observe that the slopes of the main axis of the Lissajous curves are similar. The phase change increases slightly with the rise of the tube amplitude. This fact confirms the quasi-linear behavior of the model (all forces are linear but the capillary forces).

Effect of the viscosity

Table 5-9 Dynamic viscosity of water at different temperature[234]

T, ºC	10	20	30	40
μ, mPas	*1.307*	*1.002*	*0.797*	*0.653*

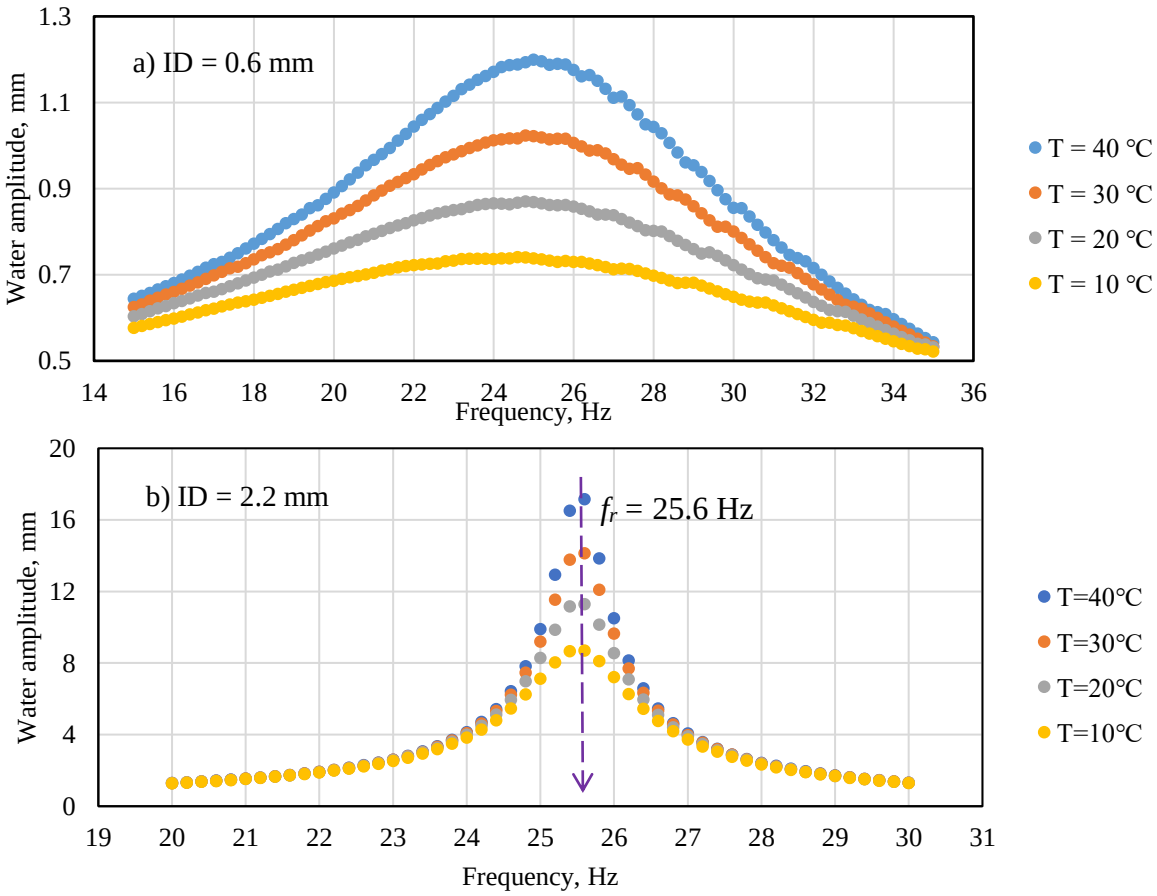

Figure 5-24 The evolution of water amplitude-frequency curves with viscosity (a. ID = 0.6 mm, A = 0.5 mm, f = 15-35 Hz with an interval of 0.2 Hz ; b. ID = 2.2 mm, A = 0.5 mm, f = 20-30 Hz with an interval of 0.2 Hz).

We choose the dynamic viscosities of water at five different temperatures to test its effect on water behavior. The relationship between the viscosity and the temperature is listed in Table 5-9. The effect of viscosity on the water amplitude is obvious, with a clear decrease of water amplitude as the viscosity increases (Figure 5-24). The effect is remarkable especially near the resonance frequency. Because the increase of the viscosity results in a higher viscous force between the capillary inner wall and the water index. the water motion is further damped.

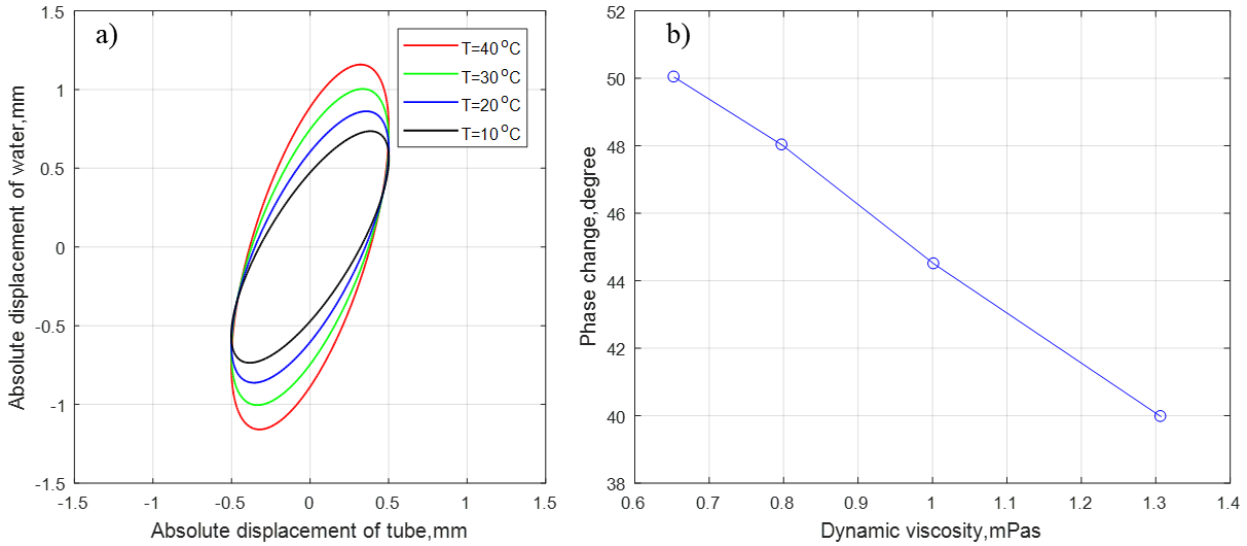

Figure 5-25 Lissajous curves and phase change as a function of dynamic viscosity (ID = 0.6 mm, A = 0.5 mm, f = 23.8 Hz; a. Lissajous curves; b. phase change).

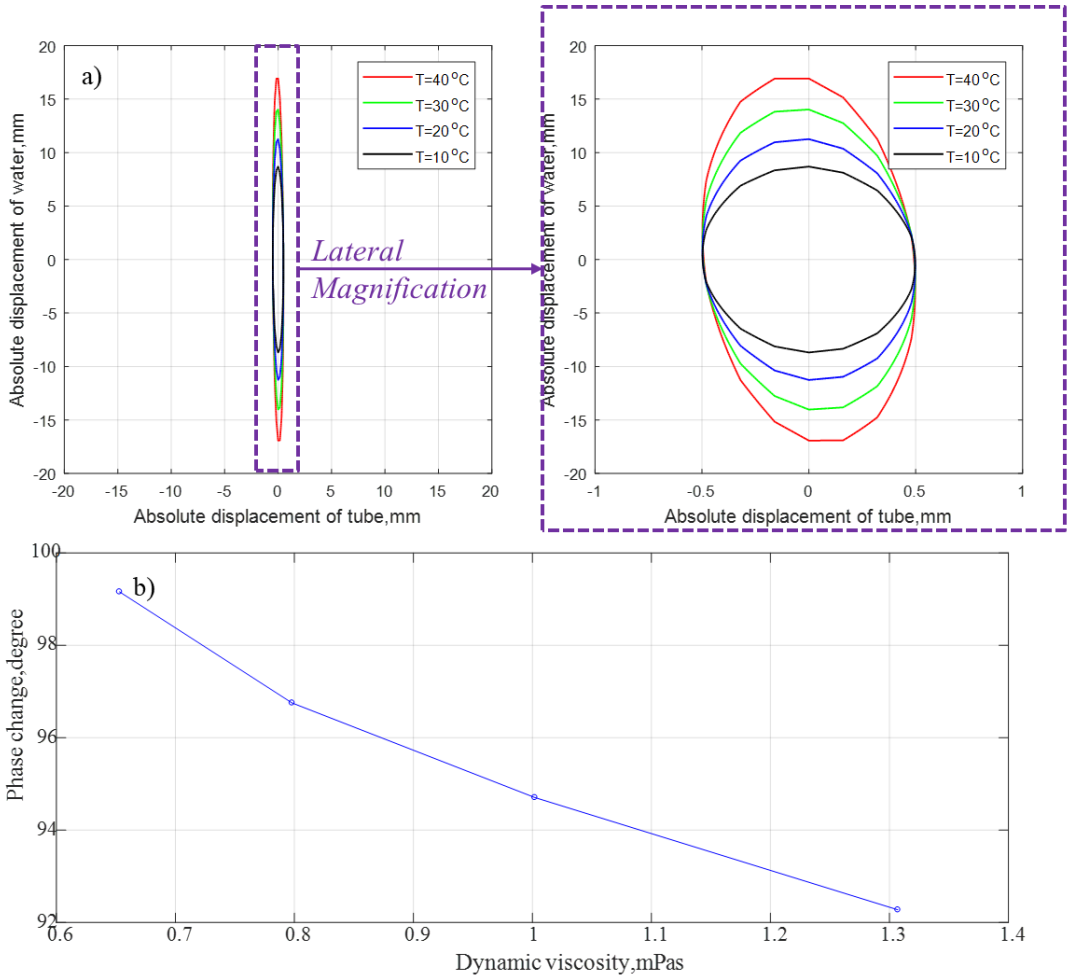

Figure 5-26 Lissajous curves and phase change as a function of dynamic viscosity (ID = 2.2 mm, A = 0.5 mm, f = 25.6 Hz; a. Lissajous curves; b. phase change).

Figure 5-25 and Figure 5-26 present the Lissajous curves and the corresponding phase change for the 0.6 mm tube and the 2.2 mm tube, respectively, under different dynamic viscosities. The slope of the main axis of the Lissajous curves seems to be obviously impacted by viscosity in 0.6 mm tube but be less affected by viscosity in 2.2 mm tube. In both figures, the phase change decreases gradually with the rise of viscosity. It is due to the decrease of the inertia. We have known that, in addition to the decrease of water amplitude decreases, the resonance frequency also decreases with the increase of viscosity. This is likely to explain the shift in phase change.

Effect of the contact angle

Table 5-10 Selected values of advancing and receding contact angles and the absolute difference of their cosine values

θ_a	θ_r	$cos\theta_r - cos\theta_a$
40 °	*4 °*	*0.024*
50 °	*4 °*	*0.038*
60 °	*4 °*	*0.054*
70 °	*4 °*	*0.074*
80 °	*4 °*	*0.097*

As described in the model, we can know that the capillary force is determined by $\cos\theta_r$-$\cos\theta_a$ and the surface tension. We selected a set of different values to test the effect of the capillary forces (Table 5-10).

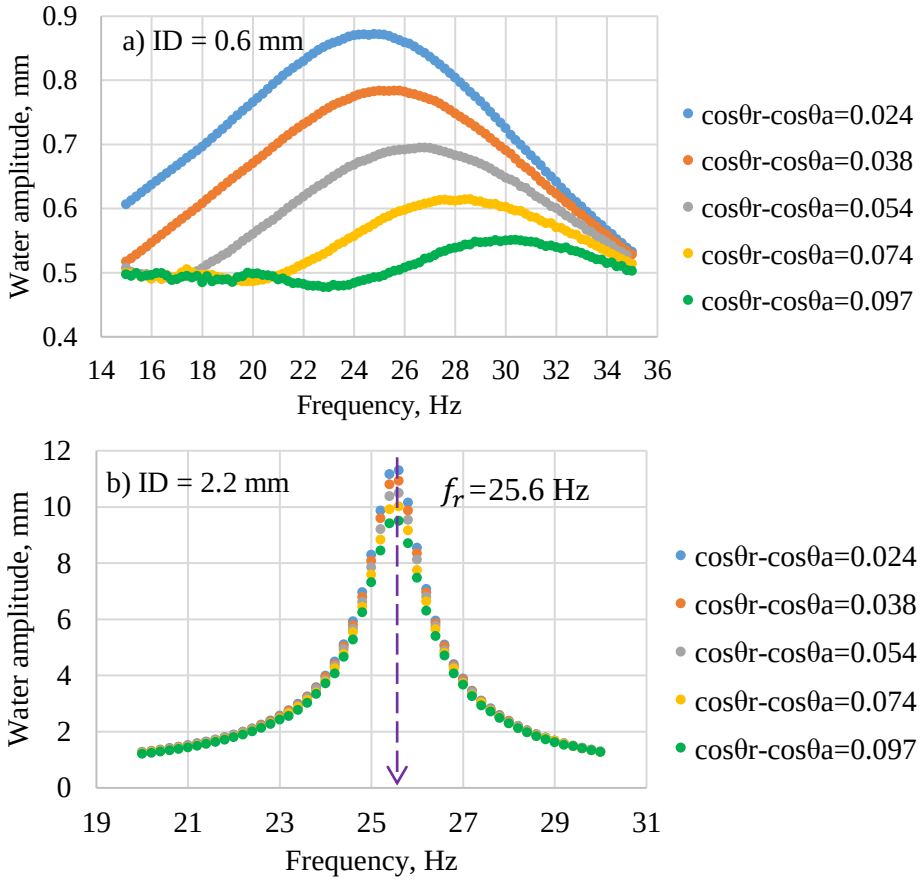

Figure 5-27 The water amplitude-frequency curves for different values of $\cos\theta_r$-$\cos\theta_a$ (a. ID = 0.6 mm; b. ID = 2.2 mm)

Figure 5-27 plots the effect of the hysteresis in contact angle on the water amplitude in the two types of tubes. Primarily, one can see that the absolute difference between $\cos\theta_r$ and $\cos\theta_a$ significantly impacts the resonance frequency in the small tube, but does not impact the resonance frequency in the large tube. Indeed, the capillary force is inversely proportional to the inner diameter of tube. It means that the capillary force will be greater compared with the inertia in the small tube, and hinder the water motion. But in large tube, the capillary force is relatively weaker compared with the inertia. With the increase in the contact angle difference, the water amplitude decreases slightly as a direct effect of the rise in capillary forces.

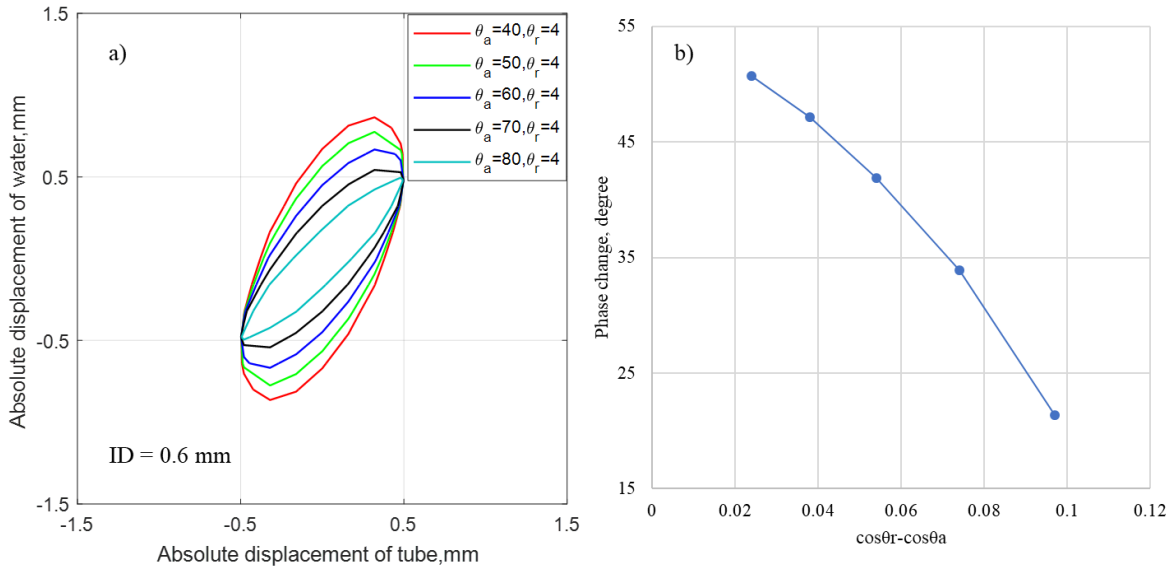

Figure 5-28 Lissajous curves and phase change with respect to ($\cos\theta_r$-$\cos\theta_a$) (ID = 0.6 mm, A = 0.5 mm, f = 23.8 Hz; a. Lissajous curves; b. phase change)

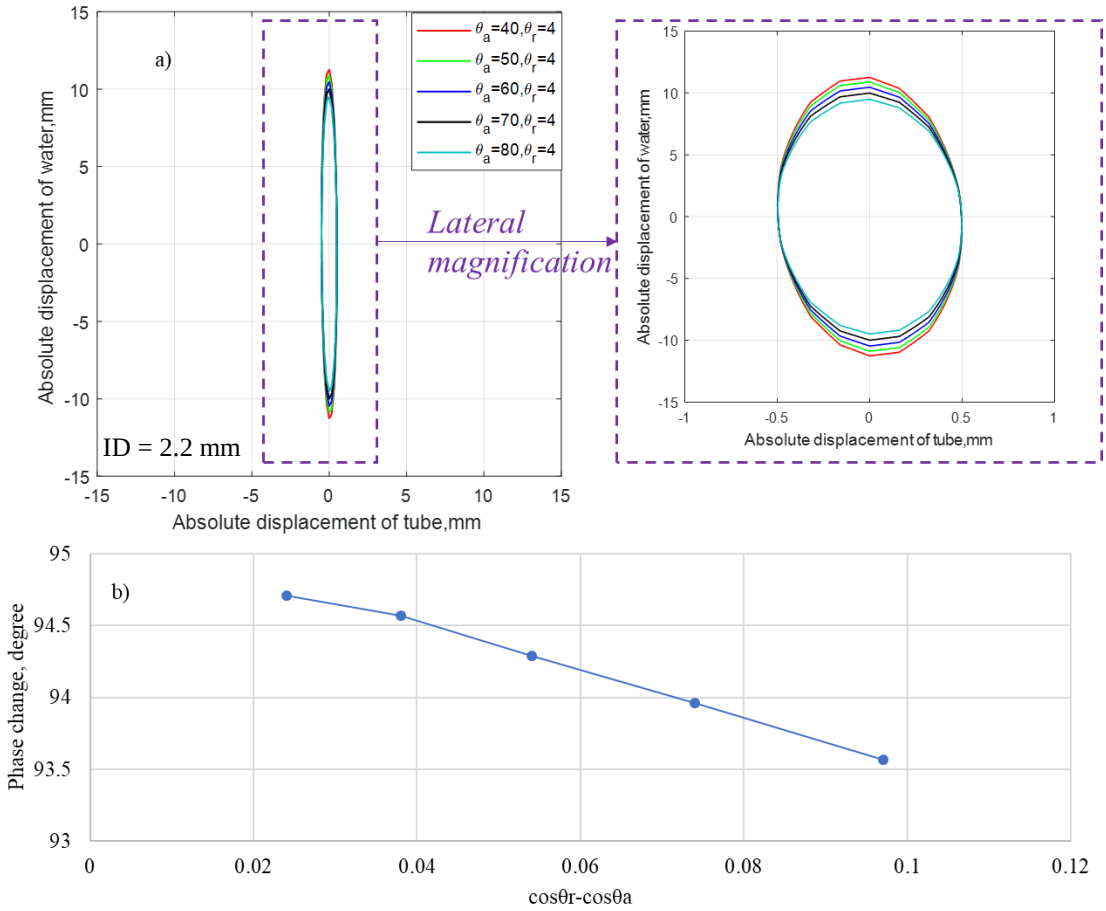

Figure 5-29 Lissajous curves and phase change with respect to ($cos\theta_r$-$cos\theta_a$) (ID = 2.2 mm, A = 0.5 mm, f = 25 Hz; a. Lissajous curves; b. phase change)

Figure 5-28 and Figure 5-29 plot the Lissajous curves and phase change for the 0.6 mm ID tube and the 2.2 mm ID tube with different values of $cos\theta_r$-$cos\theta_a$. The change of the orientation of the Lissajous curves is obvious for the small tube but not obvious for the large one. For the phase change, we can know the effect is remarkable in the small tube (Figure 5-28b), but only little change can be found in the large tube (Figure 5-29b). This is due to a lower ratio of capillary force over inertia.

5.3.2 Spatial-temporal evolution: the 1-D model

In this section, besides the temporal description, the absolute displacement of the water index will be spatially studied along the radius *r*.

5.3.2.1 Spatial discretization

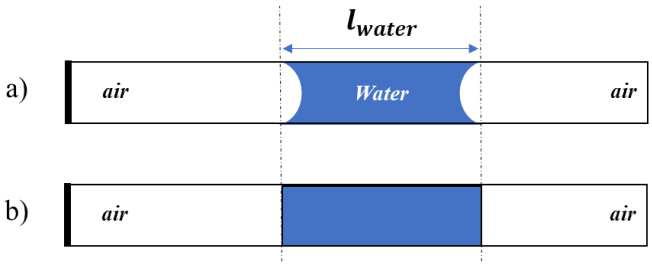

Figure 5-30 Schematic diagram of water index inside the capillary tube with asymmetrical geometry (a. realistic projection; b. simplified projection)

To simplify the model, we assume that the capillary forces are neglected, so the profile of the meniscus is flat and, according to *r*, the length of the water index is constant, equals to l_{water}. Based on these assumptions, the projection of the water index is simplified as shown in Figure 5-30. During vibration, we assume that there is no internal recirculation. Therefore, the length of the water index is constant whatever the radius, equals to l_{water}.

We can discretize the water index along the radius using the control volume approach (Figure 5-31).

From the axis of the water index (also the axis of the tube) to the internal wall, we set *n* interval, hence n+1 control volumes whose position are represented by the red points in the figure. The distance between two adjacent points is $\Delta r = \frac{r}{n}$.

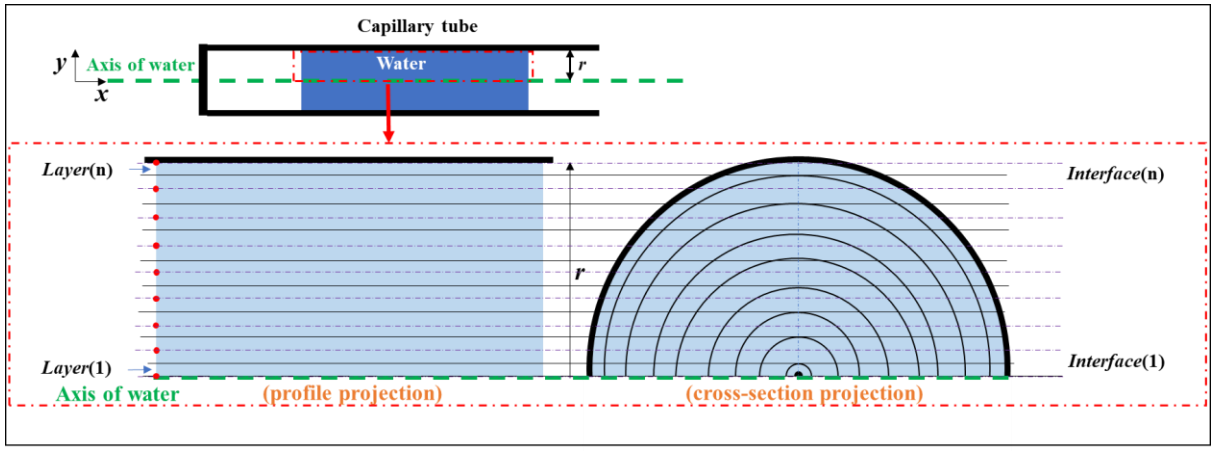

Figure 5-31 Spatial discretization of the water index

The control surface between two control volume is represented by the black full-lines. The contact surface between water and tube is the external control surface where the boundary conditions will be applied. The thickness of each control volume is $\frac{r}{n}$, except the tow external CVs for which the thickness equals $\frac{r}{2n}$.

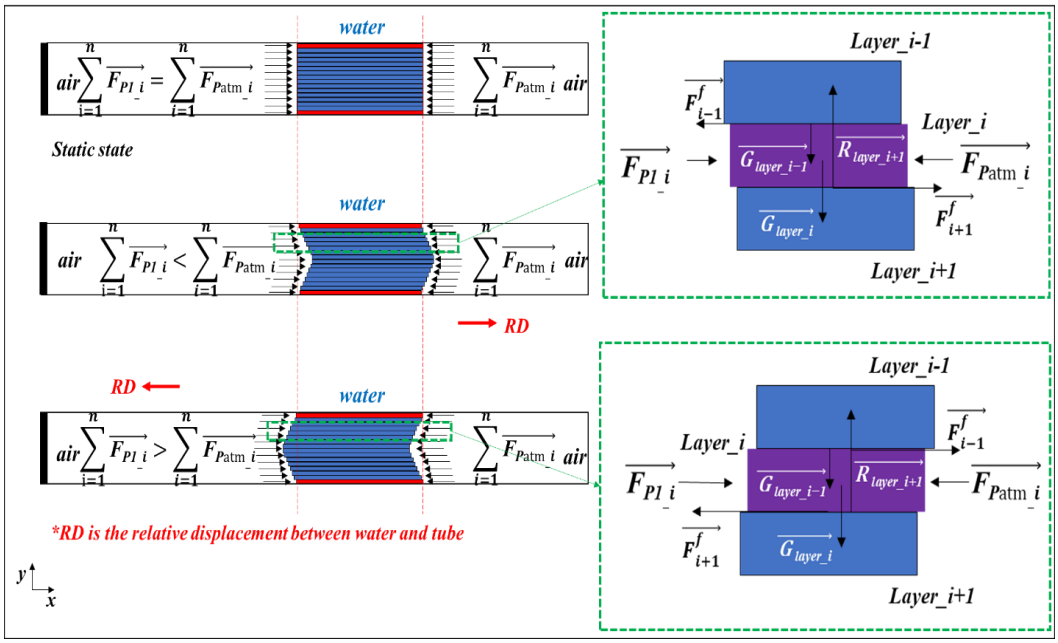

Figure 5-32 Force analysis of spatial-temporal model

Based on this spatial discretization, we can make force analysis for each CV. The blue ones represent the other part of the water index. Figure 5-32 gives the force analysis of one of the intermediate CV. According to the second Newton's law, we have:

$$m_i\overrightarrow{a_{water\_i}} = \overrightarrow{F_i} = \overrightarrow{G_{layer\_i}} + \overrightarrow{G_{layer\_i\text{-}1}} + \overrightarrow{R_{layer\_i+1}} + \overrightarrow{F_{P1\_i}} + \overrightarrow{F_{Patm\_i}} + \overrightarrow{F^f_{i-1}} + \overrightarrow{F^f_{i+1}}$$

Equation 5-33

where $\overrightarrow{F_i}$ is the resultant force on layer *i*; m_i is the mass of the layer *i*, equals to:

$$m_i = \rho_{water} V_i$$ Equation 5-34

V_i is the volume of layer *i*, given as

$$V_i = S_i l_{water}$$ Equation 5-35

S_i is the surface of the cross-section of each layer equals to:

$$S_i = \pi({r_{i+1}}^2 - {r_i}^2)$$ Equation 5-36

r_i is the position of each intermediate interface, as:

$$r_i = \frac{r}{2n} + \frac{r}{n}(i-2)$$ Equation 5-37

where *i* is the index of the interface and $2 \leq i \leq$ n 2. $r_1 = 0$ and $r_{n+1} = r$.

$\overrightarrow{G_{layer\_i}}$ is the weight of layer *i*, equals to:

$$\overrightarrow{G_{layer\_i}} = \rho_{water}\pi(r_{i+1}^2 - r_i^2) l_{water}\,\vec{g}$$ Equation 5-38

The force balance will be projected on the x-axis later. As the weight is purely vertical, it is not required to go further in the analysis of the interaction of the gravity forces between CVs.

$\overrightarrow{F_{P1\_i}}$ is the force from the blocked air acting on the layer *i*, $\overrightarrow{F_{Patm\_i}}$ is the force from the atmosphere acting on the layer *i*, we have:

$$\overrightarrow{F_{P1\_i}} + \overrightarrow{F_{Patm\_i}} = \frac{P_{atm}.S_i}{l_{air}(t=0)} \Delta l_{air}\,\overrightarrow{u_x}$$ Equation 5-39

Δl_{air} is the length change of the blocked air, it is assumed as the difference between the absolute displacement of the tube and the volumetric averaged displacement of the water index, as:

$$\Delta l_{air} = (x_{tube} - \overline{x_{water}})$$ Equation 5-40

x_{tube} is the absolute displacement of the tube:

$$x_{tube} = A_{tube}\sin(\omega t) \qquad \text{Equation 5-41}$$

$\overline{x_{water}}$ is the averaged displacement of the water index, it is given by:

$$\overline{x_{water}} = \frac{\sum x_i S_i}{S} \qquad \text{Equation 5-42}$$

Where S is the cross-section of the tube, x_i is the displacement of layer *i* and S_i the cross-section area of layer *i*, given by

$$S_i = \pi(r_{i+1}^2 - r_i^2) \qquad \text{Equation 5-43}$$

Then we can have

$$\overrightarrow{F_{P1\_i}} + \overrightarrow{F_{Patm\_i}} = \frac{P_{atm}.S_i}{l_{air}(t=0)}\left(\overrightarrow{x_{tube}} - \overrightarrow{\overline{x_{water}}}\right) \qquad \text{Equation 5-44}$$

$\overrightarrow{F_{i-1}^f}$ is the viscous force between layer *i* and layer *i*-1, calculated as a first order approximation of the shear stress

$$\overrightarrow{F_{i-1}^f} = \frac{2\pi\frac{(r_i + r_{i-1})}{2}\mu l_{water}(\overrightarrow{v_{i-1}} - \overrightarrow{v_i})}{\Delta r} \qquad \text{Equation 5-45}$$

where $\overrightarrow{v_{i-1}}$ and $\overrightarrow{v_i}$ are the velocity of layer *i*-1 and *i* respectively.

$\overrightarrow{F_{i+1}^f}$ is the viscous force between layer *i* and layer *i*+1, evaluated following the same approximation.

As already stated, the force balance is projected along the x-axis:

$$m_i a_{water\_i} = F_i = \frac{2\pi\frac{(r_i + r_{i-1})}{2}\mu l_{water}(v_{i-1} - v_i)}{\Delta r} + \frac{2\pi\frac{(r_{i+1} + r_i)}{2}\mu l_{water}(v_i - v_{i+1})}{\Delta r} + \frac{P_{atm}.\pi(r_{i+1}^2 - r_i^2)}{l_{air}(t=0)}(x_{tube} - \overline{x_{water}}) \qquad \text{Equation 5-46}$$

Then, the acceleration of layer *i* can be obtained as:

$$a_{water\_i} = \frac{F_i}{m_i} = \frac{2\pi\frac{(r_i + r_{i-1})}{2}\mu(v_{i-1} - v_i) + 2\pi\frac{(r_{i+1} + r_i)}{2}\mu(v_i - v_{i+1})}{\Delta r\rho_{water}(r_{i+1}^2 - r_i^2)} + \frac{P_{atm}\left(x_{tube} - \frac{\sum x_i S_i}{S}\right)}{l_{air}(t=0)\cdot\rho_{water} l_{water}} \quad \text{Equation 5-47}$$

To calculate the displacement of each layer *i* (x_i), we need a time integration.

5.3.2.2 Time integration

The time integration is achieved by the second-order explicit Newton's approach[232].

According to this approach, the displacement of layer *i* at time $t+\Delta t$ is given by:

$$x_i(t + \Delta t) = x_i(t) + \frac{v_i(t) + v_i(t+\Delta t)}{2}\Delta t \quad \text{Equation 5-48}$$

The velocity of layer *i* at time $t+\Delta t$ is given by:

$$v_i(t + \Delta t) = v_i(t) + \frac{a_i(t) + a_i(t+\Delta t)}{2}\Delta t \quad \text{Equation 5-49}$$

The acceleration of the other layers at time *t* is given as:

$$a_i(t) = \frac{F_i(t)}{m_i} = \frac{2\pi\frac{(r_i + r_{i-1})}{2}\mu\big(v_{i-1}(t) - v_i(t)\big) + 2\pi\frac{(r_{i+1} + r_i)}{2}\mu\big(v_i(t) - v_{i+1}(t)\big)}{\Delta r\rho_{water}(r_{i+1}^2 - r_i^2)} + \frac{P_{atm}\left(x_{tube}(t) - \frac{\sum x_i(t) S_i}{S}\right)}{l_{air}(t=0)\cdot\rho_{water} l_{water}} \quad \text{Equation 5-50}$$

$$a_i(t + \Delta t) = \frac{F_i(t + \Delta t)}{m_i} = \frac{2\pi\frac{(r_i + r_{i-1})}{2}\mu\big(v_{i-1}(t + \Delta t) - v_i(t + \Delta t)\big)}{\Delta r\rho_{water}(r_{i+1}^2 - r_i^2)} + \frac{2\pi\frac{(r_{i+1} + r_i)}{2}\mu\big(v_i(t+\Delta t) - v_{i+1}(t+\Delta t)\big)}{\Delta r\rho_{water}(r_{i+1}^2 - r_i^2)} + \frac{P_{atm}\left(x_{tube}(t+\Delta t) - \frac{\sum x_i(t+\Delta t) S_i}{S}\right)}{l_{air}(t=0)\cdot\rho_{water} l_{water}} \quad \text{Equation 5-51}$$

At time $t + \Delta t$, the velocity and displacement of each layer except the boundary layer is initially calculated by the first-order Newton's approach as:

$$v_i(t + \Delta t) = v_i(t) + a_i(t)\Delta t \quad \text{Equation 5-52}$$

$$x_i(t + \Delta t) = x_i(t) + v_i(t)\Delta t \quad \text{Equation 5-53}$$

To compute the shear stress at the inner wall, we assume the absence of slip flow:

$$x_n(t) = x_{tube}(t) = A_{tube}\sin(\omega t) \quad \text{Equation 5-54}$$

$$v_n(t) = x_{tube}(t) = \omega A_{tube}\cos(\omega t) \quad \text{Equation 5-55}$$

with the initial value $v_i(t = 0) = \omega A_{tube}$, and $x_i(t = 0) = 0$

To ensure convergence, the time interval should be smaller than the characteristic diffusion time (τ) [235], which is given by $\tau = \frac{\rho r^2}{\mu}$. We assumed that $\Delta t = 0.5\frac{\rho(r/n)^2}{\mu} < \tau$.

5.3.2.3 Numerical results with the 1-D model

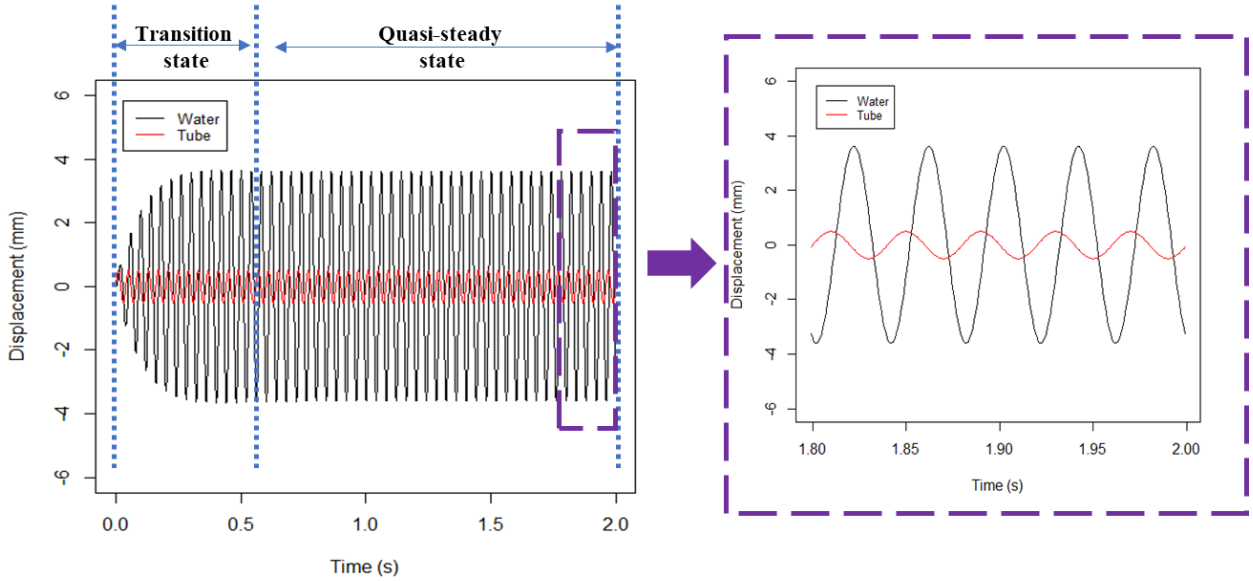

Figure 5-33 The displacement of water and tube simulated by the 1-D model (ID = 2.2 mm, A = 0.5 mm, f = 25 Hz)

By the 1-D model, we can get the variation of the mean displacement of the water index according to time. Figure 5-33 gives an example of simulation, using the parameter values summarized in Table 5-11. The mean displacement is an averaged value given by Equation 5-42.

Table 5-11 Parameters for the spatial-temporal model

ID	l_{water}	$l_{air}(t=0)$	*Dynamic viscosity (μ)*	*f*	*A*	*Time step*	*n*
2.2 mm	*76 mm*	*51 mm*	*1.002 mPa/s*	*20 ~ 30 Hz*	*0.5 mm*	$0.5\frac{\rho(r/n)^2}{\mu}$	50

As for the 0-D model, the simulation predicts the transition state needed to reach an established vibration regime. Thanks to this 1-D model, the displacement field can also be plotted at different times for further analysis. The established regime is used for that purpose.

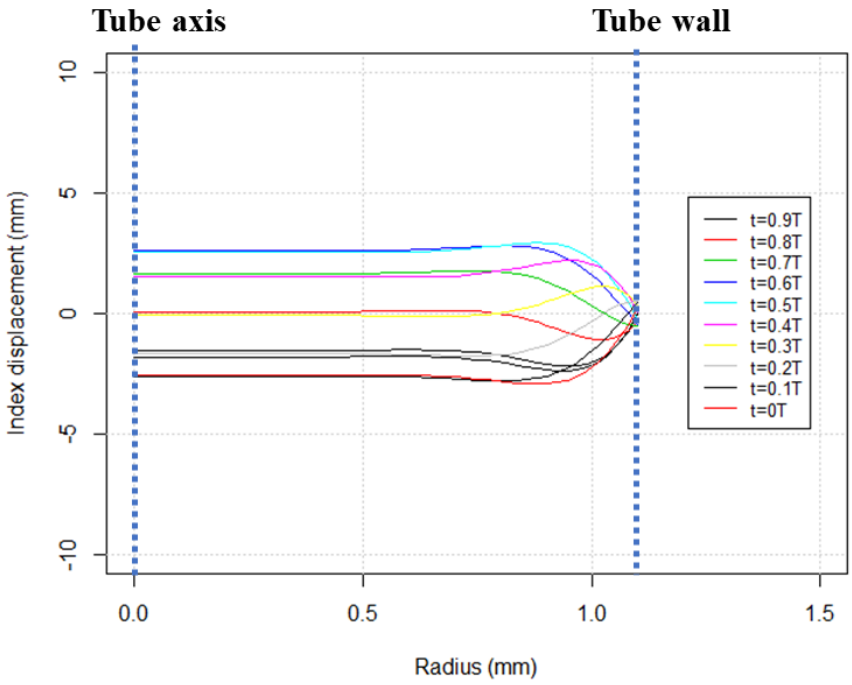

Figure 5-34 The displacement field along the radius at various instants (ID = 2.2 mm, A = 0.5 mm, f = 25 Hz)

One of the improvements of the 1-D model is that, the evolution of meniscus can be predicted due to the spatial discretization. It allows also the viscous effect at the inner wall to be captured, even though the profile is not at equilibrium along the radius. In Figure 5-34, we selected 10 instants regularly spread over one period.

It provides an intuitive way to observe the evolution of the meniscus during vibration. It shows a good consistency with what we observed from the experiment. The water displacement in the center part is much larger than that near the inner wall. In Figure 5-34, one can find a part near the tube wall with an amplitude higher than that in the center. It may be due to the neglecting of contact angle and surface tension.

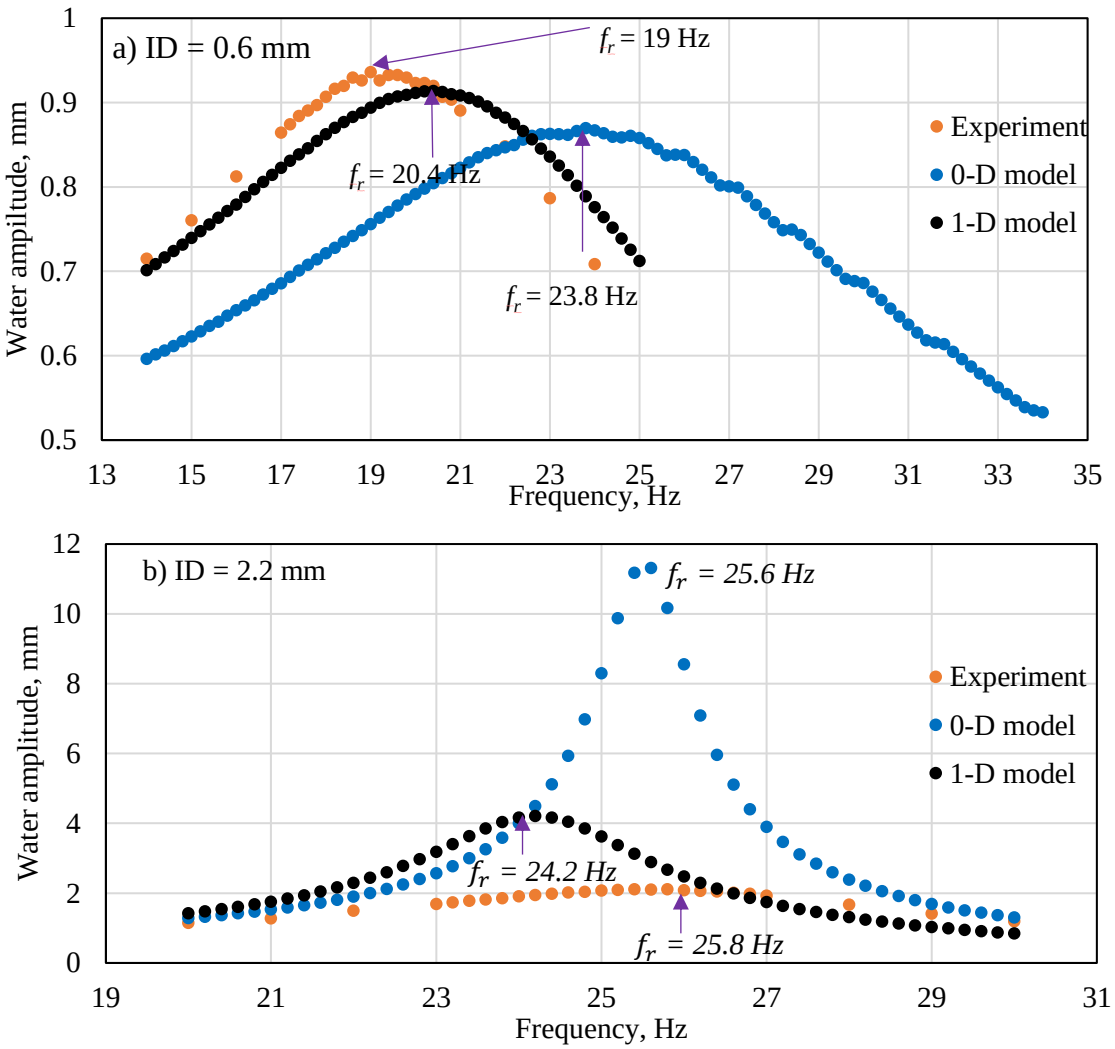

Figure 5-35 The water amplitude versus frequency / comparison of experimental and numerical results. (a for ID 0.6 mm tube; b for ID 2.2 mm tube)

Figure 5-35 plots the water amplitude versus frequency for the 0-D model, 1-D model and the experiment. The trends of the simulated results in 1-D model is in a reasonably good agreement with the experimental results.

For the small tube (Figure 5-35a), the water amplitude evolutions in numerical and experimental results are very similar. The simulated resonance frequency (20.4 Hz) is slightly higher than the experimental one (19 Hz), but the curves are almost superposed. We can find an obvious improvement in the 1-D model compared with the 0-D model.

For the large tube (Figure 5-35b), the water amplitude from 1-D model (4 mm) is significantly higher than that in the experiments but much lower than that in 0-D model (12 mm). The resonance frequency (24.2 Hz) obtained from the 1-D model is lower than the experimental result. The difference may be due to large capillary force when the meniscus near the interface undergoes large deformations.

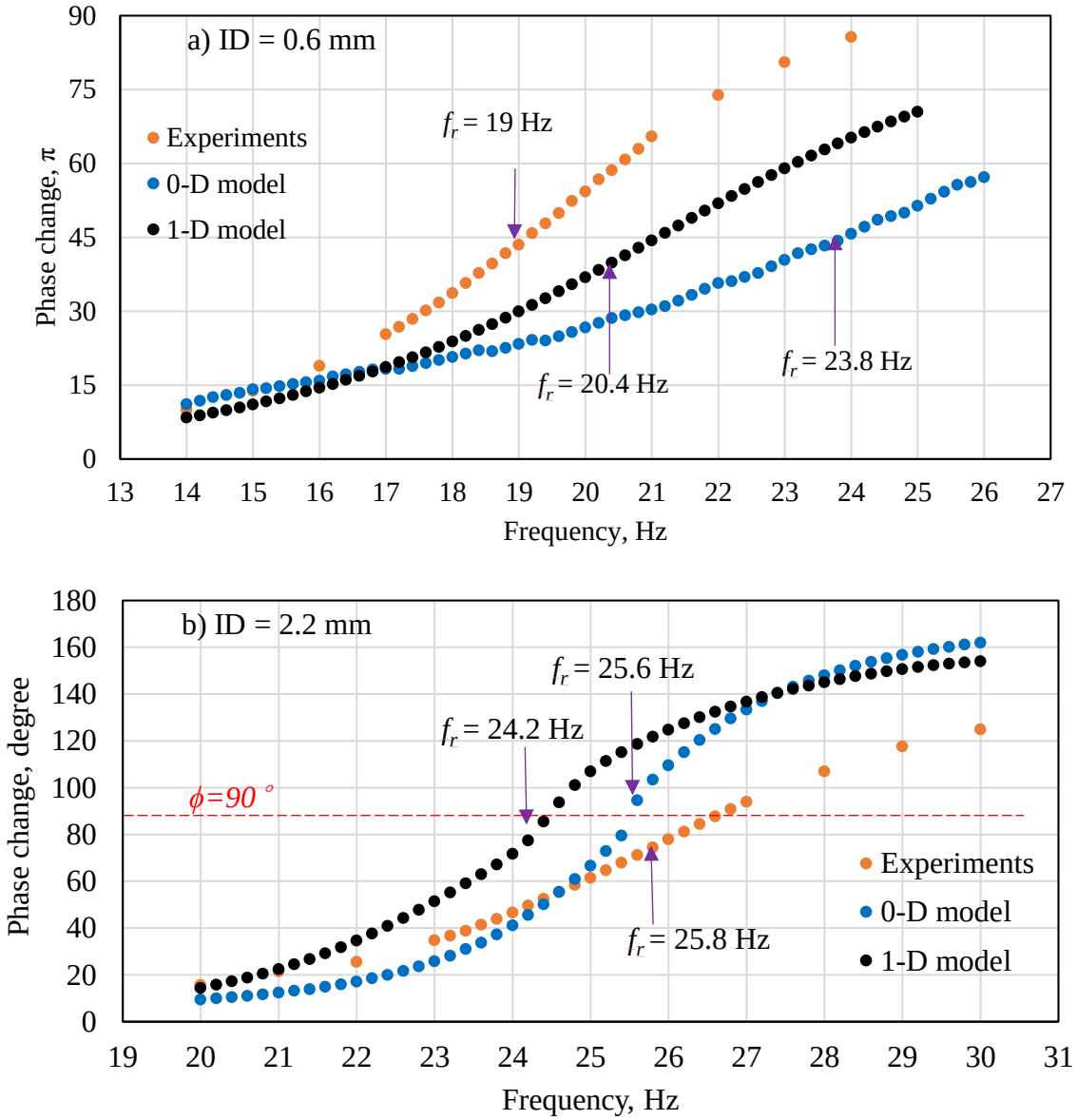

Figure 5-36 The phase change between the water-motion and the tube-motion obtained by experimental and numerical methods (a for ID 0.6 mm tube; b for ID 2.2 mm tube)

Figure 5-36 shows a comparison of the phase change evolution with respect to frequency for experiments, 0-D model and 1-D model. The phase change is obtained by analyzing the Lissajous curves.

For the small tube, the numerical results depict a trend similar to the experimental ones. But the results from the 1-D model is closer to the experimental ones compared with that from 0-D model. The model is just a little beneath the experiment all over the frequency range. The phase changes at the corresponding resonance frequencies are about the same. The little difference of curves due to the similar shape of the amplitude-frequency curves with a slight shift of the resonance frequency.

For the large tube, again, the discrepancy between simulation and experiment is more pronounced. Consistently with a higher resonance peak, the phase change spread over a much higher range than the experimental results. Again, we guess that the large change of contact angle due to the high shear rate of water near the tube wall is likely to explain the difference between the model and the experiment.

5.3.3. Summary of models

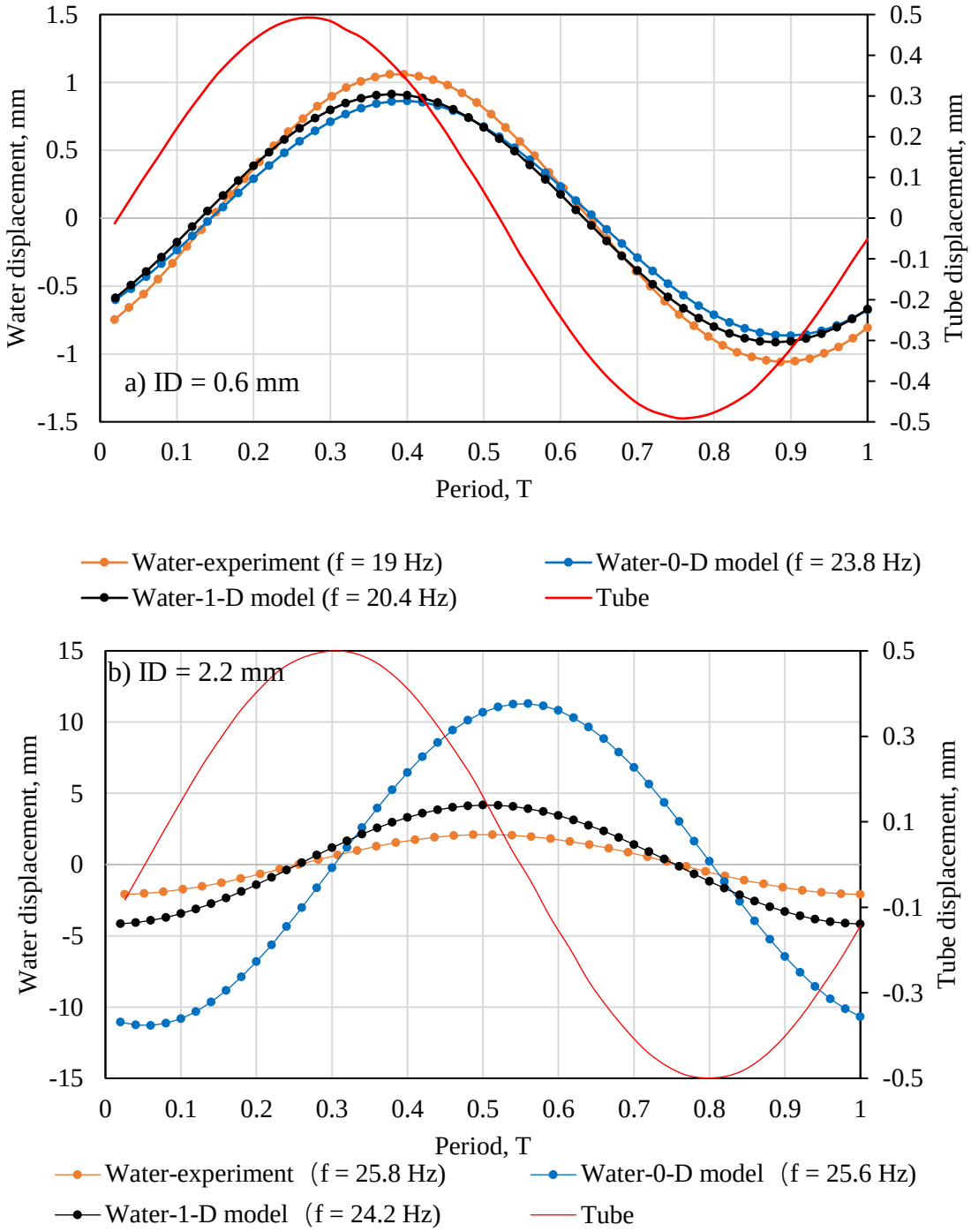

Figure 5-37 The displacement of tube and water in experiment and two models at resonance frequency over one period (a. ID = 0.6 mm, A = 0.5 mm ; b. ID = 2.2 mm, A = 0.5 mm)

Here, we compared the results at the corresponding resonance frequencies in two tubes (respectively 19 Hz ,23.8 Hz, and 20.4 Hz for the experiment and the 0-D and 1-D models for the small tube; 25.8 Hz, 25.6 Hz and 24.2 Hz for the experiment and the 0-D and 1-D models for the large tube), as shown in Figure 5-37. In both tubes, the displacement is much better predicted for the 1-D model, which confirms the importance of accounting for the unsteady regime near the tube wall.

In the Figure 5-37a, one can find that the results from both models at resonance frequency are almost similar to the experimental ones, in aspect of both amplitude and phase change. But the prediction results in the large tube is not as good as in the small one.

It can be summarized that the 1-D model is therefore much better in its prediction than the 0-D mode: the predictions are now quite good for the small tube and, for the large tube, the resonance peak is much smaller with the 1-D model.

5.4 Conclusions and perspectives

In this chapter, to simulate dead-end pores of a porous medium containing water, an asymmetrical configuration was studied. One end of the tube was closed to form a spring-mass system, composed of the blocked air and the water index. We performed two series of experiments for two tube sizes, over a frequency range able to capture the resonance frequency. We found that the resonance frequency for ID 0.6 mm tube is 19 Hz, and the one for ID 2.2 mm tube is 25.8 Hz. The resonance frequency is close to the prediction of a simple spring-mass system for the large tube but much smaller for the small tube (with the simple model, the resonance frequency does not depend on the tube diameter). The viscous effects are therefore quite important for the small tube.

We compared the water evaporation with this asymmetrical configuration with the symmetrical

configuration studied in the previous chapter. An interesting result should be noticed: thanks to the resonance, which produces an amplitude more than 3 times higher, the evaporation rate for the asymmetrical configuration is about 2.4 times that of the symmetrical one, even though the asymmetrical configuration has just one open end. Consistently, the amplitude of the curvature radius is also much higher for the asymmetrical configuration.

To better understand the interaction between all forces involved in this system, we proposed a stepwise computational approach:

- A 0-D model, able to account for the change of contact angle, by assuming an established velocity profile along the radius
- A 1-D model, that accounts for the actual shear rate at the inner wall, but neglects the capillary forces.

Both models, written in R, use second-order explicit Newton method for time integration. The 1-D model is based on the control volume method.

As a short summary, we found that the 0-D model is able to capture quite nicely the trends observed for the small tube. For the range of frequency studied, the assumption of an established velocity field along the radius is relevant. This is not the case for the large tube.

The 1-D model is much better in its prediction: it allows the simulations of the small tube to be very close to the experiment. In spite of a clear improvement compared to the 0-D model, the 1-D model is not as good for the large tube.

This fact opens some short-term perspectives: to try to include the surface tension in the 1-D model to improve its prediction. This could be done just by adding a surface tension term between successive layers, as a result of their difference in displacement.

Obviously, a full asymmetrical model, with full treatment of the meniscus shape would be even better, but it would require a full shape optimization to be implemented in a 2-D model, which is a huge task.

Chapter 6 Conclusions and perspectives

6.1 General conclusions

The main objective of this thesis was to study the effect of parameters of sinusoid vibrations (amplitude and frequency) on the water behavior (water amplitude, phase change, and evolution of meniscus curvature radius) inside capillary tubes with symmetrical and asymmetrical geometries.

The main contributions and conclusions are summarized as below:

In this study, we built an experimental device which is efficient and easy to use. The selected camera and the objectives can provide a high image quality. The strict protocol was made to make sure the repeatability of the experiments. The chosen parameters can make sure the obtained images are relevant and easy to process. Moreover, an image processing and analyzing method was developed with the function of identifying the variation of the air/water interface and the motion of the capillary tube.

In the study of water behavior in a symmetrical configuration, sinusoid vibrations are verified as an efficient way to intensify the evaporation compared with that in a static capillary tube. With this study, we have known that how the signal amplitude and frequency may intensify the drying process of the porous media. The process may be intensified by (1) the pumping effect (through the amplitude of the water relative displacement); (2) the increasing external transfer coefficients close to the meniscus, due to the periodic deformations of the water index; (3) the viscous dissipation, which is also due to the deformations of the water index.

In the study of water behavior in an asymmetrical configuration, it was first surprising to find that the sinusoid vibrations have a more intensification effect on the evaporation compared to symmetrical configuration even if only one end of the tube is open. It may be due to (1) a much

higher amplitude of relative displacement between tube and water index (increasing the pumping effect); (2) a much higher amplitude of the curvature radius due to resonance of the system. To better understand the interaction between all forces involved in this system, we proposed two models: (1) 0-D model, which is able to account for the change of contact angle, by assuming an established velocity profile along the radius, which is discretized in time according a second-order explicit Newton scheme; (2) 1-D model, that can account for the actual shear rate at the inner wall, and is built using the control volume method. The simulation results show that the 0-D model could capture quite nicely the trends observed for the small tube. But it is not the case for the larger tube. The prediction of 1-D model is much better, it allows the simulations of the small tube to be very close to the experiment. For the larger tube, despite an obvious improvement compared to the 0-D model, the 1-D model still have to be improved to provide satisfactory simulations.

6.2 Perspectives

Within the understanding the intensification mechanism resulted by sinusoid vibrations for drying of porous media, some questions were also found to be further explored.

In the study of water behavior within a symmetrical configuration, we found that the capillary effect cannot provide a good explanation for the water behavior under a lower viscous effect ($N_v < 0.1$). Thus, we assume that a new dimensionless number: the ratio of the friction force over inertia, can be proposed for a better understanding the interaction between tube and water index. It demands a further study for a better characterization of this friction force.

In numerical part, we have known that 1-D model is promising in the prediction of the water behavior, especially for the small tube. It can be further improved by considering the surface tension to achieve a better prediction. It could be realized by adding a surface tension term between

successive layers, as a result of their difference in displacement. It requires to consider the internal recirculation of water, from each layer to its neighbors. This could also allow to simulate the development of the thin water film observed is the case of high relative displacement of water (asymmetrical configuration at the resonance frequency).

Moreover, a full asymmetrical model, with full treatment of the meniscus shape, including the gravity effect especially for the larger tube, would provide a better description of water behavior. A 2-D model has to be developed in order to simulate the full shape of the meniscus.

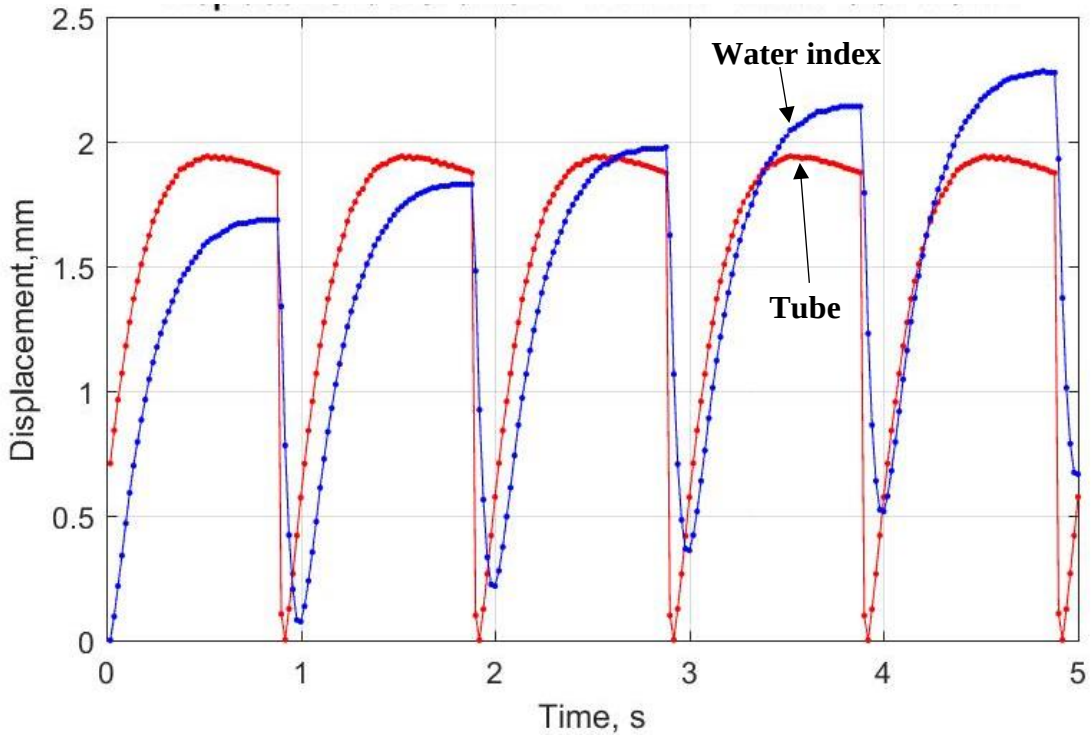

Figure 6-1 Absolute displacements of water and tube under asymmetrical vibration (ID = 2.2 mm, f = *1 Hz, A* = 0.97 mm)

Finally, an exploratory test using an asymmetrical signal (saw-tooth wave) applied on a tube with symmetrical geometry proved that the index movement can be forced in a chosen direction (Figure 6-1). Indeed, with a low frequency, we obtained an obvious global movement of the index to the right along the successive periods. This trend was inverted when changing the phase of the signal,

which proves that the water movement is really due to the asymmetric signal. However, although this approach is promising, the effect of asymmetrical signal cannot be analyzed quantitatively from these data because the precision of inner diameter along the capillary tube was not sufficient; we observed local changes in behavior of water depending on the location of the index. A laser perforated capillary tube with uniform inner diameter may be produced to achieve the study of this intensification approach with asymmetrical signals.

Appendix

Résumé

Les milieux poreux sont des matériaux comprenant une matrice et des pores. Ils existent couramment dans notre vie quotidienne, comme les céréales, le papier, le bois, les vêtements, etc. Un matériau poreux humide est facile à détériorer ou à déformer. Pour la conservation ou l'utilisation de ces milieux poreux, le séchage semble particulièrement important.

Dans l'industrie moderne, la technologie de séchage est largement appliquée dans différents domaines, tels que l'industrie alimentaire et l'industrie pharmaceutique. C'est aussi l'une des unités les plus énergivores de la chaine de production. Depuis la crise énergétique des années 70, les questions liées aux économies d'énergie et à l'amélioration de l'efficacité de la production retiennent de plus en plus l'attention. Plusieurs nouvelles technologies ont été introduites pour intensifier le procédé de séchage, telles que l'infrarouge, le séchage sous vide, les micro-ondes/ondes à haute fréquence et les vibrations. Des investigations sont menées pour comprendre les mécanismes d'intensification et permettre d'optimiser les paramètres des unités de séchage (tels que la température, l'humidité relative et la vitesse de l'air).

Les vibrations s'avèrent être une approche efficace. Les coefficients de transfert externes de chaleur et de masse à la surface des matériaux humides peuvent être améliorés par la turbulence de l'air, en raison de la vibration de l'échantillon. La migration de l'humidité à l'intérieur des matériaux humides peut être améliorée en activant l'eau liquide, l'effet de cavitation, etc. La vibration peut agir sur les phases solide, liquide et gazeuse et intensifier le processus de séchage à basse température sans provoquer un échauffement important de l'échantillon. Cette approche

d'intensification est judicieuse pour le séchage des matériaux sensibles à la chaleur, tels que certains produits pharmaceutiques.

Bien que l'intensification du séchage des milieux poreux assisté par vibration ait été observée, une meilleure compréhension des mécanismes impliqués est encore nécessaire. Les défis en vue de comprendre le comportement de l'eau dans deux modèles de pores simplifiés (géométries symétrique et asymétrique), étudiés dans cette thèse, peuvent être résumés ainsi :

1. Développer des outils expérimentaux et numériques efficaces pour observer et caractériser le comportement de l'eau dans un pore unique soumis à des vibrations,

2. Étudier l'effet des paramètres des vibrations sinusoïdales (fréquence et amplitude) sur le comportement de l'eau.

Dans le chapitre 1, le séchage des milieux poreux est brièvement introduit : (*i*) concepts fondamentaux du séchage, (*ii*) approches d'intensification applicables au procédé industriel et (*iii*) mécanismes impliqués.

Dans le chapitre 2, le dispositif expérimental utilisé pour étudier le comportement de l'eau sous vibration sinusoïdale est présenté. Il se compose d'un tube capillaire (simulant un pore) partiellement rempli d'eau, d'une chaîne de vibration, d'un banc optique et d'un capteur de température et d’humidité relative.

Dans le chapitre 3, nous présentons une procédure de traitement d'image pour identifier automatiquement l'interface eau/air et analyser le comportement du liquide dans le tube capillaire au cours de la vibration.

Dans le chapitre 4, nous mettons en œuvre des méthodes expérimentales pour étudier les effets des paramètres des vibrations sinusoïdales sur le comportement de l'eau dans des tubes à géométrie symétrique. Deux nouveaux nombres adimensionnels sont introduits pour identifier les conditions pertinentes à appliquer en vue d'étudier les effets couplés de l'amplitude et de la fréquence.

Dans le chapitre 5, nous nous concentrons sur le comportement de l'eau dans des tubes à géométrie asymétrique sous vibrations sinusoïdales. En première apporche, un modèle simpliste nous permet de prédire la fréquence de résonance du système afin de trouver la gamme de fréquence pertinente pour les essais. Les effets de la fréquence sur le comportement de l'eau (amplitude de l'eau et changement de phase) sont discutés. Avec des outils numériques avancés, les effets de l'amplitude du tube, de la viscosité dynamique du liquide et de l'angle de contact sur le comportement de l'eau sont enfin étudiés.

References

(1) Tsotsas, E.; Mujumdar, A. S. *Modern Drying Technology*; Wiley-VCH Verlag & Co. KGa A, 2014.

(2) Sabarez, H. T.; Gallego-Juarez, J. A.; Riera, E. Ultrasonic-Assisted Convective Drying of Apple Slices. *Dry. Technol.* 2012, *30* (9), 989–997. https://doi.org/10.1080/07373937.2012. 677083.

(3) Riera-Franco De Sarabia, E.; Gallego-Juárez, J. A.; Rodríguez-Corral, G.; Acosta-Aparicio, V. M.; Andrés-Gallegos, E. Application of High-Power Ultrasound for Drying Vegetables. *Forum Acoust.* 2002.

(4) Srikiatden, J.; Roberts, J. S. Measuring Moisture Diffusivity of Potato and Carrot (Core an d Cortex) during Convective Hot Air and Isothermal Drying. *J. Food Eng.* 2006, *74* (1), 14 3–152. https://doi.org/10.1016/j.jfoodeng.2005.02.026.

(5) Zheng, L.; Sun, D. W. Innovative Applications of Power Ultrasound during Food Freezing Processes - A Review. *Trends Food Sci. Technol.* 2006, *17* (1), 16–23. https://doi.org/10.1 016/j.tifs.2005.08.010.

(6) Vehring, R. Pharmaceutical Particle Engineering via Spray Drying. *Pharm. Res.* 2008, *25* (5), 999–1022. https://doi.org/10.1007/s11095-007-9475-1.

(7) Grdzelishvili, G.; Hoffman, P. Infrared Drying of Food Products. *Czech Tech. Univ. Pragu e, Dep. Process Eng.* 2012.

(8) Efremov, G. Infrared Drying. In *Modern Drying Technology Volume 5: Process Intensifica tion*; Tsotsas, E., Mujumdar, A. S., Eds.; Wiley-VCH Verlag GmbH & Co. KGaA, 2014; V ol. 5, pp 317–355.

(9) Möttönen, V. Variation in Drying Behavior and Final Moisture Content of Wood during C onventional Low Temperature Drying and Vacuum Drying of Betula Pendula Timber. *Dry. Technol.* 2006, *24* (11), 1405–1413. https://doi.org/10.1080/07373930600952750.

(10) Chen, Z. J.; Lamb, F. M. Investigation of Boiling Front during Vacuum Drying of Wood. *Wood Fiber Sci.* 2001, *33* (4), 639–647.

(11) Jomaa, W.; Baixeras, O. Discontinuous Vacuum Drying of Oak Wood: Modelling and Exp erimental Investigations. *Dry. Technol.* 1997, *15* (9), 2129–2144. https://doi.org/10.1080/0 7373939708917355.

(12) Fohr, J.-P.; Chakir, A.; Arnaud, G.; Peuty, M. A. du. Vacuum Drying of Oak Wood. *Dry. T echnol.* 2007, *13* (8–9), 1675–1693. https://doi.org/10.1080/07373939508917046.

(13) Wang, Y.; Zhang, M.; Mujumdar, A. Microwave-Assisted Drying of Foods–Equipment, Pr ocess and Product Quality. *Mod. Dry. Technol. …* 2014, *5*, 317–355.

(14) Datta, A. K. *Handbook of Microwave Technology for Food Application*; M. Dekker, 2018. https://doi.org/10.1201/9781482270778.

(15) Ozyurt, D.; Goc, B.; Demirata, B.; Apak, R. Effect of Oven and Microwave Heating on the Total Antioxidant Capacity of Dietary Onions Grown in Turkey. *Int. J. Food Prop.* 2013, *16* (3), 536–548. https://doi.org/10.1080/10942912.2011.555900.

(16) Perré, P.; Turner, I. W. Microwave Drying of Softwood in an Oversized Waveguide: Theor y and Experiment. *AIChE J.* 1997, *43* (10), 2579–2595. https://doi.org/10.1002/aic.690431 019.

(17) Park, K. -a.; Bergles, a. E. Ultrasonic Enhancement of Saturated and Subcooled Pool Boili ng. *Int. J. Heat Mass Transf.* 1988, *31* (3), 664–667. https://doi.org/10.1016/0017-9310(88) 90049-X.

(18) Kowalski, S. J. *Transport of Porous Materials*; 2007; Vol. 66. https://doi.org/10.1007/s112 42-006-9021-3.

(19) Gallego-Juárez, J. Ultrasound Technologies for Food and Bioprocessing. In *Ultrasound in food processing*; Thomson Science: London, 1998; pp 617–641. https://doi.org/10.1007/97 8-1-4419-7472-3.

(20) Garcia-Perez, J. V.; Carcel, J. a.; Riera, E.; Rosselló, C.; Mulet, A. Intensification of Low-Temperature Drying by Using Ultrasound. *Dry. Technol.* 2012, *30* (11–12), 1199–1208. htt ps://doi.org/10.1080/07373937.2012.675533.

(21) Mulet, a; Bon, J.; Science, F. Food Science and Technology International. *Food Sci. Techn ol. Int.* 2003, 215–221. https://doi.org/10.1177/108201303034641.

(22) Jöger, H.; Schössler, K.; Knorr, D. Process-Induced Minimization of Mass Transfer Barrier s for Improved Drying. *Mod. Dry. Technol.* 2014, *5*, 191–236. https://doi.org/10.1002/9783 527631704.ch07.

(23) Léal, L.; Miscevic, M.; Lavieille, P.; Amokrane, M.; Pigache, F.; Topin, F.; Nogar??de, B.; Tadrist, L. An Overview of Heat Transfer Enhancement Methods and New Perspectives: F ocus on Active Methods Using Electroactive Materials. *Int. J. Heat Mass Transf.* 2013, *61* (1), 505–524. https://doi.org/10.1016/j.ijheatmasstransfer.2013.01.083.

(24) Chen, X.; Seyfang, K.; Steckel, H. Development of a Micro Dosing System for Fine Powd er Using a Vibrating Capillary. Part 1: The Investigation of Factors Influencing on the Dosi ng Performance. *Int. J. Pharm.* 2012, *433* (1–2), 34–41. https://doi.org/10.1016/j.ijpharm.2 012.04.068.

(25) Babu, A. K.; Kumaresan, G.; Raj, V. A. A.; Velraj, R. Review of Leaf Drying: Mechanism and Influencing Parameters, Drying Methods, Nutrient Preservation, and Mathematical M odels. *Renew. Sustain. Energy Rev.* 2018, *90*, 536–556. https://doi.org/10.1016/J.RSER.20 18.04.002.

(26) Perré, P.; Keey, R. B. Drying of Wood. *Handb. Ind. Dry.* 2015, 797–846.

(27) Jachuck, R. J.; Lee, J.; Kolokotsa, D.; Ramshaw, C.; Valachis, P.; Yanniotis, S. Process Int ensification for Energy Saving. *Appl. Therm. Eng.* 1997, *17* (8–10), 861–867. https://doi.or g/10.1016/S1359-4311(96)00048-8.

(28) Arévalo-Pinedo, A.; Murr, F. E. X. Kinetics of Vacuum Drying of Pumpkin (Cucurbita Ma xima): Modeling with Shrinkage. *J. Food Eng.* 2006, *76* (4), 562–567. https://doi.org/10.10 16/j.jfoodeng.2005.06.003.

(29) Toğrul, H. Suitable Drying Model for Infrared Drying of Carrot. *J. Food Eng.* 2006, *77* (3), 610–619. https://doi.org/10.1016/J.JFOODENG.2005.07.020.

(30) Efremov, G. Infrared Drying. In *Modern Drying Technology*; 2014; Vol. 5, pp 317–355.

(31) Zhang, M.; Tang, J.; Mujumdar, A. S.; Wang, S. Trends in Microwave-Related Drying of F ruits and Vegetables. *Trends in Food Science and Technology*. Elsevier October 1, 2006, p p 524–534. https://doi.org/10.1016/j.tifs.2006.04.011.

(32) Antti, a. L.; Perre, P. A Microwave Applicator for on Line Wood Drying: Temperature an d Moisture Distribution in Wood. *Wood Sci. Technol.* 1999, *33*, 123–138. https://doi.org/1 0.1007/s002260050104.

(33) Kowalski, S. J.; Pawłowski, A.; Szadzińska, J.; Łechtańska, J.; Stasiak, M. High Power Air borne Ultrasound Assist in Combined Drying of Raspberries. *Innov. Food Sci. Emerg. Tec hnol.* 2016, *34*, 225–233. https://doi.org/10.1016/j.ifset.2016.02.006.

(34) Zanoelo, E. F.; di Celso, G. M.; Kaskantzis, G. Drying Kinetics of Mate Leaves in a Packe d Bed Dryer. *Biosyst. Eng.* 2007, *96* (4), 487–494. https://doi.org/10.1016/j.biosystemseng. 2006.12.006.

(35) Ratti, C.; Mujumdar, A. S. Simulation of Packed Bed Drying of Foodstuffs with Airflow R eversal. *J. Food Eng.* 1995, *26* (3), 259–271. https://doi.org/10.1016/0260-8774(94)00007-V.

(36) Belhamri, A.; Bennamoun, L.; Belhamri, A. Study of Heat and Mass Transfer in Porous M edia: Application to Packed-Bed Drying Article in Fluid Dynamics and Materials Processin g · Study of Heat and Mass Transfer in Porous Media: Application to Packed-Bed Drying. *FDMP* 2008, *4* (4), 221–230. https://doi.org/10.3970/fdmp.2008.004.221.

(37) Zik Stavans, O. J. Self-Diffusion in Granular Flows. *EPL* 1991, *16* (3), 255–258. https://do i.org/10.1209/0295-5075/16/3/006.

(38) Barzegar, M.; Zare, D.; Stroshine, R. L. An Integrated Energy and Quality Approach to Op timization of Green Peas Drying in a Hot Air Infrared-Assisted Vibratory Bed Dryer. *J. Fo od Eng.* 2015, *166*, 302–315. https://doi.org/10.1016/j.jfoodeng.2015.06.026.

(39) Dhuri, S. S. Manufactured Sand. *Indian Concr. J.* 2012, *86* (8), 24–26.

(40) Mitov, M. Cholesteric Liquid Crystals in Living Matter. *Soft Matter* 2017, *13* (23), 4176–4209. https://doi.org/10.1039/c7sm00384f.

(41) Liu, C.; Wang, L.; Wu, P.; Xiang, F. Size Distribution in Gas Vibration Bed and Its Application on Grain Drying. *Powder Technol.* 2012, *221*, 192–198. https://doi.org/10.1016/j.powtec.2012.01.001.

(42) Plumb, O. a.; Spolek, G. a.; Olmstead, B. a. a; Plumb, a. Heat and Mass Transfer in Wood during Drying. *Int. J. Heat Mass Transf.* 1985, *28* (9), 1669–1678. https://doi.org/10.1016/0017-9310(85)90141-3.

(43) Sherwood, T. K. The Drying of Solids—III1 Mechanism of the Drying of Pulp and Paper. *Ind. Eng. Chem.* 1930, *22* (2), 132–136. https://doi.org/10.1021/ie50242a009.

(44) van Deventer, H. C. Feasibility of Energy Efficient Steam Drying of Paper and Textile Including Process Integration. *Appl. Therm. Eng.* 1997, *17* (8–10), 1035–1041. https://doi.org/10.1016/S1359-4311(97)00042-2.

(45) Mavko, G.; Mukerji, T.; Dvorkin, J. *The Rock Physics Handbook: Tools for Seismic Analysis in Porous Media, 329 Pp*; Cambridge University Press, 1998.

(46) P. S. Liu and G. F. Chen. *Porous Materials*; Butterworth-Heinemann, 2014. https://doi.org/10.1016/B978-0-12-407788-1.00001-0.

(47) Kantzas, Apostolos; Bryan Jonathan; Taheri, S. Fundamentals of Fluid Flow in Porous Media, 2015.

(48) Devahastin, S. Review of:"International Encyclopedia of Heat and Mass Transfer" Edited by G. F. Hewitt, G.L. Shires and Y.V. Polezhaev CRC Press, Boca Raton, Florida, USA 1997, 1312 Pages. *Dry. Technol.* 1998, *16* (7), 1521–1521. https://doi.org/10.1080/07373939808917476.

(49) Liu, M.; Wu, J.; Gan, Y.; Hanaor, D. A. H.; Chen, C. Q. Evaporation Limited Radial Capillary Penetration in Porous Media. *Langmuir* 2016, *32* (38), 9899–9904. https://doi.org/10.1021/acs.langmuir.6b02404.

(50) D. G. Overhults; G. M. White; H. E. Hamilton; I. J. Ross. Drying Soybeans With Heated Air. *Trans. ASAE* 2013, *16* (1), 0112–0113. https://doi.org/10.13031/2013.37459.

(51) DULLIEN, F. A. L. *Porous Media: Fluid Transport and Pore Structure*; Academic Press, 1992. https://doi.org/10.1016/B978-0-12-223650-1.50008-5.

(52) Duran, J.; Mazozi, T.; Clément, E.; Rajchenbach, J. Size Segregation in a Two-Dimensional Sandpile: Convection and Arching Effects. *Phys. Rev. E* 1994, *50* (6), 5138–5141. https://doi.org/10.1103/PhysRevE.50.5138.

(53) Grioui, N.; Halouani, K.; Zoulalian, A.; Halouani, F. Experimental Study of Thermal Effec t on Olive Wood Porous Structure during Carbonization. *Maderas-Ciencia Y Tecnol.* 2007, *9* (1), 15–28. https://doi.org/10.4067/S0718-221X2007000100002.

(54) Rezaei, H. Physical and Thermal Characterization of Ground Wood Chip and Ground Woo d Pellet Particles, University of British Columbia, 2017. https://doi.org/10.14288/1.034323 5.

(55) Lauriks, W.; Boeckx, L.; Leclaire, P. Characterization of Porous Acoustic Materials. In *SA PEM 2005 Symposium on the Acoustics of Poro-Elastic Materials*; 2005; pp 1–14.

(56) Bo-Ming, Y.; Jian-Hua, L. A Geometry Model for Tortuosity of Flow Path in Porous Medi a. *Chinese Phys. Lett.* 2004, *21* (8), 1569–1571. https://doi.org/10.1088/0256-307x/21/8/04 4.

(57) Louis, L.; Baud, P.; Wong, T.-F. Characterization of Pore-Space Heterogeneity in Sandsto ne by X-Ray Computed Tomography. *Geol. Soc. London, Spec. Publ.* 2007, *284* (1), 127–1 46. https://doi.org/10.1144/sp284.9.

(58) Chemistry, S. Terminology and Symbols in Colloid and Surface Chemistry Part 1.13. Defi nitions, Terminology and Symbols for Rheological Properties. *Pure Appl. Chem.* 2007, *51* (5), 1213–1218. https://doi.org/10.1351/pac197951051213.

(59) Bhattacharya, S.; Gubbins, K. E. Fast Method for Computing Pore Size Distributions of M odel Materials. *Langmuir* 2006, *22* (18), 7726–7731. https://doi.org/10.1021/la052651k.

(60) Vinegar et al. In-Situ Method for Determining Pore Size Distribution, Capillary Pressure a nd Permeability, 19 March 1984.

(61) Seaton, N. A.; Walton, J. P. R. B.; Quirke, N. A New Analysis Method for the Determinati on of the Pore Size Distribution of Porous Carbons from Nitrogen Adsorption Measuremen ts. *Carbon N. Y.* 1989, *27* (6), 853–861. https://doi.org/10.1016/0008-6223(89)90035-3.

(62) Ishikiriyama, K.; Todoki, M.; Motomura, K. Pore Size Distribution (PSD) Measurements o f Silica Gels by Means of Differential Scanning Calorimetry. i. Optimization for Determina tion of Psd. *J. Colloid Interface Sci.* 1995, *171* (1), 92–102. https://doi.org/10.1006/jcis.199 5.1154.

(63) Baklanov, M. R.; Mogilnikov, K. P.; Polovinkin, V. G.; Dultsev, F. N. Determination of Po re Size Distribution in Thin Films by Ellipsometric Porosimetry. *J. Vac. Sci. Technol. B Mi croelectron. Nanom. Struct.* 2002, *18* (3), 1385. https://doi.org/10.1116/1.591390.

(64) Diamond, S. Mercury Porosimetry. *Cem. Concr. Res.* 2002, *30* (10), 1517–1525. https://do i.org/10.1016/s0008-8846(00)00370-7.

(65) Kuila, U.; Prasad, M. Specific Surface Area and Pore-Size Distribution in Clays and Shale s. *Geophys. Prospect.* 2013, *61* (2), 341–362. https://doi.org/10.1111/1365-2478.12028.

(66) Heege, H. J. Sensing of Natural Soil Properties. In *Precision in Crop Farming: Site Specifi c Concepts and Sensing Methods: Applications and Results*; Springer Netherlands: Dordrec ht, 2013; pp 52–102. https://doi.org/10.1007/978-94-007-6760-7_5.

(67) Bracco, G.; Holst, B. *Surface Science Techniques*; Springer, Berlin, Heidelberg, 2013.

(68) Mortimer. R.G. *Physical Chemistry*; Academic Press, 2008.

(69) Moldoveanu, S. C.; David, V. *RP-HPLC Analytical Columns*; 2017. https://doi.org/10.101 6/B978-0-12-803684-6.00007-X.

(70) Lam, C. N. .; Wu, R.; Li, D.; Hair, M. .; Neumann, A. . Study of the Advancing and Recedi ng Contact Angles: Liquid Sorption as a Cause of Contact Angle Hysteresis. *Adv. Colloid I nterface Sci.* 2002, *96* (1–3), 169–191. https://doi.org/10.1016/S0001-8686(01)00080-X.

(71) Net Industries. Capillary Action - Liquid, Force, Water, and Surface - JRank Articles http:/ /science.jrank.org/pages/1182/Capillary-Action.html (accessed Sep 20, 2018).

(72) Sturgess, J. Fluids. In *A Surgeon's Guide to Anaesthesia and Peri-Operative Care*; Elsevie r, 2014; pp 273–276. https://doi.org/10.1017/CBO9781139628808.025.

(73) AMS. Saturation Vapor Pressure. In *Van Nostrand's Scientific Encyclopedia*; John Wiley & Sons, Inc.: Hoboken, NJ, USA, 2007. https://doi.org/10.1002/9780471743989.vse10125.

(74) Rai;, K. N.; Pandey, R. N. Heat and Mass Transfer in Porous Bodies of Simple Geometry. *Indian J. Pure Appl. Math.* 1982, *13* (1), 96–109.

(75) Shokri, N.; Or, D.; Weisbrod, N.; Prat, M. Drying of Porous Media. *Transp. Porous Media* 2015, *110* (2), 171–173. https://doi.org/10.1007/s11242-015-0577-7.

(76) Kowalski, S. J.; Pawlowski, A. Intensification of Apple Drying Due to Ultrasound Enhanc ement. *J. Food Eng.* 2015, *156*, 1–9. https://doi.org/10.1016/j.jfoodeng.2015.01.023.

(77) Vergnaud, J. M. Dying of Polymeric and Solid Materials. *Dry. Technol.* 2007, *11* (5), 1135 –1136. https://doi.org/10.1080/07373939308916890.

(78) Hall, C.; Hoff, W. D.; Nixon, M. R. Water Movement in Porous Building Materials-VI. Ev aporation and Drying in Brick and Block Materials. *Build. Environ.* 1984, *19* (1), 13–20. ht tps://doi.org/10.1016/0360-1323(84)90009-X.

(79) Sherwood, T. K. The Drying of Solids I. *Ind. Eng. Chem.* 1928, *21* (1), 12–16.

(80) Sherwood, T. K. The Drying of Solids-II. *Ind. Eng. Chem.* 1929, *21* (10), 13.

(81) Perré, P.; Keey, R. B. Drying of Wood Principles and Practices. In *Handbook of Industrial Drying, Fourth Edition*; Mujumdar A, Ed.; CRC Press: Boca Raton, 2014; pp 797–846. htt ps://doi.org/10.1201/b17208.

(82) Velić, D.; Planinić, M.; Tomas, S.; Bilić, M. Influence of Airflow Velocity on Kinetics of Convection Apple Drying. *J. Food Eng.* 2004, *64* (1), 97–102. https://doi.org/10.1016/j.jfoodeng.2003.09.016.

(83) Putra, R. N.; Ajiwiguna, T. A. Influence of Air Temperature and Velocity for Drying Process. In *Procedia Engineering*; Elsevier, 2017; Vol. 170, pp 516–519. https://doi.org/10.1016/j.proeng.2017.03.082.

(84) Sturm, B.; Nunez Vega, A. M.; Hofacker, W. C. Influence of Process Control Strategies on Drying Kinetics, Colour and Shrinkage of Air Dried Apples. *Appl. Therm. Eng.* 2014, *62* (2), 455–460. https://doi.org/10.1016/j.applthermaleng.2013.09.056.

(85) Yılmaz, F. M.; Yüksekkaya, S.; Vardin, H.; Karaaslan, M. The Effects of Drying Conditions on Moisture Transfer and Quality of Pomegranate Fruit Leather (Pestil). *J. Saudi Soc. Agric. Sci.* 2017, *16* (1), 33–40. https://doi.org/10.1016/j.jssas.2015.01.003.

(86) Tzempelikos, D. A.; Vouros, A. P.; Bardakas, A. V.; Filios, A. E.; Margaris, D. P. Case Studies on the Effect of the Air Drying Conditions on the Convective Drying of Quinces. *Case Stud. Therm. Eng.* 2014, *3*, 79–85. https://doi.org/10.1016/j.csite.2014.05.001.

(87) Leong, E.; Rahardjo, H. Permeability Functions for Unsaturated Soils.Pdf. *J. Geotech. Geoenvironmental Eng.* 1997, *123* (12), 1118–1126. https://doi.org/10.1061/(ASCE)1090-0241(1997)123:12(1118).

(88) Stanish, M. A.; Schajer, G. S.; Kayihan, F. A Mathematical Model of Drying for Hygroscopic Porous Media. *AIChE J.* 1986, *32* (8), 1301–1311. https://doi.org/10.1002/aic.690320808.

(89) Klinkenberg, L. J. The Permeability of Porous Media to Liquids and Gases, Drilling and Production Practice. *Am. Pet. Inst.* 1941, 200–213.

(90) Zlatanović, I.; Komatina, M.; Antonijević, D. Low-Temperature Convective Drying of Apple Cubes. *Appl. Therm. Eng.* 2013, *53* (1), 114–123. https://doi.org/10.1016/j.applthermaleng.2013.01.012.

(91) Sacilik, K.; Elicin, A. K. The Thin Layer Drying Characteristics of Organic Apple Slices. *J. Food Eng.* 2006, *73* (3), 281–289. https://doi.org/10.1016/j.jfoodeng.2005.03.024.

(92) Strømmen, I.; Eikevik, T. M.; Alves-filho, O.; Syverud, K.; Jonassen, O. Low Temperature Drying with Heat Pumps Principles of Heat Pump Drying. In *Proceeding in 13th International Drying Symposium*; 2002; pp 27–30.

(93) Currie, J. A. Gaseous Diffusion in Porous Media. Part 2. - Dry Granular Materials. *Br. J. Appl. Phys.* 1960, *11* (8), 318–324. https://doi.org/10.1088/0508-3443/11/8/303.

(94) Aral, S.; Beşe, A. V. Convective Drying of Hawthorn Fruit (Crataegus Spp.): Effect of Experimental Parameters on Drying Kinetics, Color, Shrinkage, and Rehydration Capacity. *Food Chem.* 2016, *210*, 577–584. https://doi.org/10.1016/j.foodchem.2016.04.128.

(95) Wojdyło, A.; Figiel, A.; Lech, K.; Nowicka, P.; Oszmiański, J. Effect of Convective and V acuum-Microwave Drying on the Bioactive Compounds, Color, and Antioxidant Capacity of Sour Cherries. *Food Bioprocess Technol.* 2014, *7* (3), 829–841. https://doi.org/10.1007/s11947-013-1130-8.

(96) Moraghan, J. T. Manganese Nutrition of Flax as Affected by FeEDDHA and Soil Air Dryi ng1. *Soil Sci. Soc. Am. J.* 2010, *49* (3), 668. https://doi.org/10.2136/sssaj1985.03615995004900030028x.

(97) Vega-Gálvez, A.; Ah-Hen, K.; Chacana, M.; Vergara, J.; Martínez-Monzó, J.; García-Segovia, P.; Lemus-Mondaca, R.; Di Scala, K. Effect of Temperature and Air Velocity on Drying Kinetics, Antioxidant Capacity, Total Phenolic Content, Colour, Texture and Microstructure of Apple (Var. Granny Smith) Slices. *Food Chem.* 2012, *132* (1), 51–59. https://doi.org/10.1016/j.foodchem.2011.10.029.

(98) Fernandez, E. M.; Rosolem, C. A.; Maringoni, A. C.; Oliveira, D. M. T. Fungus Incidence on Peanut Grains as Affected by Drying Method and Ca Nutrition. *F. Crop. Res.* 1997, *52* (1–2), 9–15. https://doi.org/10.1016/S0378-4290(96)03461-2.

(99) Pabis, S. Theoretical Models of Vegetable Drying by Convection. *Transp. Porous Media* 2007, *66* (1–2), 77–87. https://doi.org/10.1007/s11242-006-9023-1.

(100) Babalis, S. J.; Papanicolaou, E.; Kyriakis, N.; Belessiotis, V. G. Evaluation of Thin-Layer Drying Models for Describing Drying Kinetics of Figs (Ficus Carica). *J. Food Eng.* 2006, *75* (2), 205–214. https://doi.org/10.1016/J.JFOODENG.2005.04.008.

(101) Boukadida, N.; Nasrallah, S. Ben. Two Dimensional Heat and Mass Transfer during Convective Drying of Porous Media. *Dry. Technol.* 1995, *13* (3), 661–694. https://doi.org/10.1080/07373939508916979.

(102) Kadem, S.; Lachemet, A.; Younsi, R.; Kocaefe, D. 3d-Transient Modeling of Heat and Mass Transfer during Heat Treatment of Wood. *Int. Commun. Heat Mass Transf.* 2011, *38* (6), 717–722. https://doi.org/10.1016/j.icheatmasstransfer.2011.03.026.

(103) Perré, P.; Turner, I. W. A 3-D Version of TransPore: A Comprehensive Heat and Mass Transfer Computational Model for Simulating the Drying of Porous Media. *Int. J. Heat Mass Transf.* 1999, *42* (24), 4501–4521. https://doi.org/10.1016/S0017-9310(99)00098-8.

(104) Fox, B.; Bellini, G.; Pellegrini, L. Drying. In *Fermentation and Biochemical Engineering Handbook (Third Edition)*; Vogel, H. C., Todaro, C. M., Eds.; William Andrew Publishing: Boston, 2014; pp 283–305. https://doi.org/https://doi.org/10.1016/B978-1-4557-2553-3.00014-3.

(105) Prat, M. Recent Advances in Pore-Scale Models for Drying of Porous Media. *Chem. Eng. J.* 2002, *86* (1990), 153–164.

(106) Le, K. H.; Kharaghani, A.; Kirsch, C.; Tsotsas, E. Pore Network Simulations of Heat and Mass Transfer inside an Unsaturated Capillary Porous Wick in the Dry-out Regime. *Transp. Porous Media* 2016, *114* (3), 623–648. https://doi.org/10.1007/s11242-016-0737-4.

(107) Vorhauer, N.; Metzger, T.; Tsotsas, E. On the Influence of Temperature Gradients on Drying of Pore Networks. In *European Drying Conference - EuroDrying'2011*; 2011; pp 26–28.

(108) Blunt, M. J. Physically-Based Network Modeling of Multiphase Flow in Intermediate-Wet Porous Media. *J. Pet. Sci. Eng.* 1998, *20* (3–4), 117–125. https://doi.org/10.1016/S0920-4105(98)00010-2.

(109) Sun, Y.; Kharaghani, A.; Tsotsas, E. Micro-Model Experiments and Pore Network Simulations of Liquid Imbibition in Porous Media. *Chem. Eng. Sci.* 2016, *150*, 41–53. https://doi.org/10.1016/j.ces.2016.04.055.

(110) Xiong, Q.; Baychev, T. G.; Jivkov, A. P. Review of Pore Network Modelling of Porous Media: Experimental Characterisations, Network Constructions and Applications to Reactive Transport. *J. Contam. Hydrol.* 2016, *192*, 101–117. https://doi.org/10.1016/j.jconhyd.2016.07.002.

(111) Plourde, F.; Prat, M. Pore Network Simulations of Drying of Capillary Porous Media. Influence of Thermal Gradients. *Int. J. Heat Mass Transf.* 2003, *46* (7), 1293–1307. https://doi.org/10.1016/S0017-9310(02)00391-5.

(112) Vorhauer, N.; Tsotsas, E.; Prat, M. Temperature Gradient Induced Double Stabilization of the Evaporation Front within a Drying Porous Medium. *Phys. Rev. Fluids* 2018, *3* (11), 114201. https://doi.org/10.1103/PhysRevFluids.3.114201.

(113) Le Bray, Y.; Prat, M. Three-Dimensional Pore Network Simulation of Drying in Capillary Porous Media. *Int. J. Heat Mass Transf.* 1999, *42* (22), 4207–4224. https://doi.org/10.1016/S0017-9310(99)00006-X.

(114) Moghaddam, A. A.; Kharaghani, A.; Tsotsas, E.; Prat, M. Kinematics in a Slowly Drying Porous Medium: Reconciliation of Pore Network Simulations and Continuum Modeling. *Phys. Fluids* 2017, *29* (2), 022102. https://doi.org/10.1063/1.4975985.

(115) Wu, R.; Cui, G. M.; Chen, R. Pore Network Study of Slow Evaporation in Hydrophobic Porous Media. *Int. J. Heat Mass Transf.* 2014, *68*, 310–323. https://doi.org/10.1016/j.ijheatmasstransfer.2013.09.042.

(116) Metzger, T.; Tsotsas, E. Network Models for Capillary Porous Media: Application to Drying Technology. *Chemie-Ingenieur-Technik* 2010, *82* (6), 869–879. https://doi.org/10.1002/cite.201000023.

(117) Wang, Y.; Kharaghani, A.; Metzger, T.; Tsotsas, E. Pore Network Drying Model for Particle Aggregates: Assessment by X-Ray Microtomography. *Dry. Technol.* 2012, *30* (15), 1800–1809. https://doi.org/10.1080/07373937.2012.713422.

(118) Le Bray, Y.; Prat, M. Three-Dimensional Pore Network Simulation of Drying in Capillary Porous Media. *Int. J. Heat Mass Transf.* 1999, *42* (22), 4207–4224. https://doi.org/10.1016/S0017-9310(99)00006-X.

(119) Yiotis, A. G.; Stubos, A. K.; Boudouvis, A. G.; Yortsos, Y. C. A 2-D Pore-Network Model of the Drying of Single-Component Liquids in Porous Media. *Adv. Water Resour.* 2001, *24* (3–4), 439–460. https://doi.org/10.1016/S0309-1708(00)00066-X.

(120) Kharaghani, A.; Metzger, T.; Tsotsas, E. An Irregular Pore Network Model for Convective Drying and Resulting Damage of Particle Aggregates. *Chem. Eng. Sci.* 2012, *75*, 267–278. https://doi.org/10.1016/j.ces.2012.03.038.

(121) Xiong, Q.; Baychev, T. G.; Jivkov, A. P. Review of Pore Network Modelling of Porous Media: Experimental Characterisations, Network Constructions and Applications to Reactive Transport. *J. Contam. Hydrol.* 2016, *192*, 101–117. https://doi.org/10.1016/j.jconhyd.2016.07.002.

(122) Metzger, T.; Irawan, A.; Tsotsas, E. Influence of Pore Structure on Drying Kinetics: A Pore Network Study. *AIChE J.* 2007, *53* (12), 3029–3041. https://doi.org/10.1002/aic.11307.

(123) Segura, L. A.; Toledo, P. G. Pore-Level Modeling of Isothermal Drying of Pore Networks: Effects of Gravity and Pore Shape and Size Distributions on Saturation and Transport Parameters. *Chem. Eng. J.* 2005, *111* (2–3), 237–252. https://doi.org/10.1016/j.cej.2005.02.004.

(124) Metzger, T.; Irawan, A.; Tsotsas, E. Isothermal Drying of Pore Networks: Influence of Friction for Different Pore Structures. *Dry. Technol.* 2007, *25* (1), 49–57. https://doi.org/10.1080/07373930601152640.

(125) Metzger, T.; Irawan, A.; Tsotsas, E. Isothermal Drying of Pore Networks: Influence of Friction for Different Pore Structures. *Dry. Technol.* 2007, *25* (1), 49–57. https://doi.org/10.1080/07373930601152640.

(126) Metzger, T.; Irawan, A.; Tsotsas, E. Influence of Pore Structure on Drying Kinetics: A Pore Network Study. *AIChE J.* 2007, *53* (12), 3029–3041. https://doi.org/10.1002/aic.11307.

(127) Perkins, T. K.; Johnston, O. C. A Review of Diffusion and Dispersion in Porous Media. *Soc. Pet. Eng. J.* 2007, *3* (01), 70–84. https://doi.org/10.2118/480-pa.

(128) Metzger, T.; Tsotsas, E. Influence of Pore Size Distribution on Drying Kinetics: A Simple Capillary Model. *Dry. Technol.* 2005, *23* (9–11), 1797–1809. https://doi.org/10.1080/07373930500209830.

(129) Prat, M. On the Influence of Pore Shape, Contact Angle and Film Flows on Drying of Capillary Porous Media. *Int. J. Heat Mass Transf.* 2007, *50* (7–8), 1455–1468. https://doi.org/10.1016/j.ijheatmasstransfer.2006.09.001.

(130) Chauvet, F.; Duru, P.; Geoffroy, S.; Prat, M. Three Periods of Drying of a Single Square C apillary Tube. *Phys. Rev. Lett.* 2009, *103* (12), 1–4. https://doi.org/10.1103/PhysRevLett.1 03.124502.

(131) Camassel, B.; Sghaier, N.; Prat, M.; Nasrallah, S. Ben. Evaporation in a Capillary Tube of Square Cross-Section: Application to Ion Transport. *Chem. Eng. Sci.* 2005, *60* (3), 815–82 6. https://doi.org/10.1016/j.ces.2004.09.044.

(132) Camassel, B.; Sghaier, N.; Prat, M.; Nasrallah, S. Ben. Evaporation in a Capillary Tube of Square Cross-Section: Application to Ion Transport. *Chem. Eng. Sci.* 2005, *60* (3), 815–82 6. https://doi.org/10.1016/j.ces.2004.09.044.

(133) Gray, W. G.; Hassanizadeh, S. M. Thermodynamic Basis of Capillary Pressure in Porous Media. *Water Resour. Res.* 1993, *29* (10), 3389–3405.

(134) Morrow, N. R. Physics and Thermodynamics of Capillary, A Thermodynamic Theory and a Detailed Mechanism of Immiscible Displacement in Porous Media Are Developed in Ter ms of a Quantized Model. *Ind. Eng. Chem.* 1970, *62*, 32–56.

(135) Hirasaki, G. J.; Lawson, J. B. Mechanisms of Foam Flow in Porous Media: Apparent Visc osity in Smooth Capillaries. *Soc. Pet. Eng. J.* 1985, *25* (02), 176–190. https://doi.org/10.21 18/12129-pa.

(136) Polezhaev, D.; Duru, P.; Plouraboué, F. Enhanced Evaporation from an Oscillating Liquid in a Capillary Tube. *Int. J. Heat Mass Transf.* 2016, *95*, 288–295. https://doi.org/10.1016/j. ijheatmasstransfer.2015.12.012.

(137) Chauvet, F.; Cazin, S.; Duru, P.; Prat, M. Use of Infrared Thermography for the Study of E vaporation in a Square Capillary Tube. *Int. J. Heat Mass Transf.* 2010, *53* (9–10), 1808–18 18. https://doi.org/10.1016/j.ijheatmasstransfer.2010.01.008.

(138) Chauvet, F.; Cazin, S.; Duru, P.; Prat, M. Use of Infrared Thermography for the Study of E vaporation in a Square Capillary Tube. *Int. J. Heat Mass Transf.* 2010, *53* (9–10), 1808–18 18. https://doi.org/10.1016/j.ijheatmasstransfer.2010.01.008.

(139) Preiss, G.; Wayner, P. C. Evaporation from a Capillary Tube. *Trans. ASME, J. Heat Trans f.* 1976, *98* (May 1976), 178–181. https://doi.org/10.1115/1.3450515.

(140) Stange, M.; Dreyer, M. E.; Rath, H. J. Capillary Driven Flow in Circular Cylindrical Tube s. *Phys. Fluids* 2003, *15* (9), 2587–2601. https://doi.org/10.1063/1.1596913.

(141) Hallinan, K. P.; Chebaro, H. C.; Kim, S. J.; Chang, W. S. Evaporation from an Extended M eniscus for Nonisothermal Interfacial Conditions. *J. Thermophys. Heat Transf.* 1994, *8* (4), 709–716. https://doi.org/10.2514/3.602.

(142) Mukherjee, A.; Kandlikar, S. G. Numerical Study of an Evaporating Meniscus on a Movin g Heated Surface. *J. Heat Transfer* 2006, *128* (12), 1285. https://doi.org/10.1115/1.239709 3.

(143) Maroo, S. C.; Chung, J. N. Heat Transfer Characteristics and Pressure Variation in a Nanos cale Evaporating Meniscus. *Int. J. Heat Mass Transf.* 2010, *53* (15–16), 3335–3345. https:/ /doi.org/10.1016/j.ijheatmasstransfer.2010.02.030.

(144) Potash, M.; Wayner, P. C. Evaporation from a Two-Dimensional Extended Meniscus. *Int. J. Heat Mass Transf.* 1972, *15* (10), 1851–1863. https://doi.org/10.1016/0017-9310(72)900 58-0.

(145) Pratt, D. M.; Hallinan, K. P. Thermocapillary Effects on the Wetting Characteristics of a H eated Curved Meniscus. *J. Thermophys. Heat Transf.* 1997, *11* (4), 519–525. https://doi.or g/10.2514/2.6293.

(146) L.Plawsky; Chatterjee;, A.; Peter C. Wayner, J. MODELING CONACT LINE DYNAMIC S IN EVAPORATING MENISCI. In *the Proceedings of the COMSOL Conference*; 2009.

(147) Höhmann, C.; Stephan, P. Microscale Temperature Measurement at an Evaporating Liquid Meniscus. *Exp. Therm. Fluid Sci.* 2002, *26* (2–4), 157–162. https://doi.org/10.1016/S0894 -1777(02)00122-X.

(148) Khrustalev, D.; Faghri, A. Fluid Flow Effects in Evaporation From Liquid–Vapor Meniscu s. *J. Heat Transfer* 1996, *118* (3), 725. https://doi.org/10.1115/1.2822692.

(149) Wayner, P. C.; Kao, Y. K.; LaCroix, L. V. The Interline Heat-Transfer Coefficient of an E vaporating Wetting Film. *Int. J. Heat Mass Transf.* 1976, *19* (5), 487–492. https://doi.org/1 0.1016/0017-9310(76)90161-7.

(150) Buffone, C.; Sefiane, K. Investigation of Thermocapillary Convective Patterns and Their R ole in the Enhancement of Evaporation from Pores. *Int. J. Multiph. Flow* 2004, *30* (9), 107 1–1091. https://doi.org/10.1016/j.ijmultiphaseflow.2004.05.010.

(151) Buffone, C.; Sefiane, K.; Christy, J. Infra-Red Measurements of an Evaporating Meniscus with Imposed Contact Angle. *Int. J. Therm. Sci.* 2017, *121*, 89–98. https://doi.org/10.1016/ j.ijthermalsci.2017.07.005.

(152) Abe, T.; Afzal, T. M. Thin-Layer Infrared Radiation Drying of Rough Rice. *J. Agric. Eng. Res.* 1997, *67* (4), 289–297. https://doi.org/10.1006/jaer.1997.0170.

(153) Afzal, T. M.; Abe, T. Diffusion in Potato during Far Infrared Radiation Drying. *J. Food En g.* 1998, *37* (4), 353–365. https://doi.org/10.1016/S0260-8774(98)00111-3.

(154) Nowak, D.; Lewicki, P. P. Infrared Drying of Apple Slices. *Innov. Food Sci. Emerg. Techn ol.* 2004, *5* (3), 353–360. https://doi.org/10.1016/j.ifset.2004.03.003.

(155) Umesh Hebbar, H.; Rastogi, N. K. Mass Transfer during Infrared Drying of Cashew Kerne l. *J. Food Eng.* 2001, *47* (1), 1–5. https://doi.org/10.1016/S0260-8774(00)00088-1.

(156) Adak, N.; Heybeli, N.; Ertekin, C. Infrared Drying of Strawberry. *Food Chem.* 2017, *219*, 109–116. https://doi.org/10.1016/j.foodchem.2016.09.103.

(157) Pawar, S. B.; Pratape, V. M. Fundamentals of Infrared Heating and Its Application in Dryi ng of Food Materials: A Review. *J. Food Process Eng.* 2017, *40* (1), e12308. https://doi.or g/10.1111/jfpe.12308.

(158) Ratti, C.; Mujumdar, A. S. Infrared Drying. In *Handbook of Industrial Drying, Fourth Edit ion*; Mujumdar, A. S., Ed.; CRC Press, 2014; pp 405–420. https://doi.org/10.1201/b17208.

(159) Chakraverty, A. *Handbook of Postharvest Technology : Cereals, Fruits, Vegetables, Tea, a nd Spices*; Marcel Dekker, 2003.

(160) Möttönen, V. Variation in Drying Behavior and Final Moisture Content of Wood during C onventional Low Temperature Drying and Vacuum Drying of Betula Pendula Timber. *Dry. Technol.* 2006, *24* (11), 1405–1413. https://doi.org/10.1080/07373930600952750.

(161) Chen, Z.; Lamb, F. M.; Nelson, D. J.; White, M. S. Primary Driving Force in Wood Vacuu m Drying. 1997.

(162) Pagnozzi, V.; Pagnozzi, E. G. Vacuum Drying Kiln, 4 May 1977.

(163) Suresh Kumar, S. V. R. Recent Advances in Drying and Dehydration of Fruits and Vegeta bles: A Review. *J Food Sci Technol Mysore J Food Sci Technol 47* (471), 15–2615.

(164) Yamsaengsung, R.; Sattho, T. Superheated Steam Vacuum Drying of Rubberwood. *Dry. T echnol.* 2008, *26* (6), 798–805. https://doi.org/10.1080/07373930802046518.

(165) Bescher, E.; Sambol, M.; Rice, E. K.; Mackenzie, J. D. Determination of Water-to-Cement Ratio in Freshly Mixed Rapid-Setting Calcium Sulfoaluminate Concrete Using 2.45 GHz Microwave Radiation. *Cem. Concr. Res.* 2004, *34* (5), 807–812. https://doi.org/10.1016/J.C EMCONRES.2003.09.023.

(166) Tulasidas, T.; Ratti, C.; Raghavan, G. Modelling Microwave Drying of Grapes. *Can. Agicu ltural Eng.* 1997, *39* (1), 57–67.

(167) Changrue, V.; Raghavan, V. G.; Orsat, V.; Vijaya Raghavan, G. Microwave Drying of Frui ts and Vegetables. *Stewart Postharvest Rev.* 2006, *2* (6), 1–7. https://doi.org/10.2212/spr.2 006.6.4.

(168) Muralidhara, H. S.; Ensminger, D.; Putnam, A. Acoustic Dewatering And Drying (Low An d High Frequency): State Of The Art Review. *Dry. Technol.* 1985, *3* (4), 529–566. https://d oi.org/10.1080/07373938508916296.

(169) Ramisetty, K. A.; Pandit, A. B.; Gogate, P. R. Investigations into Ultrasound Induced Ato mization. *Ultrason. Sonochem.* 2013, *20* (1), 254–264. https://doi.org/10.1016/j.ultsonch.2 012.05.001.

(170) Goodridge, C. L.; Shi, W. T.; Hentschel, H. G. E.; Lathrop, D. P. Viscous Effects in Dropl et-Ejecting Capillary Waves. *Phys. Rev. E* 2002, *56* (1), 472–475. https://doi.org/10.1103/p hysreve.56.472.

(171) Lang, R. J. Ultrasonic Atomization of Liquids. *J. Acoust. Soc. Am.* 1962, *34* (1), 6–8. https://doi.org/10.1121/1.1909020.

(172) Levy, E. K.; Celeste, B. Combined Effects of Mechanical and Acoustic Vibrations on Fluidization of Cohesive Powders. *Powder Technol.* 2006, *163* (1–2), 41–50. https://doi.org/10.1016/j.powtec.2006.01.004.

(173) Peng, C.; Ravi, S.; Patel, V. K.; Momen, A. M.; Moghaddam, S. Physics of Direct-Contact Ultrasonic Cloth Drying Process. *Energy* 2017, *125*, 498–508. https://doi.org/10.1016/j.energy.2017.02.138.

(174) Carcel, J. .; García-Pérez, J. V.; Riega, E.; Rosselló, C.; Mulet, A. Drying Assisted by Power Ultrasound. *Mod. Dry. Technol. Process Intensif.* 2014, *5*, 237–277.

(175) Strumiłło, C.; Kudra, T. *Drying : Principles, Applications, and Design*; Gordon and Breach Science Publishers, 1986.

(176) Marinos-Kouris, D.; Maroulis, Z. B. Transport Properties in the Drying of Solids. In *Handbook of Industrial Drying, 3rd Edition*; Arun S. Mujumdar, Ed.; CRC Press: Boca Raton, 2006; pp 77–110. https://doi.org/10.1201/b17208.

(177) Liu, Y.; Sun, Y.; Miao, S.; Li, F.; Luo, D. Drying Characteristics of Ultrasound Assisted Hot Air Drying of Flos Lonicerae. *J. Food Sci. Technol.* 2015, *52* (8), 4955–4964. https://doi.org/10.1007/s13197-014-1612-3.

(178) Cárcel, J. a.; García-Pérez, J. V.; Riera, E.; Mulet, A. Influence of High Intensity Ultrasound on Drying Kinetics of Persimmon. *Dry. Technol.* 2007, *25* (May 2013), 185–193. https://doi.org/10.1080/07373930601161070.

(179) de la Fuente-Blanco, S.; Riera-Franco de Sarabia, E.; Acosta-Aparicio, V. M.; Blanco-Blanco, A.; Gallego-Ju??rez, J. A. Food Drying Process by Power Ultrasound. *Ultrasonics* 2006, *44* (SUPPL.), 523–527. https://doi.org/10.1016/j.ultras.2006.05.181.

(180) Awad, T. S.; Moharram, H. A.; Shaltout, O. E.; Asker, D.; Youssef, M. M. Applications of Ultrasound in Analysis, Processing and Quality Control of Food: A Review. *Food Res. Int.* 2012, *48* (2), 410–427. https://doi.org/10.1016/j.foodres.2012.05.004.

(181) Malhotra, K.; Law-Kwet-Cheong, L.; Mujumdar, A. S. Pressure-Drop Characteristics for Vibrated Beds of Dry and Sticky Particles. *Powder Technol.* 1984, *39* (1), 101–105. https://doi.org/10.1016/0032-5910(84)85026-3.

(182) Chen, Y. L.; Lin, P. S.; Peng, Y. L. Particle Agglomeration Characteristics in Vibro-Fluidized Bed Dryers. *Journal of Chemical Engineering of Japan*. 1991, pp 669–673.

(183) Telis-Romero, J.; Beristain, C. I.; Gabas, A. L.; Telis, V. R. N. Effect of Apparent Viscosity on the Pressure Drop during Fluidized Bed Drying of Soursop Pulp. *Chem. Eng. Process. Process Intensif.* 2007, *46* (7), 684–694. https://doi.org/10.1016/j.cep.2006.09.001.

(184) Meili, L.; Daleffe, R. V.; Ferreira, M. C.; Freire, J. T. Analysis of the Influence of Dimensi onless Vibration Number on the Drying of Pastes in Vibrofluidized Beds. *Dry. Technol.* 20 10, *28* (3), 402–411. https://doi.org/10.1080/07373931003645298.

(185) Nag, P. K.; Bhattacharya, A. Effect of Vibration on Natural Convection Heat Transfer from Vertical Fin Arrays. *Lett. Heat Mass Transf.* 1982, *9* (6), 487–498. https://doi.org/10.1016 /0094-4548(82)90020-0.

(186) Dawood, a. S.; Manocha, B. L.; Ali, S. M. J. The Effect of Vertical Vibrations on Natural Convection Heat Transfer from a Horizontal Cylinder. *Int. J. Heat Mass Transf.* 1981, *24* (3), 491–496. https://doi.org/10.1016/0017-9310(81)90056-9.

(187) Rao, M.; Lefèvre, F.; Khandekar, S.; Bonjour, J. Heat and Mass Transfer Mechanisms of a Self-Sustained Thermally Driven Oscillating Liquid-Vapour Meniscus. *Int. J. Heat Mass T ransf.* 2015, *86*, 519–530. https://doi.org/10.1016/j.ijheatmasstransfer.2015.03.015.

(188) Bakker, H. J.; Kropman, M. F.; Omta, A. W. Effect of Ions on the Structure and Dynamics of Liquid Water. *J. Phys. Condens. Matter* 2005, *17* (45), S3215–S3224. https://doi.org/10. 1088/0953-8984/17/45/004.

(189) Husseini, D. Al. Effects of Anions and Amino Acids on Surface Tension of Water, 2015. h ttps://doi.org/10.1021/ja012052.

(190) Leelamanie, D. A. L.; Karube, J. Soil-Water Contact Angle as Affected by the Aqueous El ectrolyte Concentration. *Soil Sci. Plant Nutr.* 2013, *59* (4), 501–508. https://doi.org/10.108 0/00380768.2013.809601.

(191) Merck Millipore. Système de purification d'eau Elix® 20 http://www.merckmillipore.com/ FR/fr/product/Elix-20-Water-Purification-System-120V,MM_NF-ZLXS60020?ReferrerU RL=https%3A%2F%2Fwww.google.fr%2F (accessed Sep 24, 2018).

(192) Padma, A. M.; Tiemann, T. T.; Alshaikh, A. B.; Akouri, R.; Song, M. J.; Hellström, M. Pro tocols for Rat Uterus Isolation and Decellularization: Applications for Uterus Tissue Engin eering and 3D Cell Culturing. In *Methods in Molecular Biology*; 2018; Vol. 1577, pp 161– 175. https://doi.org/10.1007/7651_2017_60.

(193) BRAND. Universal detergents https://www.brand.de/en/products/general-lab-products/det ergentsdisinfectents/universal-detergents/ (accessed Sep 25, 2018).

(194) Brüel&Kjær. Product Data of Type 4809 Vibration Exciter https://www.bksv.com/-/media/ literature/Product-Data/bp0231.ashx.

(195) Brüel&Kjær. Product Date of Type 8001 Impedance Head https://www.bksv.com/-/media/ literature/Product-Data/bp0244.ashx.

(196) Brüel&Kjær. System Data of LDS LASER_USB Vibration Control System https://www.b ksv.com/-/media/literature/Product-Data/bu3079.ashx.

(197) Brüel & Kjær. Specifications-LASER USB Shaker Control System https://www.bksv.com/-/media/literature/Product-Data/bu3079.ashx (accessed Sep 24, 2018).

(198) Brüel&Kjær. Product Data of Type 2718 Power Amplifier https://www.bksv.com/-/media/literature/Product-Data/bp1928.ashx.

(199) Global-Laser. LaserLyte-Flex Alignment System http://www.global-lasertech.co.uk/our-products/alignment-laser/laserlyte-flex-system/.

(200) Canon. Canon MP-E 65mm f/2.8 1-5x Macro Photo - Objectifs - Objectifs photo - Canon France https://www.canon.fr/lenses/mp-e-65mm-f-2-8-1-5x-macro-photo-lens/?utm_source=yieldkit&utm_medium=affiliate&utm_campaign=affiliate_window_FR&utm_term=143466 (accessed Oct 9, 2018).

(201) Sensirion. Datasheet SHT7x (SHT71, SHT75) www.sensirion.com (accessed Oct 10, 2018).

(202) Ntirogiannis, K.; Gatos, B.; Pratikakis, I. A Combined Approach for the Binarization of Handwritten Document Images. *Pattern Recognit. Lett.* 2014, *35* (1), 3–15. https://doi.org/10.1016/j.patrec.2012.09.026.

(203) Kalaiselvi, T. A Comparative Study on Thresholding Techniques for Gray Image Binarization. *Int. J. Adv. Res. Comput. Sci.* 2017, *8* (7), 1168–1172. https://doi.org/10.26483/ijarcs.v8i7.4510.

(204) Ntirogiannis, K.; Gatos, B.; Pratikakis, I. Performance Evaluation Methodology for Historical Document Image Binarization. *IEEE Trans. Image Process.* 2013, *22* (2), 595–609. https://doi.org/10.1109/TIP.2012.2219550.

(205) Sezgin, M.; Sankur, B. Survey over Image Thresholding Techniques and Quantitative Performance Evaluation. *J. Electron. Imaging* 2004, *13* (1), 146. https://doi.org/10.1117/1.1631315.

(206) Otsu, N. A Threshold Selection Method from Gray-Level Histograms. *IEEE Trans. Syst. Man. Cybern.* 1979, *9* (1), 62–66. https://doi.org/10.1109/TSMC.1979.4310076.

(207) Gatos, B.; Pratikakis, I.; Perantonis, S. J. Adaptive Degraded Document Image Binarization. *Pattern Recognit.* 2006, *39* (3), 317–327. https://doi.org/10.1016/j.patcog.2005.09.010.

(208) Farrahi Moghaddam, R.; Cheriet, M. AdOtsu: An Adaptive and Parameterless Generalization of Otsu's Method for Document Image Binarization. *Pattern Recognit.* 2012, *45* (6), 2419–2431. https://doi.org/10.1016/j.patcog.2011.12.013.

(209) Bataineh, B.; Abdullah, S. N. H. S.; Omar, K. An Adaptive Local Binarization Method for Document Images Based on a Novel Thresholding Method and Dynamic Windows. *Pattern Recognit. Lett.* 2011, *32* (14), 1805–1813. https://doi.org/10.1016/j.patrec.2011.08.001.

(210) Valizadeh, M.; Kabir, E. Binarization of Degraded Document Image Based on Feature Spa ce Partitioning and Classification. *Int. J. Doc. Anal. Recognit.* 2012, *15* (1), 57–69. https:// doi.org/10.1007/s10032-010-0142-4.

(211) Chaki, N.; Shaikh, S. H.; Saeed, K. Exploring Image Binarization Techniques. *Stud. Comp ut. Intell.* 2014, *560*, 5–16. https://doi.org/10.1007/978-81-322-1907-1.

(212) Trier, ØOsivind Due; Jain, A. K. Goal-Directed Evaluation of Binarization Methods. *IEEE Trans. Pattern Anal. Mach. Intell.* 1995, *17* (12), 1191–1201. https://doi.org/10.1109/34.47 6511.

(213) Chen, S.; Li, D. Image Binarization Focusing on Objects. *Neurocomputing* 2006, *69* (16–1 8), 2411–2415. https://doi.org/10.1016/j.neucom.2006.02.014.

(214) Qidwai, U.; Chen, C. H.; Chen, C. H. *Digital Image Processing*; Prentice Hall, 2009. https: //doi.org/10.1201/9781420079517.

(215) Varade, M. R. R.; Dhotre, P. M. R.; Pahurkar, M. A. B. A Survey on Various Median Filte ring Techniques for Removal of Impulse Noise from Digital Images . 2013, *2* (2), 606–609.

(216) AL-KHAZALI, H. A. H. Geometrical and Graphical Representations Analysis of Lissajous Figures in Rotor Dynamic System. *IOSR J. Eng.* 2013, *02* (05), 971–978. https://doi.org/1 0.9790/3021-0205971978.

(217) Wu, M.-S.; Tsai, W. H. Corrections for Lissajous Figures in Books. *Am. J. Phys.* 1983, *52* (7), 657–658. https://doi.org/10.1119/1.13960.

(218) Reynolds, O. An Experimental Investigation of the Circumstances Which Determine Whet her the Motion of Water Shall Be Direct or Sinuous, and of the Law of Resistance in Parall el Channels. *Philos. Trans. R. Soc. London* 1883, *174* (0), 935–982. https://doi.org/10.1098 /rstl.1883.0029.

(219) McKinley, G. H.; Renardy, M. Wolfgang von Ohnesorge. *Phys. Fluids* 2011, *23* (12). http s://doi.org/10.1063/1.3663616.

(220) Incropera; DeWitt; Bergman; Lavine. Fundamentals Of Heat And Mass Transfer. Wiley 20 06. https://doi.org/10.1016/j.applthermaleng.2011.03.022.

(221) De Corcuera JIR, C. R. P. Encyclopedia of Agricultural, Food, and Biological Engineering. *Choice Rev. Online* 2013, *41* (07), 41-3799-41–3799. https://doi.org/10.5860/choice.41-37 99.

(222) Ahn, S. J.; Rauh, W.; Warnecke, H.-J. Least-Squares Orthogonal Distances Fiting of Circl e, Sphere, Ellipse, Hyperbola, and Parabola. *Pattern Recognit.* 2001, *34*, 2283–2303. https: //doi.org/10.1016/B978-0-12-374709-9.00002-X.

(223) Ridruejo, A.; De Acha, N.; Elosúa, C.; Matías, I. R.; Arregui, F. J. An Optimized Method Based on Digitalized Lissajous Curve to Determine Lifetime of Luminescent Materials on

Optical Fiber Sensors. *J. Sensors* 2016, *2016*, 41–46. https://doi.org/10.1155/2016/6019439.

(224) Hoffman, J. W. Insulation Enhancement with Heat-Shrinkable Components. I. Medium Voltage. *IEEE Electr. Insul. Mag.* 2002, *7* (3), 16–23. https://doi.org/10.1109/57.79583.

(225) Ash, D. O.; Bagdzinski, I.; Clabburn, R. J. T. Heat-Shrinkable Plastics for Termination and Jointing of Power and Auxiliary Cables. *Proc. Inst. Electr. Eng.* 2010, *117* (7), 1365. https://doi.org/10.1049/piee.1970.0261.

(226) Zhang, M.; Wang, W.; Huang, Z.; Baghdadi, M.; Yuan, W.; Kvitkovic, J.; Pamidi, S.; Coombs, T. A. AC Loss Measurements for 2G HTS Racetrack Coils with Heat-Shrink Tube Insulation. *IEEE Trans. Appl. Supercond.* 2014, *24* (3), 1–4. https://doi.org/10.1109/TASC.2013.2285334.

(227) Kandasamy, R.; Hashim, I. Effect of Chemical Reaction, Heat and Mass Transfer on Nonlinear Boundary Layer Past a Porous Shrinking Sheet in the Presence of Suction. *Nucl. Eng. Des.* 2010, *240*, 933–939. https://doi.org/10.1016/j.nucengdes.2009.12.024.

(228) Hilpert, M.; Jirka, G. H.; Plate, E. J. Capillarity-induced Resonance of Oil Blobs in Capillary Tubes and Porous Media. *GEOPHYSICS* 2002, *65* (3), 874–883. https://doi.org/10.1190/1.1444784.

(229) Charlaix, E.; Gayvallet, H. Dynamics of a Harmonically Driven Fluid Interface in a Capillary. *J. Phys. II* 2003, *2* (11), 2025–2038. https://doi.org/10.1051/jp2:1992249.

(230) Dimon, P.; Kushnick, A. P.; Stokes, J. P. Resonance of a Liquid-Liquid Interface. *J. Phys.* 2007, *49* (5), 777–785. https://doi.org/10.1051/jphys:01988004905077700.

(231) Yuan, Y.; Lee, T. R. Contact Angle and Wetting Properties. In *Surface Science Techniques*; Bracco, G., Holst, B., Eds.; Springer Berlin Heidelberg: Berlin, Heidelberg, 2013; pp 3–34. https://doi.org/10.1007/978-3-642-34243-1_1.

(232) Yu, Z.; Dutton, R. W. Second Order Newton Iteration Method and Its Application to MOS Compact Modeling and Circuit Simulation. *VLSI Des.* 1998, *6* (1–4), 141–145. https://doi.org/10.1155/1998/59514.

(233) Ethington, E. F. Interfacial Contact Angle Measurements of Water, Mercury, Organic Liquids on Quartz, Calcite, Montmorillonite. *Constr. Build. Mater.* 1990, No. July, 583. https://doi.org/10.1016/j.conbuildmat.2005.09.001.

(234) Kestin, J.; Sokolov, M.; Wakeham, W. A. Viscosity of Liquid Water in the Range −8 °C to 150 °C. *J. Phys. Chem. Ref. Data* 2010, *7* (3), 941–948. https://doi.org/10.1063/1.555581.

(235) Mortensen, N. A.; Bruus, H. Universal Dynamics in the Onset of a Hagen-Poiseuille Flow. *Phys. Rev. E - Stat. Nonlinear, Soft Matter Phys.* 2006, *74* (1). https://doi.org/10.1103/PhysRevE.74.017301.

Titre : Étude microscopique du comportement de l'eau dans un pore unique soumis à des vibrations pour intensifier le séchage

Mots clés : Intensification du séchage, vibration, échelle du pore, traitement d'image, configurations symétriques et asymétriques

Une meilleure performance économique du séchage industriel consiste à la fois en l'amélioration de la qualité des produits et de l'optimisation énergétique. Plusieurs technologies peuvent être appliquées pour intensifier le processus de séchage. Ce travail s'intéresse à l'effet des vibrations, qui peuvent accélérer le séchage via un échauffement par dissipation visqueuse, une amélioration de la migration de l'eau liquide et de la vapeur à l'intérieur du milieu poreux et une augmentation des coefficients de transferts externes de chaleur de masse. Toutefois, malgré les études numériques et expérimentales antérieures, l'évaluation de l'importance relative de ces mécanismes d'intensification doit encore être améliorée.

Ce travail porte sur l'échelle du pore, simulée par un tube capillaire, partiellement rempli d'eau soumis à des vibrations sinusoïdales. Un dispositif expérimental complet a été conçu, développé et utilisé. Grâce à une procédure de traitement d'images pertinente, le comportement de l'eau à l'intérieur du tube (déplacement et le rayon du ménisque) ont été étudiés pour différentes configurations de vibrations (fréquence, amplitude, taille du tube). Les expériences avec des géométries symétriques et asymétriques sont destinées à imiter le transfert d'humidité pendant le séchage d'un milieu poreux. Quelle que soit la configuration étudiée, l'intensification du séchage a été clairement confirmée.

Pour la configuration symétrique, une nouvelle cartographie 2D basée sur des nombres adimensionnels est définie pour résumer les effets capillaires et visqueux, et ainsi expliquer le comportement de l'eau en fonction des conditions vibratoires (rayon du tube, fréquence et amplitude). Pour la configuration asymétrique, les résultats expérimentaux sont discutés et comparés aux simulations obtenues avec deux modèles numériques (un modèle 0-D et un modèle 1-D). Le potentiel de la modélisation a été mis en évidence, mais il est encore limité par les hypothèses physiques aux interfaces. D'autres développements sont proposés afin d'augmenter la plage de validité et d'approfondir l'étude de ce système physique.

Title: Microscopic study of the behavior of water in a single pore under vibration to intensify drying

Keywords: Drying intensification, vibration, pore scale, image processing, symmetrical and asymmetrical configurations

A better economic performance of industrial drying consists both in product quality improvement and energy efficiency enhancement. Several technologies can be applied to intensify the drying process. This work is focused on the effect of vibration that can assist the drying through heating-up due to viscous dissipation, enhancement of liquid and vapor migration inside the porous medium and the increase of the external heat and mass transfer. However, despite previous numerical and experimental studies, the assessment of the relative importance of these intensification mechanisms has still to be improved.

This work is focused on the pore scale, simulated by a capillary tube, partially filled with water subjected to sinusoidal vibrations. A full experimental device was conceived, developed and used. Thanks to a relevant image processing chain, the behavior of water inside the tube (displacement and meniscus radius), was investigated for various vibration configurations (frequency, amplitude, tube size). Experiments with both symmetrical and asymmetrical geometries are intended to mimic the moisture transfer during drying of a porous medium. Whatever the configuration, the drying intensification was clearly confirmed.

For the symmetrical configuration, a new 2D dimensionless number map is set to summarize the capillary and viscous effects and thus to explain the water behavior depending on vibration conditions (tube radius, frequency and amplitude). For the asymmetrical configuration, the experimental results are discussed and compared to the simulations obtained with two computational models (a 0-D model and 1-D model). The potential of modeling was evidenced but still limited by the surrounding physical assumptions. Further developments are proposed to increase the validity range and further investigate this physical system.